LIGHT-TISSUE INTERACTIONS FOR DEVELOPING PORTABLE AND WEARABLE OPTOELECTRONIC DEVICES FOR SENSING OF TISSUE CONDITION, DIAGNOSTICS AND TREATMENT IN PHOTODYNAMIC THERAPY (PDT)

Olena Kulyk

A Thesis Submitted for the Degree of PhD
at the
University of St Andrews

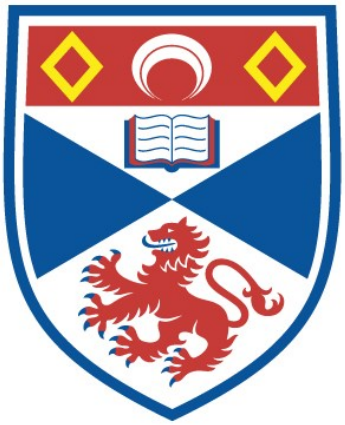

2016

Light-tissue interactions for developing portable and wearable optoelectronic devices for sensing of tissue condition, diagnostics and treatment in Photodynamic therapy (PDT)

Olena Kulyk

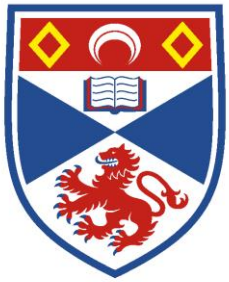

University of
St Andrews

This thesis is submitted in partial fulfilment for the degree of PhD
at the
University of St Andrews

September 2015

Abstract

This thesis presents the development and *in-vivo* applications of wearable and portable devices for the investigation of light interaction with tissue involved in Photodynamic therapy (PDT) and during contraction of muscles.

A hand-held device and a clinical method were developed for time course *in-vivo* imaging of the fluorescence of the photosensitizer Protoporphyrin IX (PpIX) in healthy and diseased skin with the aim to guide improvement of PDT protocols. The device was used in a small clinical study on 11 healthy volunteers and 13 patients diagnosed with non-melanoma skin cancer (NMSC). Two types of PpIX precursors were administered: Ameluz gel and Metvix® cream. The fluorescence was imaged with a 10 minute time step over three hours which was the recommended metabolism time before commencing PDT treatment at Ninewells Hospital, Dundee. The fluorescence time course was calculated by integrating the areas with the highest intensity. The fluorescence continued to grow in all subjects during the three hours. The time course varied between individuals. There was no statistical significance between either healthy volunteers or patients in Ameluz vs Metvix® groups; nor was there statistical difference between the three lesions groups (Actinic keratosis (AK) Ameluz vs AK Metvix® vs Basal cell carcinoma (BCC) Metvix®). The p-value was larger than 0.05 in a two sample t-test with unequal variances for all the groups. However, there was strong body site dependence between the head & neck compared to the lower leg & feet, or the trunk & hands body site groups (p-value<0.01). One of the possible explanations for this was temperature and vasculature variation in skin at different body sites: the temperature is higher and the vasculature structure is denser at the head and the neck compared to the lower leg or the trunk. The temperature was not measured during the study. So in order to support this hypothesis, typical skin temperatures at the lesion sites were taken from the IR thermal images of healthy skin available in literature. PpIX fluorescence had a positive correlation to temperature. If this hypothesis is true, it will be highly important to PDT treatment. Increasing the temperature could speed up the metabolism and reduce the waiting time before starting the treatment; ambient temperature should be taken into account for daylight PDT; cooling air as pain management should be administered with caution.

Potential improvements for wearable PDT light sources were investigated by modelling light transport in skin for the current LED-based Ambulight PDT device, a commercial OLED for future devices and a directional OLED developed in the group. The optical models were implemented in commercial optical software (with intrinsic Monte Carlo ray tracing and Henyey-Greenstein scattering approximation) which was

validated on diffuse reflectance and transmittance measurements using in-house made tissue phantoms. The modelling was applied to investigate the benefits from diffusive and forward scattering properties of skin on light transmission in treatment light sources. 1 mm thick skin can only compensate approximately 10% of non-uniform irradiance. It means that uniform illumination is crucial for the treatment light sources. Forward scattering in skin showed a 10% improved light transmission from a collimated emission compared to a wide angle Lamberian emission. However, depth-dependent transmission measurements of directional vs Lambertian emission from organic light emitting films (a nano-imprinted grating was fabricated to provide directional emission in one of the films), collimated vs diffused HeNe laser light through fresh porcine skin did not show the expected improvement. This could be explained by skin roughness which was previously found to change the optical properties and may also affect light coupling.

The modelling was applied to guide an optical design of another wearable device – a muscle contraction sensor. Muscle is fibrous and because of that scatters light differently in different directions. The sensor detects the change in backscattered light in parallel and perpendicular directions with respect to muscle fibres. The sensor was implemented on a wearable bandage on fully flexible substrate with flexible OLED and organic photodiodes. The major advantages of organic optoelectronic sensing compared to conventional electromyography (EMG) sensors are the ability to distinguish two types of contractions (isotonic and isometric), insensitivity to electromagnetic interference and the absence of an immune response due to non-invasive electrode-free sensing. Optical modelling was performed to understand the operation of the sensor. A 3D anisotropic optical model of scattering in muscle was created by geometrical manipulations with the standard Henyey-Greenstein scattering volumes. The penetration depth from the Super Yellow OLED was found to be 20-25 mm; the optimal separation between the source and the detector was found to be 20 mm. This distance provided a still detectable signal along with the best discrimination between the two backscatterings. When a 2 mm thick layer of skin and a 2 mm thick layer of adipose tissue were added to the model, the signal was hugely diffused. The discrimination between the two backscatterings decreased by three orders of magnitude, the penetration depth in muscle was reduced, and the intensity of the signal dropped down but was still detectable. With 5 mm thick adipose tissue and 2 mm thick skin the signal was too diffused and interacted with very shallow layers of muscle which approached the limits of the optical sensing of muscle activity.

Declaration

I, Olena Kulyk, hereby certify that this thesis, which is approximately 47,000 words in length, has been written by me, and that it is the record of work carried out by me, or principally by myself in collaboration with others as acknowledged, and that it has not been submitted in any previous application for a higher degree.

I was admitted as a research student in September 2011 and as a candidate for the degree of Doctor of Philosophy in September 2011; the higher study for which this is a record was carried out in the University of St Andrews between 2011 and 2015.

September 24, 2015 Olena Kulyk

I hereby certify that the candidate has fulfilled the conditions of the Resolution and Regulations appropriate for the degree of Doctor of Philosophy in the University of St Andrews and that the candidate is qualified to submit this thesis in application for that degree.

September 24, 2015 Ifor D.W. Samuel

Copyright Declaration

In submitting this thesis to the University of St Andrews we understand that we are giving permission for it to be made available for use in accordance with the regulations of the University Library for the time being in force, subject to any copyright vested in the work not being affected thereby. We also understand that the title and the abstract will be published, and that a copy of the work may be made and supplied to any bona fide library or research worker, that my thesis will be electronically accessible for personal or research use unless exempt by award of an embargo as requested below, and that the library has the right to migrate my thesis into new electronic forms as required to ensure continued access to the thesis. We have obtained any third-party copyright permissions that may be required in order to allow such access and migration or have requested the appropriate embargo below.

September 24, 2015 Olena Kulyk

September 24, 2015 Ifor D.W. Samuel

Embargo

The following is an agreed request by candidate and supervisor regarding the electronic publication of this thesis:

Access to all of the printed copy but embargo of all of the electronic publication of thesis for a period of 1 year on the following ground: publication would preclude future publication.

September 24, 2015 Olena Kulyk

September 24, 2015 Ifor D.W. Samuel

Acknowledgements

They have been hard yet great times during which I have gained experience and knowledge from the industry, in hospital and academia. I am grateful to the main person without whom this PhD would not be possible, to my supervisor, *Prof Ifor Samuel*. Ifor, thank you first of all for giving me the opportunity to undertake this PhD, then for sharing the knowledge, giving guidance and being supportive during this long slow journey. I learned from you not only the science, wearable organic optoelectronics and optical measurements but many other skills which I will be taking advantage of during the rest of my career. Among the most important interpersonal and public speaking skills for which I am particularly grateful are how to communicate and present my work to people from different backgrounds. From you, another invaluable skill I only partially mastered was of course how to be British – don't panic, have a cup of tea, and talk about the weather.

The working environment is a part of the ultimate success, I have been lucky to be surrounded by so many great and bright people in the group. I would like to thank to all the members (past and present) of the Organic Semiconductor Optoelectronics (OSO) Group for your help, support and the good times we had together. I really enjoyed being part of the OSO and will always remember my times there.

I am also thankful to my clinical supervisors, *Dr Sally Ibbotson, Prof Harry Moseley* and *Prof James Ferguson* for giving me an opportunity to work on and guiding me through clinically relevant questions. I am grateful for all the medical and biophysical knowledge you have shared with me. The research experience and knowledge I gained during the fluorescence study was priceless. Also, I would like to say thank you to my colleague *Dr Ronan Valentine* for his contribution to this study, for all the discussions and support.

I am grateful to *June Gardner*, my research coordinator who helped me to comply with the regulations, principles and standards of good clinical practice (GCP) of The Medicines for Human Use (Clinical Trials) regulations, guidance with the study protocol, supporting documentation, IRAS application, recruiting and consenting the participants for the study. Special thanks for the cookies, coffees and chit chat which made my journeys to Ninewells less useless after every next dropping out patient from my study.

I would like to say thank you for all of the technical staff at the Photobiology Unit, Ninewells hospital: *Lynn Fullerton, Andrea Cochrane, Leona Johnston, Laura Patullo, Shelagh Blackwood, Lesley Knight, Ronald Buist, & Gordon Brown* at PBU for helping during the measurements on healthy volunteers and patients. *Andrea,* massive thank you for helping with looking up my study patients records after I left St Andrews.

I am truly thankful to *Dr Ashu Bansal* for your valuable expertise, assistance and encouragement during my PhD. I deeply appreciate your contribution in light transmission measurements on porcine tissue and the opportunity to apply optical modelling for a wearable muscle contraction sensor. Thanks to your family for the dinners and little presents.

I would like to thank *Dr Shuyu Zhang* and *Dr Guohua Xie* for helping with characterisations of OLED light sources and fabricating organic light emitting films for studying light transmission in tissue.

I am thankful for *Dr Marion Giardini* for sharing his expertise on a broad range of subjects, using prototype equipment and the robotic arm for the work on the muscle contraction sensor. I would like thank to both Mario and his student *Pheng Toh* for the opportunity to use optical modelling for the study on wireless IR power transmission through brain phantom.

I am grateful to *Dr Andrew McNeill, Ambicare Health* for guidance in the industrial direction of my work and Ambulight PDT devices for testing.

Thank you, *Dr Gordon Hedley* for the IT businesses, for FRED, and keeping my remote desktop connections alive during my writing. I would like to jointly thank *Gordon* and *Dr Dimali Vithanage* for their cheering support.

I am grateful to *Dr Cameron Rae* for supervising my teaching at the University and advice on laser safety regulations.

I am thankful to *Scott Johnston*, *Martin McLaren & George* and *Chris Booth* for procurement and workshop jobs.

I would like to thank to the administrative staff *Wendy Clark, Lesley Aitken, Lee Stainford* and *Linda Cousins* and to the Department coffee-lady *Barbara*.

I have been privileged to share my “PhD experiences” with other fantastic PhDs in St Andrews and Dundee: *Guy Whitworth, Calvyn Howells, Alex Ward, Bernd Ebenhoch, & Paulina Morawska & Mateusz Tyrk*, and two home friends *Julia Solopchuk* and *Tetiana Voitsekhivska.* I will never forget what a great times we had! Guy thanks for all the activities we have done together: SPIE projects, kayaking, climbing and ballroom. Also I would like to thank my tango-friend *Phillip* for proof reading this thesis.

I would like to acknowledge the support from *the Scottish Funding Council* via a *SUPA INSPIRE studentship*, *the Organic Semiconductor Centre*, *the Photobiology Trust Fund*; and *the Minick of St Andrews butchers shop* for providing fresh porcine skin for light transmission measurements.

This work is dedicated to my parents and my sister

For Vira, Oleksandr and Ulyana

"And once the storm is over, you won't remember how you made it through, how you managed to survive. You won't even be sure, whether the storm is really over. But one thing is certain. When you come out of the storm, you won't be the same person who walked in. That's what this storm's all about."

— Haruki Murakami,

Hard-Boiled Wonderland and the End of the World

Abbreviations

AK – Actinic keratosis
ALA – 5-Aminolevulinic acid
Al_2O_3 – Aluminium oxide

BCC – Basal cell carcinoma,
BCC – Basal cell carcinoma
BD – Bowen disease

CAD – Computer-aided design
CCD – A charge-coupled device
CI – Chief Investigator
CO_2 – Carbon dioxide
CTA – Clinical trial authorisation
CWL – Central wavelength

EEG – Electroencephalographic
EMG – Electromyography
EoSRES – the East of Scotland Research Ethics Service
EUV – Extreme ultraviolet

FRED – a name of optical software, it doesn't stand for anything
FTDI – Future Technology Devices International, s Scottish semiconductor
FWHM - Full width at half maximum

GCP – Good Clinical Practice
GUI – Graphical user interface
GUIDE – Graphical user Interface development environment

HeNe – Helium Neon
HWHM - Half width at half maximum

IR – Infra red
IRAS – the Integrated Research Approval System

ISO – International Standards Organization

LED – Light emitting diode

MAL - Methyl Ester of 5-Aminolevulinic acid
MC – Monte Carlo
MHRA – Medicines and Healthcare products Regulatory Agency
MOSFET – Metal–oxide–semiconductor field-effect transistor

NA – Numerical aperture
ND – Neutral density
NEP – Noise equivalent power
NIR – Near infrared
NMSC – Non-melanoma skin cancer

$^1O_2$ – Singlet oxygen
$^3O_2$ – Triplet molecular oxygen
OBS – Optical biopsy system
OD – Optical density
OLED – Organic light emitting dioed
OMLC – Oregon Medical Laser Centre
OPD – Organic photodiodes

PBU – Photobiology unit, Ninewells hospital, Dundee
PCB – Printed circuit board
PDT – Photodynamic therapy
PI – Principal investigator
PIS – Participant Information Sheet
PLA – Polylactide plastic
PMMA – Polymethylmethacrylate (Acrylic) plastic
PpIX – Protoporphyrin IX

RANSAC – Random sample consensus geometrical transformation
RTV – Room temperature vulcanised

S_0 – Ground energy state
S_1 – Singlet energy state

sBCC – Superficial basal cell carcinoma

SCC – Squamous cell carcinoma

sEMG - Surface electromyography

SOP – Standard Operating Procedure

SY – Super Yellow polymer

T_1 – Triplet state

TACS – the Tayside medical science Centre

UV, UVA, UVB – Ultra violet, Ultra violet A, Ultra violet B

UTREC – The University of St Andrews Teaching and Research Ethics

UV-NIL – Ultra Violet Nanoimprint lithography

Vis – Visible

XUV – Extreme ultraviolet

Contents

Appendixes:

Chapter 1

From the visible cognize the invisible.

— Gregory Skovoroda (Григорій Сковорода), (1722 - 1794)
Ukrainian educator, humanist, philosopher, poet, composer

1.1 Introduction

Allegedly, as far back in history as before Christianity, the Egyptians and the Greeks split sunlight into colours through gems and built temples to expose the sick to individual colours of light believing that such heliotherapy (treating disease by sunlight) or chromo-therapy (treatment by colour) can heal illnesses[1,2]. The first scientific discovery that light could be used for treatment of diseases was made in 1893 by Finsen when he published his dissertation "On Light's Effect on the Skin." Later he used artificial light – an arc lamp to treat cutaneous tuberculosis (lupus vulgaris) (***Figure 1).*** In 1896 Finsen's work "On the application of concentrated chemical light beams in medicine" was published and the Finsen Institute for Phototherapy was founded. In 1903 he was awarded the second Nobel Prize in Physiology or Medicine 1903 "in recognition of his contribution to the treatment of diseases, especially lupus vulgaris, with concentrated light radiation, whereby he has opened a new avenue for medical science"[3].

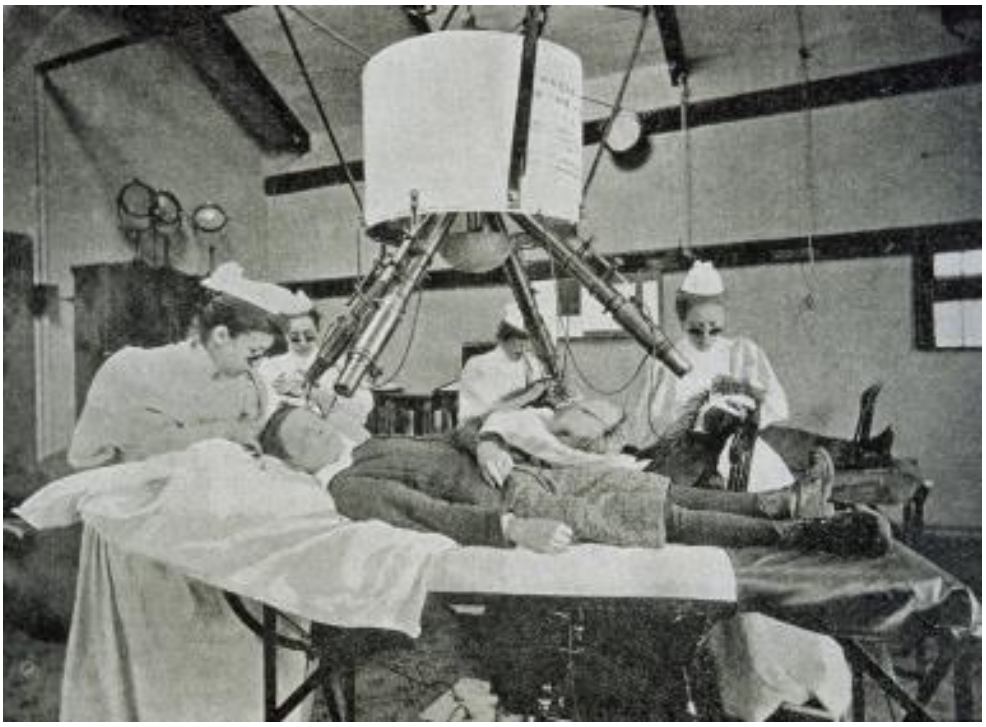

Figure 1: *Finsen light treatment for Lupus, 1900*

Further improvement after the development of artificial light was the application of photosensitising agents in combination with light to treat tumours. Finsen, Raab and Von Tappeiner were pioneers of light therapy and photobiology[4]. However, at that time there were a number of limitations in drugs and light delivery systems which delayed the widespread use of light therapy for decades. Light therapy saw renewed interest in the 1950s with the use of hematoporphyrin as a photosensitiser. The first governmental approval of PDT in clinic was in 1993 in Canada for treatment of bladder cancer using purified hematoporphyrin – Photofrin[5]. Now PDT has been used to treat about 30 types of skin diseases[6], and other cancers which are localized and do not proliferate such as cancer of the oesophagus and lung cancer [7,8].

Blue light alone can treat acne. The bacteria in sebaceous glands which cause acne generate endogenous porphyrins similar to the ones used from precursors in classical PDT treatment[9,10]. Blue light excites those porphyrins which results in a photodynamic reaction and toxic effect to the bacteria[11]. Although blue light is a part of the daylight spectrum; more intense and wavelength-specific blue light is more effective in fighting acne[12].

There is evidence that light can treat fungal infection of nails. Infrared laser light was reported to decrease trans-membrane potentials and generate reactive oxygen species (ROS)

which result in oxidative stress and death of bacteria and fungi[13]. It is listed as a 90% effective treatment for fungal nail infection on the NHS website[14].

Low Level Light therapy began in 1989 and suggested that IR and visible monochromatic light affects respiratory mitochondrial chains and ATP energy transport in cells[15]. At the start it was used to stimulate healing, reduce inflammation[17], and repair function for hair re-growth[18]. Current reports show that LLLT has clinical significance in treating herpes[19] and even brain injury[20].

Lasers are used to treat venous malformation and birth marks mostly due to overheating of tissue[21],[22]. The same controlled overheating effect induced by the lasers is widely used in aesthetics for hair and tattoo removal[23], skin resurfacing for scar removal and rejuvenation[24].

UVA and UVB light have been widely used for treating psoriasis[25]. The mechanisms of how UV light slows down the growth of psoriasis cells is not completely understood. Some of the reports found evidence that UV light slows down signal pathways in epidermal RNA gene expression which is responsible for proliferation of prosirasis[26]. This supports the theory that living cells may in fact use biophotons for communication[27,28]. Biophoton or ultra-weak spontaneous photon was described as a spontaneous weak emission of light by biological cells[29]. It is claimed to be a non-stimulated emission which is supposedly different and distinguishable from bioluminescence, fluorescence, phosphorescence or black body radiation[30,31]. Biophoton emission can be imaged with highly sensitive cooled CCD cameras in a controlled environment[32] to detect viability of cancer tissue[33,34], oxidative metabolic, intrinsic and stimulated antioxidant processes in skin as a response to UV radiation and other environmental factors[35,36].

This brings us to the use of light for sensing. There is a virtually limitless number of applications starting from fluorescence and finishing with optical coherence tomography. Naturally fluorescent proteins have revolutionised biology by visualising important aspects of diseases including tumour cell mobility, invasion, metastasis and angiogenesis[37]. Fluorescence can be excited in many biological molecules and studied using relatively simple microscopes or fluorescence cameras[38]. Among recent advances are: fluorescence life time imaging which can be used to study protein-protein interaction[39]; and FRET-based biosensors for real time imaging of HIV virus penetration in cells[40]. Another fluorescence imaging technique is based on tagging cells with green fluorescent protein (GFP). This was discovered in 2008 by Shimomura, Chalfie and Tsien who received a Nobel prize in Chemistry for GFP[41]. GFP is a fluorescent marker which enabled to the study of cell dynamics[42]. Nowadays GFP is used for single molecular super resolution imaging[43]. Betzig,Hell and Moerner were awarded the Nobel Prize for Chemistry in

2014 "for the development of super-reolved fluorescence microscopy[44]. Another advance is novel GFP synthesis suitable for two-photon absorption; potentially this could be used for non-invasive optical imaging of deep in tissue and in brain[45].

All the above demonstrates the enormous number of applications where light can be used for sensing, treatment and aesthetics employing various mechanisms of light-tissue interactions (***Figure*** *Error! No text of specified style in document.**.2***).

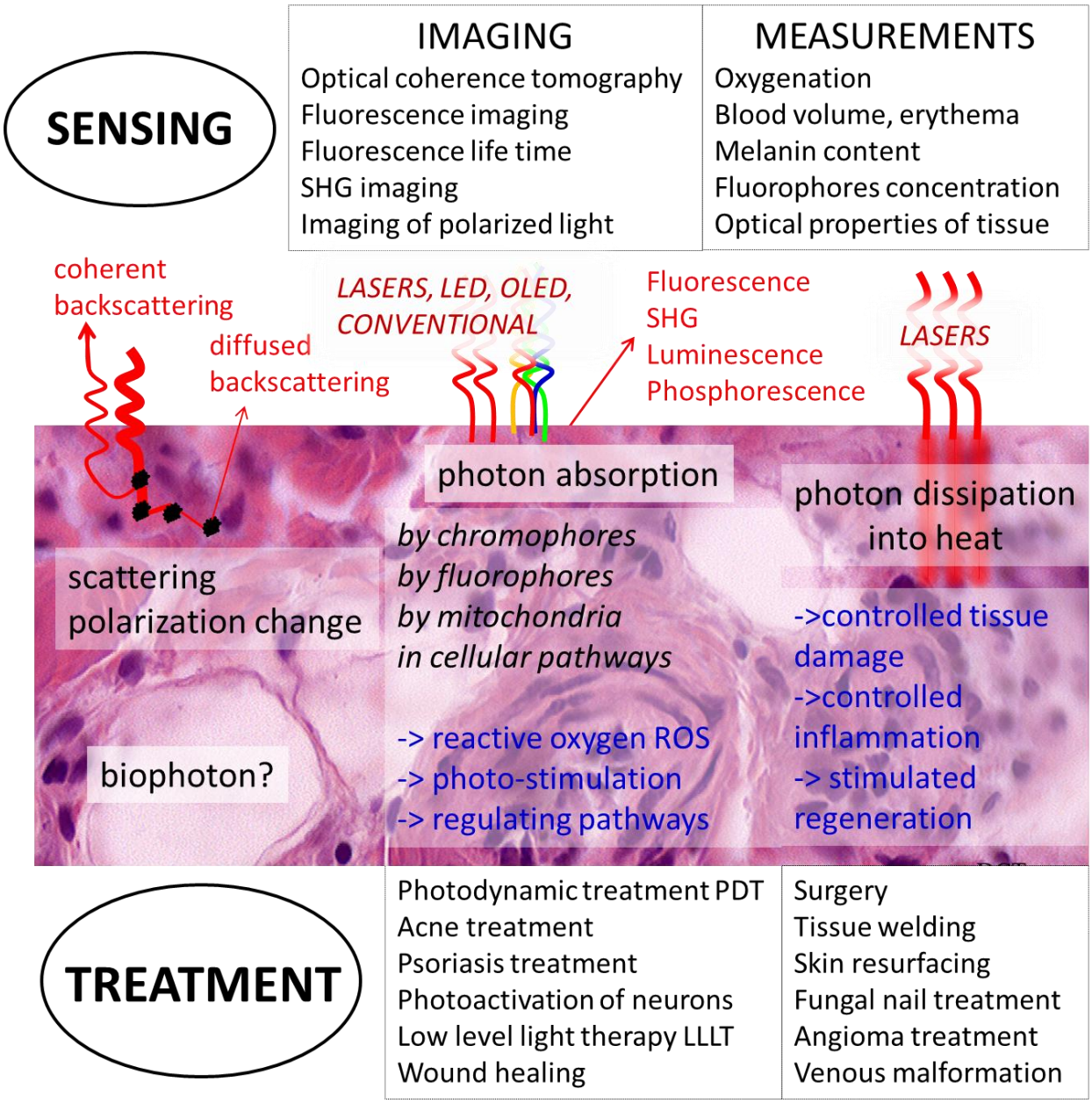

Figure Error! No text of specified style in document.**.2:** *Major light-tissue interactions and examples of their applications in treatment and sensing*

Technological advances in light sources, electronics and mobile technology gave rise to the development of cheap wearable sensors and treatment devices. Wearable technology and devices based on cell phones is a booming field nowadays[46]. R&D/venture creation firm PureTech published a review on digital medicine's emergence and listed some brand companies (not all!) working on the development of wearable sensors and mobile applications (***Figure** Error! No text of specified style in document.**.3***) [47].

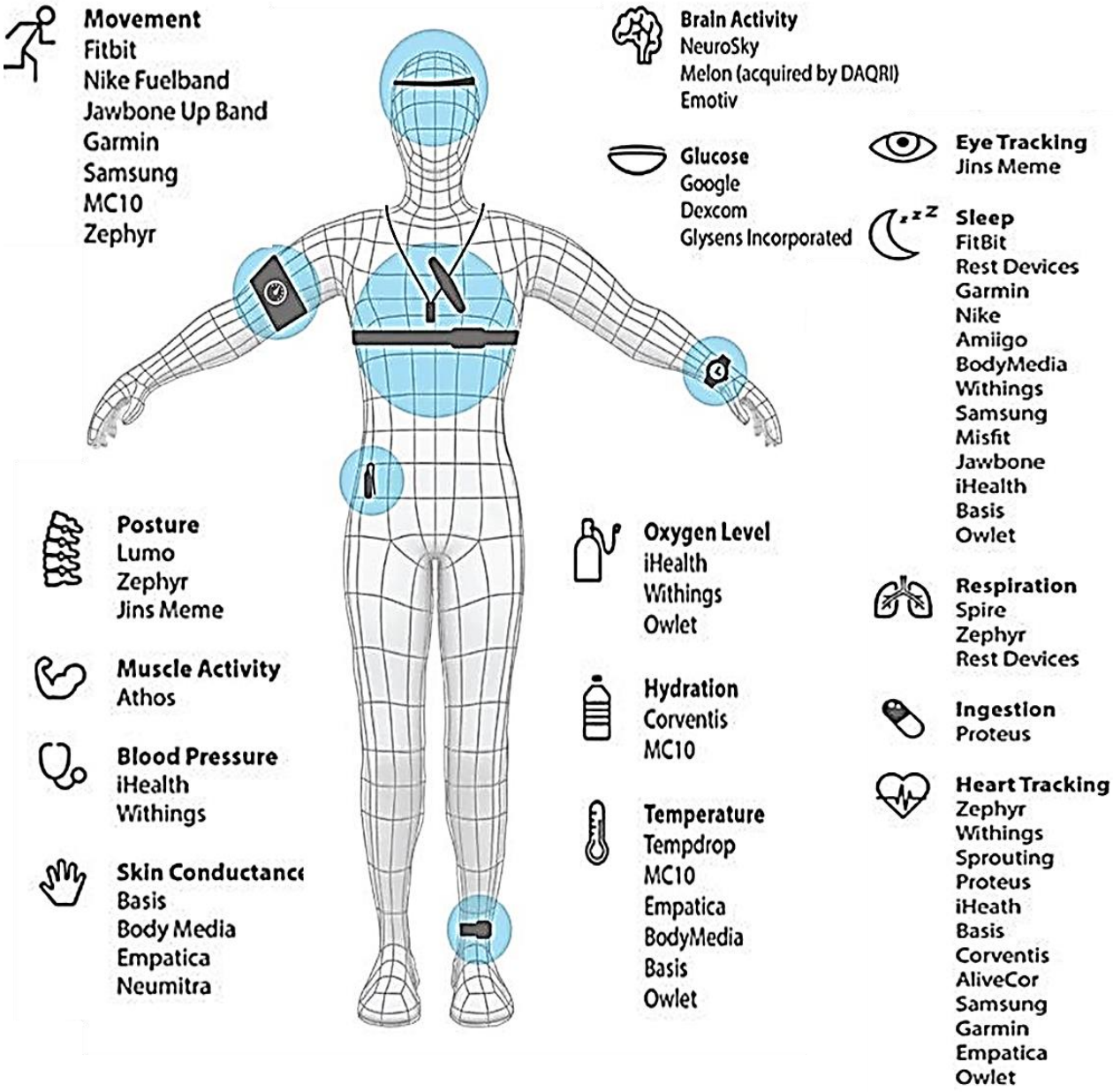

Figure Error! No text of specified style in document.**.3:** *Wearable sensors under development*[47]

Some of the examples of wearable devices based on smart phone technology include a Apple Watch which can track your daily activity now[48]. Smartphones can be used for sensing in ophthalmology, bodily fluids, monitoring bacteria, allergens and hormones in food[49]. Smartphones have also been recognised as providing reliable imaging devices for telemedicine to evaluate stroke patients in remote locations[50]; smartphone-based applications could help to prevent and manage cardiovascular disease and rehabilitation in groups of people with low socioeconomic status and developing countries[51].

Our Organic Semiconductor Centre has contributed to the field of wearable devices by developing and bringing to market ambulatory light sources for skin cancer[6,52,53] and acne treatment[12]; and the development of an optical muscle contraction sensor[54,55]. It is worth mentioning that organic electronics was used in both cancer treatment light sources and a muscle contraction sensor. The application of organic electronics in wearable technology and healthcare is another emerging field, offering appealingly thin, flexible, repeating the body shapes devices, and also tuneable properties for many applications[56,57]. Fabrication technology for organic devices is potentially cheap simply by spin-coating from solution[58,59].

PDT and PpIX fluorescence assisted cancer diagnostics were not left aside. Light sources based on a smartphone camera flash with some external accessories were reported to deliver the PDT treatment dose; also there is an accessory which enables PpIX imaging for assisting with PDT diagnostics or cancer detection[60]. Another portable device for PpIX fluorescence imaging was tested with a combination of cameras from a Sony Xperia® model "P" mobile phone and an Apple Ipod® to potentially assist with the display and imaging during the cervical intraepithelial neoplasia treatment[61].

The interest of this thesis only refers to a small part of this exciting area: Photodynamic therapy, fluorescence diagnostics and wearable devices. The concern of the thesis was mostly to pave ways to improve photodynamic treatment; the focus was on the development of portable instruments for convenient clinical studies and wearable light sources for ambulatory treatment and point-of-care diagnostics.

1.2 Thesis outline

The work in this thesis is connected by the theme of light tissue-interaction and developing wearable light sources for treatment and sensing. However, the application

described in each chapter relates to slightly different areas. Therefore each chapter has its own introduction and methods sections.

Chapter 2

This chapter is fully devoted to the development of a portable fluorescence imaging camera for the clinical study of protoporphyrin IX photosensitizer (PpIX) formation used for PDT. A number of fast prototyping techniques for developing optical and mechanical designs, 3D plastic printing, registering and working with images in Matlab, fabricating tissue phantoms and testing fluorescence imaging devices for clinical studies is outlined in the Methods section. The chapter will guide the reader through the important considerations for the development of a clinical research device with the focus on the NHS Good Clinical Practice (GCP) regulation for non-drug/device studies in terms of electrical safety, optical power output for implication in eye and skin safety, infection control, and allergic reactions. The results of the testing of the device on fluorescent phantoms, standard fluorescent solutions, PpIX fluorescence developed in the skin of a healthy volunteer administered Ameluz gel and two patients diagnosed with Actinic keratosis (AK) administered Ameluz PDT and biopsy-confirmed Basal cell carcinoma (BCC) administered Metvix® PDT are presented.

Chapter 3

This chapter describes the application of the developed hand-held fluorescence imaging camera in a small clinical study of healthy volunteers and patients representing non-melanoma skin cancer (NMSC). The reader can find guidance for developing clinical study protocols, ethical requirements and procedures to conduct a research study at Ninewells hospital, Dundee. There is a description of a the development of a fluorescence time course imaging method which is integrated in the routine PDT treatment of patients with NMSC at the Photobiology unit at Ninewells hospital. Observations from 11 healthy volunteers and 13 patients diagnosed with AK and BCC and administered two types of creams (Ameluz and Metvix®) are discussed. The images were processed in Matlab; the peak fluorescence areas were selected and the fluorescence was integrated for the time course analysis. The statistical significance in the fluorescence time course was calculated using two sample t-test with unequal variances. There results report on the statistical significance between two healthy volunteers groups: Ameluz v.s. Metvix®, three patients groups: AK Ameluz v.s. AK Metvix® v.s. BCC Metvix® groups, and three body side dependence patients groups: Head & Neck v.s. Trunk v.s. Lower leg & Hands. Body

side dependence which was discovered during this study was attributed to the temperature dependence and the vascularization density of the skin.

Chapter 4

This chapter is fully devoted to developing optical modelling, measurements and regression testing for characterising optical properties of tissue phantoms. The development of this apparatus was a necessary step for developing and testing devices and concepts for improving light propagation in skin. The approach taken was to use commercial optical design software for modelling light transport in comparison to previous groups which used custom programs in C or open source software. The capabilities of the software to model light propagation in tissue was tested on the previous results from one of the predecessors groups who used a custom Monte Carlo program in C programming language and diffuse reflectance measurements. The results of the simulations were in good agreement with the modelling and measurements from that group. The next step was to fabricate optical phantoms and build a diffuse reflectance measurements set up. The modelling was validated on the measurements on scattering silicone solid phantoms; the initial optical properties of the phantoms were adjusted with the help of regression (reverse) Monte Carlo modelling. This completed the development of optical apparatus for the development of the device and studying light transport in tissue. This apparatus was used for assisting with a feasibility study on wireless optical power transmission through gel brain phantom for potential application in implantable robotics. In this project an absolute power comparison was carried out and the conclusions were drawn on the most effective design of the solar panel. The final application of the optical apparatus which will be presented in this chapter was investigation of light propagation from ambulatory wearable devices (Ambulight PDT) through skin. The uniformity of light distribution, compensation of non-uniformities by diffusion in skin and the precautions in the drop of intensity at the edges was evaluated. The uniformity of the illumination field was cross-referenced with a commercial PDT lamps and compered with a potential OLED device. At the end there is an outline of important considerations for future devices.

Chapter 5

This chapter investigates the potential of directional OLEDs as improved light sources for PDT treatment. Skin has very strong forward scattering properties. So structured laser-like emission or collimated light could potentially improve penetration depth in the skin. This concept

was tested by the modelling and measurements of structured light from organic emitting films through porcine skin. The intention for this measurement was to obtain a comparison in the transmission from the two light sources which would have an impact on the medical community. Porcine skin seemed to be the best analogue to human skin. Although, surprisingly there was very little information in the literature on transmission measurements using porcine skin for the visible range. Also there was huge variation among the groups; the groups also reported that they observed large variations in their own measurements. However, considering that the experiment in this chapter did not intend to characterise porcine skin but have comparable measurements on the same skin samples for two light sources, the variation in the previous reports seemed to be not relevant for this experiment. Nonetheless, there were a few challenges to overcome First was how to dissect fresh porcine skin to enable depth dependent measurements. The thickness of the skin relevant to PDT treatment is 1-2 mm, so the step had to be at least 0.5 mm. Fresh skin is very greasy, stretchable and flexible which makes it challenging to fix and cut. In order to use standard dissection tools available in the School of Neurology or Biology the skin had to be frozen which would change the optical properties. So fresh tissue was dissected with a surgical scalpel with 0.5, 1.0, 1.5, 2.0, 2.5, 3 mm thickness. Another question was the change in optical properties of skin when the experiment was conducted in air. Due to the fact that there was a significant change over 3.5 hours, samples were placed in ultrasound gel. The transmission was imaged with a CCD camera using the organic films. The experiment was complemented with imaging the transmission from collimated and diffused laser light. Transmission was integrated over a few millimetres on the skin (30-150 pixels on the images). This area corresponded to the centre of the incident beams. The result was normalised on the incident power and compared with the modelling.

Chapter 6

The work in this chapter is an application of the optical modelling developed. Optical modelling was applied to understand the design of a wearable optical muscle contraction sensor. Due to the fibrous nature of muscle it scatters light in different proportions along and across the muscle fibres. When muscle contracts the fibre aspect ratio changes: the fibres become shorter and thicker. In the contracted muscle more light scatters across the muscle compared to the relaxed or elongated muscle. Measuring the relative difference in light scattering along and across the fibres enabled the development of an optical muscle contraction sensor[62]. The reported inorganic sensor was then implemented on a wearable bandage using fully flexible substrates and organic devices. It was used to drive a robotic arm to demonstrate the potential

of actuating prosthetic devices. My work was to investigate in the literature optical modelling and measurements for muscle tissue. First, a standard model of muscle with one dimensional Henyey-Greenstein scattering approximation was implemented in the same optical software. Light propagation from OLED made of Super Yellow polymer was modelled through individual layers of the tissue and then for the layered tissue. This helped to find penetration depth; study the effect of skin and fatty tissue to the probed signals, evaluate appropriate distance between the light source and the detectors. Then it was established what was responsible for 3D anisotropic scattering in muscle from the literature and this led to the implementation of a 3D optical model of muscle in the software. This model helped to better understand light propagation in layered tissue and make final conclusions for the best design of the sensor.

Chapter 7

This chapter presents the colclusions. The work outlined in this thesis looks at two major factors which are responsible for PDT treatment outcomes: the metabolism of PpIX and light transport. A prototype device developed to study PpIX formation in healthy and diseased skin was used in a small clinical study; the results of this study made a few interesting discoveries one of which is the effect of skin temperature on drug metabolism which can guide improvements in treatment protocols.

An optical apparatus developed during the PhD project was applied to investigate the possibility of wireless optical power transmission in brain phantoms and study the light transmission in skin for potential improvements in treatment PDT devices. A transmission measurements set up and a measurements procedure in fresh pork samples were developed to support the modelling results. In the end optical modelling was used to understand the design of a wearable fully organic muscle contraction sensor for potential application in a new generation of improved prosthetic devices.

The biggest ambition would be to integrate all the developed instruments and techniques (the regression (reverse) modelling for extracting optical properties, diffuse reflectance measurements and fluorescence imaging) with a treatment light source and add an oximeter to it. This configuration would enable measuring optical properties, PpIX concentration and oxygenation in real time. Information about the combination of these three parameters would enable the adjustments of light delivery in real time. In addition it would be useful to have

thermal imaging as well as it seems to correlate with the fluorescence. This is a subject for future investigation.

1.3 References

1. Conner-Kerr T. Light Therapy. In: Company FAD, ed. *Wund Healing. Evidence Based Management*. 4th ed. PA, USA; 2009:576-593.

2. Liberman J. *Light: Medicine of the Future*. (Vivino G, ed.). Rochester, Vermont: Bear & Company; 1990.

3. The Nobel Prize in Physiology or Medicine 1903. 2012. http://www.nobelprize.org/nobel_prizes/medicine/laureates/1903/.

4. Ackroyd R, Kelty C, Brown N, Reed M. The history of photodetection and photodynamic therapy. *Photochem Photobiol*. 2001;74(5):656-669. http://www.ncbi.nlm.nih.gov/pubmed/11723793.

5. Wilson B, Tuchin V. Advances in biophotonics. *NATO Sci Ser Ser I Life Behav Sci*. 2005;369:283.

6. I.D.W. Samuel JF and AM. OLEDS: Next generation photodynamic therapy of skin cancer. In: *PDT Book Chapter*.; :1-6.

7. Brown SB, Brown EA, Walker I. The present and future role of photodynamic therapy in cancer treatment. *Lancet Oncol*. 2004;5(8):497-508. doi:10.1016/S1470-2045(04)01529-3.

8. Photodynamic Therapy. *Am Cancer Soc Inc*. 2015. http://www.cancer.org/treatment/treatmentsandsideeffects/treatmenttypes/photodynamic-therapy.

9. Shu M, Kuo S, Wang Y, et al. Porphyrin metabolisms in human skin commensal Propionibacterium acnes bacteria: potential application to monitor human radiation risk. *Curr Med Chem*. 2013;20(4):562-568.

10. Borelli C, Merk K, Schaller M, et al. In vivo Porphyrin Production by P. acnes in Untreated Acne Patients and its Modulation by Acne Treatment. *Acta Derm Venereol*. 2006;86(4):316-319. doi:10.2340/00015555-0088.

11. Ashkenazi H, Malik Z, Harth Y, Nitzan Y. Eradication of Propionibacterium acnes by its endogenic porphyrins after illumination with high intensity blue light. *FEMS Immunol Med Microbiol*. 2003;35(1):17-24. doi:10.1016/S0928-8244(02)00423-6.

12. AmbicareHealthLtd. Lustre Pure Light treatment for acne. 2015. http://www.lustrepurelight.com/.

13. Bornstein E, Hermans W, Gridley S, Manni J. Near-infrared Photoinactivation of Bacteria and Fungi at Physiologic Temperatures. *Photochem Photobiol*. 2009;85(6):1364-1374. doi:10.1111/j.1751-1097.2009.00615.x.

14. NHS. NHS Choices: Treating a fungal nail infection. 2014. http://www.nhs.uk/Conditions/Fungal-nail-infection/Pages/Treatment.aspx. [accessed 12 Sept 2015]

15. Karu T. Laser biostimulation: a photobiological phenomenon. *J Photochem Photobiol B*. 1989;3(4):638-640. doi:2507763.

16. Manuscript A. NIH Public Access. *Changes*. 2012;29(6):997-1003. doi:10.1016/j.biotechadv.2011.08.021.Secreted.

17. Photobiomodulation - Low Level Light Therapy (LLLT). *Am Soc Laser Med Surg*. 2010. http://www.aslms.org/public/LowLevelLight.shtml.

18. Avci P, Gupta GK, Clark J, Wikonkal N, Hamblin MR. Low-level laser (light) therapy (LLLT) for treatment of hair loss. *Lasers Surg Med*. 2014;46(2):144-151. doi:10.1002/lsm.22170.

19. Schindl A, Neumann R. Low-Intensity Laser Therapy is an Effective Treatment for Recurrent Herpes Simplex Infection. Results from a Randomized Double-Blind Placebo-Controlled Study. *J Invest Dermatol*. 1999;113(2):221-223. doi:10.1046/j.1523-1747.1999.00684.x.

20. Dong T, Zhang Q, Hamblin MR, Wu MX. Low-level light in combination with metabolic modulators for effective therapy of injured brain. *J Cereb Blood Flow Metab*. 2015;35(9):1435-1444. doi:10.1038/jcbfm.2015.87.

21. Endovenous laser treatment. *2014F1096 GOSH NHS*. 2014. http://www.gosh.nhs.uk/medical-information/procedures-and-treatments/endovenous-laser-treatment. [accessed 12 Sept 2015]

22. Laser treatment for birthmarks. *2014F0339 GOSH NHS*. 2014. http://www.gosh.nhs.uk/medical-information/procedures-and-treatments/laser-treatment-birthmarks. [accessed 12 Sept 2015]

23. Non-surgical cosmetic procedures. *NHS Choices*. 2015. http://www.nhs.uk/Conditions/non-surgical-cosmetic-treatments/Pages/Introduction.aspx. [accessed 12 Sept 2015]

24. Fitzpatrick RE. Laser resurfacing. *Adv Dermatol*. 1997;13:463-501.

25. NHS. NHS Choices: Treating psoriasis. 2015. http://www.nhs.uk/conditions/psoriasis/pages/treatment.aspx. [accessed 12 Sept 2015]

26. Rácz E, Prens EP, Kurek D, et al. Effective Treatment of Psoriasis with Narrow-Band UVB Phototherapy Is Linked to Suppression of the IFN and Th17 Pathways. *J Invest Dermatol*. 2011;131(7):1547-1558. doi:10.1038/jid.2011.53.

27. Prasad A, Rossi C, Lamponi S, Pospíšil P, Foletti A. New perspective in cell communication: Potential role of ultra-weak photon emission. *J Photochem Photobiol B Biol*. 2014;(September 2015). doi:10.1016/j.jphotobiol.2014.03.004.

28. Sanders CL. Letter to the Editor: Speculations About Bystander and Biophotons. *Dose-Response*. 2014;12(4):515-517. doi:10.2203/dose-response.14-002.Sanders.

29. Popp FA, Wolf R. Biophoton Emission. New evidence for coherence and DNA as source. *Cell Biophys*. 1984;6:33-52.

30. Cifra M, Pospíšil P. Ultra-weak photon emission from biological samples: Definition, mechanisms, properties, detection and applications. *J Photochem Photobiol B Biol*. 2014;139:2-10. doi:10.1016/j.jphotobiol.2014.02.009.

31. Nerudová M, Červinková K, Hašek J, Cifra M. Optical spectral analysis of ultra-weak photon emission from tissue culture and yeast cells. In: Tománek P, Senderáková D, Páta P, eds. *Proc. SPIE 9450, Photonics, Devices, and Systems VI, 94500O (January 6, 2015)*.; 2015:94500O. doi:10.1117/12.2069897.

32. Prasad A, Pospíšil P. Towards the two-dimensional imaging of spontaneous ultra-weak photon emission from microbial, plant and animal cells. *Sci Rep*. 2013;3. doi:10.1038/srep01211.

33. Takeda M, Kobayashi M, Takayama M, et al. Biophoton detection as a novel technique for cancer imaging. *Cancer Sci*. 2004;95(8):656-661. doi:10.1111/j.1349-7006.2004.tb03325.x.

34. Takeda M, Kobayashi M, Takayama M, et al. Biophoton detection as a novel technique for cancer imaging. *Cancer Sci*. 2004;95(8):656-661. doi:10.1111/j.1349-7006.2004.tb03325.x.

35. Rastogi A, Pospíšil P. Spontaneous ultraweak photon emission imaging of oxidative metabolic processes in human skin: effect of molecular oxygen and antioxidant defense system. *J Biomed Opt*. 2011;16(9):096005. doi:10.1117/1.3616135.

36. Rastogi A, Pospíšil P. Ultra-weak photon emission as a non-invasive tool for monitoring of oxidative processes in the epidermal cells of human skin: comparative study on the dorsal and the palm side of the hand. *Ski Res Technol*. 2010. doi:10.1111/j.1600-0846.2010.00442.x.

37. Hoffman RM. The multiple uses of fluorescent proteins to visualize cancer in vivo. *Nat Rev Cancer*. 2005;5(10):796-806. doi:10.1038/nrc1717.

38. Spring KR, Davison MW. Introduction to Fluorescence Microscopy. *Nikon Microsc*. 2013. https://www.microscopyu.com/articles/fluorescence/fluorescenceintro.html.

39. Sun Y, Day RN, Periasamy A. Investigating protein-protein interactions in living cells using fluorescence lifetime imaging microscopy. *Nat Protoc*. 2011;6(9):1324-1340. doi:10.1038/nprot.2011.364.

40. Jones DM, Padilla-Parra S. Imaging real-time HIV-1 virion fusion with FRET-based biosensors. *Sci Rep*. 2015;5:13449. doi:10.1038/srep13449.

41. Nobel.org. “for the discovery and development of the green fluorescent protein, GFP.” *Nobelprize.org*. 2008;38(10):2821-2822. doi:10.1039/b917331p.

42. Shimomura O. Discovery of Green Fluorescent Protein (GFP) (Nobel Lecture). *Angew Chemie Int Ed*. 2009;48(31):5590-5602. doi:10.1002/anie.200902240.

43. Shaner NC, Lambert GG, Chammas A, et al. A bright monomeric green fluorescent protein derived from Branchiostoma lanceolatum. *Nat Methods*. 2013;10(5):407-409. doi:10.1038/nmeth.2413.

44. Forsén S. The Nobel Prize in Chemistry. *Trends Sci*. 2002;7(7):41-44. doi:10.5363/tits.7.7_41.

45. Stoltzfus CR, Barnett LM, Drobizhev M, et al. Two-photon directed evolution of green fluorescent proteins. *Sci Rep*. 2015;5:11968. doi:10.1038/srep11968.

46. Rettner R. Wearable Technology. *LiveScience*. 2015. http://www.livescience.com/topics/wearable-technology/.

47. Elenko E, Underwood L, Zohar D. Defining digital medicine. *Nat Biotechnol*. 2015;33(5):456-461. doi:10.1038/nbt.3222.

48. A smarter way to look at health and fitness. *Apple Inc Heal Fit*. 2015. http://www.apple.com/watch/health-and-fitness/. [accessed 12 Sept 2015]

49. Mobile science. *Nat Photonics*. 2014;8(10):745-745. doi:10.1038/nphoton.2014.241.

50. Demaerschalk BM, Vargas JE, Channer DD, et al. Smartphone Teleradiology Application Is Successfully Incorporated Into a Telestroke Network Environment. *Stroke*. 2012;43(11):3098-3101. doi:10.1161/STROKEAHA.112.669325.

51. Neubeck L, Lowres N, Benjamin EJ, Freedman S Ben, Coorey G, Redfern J. The mobile revolution—using smartphone apps to prevent cardiovascular disease. *Nat Rev Cardiol*. 2015;12(6):350-360. doi:10.1038/nrcardio.2015.34.

52. Moseley H, Allen JW, Ibbotson S, et al. Ambulatory photodynamic therapy: a new concept in delivering photodynamic therapy. *Br J Dermatol*. 2006;154(4):747-750. doi:10.1111/j.1365-2133.2006.07145.x.

53. Attili SK, Lesar A, McNeill A, et al. An open pilot study of ambulatory photodynamic therapy using a wearable low-irradiance organic light-emitting diode light source in the treatment of nonmelanoma skin cancer. *Br J Dermatol*. 2009;161(1):170-173. doi:10.1111/j.1365-2133.2009.09096.x.

54. Bansal AK, Hou S, Kulyk O, Bowman EM, Samuel IDW. Wearable Organic Optoelectronic Sensors for Medicine. *Adv Mater*. 2014. doi:10.1002/adma.201403560.

55. Engineering: Muscle sensor controls robot arm. *Nature*. 2015;517(7533):124-124. doi:10.1038/517124b.

56. Lochner CM, Khan Y, Pierre A, Arias AC. All-organic optoelectronic sensor for pulse oximetry. *Nat Commun*. 2014;5:5745. doi:10.1038/ncomms6745.

57. Shinar J, Shinar R. Organic light-emitting devices (OLEDs) and OLED-based chemical and biological sensors: an overview. *J Phys D Appl Phys*. 2008;41(13):133001. doi:10.1088/0022-3727/41/13/133001.

58. Forrest SR. The path to ubiquitous and low-cost organic electronic appliances on plastic. *Nature*. 2004;428(6986):911-918. doi:10.1038/nature02498.

59. Embracing the organics world. *Nat Mater*. 2013;12(7):591-591. doi:10.1038/nmat3707.

60. Hempstead J, Jones DP, Ziouche A, et al. Low-cost photodynamic therapy devices for global health settings: Characterization of battery-powered LED performance and smartphone imaging in 3D tumor models. *Sci Rep*. 2015;5:10093. doi:10.1038/srep10093.

61. Carbinatto FM, Inada NM, Lombardi W, et al. Comparison between two portable devices for widefield PpIX fluorescence during cervical intraepithelial neoplasia treatment. 2015;(MAY):953140. doi:10.1117/12.2180914.

62. Chianura A, Giardini ME. An electrooptical muscle contraction sensor. *Med Biol Eng Comput*. 2010;48(7):731-734. doi:10.1007/s11517-010-0626-x.

Chapter 2

Instrument development for measuring fluorescence and assisting with the monitoring of Photodynamic therapy (PDT) of skin cancer

> You can't connect the dots looking forward; you can only connect them looking backwards. So you have to trust that the dots will somehow connect in your future
>
> **— Steve Jobs, Entrepreneur,**
> **Stanford Report, June 14, 2005**

2.1 Introduction

In this chapter general background concerning the development of skin cancer and PDT treatment will be covered. The research focus will be made on the clinical importance of fluorescence diagnostics for studying the drug metabolism used in PDT treatment and the need for the development of a portable instrument which would enable *in-vivo* fluorescence imaging and quantities display by following a simple measurement protocol. The chapter will cover many aspects in the development of research instrumentation for clinical studies. Good clinical practice requirements for developing a prototype device and a number of fast prototyping techniques and development stages will be described. The chapter will culminate on a pre-clinical testing of the device on the fluorescence from healthy volunteers and patients diagnosed with non-melanoma skin cancer (NMSC).

Skin is the largest organ in human body. It regulates temperature when it is too cold or too hot, protects our body from injuries and infections and performs secretions functions. Skin consists of three layers – epidermis (upper layer), dermis (middle layer) and subcutaneous tissue (the lowest layer)[1]. The outermost part of epidermis is stratum corneum which consists of

corneocytes. Corneocytes are anucleated cells differentiated from nucleated keratinocytes present in deeper layers of epidermis. It was well established that the exposure to UV light results in DNA damage in keratinocytes and local immunosuppression which increases the risks of developing skin cancer[2,3]. By the recent reports only 65 % of melanoma cancers but as much as 90% of NMSC are associated with UV exposure[4]. That study also reports that sunscreen lotions do not reduce the risks of developing this cancer and chemoprotection is needed. Among the other factors responsible for promotion of the development of tumours except DNA damage is inflammation induced by UV exposure. Inflammation increases blood flow and vascular permeability which results in infiltrating leukocytes secreting a variety of proinflammatory signalling proteins which increase chances of tumour development[4]. It has already been established that melanoma skin cancer has genetic nature too. The genome of melanoma skin cancer was studied in one person and found to be able to repair cancer DNA sequences[5]. Another five-year study on 331 patients reported the discovery of four melanoma genetic subtypes[6]. There are some genomes which are associated with non-melanoma skin cancers, but the genetic nature of NMSC is still under investigation[7]. Other risk factors are immunosuppression in organ transplant patients which increases the chance of developing skin cancer to 65-250 times[8] and environmental pollutants[3]. Skin cancer starts in the epidermis. When it proliferates on the surface and into deeper layers it can lead to metastasis and the spread of tumours to other organs. That is why skin cancer has to be treated in its early stages[3].

Non-melanoma skin cancer (NMSC) is one of the most common cancers in the world. It occurs with the highest rates in Australia and is less common in Africa[9]. In Australia in 2008 there were 79,792 new cases of NMSC with 382 lethal outcomes; the growth rates doubled that year[10]. Incidence of NMSC is increasing worldwide; the UK has the highest rates in Europe[9]. The highest occurrence of NMSC in the UK is in the South West of England with the incidence of 121 cases over 100 000 people per year[9]. In total in the UK there were 102,628 new cases for all NMSC in 2011[11]. Due to a large number of NMSC cases every year, it is has become a substantial health problem to National Health Services worldwide.

The most common NMSCs are basal cell carcinoma (BCC) and Bowen's disease (BD). Actinic keratosis (AK) is a pre-malignant condition commonly occurring due to accumulation of sun damage. If left untreated AK can progress to squamous cell carcinoma (SCC)[12]. NMSC and dysplasia develop generally in fair skin mostly because of sun damage. Amongst the other risk factors there are radiation exposure, immune compromise, and human papillomavirus infections. NMSC and dysplasia differ by affecting various skin cells and layers. For instance, actinic

keratosis develops in epidermis and represents atypical keratinocytes. Basal cell carcinoma mostly affects follicular germinative cells – trichoblasts[13].

Amongst the treatment methods, topical Photodynamic therapy (PDT) has been widely used in dermatology for superficial NMSC and dysplasia with overall 70-90% clearance rates[14,15,16]. There are British and International Guidelines for the use of PDT in these conditions [14,15]. PDT can be used to treat 30 types of skin lesions[17]. The most common diagnoses treated by PDT are superficial BCC, BD, and AK[1,2,16]. Topical PDT is non-invasive, provides good tumour response, excellent healing and cosmetic outcome[18]. Topical PDT works by applying dermatological cream – pre-cursor of a photosensitizer and delivering excitation light afterwards. There are many studies to advance the photosensitizers, but this is beyond this thesis. The most clinically relevant advances in the drug development area are the developments of new upconversional particles which absorb NIR wavelength (980 nm) and re-emit in the visible range. Upconversional particles serve as a carrier and the photosensitizer is a cargo. The photosensitizer absorbs upconverted photons in the visible range; this leads to the conventional photodynamic reactions which are described in the next paragraph. The advantage of these drugs with the upconversion particles are that NIR light penetrates beyond 1 cm depth which would allow treating deeper cancers such as colon, lungs, breasts, stomach and others. A few studies reported good responses to PDT in mice studies; one of them used mesoporous silica nanoparticles with MC540 and ZnPc photosensitizers[19]. Silica nanoparticles have been successfully used for loading and transporting of drugs; without the drug silica nanoparticles have good biocompatibility and negligible phototoxic effect[20]. Another study reported similar concept: core–shell nanoconstructed particles with a titanium dioxide (TiO2) photosensitizer[21]. The study reports stable carriage of the photosensitizer to the tumours, good biocompatibility and reproducible PDT results. The most common photosensitizer for the conventional PDT is protoporphyrin IX (PpIX).

When the dermatological creams are applied (Ameluze gel, 5-Aminolaevulinic acid ALA-based or Metvix®, methylated ester MAL based) PpIX is metabolised via the haem biosynthetic pathway. Concentration of ALA and MAL in tissues depends on surface permeability[22]. PpIX metabolism in tumours is 15 times higher than in normal tissue[23]. PpIX is present in small concentrations in normal cells and is involved in synthesis of the heme molecule during normal metabolism. There are a few hypotheses for what is responsible for the increased PpIX metabolism in tumours. The first factor is attributed to reduced ferrochelatase activity or iron deficiency in abnormal cells. Enzyme ferrochelatase present in mitochondrion is responsible for catalysis of the insertion of the ferrous (form of iron) into PpIX. This catalytic reaction results in

the synthesis of PpIX into heme. Another factor can be the speed of reaction. Synthesis of PpIX into heame is relatively slow in normal cells. Abnormal cells tend to metabolise PpIX from endogenous precursors at much faster speeds than the conversion reaction of PpIX to heme[24]. And the last factor responsible for the increased PpIX metabolism in tumours could be that abnormal epidermis and stratum corneum could simply have better diffusion to the ALA and MAL pro-drugs[25].

Excitation of PpIX by light in the presence of molecular oxygen results in type II photodynamic reaction (photosensitization) during which the photosensitiser in a triplet state reacts first with molecular oxygen producing reactive oxygen. Photophysical processes involved in PDT are shown in **Figure 2.1**.

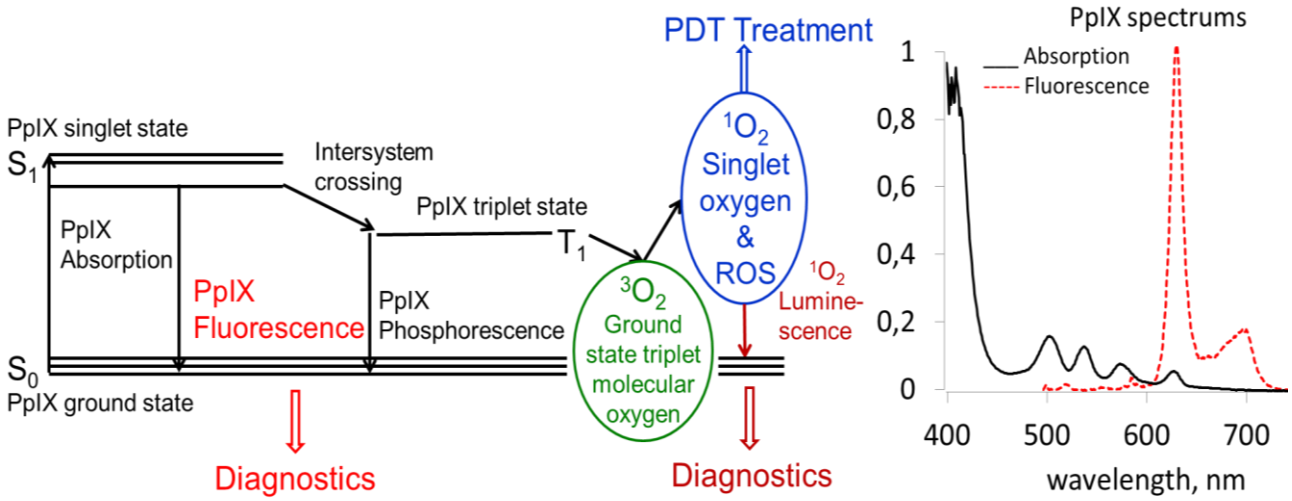

Figure 2.1: *Energy transition processes involved in Photodynamic treatment and diagnostics, photoabsorption and photoemission spectrums of PpIX*

PpIX has a few absorption peaks starting from 405 nm which is the most prominent, then a couple of green and an orange peaks at 505 nm, 540 nm and 576 nm and the last red one is 633 nm. An absorption of light excites PpIX to a singlet state that can undergo intersystem crossing to a long-lived triplet state[26,27]. Triplet state of PpIX has much longer life time than singlet state and was reported to be 52 μs[27]. Triplet state of PpIX can be quenched by the ground state of molecular oxygen which is then excited to a singlet state. Singlet oxygen can decay back to the ground state via phosphorescence or luminescence. Phosphorescence measurement of singlet oxygen at 1275 nm showed that the rise time of singlet oxygen is dependent on the concentration of PpIX, it is faster for lower concentrations of PpIX[26]. This study also reported that the life time of signet oxygen decreases with the increase of PpIX concentration. Singlet oxygen and other reactive oxygen species (ROS) are cytotoxic and induce

oxidative stress to the proteins and lipid membranes of cells. This oxidative stress ultimately results in cell death[28,29]. Although, singlet oxygen can also extensively damage DNA (strand breaks and base modification) it seems to have a secondary role and is not involved in phototoxic effect to the cells[18].

Singlet oxygen is an ultimate factor which defines the response of the lesions[30]. Singlet oxygen is luminescent at 1270 nm life time equal to 500 to 2000 ns[31]. There are many background sources at this emission wavelength such as background scattering, photosensitizer fluorescence and phosphorescence[32]. Short luminescence life time and backgrounds make it challenging to accurately measure the luminescence and extract the concentration values of singlet oxygen during PDT treatment[33]. One method could be to use single-photon counting detectors[34]. In one of the reports such a detector was based on optical fibres. The luminescent signal was verified by narrow band spectral filtering and chemical quenching of the photosensitized used in the experiments. [35] Analysing the kinetics was reported to significantly increase accuracy in estimating singlet oxygen from the luminescence measurements[31]. Another method which can be used to study the formation of singlet oxygen in cells is luminescence microspectroscopy [36]

The other emissive process involved in PDT photophysical reactions is PpIX decay from a singlet excited state back to the ground state; this process is called fluorescence[29,30]. PpIX has emission peaks are at 633 nm and broader peak at 700 nm. Fluorescence life time is 1.2 ns and shorter in living cells compared to the solutions[37]. Another study reported a 19.2 ns PpIX fluorescence life time[27]. PpIX phosphorescence is another radiative decay process, but at a longer wavelength (840 nm) and with a longer lifetime[26].

PpIX fluorescence can be used as an indicator of PpIX concentration in tissue. PpIX fluorescence shows the concentration of accumulated PpIX, but and also can be used for calculating singlet oxygen by taking into account the fluence rate of excitation light and quantum yield of singlet oxygen. Measuring PpIX fluorescence is a much simpler technique to allow for calculation of singlet oxygen compared to challenging direct measurements of luminescence of singlet oxygen. Also PpIX fluorescence diagnostics can distinguish pre-clinical malignant changes in skin, and NMSC[38,39,40]. Another use of PpIX fluorescence diagnostics is the investigation of PpIX metabolism from the pro-drugs which is of high clinical importance[29,39].

The outcomes of PDT treatment are dependent on the combination of three key treatment factors: concentration of molecular oxygen in tissue, excitation light and PpIX distribution[41]. It has been reported that lower irradiances result in more efficient generation of

singlet oxygen because of better availability of molecular oxygen. For high irradiances the diffusion of oxygen from the vessels is lower than the concentration of excited PpIX[42,43].

Pain is among one of the strongest adverse effects of PDT. In some cases it is unbearable for the patients and the treatment has to be paused or terminated[44]. Pain seems to be correlated to the size of the lesion and erythema (skin redness as a response to the treatment) but be independent of the concentration of photosensitizer[45]. Mechanisms of PDT-induced pain are unclear[44,46,47]. During one of the discussions with an expert in pain mechanisms an interesting hypothesis came up relating to one of the possible mechanisms of pain involved in PDT. Singlet oxygen may diffuse into heat receptors in skin. It then oxidises the receptors. This may induce painful sensations. Due to the fact that the depth of the heat receptors in skin varies between individuals this could explain different grades of experienced pain during PDT in different patients, and poor correlation between PpIX fluorescence and pain. Nonetheless PDT is painful, it is not recommended to interfere with reactivity of singlet oxygen for pain relief because it might have an adverse effect on the clinical outcome. Topical methods for pain relief can interfere with PDT efficacy because of their high pH, which interferes with the stability acidic ALA or MAL. Possible pain relief methods which do not have an adverse effect to clinical outcome include nerve blocks[46]. Pain can be reduced when a different light delivery is used; it was reported lower for pulsed light[48]. Also low irradiance light sources in addition to providing better clinical outcomes provide less painful PDT treatment[17,49,50]. One of the recent studies showed that reduced PpIX metabolism times increase the specificity of PpIX accumulation, reduce photo bleaching rates and reduce pain. This study reported on correlation between photobleaching and pain, and also between erythema and pain. The conclusion of this study was to shorten incubation times for PpIX and apply Pulse PDT[51]. Erythema (inflammation) after PDT can also be painful; the same group showed that administration of topical corticosteroid reduces the inflammation without compromising the response to PDT in a randomised study on AK[52].

As well as the pain factor, another problem is attributed to incomplete responses or recurrence of the lesions. The overall response rates to PDT are 70-90% depending on the type of the lesion[53]. A possible cause for recurrence or incomplete response may be insufficient PpIX metabolism in the lesions[53,54,55]. PpIX metabolism was studied by measuring PpIX fluorescence spectrum at one point by conventional non-time resolved spectrometers and analysing the peak fluorescence. PpIX metabolism reaches its plateau concentration after six hours of application of ALA (5-aminolevulinic acid) as a pro-drug with the full incubation period of 24 hours[56]. For MAL (methylester of 5-aminolevulinic acid) the plateau concentration in both BCC and AK lesions is

established after 13 hours of continuous application[57]. However, the time which is recommended for the creams to metabolise into PpIX before commencing PDT treatment is three hours[14,15]. Yet, there is insufficient information in the literature about PpIX metabolism at shorter periods of time[56,57, 58]. Detecting surface fluorescence is one of the best choices so far to study PpIX formation in the skin. There are studies which have reported development of optical spectrometers for various medical applications[39,53,55,59,60]. However, most of the systems are cumbersome and were not suitable for *in-vivo* time course imaging.

In addition to exogenous PpIX fluorescence developed from the pro-drugs, endogenous auto-fluorescence can also be used to detect malignant changes in tissue. The development of the lesions entails structural changes of the malignant skin due to the change in production of collagen, elastin and keratin. The metabolism rates and the relative amount of NADH (nicotinamide adenine dinucleotide) and FAD (flavin adenine dinucleotide) which are responsible for energy production in cells are different in normal and malignant tissue[61]. Both NADH and FAD molecules are fluorophores which means that they can also be excited by light and result in fluorescence. Due to the fact that those fluorophores develop endogenously (without any pro-drugs), the fluorescence from those molecules is called auto-fluorescence. Therefore, detecting the change in auto-fluorescence can indicate malignant changes in skin. There are reports in the literature which show that it is possible to distinguish both melanoma and non-melanoma cancers by measuring auto-fluorescence from the skin[62]. Another study shows that time-resolved fluorescence spectroscopy gives 97.4% specificity in distinguishing melanoma cancer[63]. So in addition to PpIX fluorescence, auto-fluorescence is becoming a complementary optical diagnostics for skin cancer.

The aim of this project was to develop a portable convenient device to use for clinical measurements fluorescence imaging and display system; gather fluorescence images from different types of NMSC and healthy skin; and in addition to develop flexible image analysis techniques to study the formation of fluorescence patterns in time for filling the gaps in knowledge about PpIX metabolism in healthy and diseased skin for potential improvement of PDT treatment protocols. In addition to PDT diagnostics, the same system with a different band pass filter matching the auto-fluorescence peak (NADH and FAD molecules) could also be suitable for detecting malignant changes in the skin for assisting with optical diagnosis of NMSC.

2.2 Methods

The development of the fluorescence imaging device involved selection of the camera and the collection optics, design of the illuminator, the electronics, device control and user interface, and a casing for the device to provide convenient measurements in the clinical environment. The device had to meet Good Clinical Practice (GCP) requirements for a research device, and be assessed by the Instrumentation Department at the Ninewells hospital and Medical School in Dundee.

2.2.1 Optical design software

Zemax EE 2010 optical design software was used to virtually prototype the illuminator for the device. This is an industrial standard ray tracing software similar to LightTools, ASAP, FRED Photon Engineering, LightTrans VirtualLab, OSLO, etc. Zemax has its advantages and disadvantages compared to other optical software. It is widely used by optical engineers for both imaging and illumination applications. It has many optimisation operands for imaging optics. The software develops very rapidly and new tools appear to address current needs for optical design. The library of components, materials and coatings which contains measurements and data from the manufacturers is growing and it has good import and export capabilities. Yet, it is lacking flexibility, it handles illumination problems less well as imaging, and diffractive components are not modelled as well as in dedicated diffraction optics software such as LightTrans. In addition there is a relatively long learning curve.

Zemax works in the following way. All of the optical surfaces of the components have to be defined, then rays are generated at the source, they are propagated through all components in the system until they exit from the system or are terminated by absorption or their energy is below the threshold. After ray tracing, there are numbers of detectors available which calculate desirable characteristics of the system - size of a beam waist, point spread function, irradiance, etc. Then optimisation operands can be used to automatically change combinations of different parameters - distances between the components, position, thicknesses of lenses, materials, etc. to achieve better performance – smaller aberrations, better focus, etc. There are two models available in Zemax – sequential which is typically used for imaging systems (a ray interacts with

optical surfaces in defined order) or non-sequential (a ray can intersect any optical surface multiple times in any order) for illumination optics The task for the modelling of the illuminator was to achieve even irradiance in the field of view of the camera for even excitation of PpIX. The first step for the design was to model an array of LEDs placed around the camera lens, larger in diameter that the field of view of the camera. The design would then be refined by adjusting the LEDs positions and introducing optics if needed to achieve uniform illuminations.

2.2.2 Fast prototyping

The camera system was developed using fast prototyping approaches which included electronics design using USB development modules - FTDI technology, graphical user interface and device control - Matlab, and 3D plastic printing technology for fabrication of custom made casings. In addition laser cutter was used to prepare holders for optical phantom test arrays.

(a) Electronics design and device control

After finalising the optical design, electronics design was developed in DipTrace software. It is a quality schematic capture and printed circuit board (PCB) design software that is used to create multi-layered printed boards for schematics and manufacturing. It has a big library of electronics components with schematic and physical models and allows automated and semi-automated routing between the components. DipTrace provides export of the drawings into many fabrication and CAD exchange formats - drill and gerber for PCB cutting, coper layers etching and drilling mount holes.

FTDI USB UM245R development module was used for power control of the illuminator and camera synchronisation with the illumination. A MEX file provided by the manufacturer was used to control UM245R from graphical user interface written in Matlab. The camera was controlled from the user interface using manufacturer's Matlab drivers.

The user interface was developed in Matlab GUIDE toolbox. GUIDE is a fast development environment which allows for the scripting of m-files and for working in a user development environment (GUI DE). It is similar to LabView which is the industrial standard software for instrument control, but in addition allows plugging in different data processing capabilities in the user interface without the need of installing two different software packages. In particular, display of images in calibrated axis, 3D surface plots, pixels values, 2D intensity cross sections, intensity integration, data export, etc. was implemented in the interface in addition to image acquisition and illumination control.

(b) 3D CAD design and 3D plastic printing

3D CAD Rhinoceros 4.0 software was used to design drawings for casing for the device and then the casing was printed using a RoboSavvy MakerBot® Replicator® desktop 3D printer. Rhino 4.0 is an industry-standard software similar to SolidWorks, Autodesk Inventor, etc. for designing complicated geometries, assembly and display of virtual prototypes and exporting the drawings for digital machinery fabrication, such as milling, drilling, printing, laser cutting, etc. In this work 3D CAD design was exported to stereolithography format and then imported by MakerBot Desktop software to set printer instructions. The printer uses MakerBot® polylactide (PLA) bio-thermoplastic fibre filament. A typical resolution which is achieved with the printer is 0.2 mm. Caution is needed when orienting the drawing for the print - the heaviest part should be at the bottom. If the drawing does not have optimal orientation the design can deform during the print or the support structures built in the hollow parts can simply collapse. The support structures are removed after the print is complete.

(c) CO_2 laser cutting

The last prototyping method used for the work in this chapter was CO_2 laser cutting. It was used to fabricate special shape containers for optical phantoms. The laser cutter (CTR Lasers, the UK) contains an enclosed CO_2 class 4 laser with 1024 nm emission wavelength and 150 Watt power. Interlock system and full enclosure brings the system down in the laser safety classification to class 1. The laser cutter is suitable for cutting and engraving a wide range of materials, such as acrylic plastic – PMMA sheets, wood, paper and card, fabrics and thin metal sheet. The software provided with the laser cutter - LaserCut5.3 has limited drawing capabilities and is only suitable for simple jobs. Drawings for the cutting can be prepared in any other CAD software which allows exporting into AutoCAD DXF (Drawing Interchange, or Drawing Exchange) .dxf format. The drawings in this format can be imported into LaserCut5.3 which is used to define cutting and engraving parameters - laser power, cutting/engraving speed, etc. The resolution of the laser cutter is up to 0.1 mm which is limited by the deformation of the edge of the plastic during the cut. The quality of the edge after the cut is better for thinner sheets. It becomes more challenging to achieve fine cuts for thicker plastics, and optimal parameters should be experimentally defined, for instance for thicker plastics it is better to set the focus of the laser deeper in plastic rather than on the surface. For some jobs, multiple runs over the cutting area give cleaner cuts than higher laser power.

2.2.3 Image analysis

The Image Acquisition[64], Image Processing[65] and Computer Vision[66] Matlab Toolboxes were used for all stages of working with the images. The functions for the graphical user interface for image and data display included acquisition of the images, automatic saving with automatic generation of file names, digital filtering, background subtraction, calibration, 3D display, display of pixel values and 2D cross section. Additional routines were developed for semi-automated image processing and analysis - automatic motion and distortion compensation, cropping, sectioning and integration of regions of interest, image correlation and exporting the data.

One of the most challenging steps in image processing was to align all of the time course fluorescence images in order to analyse the same area between time course measurements. Although a good procedure for the camera alignment to the imaging area was developed, there was still a 1-2 mm displacement between measurements. In addition, during the imaging of curved body surfaces such as fingers, edges of the hands and feet, displacement of the camera resulted in distortions due to imaging with slightly different angles. In order to centre, rotate and compensate for the distortions caused by imaging curved surfaces and camera misalignment between the images Random sample consensus (RANSAC) geometrical transformation was used. This transformation identifies pointers on two images which are reference points of common objects on the images. These pointers allow for calculating various transformation matrixes to manipulate the two images. In this chapter motion displacement and distortion was compensated.

2.2.4 Preparation of phantoms for optical measurements

A tissue simulating phantom is an object which mimics properties of tissue. For some measurements there is a need to simulate only optical properties in which case the mechanical properties can be different from skin. In some cases there are requirements to have both mechanical and optical properties simulating tissue properties. For optical testing of the fluorescence camera mimicking PpIX fluorescence and scattering of light were of interest. Solid PpIX fluorescent phantoms were fabricated from a silicone polymer following the protocol described in [67]. The base for the phantoms was room temperature vulcanised silicone polymer

which has a similar refractive index to skin. Alumina powder was added to mimic the scattering properties of the skin[68] and PpIX was added to provide fluorescence. Two parts, A and B of RHODORSIL RTV 141 polymer were mixed in a 1:10 ratio, 4% of alumina scattering powder was added to the mixture, and Protoporphyrin IX P8293 - ≥95% from SIGMA-ALDRICH were dissolved in Methanol. A range of PpIX concentrations of 10, 20, 40, 80, 160, 320 and 640 nM in the phantoms was made for the test. PpIX solution was thoroughly mixed with the silicone polymer and alumina powder and left at room temperature to vulcanise. The phantoms normally vulcanise and the methanol evaporates after 72 hours.

Absorption spectra of PpIX in methanol solution and solid phantoms were recorded with the Varian Cary 300 Bio UV-Vis spectrophotometer. The spectra of just the solvent or transparent silicone polymer base were recorded separately and subtracted. However, there was no absorption from the solvent or the polymer.

The PpIX emission spectrum in methanol solution with alumina powder was measured using a Fluromax 2 fluorimeter. The excitation source of the fluorimeter is a xenon bulb. A monochromator selects the wavelength that is used for excitation. A scanning emission monochromator records the emission from the sample at different wavelengths using a photomultiplier tube. The emission properties of the phantoms were compared to a standard Coproporphyrin solution in HCl which is used as a surrogate test solution for fluorescence in the medical community. Also the phantoms were compared to PpIX fluorescence developed in the skin of healthy volunteers after application of PpIX precursor – Ameluz gel.

2.2.5 Optical biopsy system for PpIX emission *in vivo* in clinical settings

As a routine practice in the Photobiology Unit, Ninewells Hospital, Dundee PpIX fluorescence in *in-vivo* experiments is measured using an optical biopsy system (OBS)[69,70,71,16]. OBS consists of an excitation source – 405 nm laser diode and fibre-coupled spectrometer. It records an emission spectrum at one point on the sample. One of the examples of *in-vivo* experiments is measurements of PpIX fluorescence decay during PDT treatment to predict PpIX photobeaching and depth profile[69,72,70].

OBS was used to measure PpIX emission from the solid PpIX phantoms, Coproporphyrin standard solution and *in-vivo* from the skin of healthy volunteers after three hours of application

of Ameluz gel. Fluorescence measurements using the OBS and the camera were compared to identify the performance of the camera.

2.3 Results

The requirements for the device were the following. The device had to be able to image PpIX fluorescence with a field of view of a few square centimetres with submillimetre resolution, had flexible image processing capabilities, preferably was handheld, portable, lightweight, easy to use in clinical experiments on patients, was able to access different sites on the patient, complied with the Good Clinical Practice standards for medical device ISO 14155:2011 Clinical investigation of medical devices for human subjects[73]. It is desirable to have multiband detection, such as combined auto-fluorescence and PpIX measurements using blue/red excitations and red/NIR PpIX emission at 635 and 710 nm. Different bands of PpIX excitation and emission would provide information of PpIX accumulation at different depths in skin. Blue 405 nm light excites PpIX at the surface and 635 nm wavelength penetrates in deeper layers. Such a configuration was considered for the design of the device at the start. However, for the proof of concept to gather initial images, to establish clinical protocols and the relevance of the fluorescence time course imaging, and to identify image analysis and statistical analysis routines, it was decided to keep the design of the device and the protocol as simple as possible. So one excitation and one emission wavelength was chosen for the initial configuration of the device. The device had to fulfil the requirements in electrical safety, allergic reactions, energy output and infection control of the Instrumentation Department at Ninewells hospital and Medical School in Dundee.

The flow chart of the development stages is shown in **Figure 2.2**. The camera for the system was chosen based on the resolution, sensitivity, power management and the cost. Lumenera LM075m had an appropriate sensor size of 640x480 pixels which provided 50 µm resolution with the field of view equal to 3.1 x 2.4 mm^2 at 8.5 cm. There was a possibility to power the camera from a USB port of a battery driven laptop which reduced electrical safety risks. In addition it was small, fast and light weight. A lens with an adjustable focal length and aperture and a removable band pass filter with central wavelength (CWL) of 635±2 nm and full width at half maximum (FWHM) of 10±2 nm were selected for the collection optics.

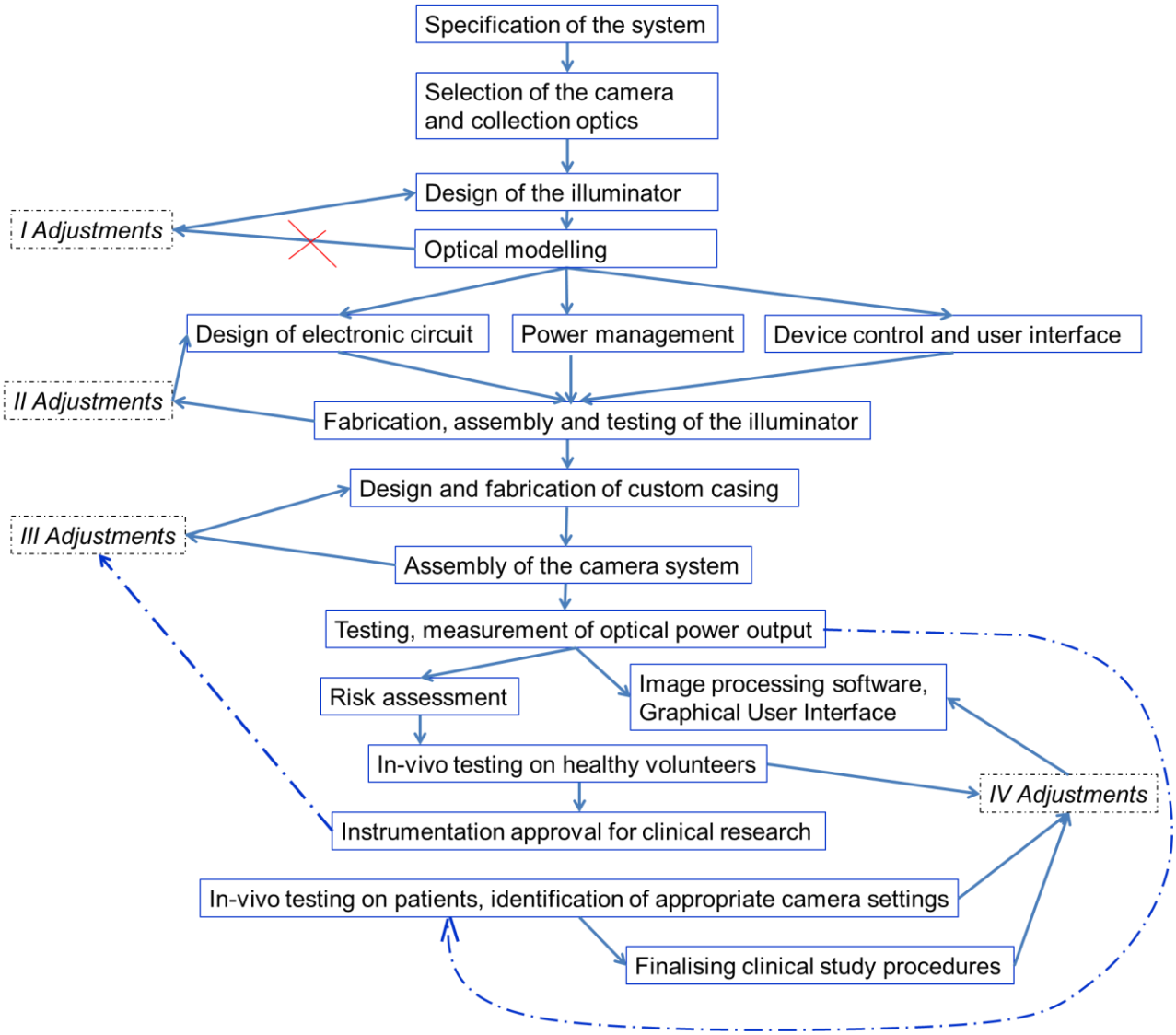

Figure 2.2: *Fluorescence camera development flow chart.*

The illuminator was developed on a custom made printed circuit board (PCB) with a low power 405 nm LED array, a separate 9 V battery power supply, and a USB control module. All components were assembled in a custom plastic casing. The casing of the camera provided a fixed distance to the imaging plane. The illumination was pulsed during the image acquisition via a custom user interface. This synchronisation was important to reduce the dose of excitation light to eliminate the possibility of PpIX photobleaching during the measurements. Also the pulsing regime improved signal to noise ratio by reducing the sensitivity to ambient light and the background. A special camera alignment procedure allowed referencing between time course images and the study area. In addition camera displacement and motion distortion compensation routines were written in Matlab Computer Vision Toolbox. The full specification

and the description of the device is available in the Appendix XIV: Capturing fluorescence – Fluorescence Imaging System Specifications v.1 09.10.2013.

In order to meet electrical safety requirements the device was designed as fully battery driven. The casing for the device was made from an inert thermoplastic which meets the allergy reaction requirements. In order to address infection control the device was made “wipe clean” – the casing did not have dust traps and the standard operating procedure was written, [Appendix IV: Capturing fluorescence – Standard Operating Procedure (SOP)]; the device did not come in contact with the skin – a disposable laminated reference frame was prepared for each experiment. The frame can be fixed with a dermatological tape to the skin of each subject. This prevents the casing tube of the camera to come in the contact with the skin of the study subjects; the camera is placed on the laminated disposable frame. Optical power output – UV, UVA and blue light exposure limits were measured for the eye and skin safety assessment. The device can be used without any special precautions as long as it is not placed directly on the unprotected eye [Appendix XIV: Capturing fluorescence – Fluorescence Imaging System Specifications v.1 09.10.2013]. The device does not become hot during continuous measurements.

The camera was tested on in-house made optical phantoms, standard fluorescent solutions and *in-vivo* on healthy volunteers The device received approval from the Head of the Instrumentation Department at Ninewells for application in a clinical research study. Two patients were recruited for preliminary data gathering, choice of appropriate camera settings and finalising the design of the clinical study which is described in the next chapter.

2.3.1 Optical design

To be of low power, compact and lightweight, the first design idea was to have a ring of LEDs around the lens of the camera, larger in diameter than the field of view of the camera. The LEDs were selected with a relatively large directional emission, in addition there was a diffusing coating on the inside walls of the illuminator tube. The datasheets for VAOL-5GUV0T4 LED with the optical power, dimensions, directional emission and the spectrum were imported to Zemax model. Then the coordinates of each LED in the illuminator were calculated and an array was created. The walls of the illuminator tube were set with 60 % diffusing coating. An irradiance detector was placed at the end of the illuminator tube with 50 μm pixel size. 1,000,000 rays were generated in the system which normally is a sufficient number to achieve a realistic distribution.

The irradiance at the detector is shown in **Figure 2.3**, (c). The end of the illuminator tube is at 8.5 cm distance – which is the focal distance of the lens. The field of view of the camera is marked as ROI – the region of interest on the irradiance detector. The irradiance is uniform with non-uniformity less than 5% which is an acceptable variance for the illumination. For instance for the Aktilite CL16 which is one of the most common PDT treatment devices based on an array of 635 nm LED the non-uniformity of the treated area of 4 x 6 cm^2 at 8.5 cm distance was estimated to vary for up to 38%[74]. As a result of the modelling, the design was confirmed and no additional iterations were needed to optimise it.

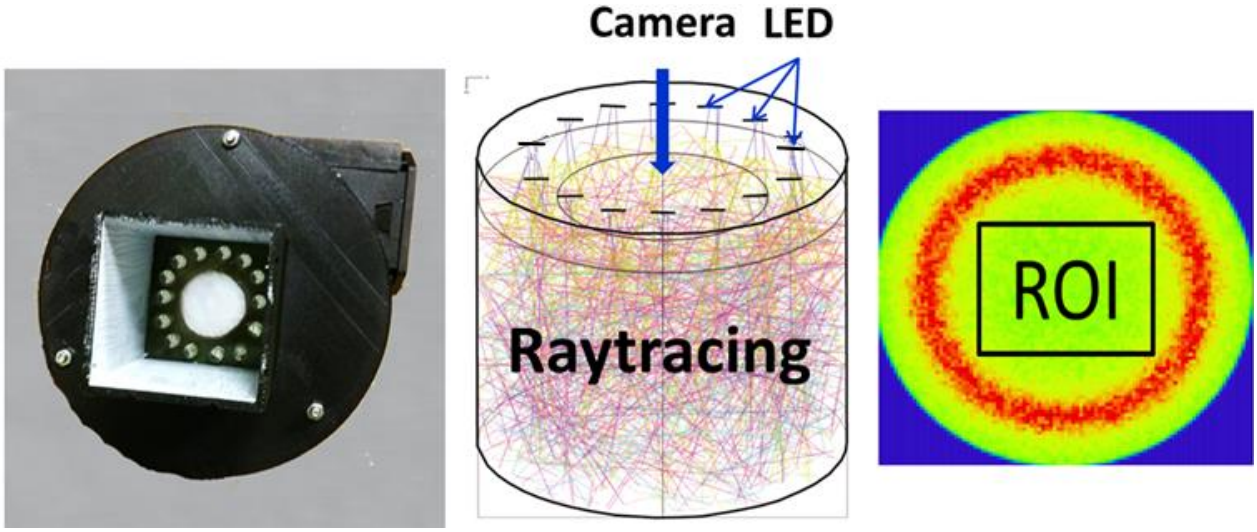

Figure 2.3: *Optical design of the illuminator and an assembly of the fluorescence imaging device.* **a** *– bottom view at the illuminator tube and an array of LED and camera lens. The camera lens is in the middle (white small circle on the image). The LED array of 405 nm LED with dome lenses mounted around the opening for the lens on a doughnut shape printed circuit board (PCB). The camera casing tube shields ambient light during the measurement which allows conducting the experiments with dimmed lights on.* **b** *- Zemax design of the illuminator and raytracing simulations.* **c** *– an irradiance detector showing that the area at the region of interest (ROI) which corresponds to the field of view of the camera is uniformly illuminated.*

2.3.2 Electronics design

After satisfactory results of optical modelling an electronic driving circuit and PCB board were designed in DipTrace. The LED array was made of VAOL-5GUV0T4 Ø5 mm (160 mcd, 3 V, 20 mA) LEDs which were connected to an INFINEON BCR402W/SOT343 surface mount LED drive and a MMBF170L/SOT23 N-MOSFET switch. The switch was connected to a 9 V battery. The switch was turned on and off from a FTDI USB development module UM245R controlled from a laptop via a user interface written in Matlab. (**Figure 2.4**). It was a single layer PCB with LEDs mounted through holes and wired connection to the battery and the USB control unit.

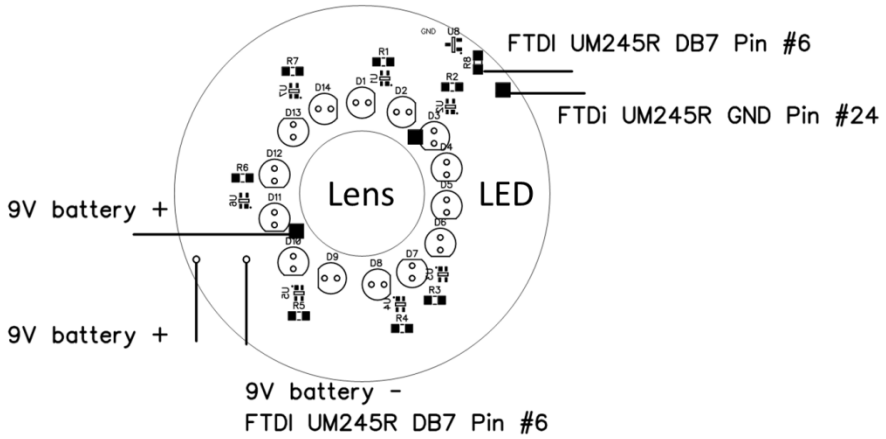

Figure 2.4: *Printed circuit board (PCB) for the illuminator. The LEDs were placed around the opening to the camera lens. Each pair of LED is connected to an LED drive and resistor. There are +/- battery terminals and a terminal for the signal and ground wires of the FTDI USB development module. The signal pin #6 of FTDI USB module is connected to a MOSFET switch. The FTDI module reads the signals from a graphical user interface and then turns the switch.*

The other layers of the drawing of the PCB can be found in the Appendix XV: Capturing fluorescence – Printed Circuit Board PCB Design. These drawings were developed for PCB fabrication – board cutting, copper layer tracking and drilling mount holes

.

2.3.3 Opto-mechanical design and system integration

After the assembly and testing of the illuminator, a 3D casing was designed in Rhino 4.0 software to contain the PCB, the battery, the USB module, and the camera. It provided a wired

connection between all of the components and an access to an adjustable aperture and the focus of the lens. The dimensions are 12.5 cm by 13.5 cm; the weight is less than 100 g. The camera mount has fixation at the sides and does not cover the camera – it allows for heat dissipation in air which eliminates any possibility of overheating during continuous measurements. There are marks on the casing which allow aligning the camera to the study area. A 3D drawing of the casing and the camera assembly are shown in **Figure 2.5**.

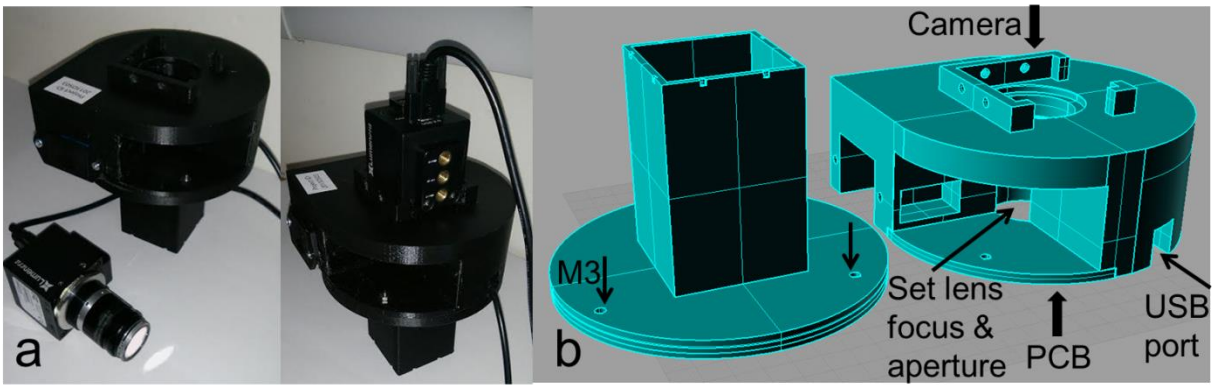

Figure 2.5: *The fluorescence camera and the 3D CAD design of the casing.* **a** *- the assembly of the camera. A lens with an emission filter is connected to the camera via C-mount. The lens slides in from the top of the plastic casing and is fixed with four M3x0.5 screws from the sides. The casing contains the illuminator PCB, 9 V battery and the USB module.* **b** *– two parts of 3D drawings for the casing. It is printed using a RoboSavvy MakerBot® Replicator® desktop plastic printer. The illuminator's PCB is sandwiched in the compartment between the two parts of the casing. Two parts of the casing are then fixed together with three M3x0.5 screws. There is a compartment for an off-the-shelf plastic casing for 9 V battery which is fixed with M3 screws, a compartment for the USB control module, camera mount and access to the lens.*

2.3.4 Optical power output and risk assessment

After the prototyping of the device, the optical power output was measured using a Thorlabs PM100D power meter and was equal to 0.1 mW/cm^2 at 8.5 cm distance – the end of the casing tube. The illumination was pulsed with the duration of the pulse less than 1 s depending on the exposure of the camera. The spectrum of the LED was measured using an Ocean Optics spectrometer, (**Figure 2.6**).

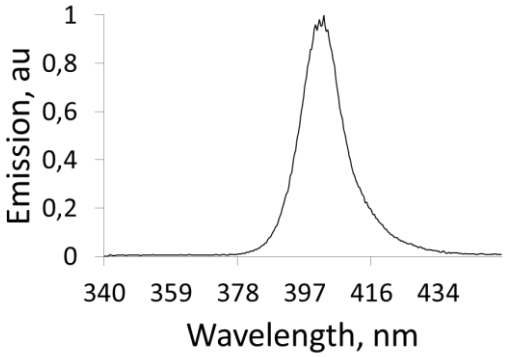

Figure 2.6: *An emission spectrum of 405 nm VAOL-5GUV0T4 LEDs. The emission peak matches the absorption peak of PpIX. This spectrum was used for the calculation in the risk assessment for the UV, UVA and blue light exposure for the eye and the skin.*

The power of the illuminator is low and should not cause significant photobleaching of PpIX, therefore it should not affect the treatment if the measurements are taken on the day of routine PDT treatment. For instance, a typical irradiance of a conventional PDT lamp such as The Aktilite CL128 or Aktilite CL16 used for the treatment with 75 J/cm^2 dose, 18 minutes duration should be 65 mW/cm^2 (in fact it varies from 74 mW/cm^2 to 49 mW/cm^2)[74], an ambulatory treatment device such as Ambulight PDT[75] delivers 75 J/cm^2 during 3 hours and has irradiance of 7 mW/cm^2.

The optical output has been evaluated for the eye and skin safety. The spectrum has UV-A (340 – 399 nm) and the visible (400 – 700 nm) wavelengths. In order to evaluate the safety, the contribution of the UV-A and Vis wavelength was calculated and found to be equal to 32 % and 68 % of the spectral power correspondingly. A risk assessment for the eye and skin safety for three wavelength ranges UV, UVA and blue light was done using the International Standard / Safety of laser[76] and the University of St Andrews local rules for lasers[77] and approved by Prof Harry Moseley, the Head of Photobiology, Department of Medical Physics, Ninewells Hospital & Medical School, Dundee (Appendix XIV: Capturing fluorescence – Fluorescence Imaging System Specifications v.1 09.10.2013 / Appendix 2). The calculations for the maximum exposure time for the UV light are listed below.

$$E_{eff} = \sum_{\lambda} E_{\lambda} S(\lambda) \Delta\lambda$$

E_{eff}– effective spectral irradiance, W/cm^2;

$S(\lambda)$ – relative spectral effectiveness, does not have any units;

E_{λ} – spectral irradiance, W/cm^2;

$$t_{max}, s = \frac{H_{eff}, \frac{J}{m^2}}{E_{eff}, \frac{W}{m^2}}$$

t_{max}, s – maximum exposure time;

H_{eff} – exposure limit.

For the UV the exposure limit is $H_{eff} = 30\ \frac{J}{m^2}$; $S(\lambda) = 0.000064$; Considering that a part of the LED spectrum is at 380 nm which is the most harmful in consideration for the eye and skin safety, this wavelength was selected for the evaluation of the maximum exposure for UV. The spectral irradiance is equal to the measured value for the UV part of the spectrum, $E_\lambda = 0.32\ \frac{mW}{m^2}$. Than the effective spectral irradiance is equal to $E_{eff} = 0.32 \times 0.000064 = 2.05\ \text{x}\ 10^{-5}, \frac{mW}{m^2}$; the maximum exposure time is

$$t_{max}, s = \frac{30\ \frac{J}{m^2}}{2.05\ \times 10^{-8}, \frac{W}{m^2}} = 15\ \times 10^8 s = 4\ 10^5 h\ \gg 8\ h$$

Maximum exposure limits will not be exceeded after 8 hours of continuous exposure to the UV light, therefore no special precautions are required. Similar calculations were done for the UV-A and the blue light. According to these calculations the eye exposure should not exceed 53 minutes and the device should not be placed on the unprotected eye.

2.3.5 User interface

The system is fully integrated in the Matlab 2012b environment and configured for the Windows 7 64-bit operating system. The system requirements, installation and operation procedure is described Appendix XVII: Capturing fluorescence – The FluoImLu3 Software Installation and Operation Instructions.

The graphical user interface (GUI) is shown in **Figure 2.7**. The GUI allows for fast clinical measurement (Record test and Record control buttons) – the illumination is pulsed when an image is recorded, a folder is automatically created when the first image is acquired, an automatic name for the folder is generated in a format of dd-mmm-yyyy, the following images on the same day are saved in that directory, automatic names are generated for the images in similar format of Test-dd-mmm-yyyy-ssmmhh.jpeg or Control-dd-mmm-yyyy- ssmmhh.jpeg. The record test button is designed to acquire a series of 3 images for averaging of background. Record control acquires only one image to minimise the exposure to UVA and blue light for

preventing photobleaching. A description and implementation of all the functions of the user interface are described in the Appendix XVII: Capturing fluorescence – The FluoImLu3 Software Installation and Operation Instructions.

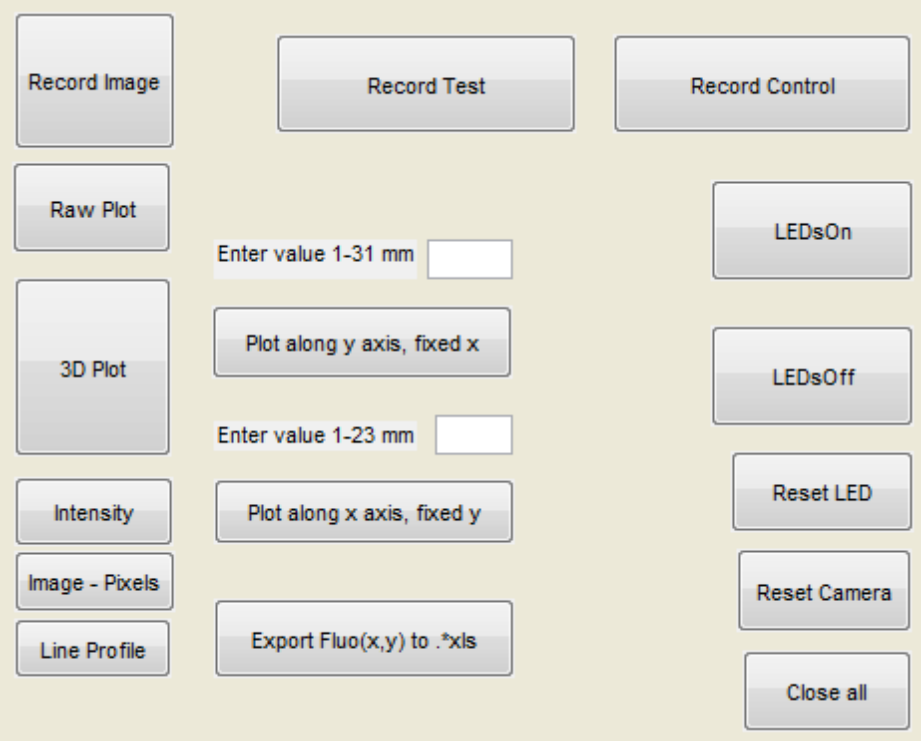

Figure 2.7: *Graphical user interface (GUI) for the camera system. The Record Test and the Record Control buttons allow pulsing the illumination during the image acquisition (the first button acquires three images in a series for averaging purposes and the other button records only one image to minimise the exposure to the UV light). When the Record Test/Control button is pressed logical "1" is sent to the USB control module which opens the MOSFET transistor switch; an image is acquired and placed in a buffer memory, the flash is immediately turned off, the image is then automatically saved in a folder dd-mmm-yyyy with the name of dd-mmm-yyyyy-ssmmhh.jpeg which is the date and time when the image was acquired. The settings for the camera and live preview are managed with the manufacturer's software which is synchronised with the Matlab GUI. The other functionality of the GUI allows turning the illumination on and off (the LEDsOn and the LEDsOff buttons), record images without illumination (the Record image button) and various displays of the images and the data – 3D surface plot in calibrated axis - millimetres and normalised fluorescence intensity (the 3D Plot button), 2D intensity cross section (the Line Profile button), display of pixels value (the Image – Pixels button), display of not processed image on monochromatic full intensity scale (the Raw Plot button), export of the 2D cross section intensity values in excel format, etc.*

2.3.6 Time course imaging procedure

In the first repeated time course measurements a marker pen was used to draw a contour on the skin to align the camera to the study area. However, the solvents in Ameluz gel

or Metvix® cream and the cleaning alcohol wipes compromised the reference contour. It was blurred or completely removed during the procedure of re-applying of the creams or cleaning the skin between the measurements. In order to have an identical reference in the time course images the following measurements procedure was developed. Previously described laminated alignment frame was firmly fixed with dermatological tape and stayed fixed during all time course measurements. There were marks on the outer edge of the reference frame corresponding to the alignment marks on the casing tube to position the camera. On the inner edge of the reference frame there was a bright orange fluorescent contour which was used as a reference for small displacements and distortion compensation in the software. (**Figure 2.8**).

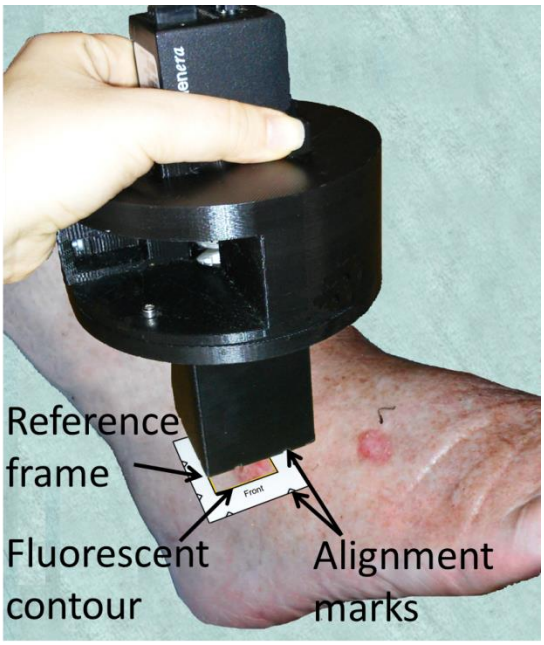

Figure 2.8: *The handheld fluorescence camera is positioned on a patient's Actinic Keratosis lesion.*

The camera displacement between the measurements was approximately 1-2 mm. These small displacements were compensated by the image processing using the reference fluorescent contour. The orange fluorescent contour appeared as a white saturated line on all the fluorescence images. The features in this contour were used for "Matching features" algorithms in RANSAC image transformation[78] (**Figure 2.9**). This transformation detects inlier points on the fluorescent contour (small cyan triangles **Figure 2.9**) and on a reference image which is normally a background fluorescence image (red circles on the red line). Using these matching points RANSAC calculates a vector matrix and allows for various transforms. In this

procedure the image was transformed to match the orientation, position and shape of the reference image. The transformed images were saved for the next processing stage.

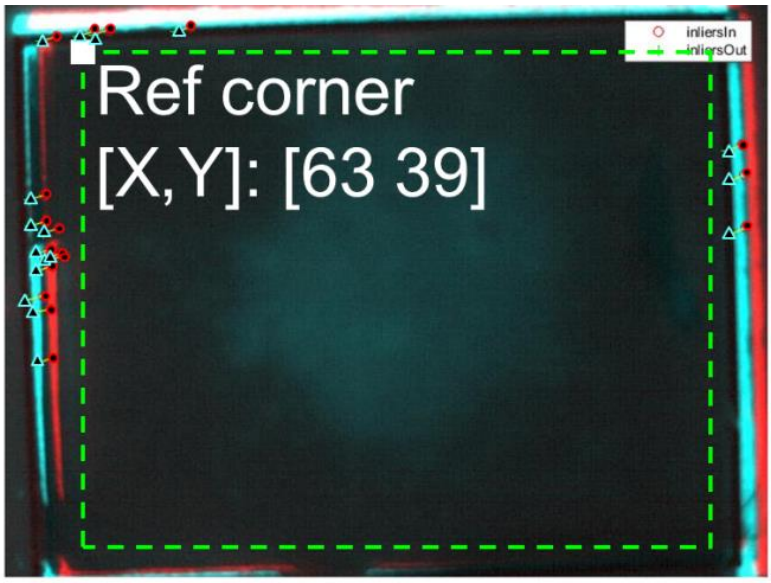

Figure 2.9: *Two image processing steps RANSAC geometrical transformation and cropping out the fluorescent reference contour. In order to compensate camera displacement during time course imaging, a Matlab m-file was written which uses RANSAC geometrical transformation function available in Computer Vision Matlab Toolbox. This file searches for matching features on the fluorescent contour and creates a matrix of translation vectors to transform the time course fluorescent images to match the position and the shape of the reference image. This transformation rotates, centres and stretches any small distortions caused by imaging of curved body surfaces in time course experiments. Cyan and red lines are fluorescence contours on a background image (reference image for RANSAC) taken at 0 min of the time course measurements and a fluorescence image taken at 60 minutes. RANSAC matching features are shown as small red circles and cyan triangles. Images are transformed and saved for the next processing step automatically. After that coordinates of a top left pixel (a small white rectangle – Ref Corner) and area size (green dashed line) are chosen and passed into another m-file to crop out the fluorescent contour. The images are cropped and saved automatically.*

At the next processing stage cropping of images was applied. A reference corner was defined manually; the coordinate of the corner and the size of the cropping area were saved in the Matlab cropping m-file. Normally the image size is reduced from 680 x 480 pixels to 540 x 380 pixels which is enough to crop out the fluorescence reference contour. The green dashed line of the figure shows the cropping area. Cropped images were saved for the next stage which is calculating integrated fluorescence. An area of interest can be selected and the coordinates are passed to the integrated intensity m-file. For the peak fluorescence time course an area with the highest fluorescence was chosen. Also the size of the area was passed to the file. This file reads all 18 fluorescence images and calculates the mean intensity over the area of interest and

automatically saves it into an excel file. Another function calculates correlation coefficient between images. The correlation analysis was meant to help identifying “fluorescence fingerprints” between different types of the lesions and look for the correlation of the fluorescence patterns to the lesion shape. The correlation coefficients were also saved to the excel file for further analysis.

All of the image processing routines are described in Appendix XVIII: Capturing fluorescence – Image Processing and Analysis Algorithms. Each of the files is dedicated to one processing or analysis stage – compensating camera displacement during time course measurements (Matching features algorithms), automatic cropping of reference contour (Cropping images algorithm), image sectioning and integrated intensity calculations (Integrated intensity algorithm).

2.3.7 System validation *ex-vivo* and *in-vivo* on skin of healthy volunteers

The camera performance was tested on solid silicone PpIX scattering phantoms, Coproporphyrin solution in HCl, and PpIX fluorescence from a healthy volunteer after three hours from the application of topical Ameluz gel in an aluminium Finn® chamber for patch tests.

A PMMA plastic sheet was used to prototype containers for the test array of the PpIX phantoms. An array of 2 cm diameter cavities which fits in the field of field of view of the camera were cut using the CTR laser cutter and glued on top of the base sheet. The phantom holder with the phantoms of different concentration of PpIX is shown on the left hand side of **Figure 2.10**.

Coproporphyrin was imaged in a standard 60 mm × 15 mm polystyrene Petri dish. In order to prevent reflections from top and bottom lids, the bottom lid of the Petri dish was engraved with the laser cutter and an opening was cut at the top lid; a piece of black beam blocking paper was glued on top of the upper lid to provide a reference (**Figure 2.10**).

The absorption and emission spectra of PpIX in Methanol solution which was used for preparing PpIX phantoms were measured with a Varian Cary 300 Bio UV-Vis spectrophotometer and a Fluromax 2 fluorimeter, and are shown on the right side of **Figure 2.11**. Emission spectrums from PpIX phantoms, Coproporphyrin solution and PpIX fluorescence from a healthy volunteer were taken with the OBS system at the Photobiology unit, Ninewells hospital in

Dundee (**Figure 2.11**) and the results compared with the images taken with the camera (**Figure 2.10**: c, d, e).

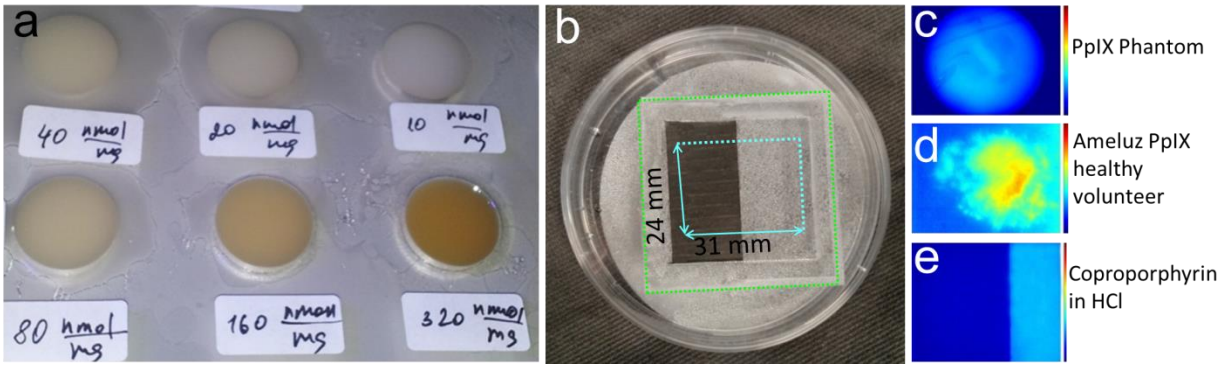

Figure 2.10: *Optical phantoms and camera validation.* **a** *- solid PpIX phantoms with a range of PpIX concentration 10, 20, 40, 80, and 160, 320 nMol/mg.* **b** *- Coproporphyrin solution in a Petri dish. The green dashed line shows the camera casing tube position.* **c, d, e** *– fluorescence images taken with the camera – PpIX phantom, PpIX fluorescence from a healthy volunteer after 3 hours of Ameluz gel application, and Coproporphyrin solution correspondingly. The camera has good specificity for PpIX emission and rejection to the other wavelength.*

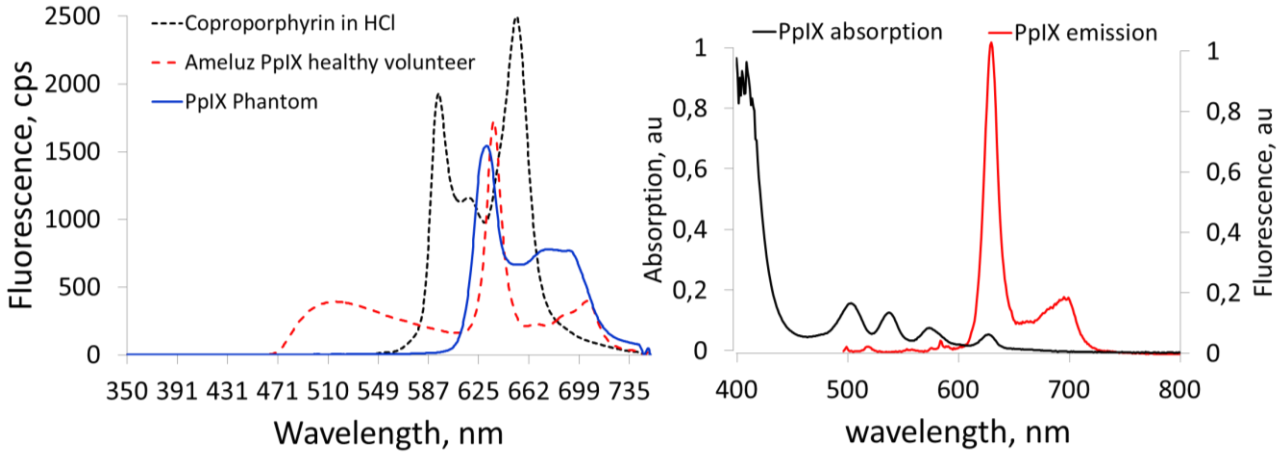

Figure 2.11: *Characteristics of optical phantoms and PpIX fluorescence in healthy skin to validate the camera performance. The graphs of the right show typical PpIX absorption and emission measured in methanol solution with Varian Cary 300 Bio UV-Vis spectrophotometer and Fluromax 2 fluorimeter. The graphs on the left show emission spectra from Coproporphyrin, PpIX solid silicone phantom with 80 nMol/mg concentration of PpIX and PpIX fluorescence in-vivo developed in the skin of a healthy volunteer after three hours from Ameluz gel application taken in clinical settings with optical biopsy system (OBS). PpIX fluorescence from a healthy volunteer gives similar fluorescence intensity to the 80 nMol/mg PpIX solid phantom. The results indicate that the camera can distinguish all tested fluorescence substances.*

A solution of PpIX in methanol had an emission spectrum with the strongest emission peak at 633 nm and the second peak at 700 nm. Solid phantoms had similar emission except

the 700 nm peak is slightly elevated. Coproporphyrin had two peaks at 594 and 653 nm. PpIX fluorescence from the skin of a healthy volunteer after three hours from topical application of Ameluz gel had a peak at 635 nm which matched the transmission wavelength of the band pass filter in the camera. The camera system has strong selection for 635 nm PpIX emission and rejects the other wavelengths. That is why PpIX fluorescence from the healthy volunteer appeared brighter on the fluorescent images than PpIX phantom or Coproporphyrin standard solution.

The current set up does not take into account melanin concentration therefore it is not possible in this procedure to compensate for the differences in the optical properties of skin between the individuals. Due to that we are not able to calculate real concentrations of PpIX from the data. However, the study was conducted in Scotland where most of the subjects have skin types I-III by Fitzpatrick scale[1] which do not have drastic variations in melanin. This in principle should allow for comparison of relative PpIX fluorescence measurements across the subjects.

2.3.8 Pre-clinical study data gathering

After the approval of the device for the electrical, infection control, allergy reactions and optical power output safety assessment by the NHS Tayside Instrumentation Department, a clinical study proceeded. The study was conducted in compliance with Good Clinical Practice (GCP) laid down in The Medicines for Human Use (Clinical Trials) regulations 2006 No. 1928. There was no requirement for clinical trial authorisation (CTA) from the UK Medicines and Healthcare products Regulatory Agency (MHRA) as the device was approved internally for the study.

Two patients were selected prior to finalising clinical study design. One patient P1 had a basal cell carcinoma lesion and was administered Metvix® PDT treatment. Routinely, there are two treatment cycles for BCC diagnoses[69]. A lesion was prepared with a curette to remove any crust, then Metvix® cream was applied and covered with occlusive dressing for three hours. After three hours the cream was wiped off, Woods lamp was used to visually assess and score the fluorescence before the treatment commences. For both treatment cycles the procedures were the same. The treatments were performed one week apart[69]. The imaging was performed before the first and the second cycle PDT treatment. The fluorescence images from two measurements are shown in **Figure 2.12**. **Figure 2.12** (*a)* shows 3D surface fluorescence from

the lesion before the first PDT treatment. The horizontal axes (x and y) are calibrated in mm; the vertical axis (z) shows fluorescence in arbitrary units. Fluorescence is normalised to the camera maxima. In **Figure 2.12** (*c)* there is a reduction in fluorescence area as well as the intensity drop compared to **Figure 2.12** (*b).* This shows the response of the tumour to the first treatment cycle.

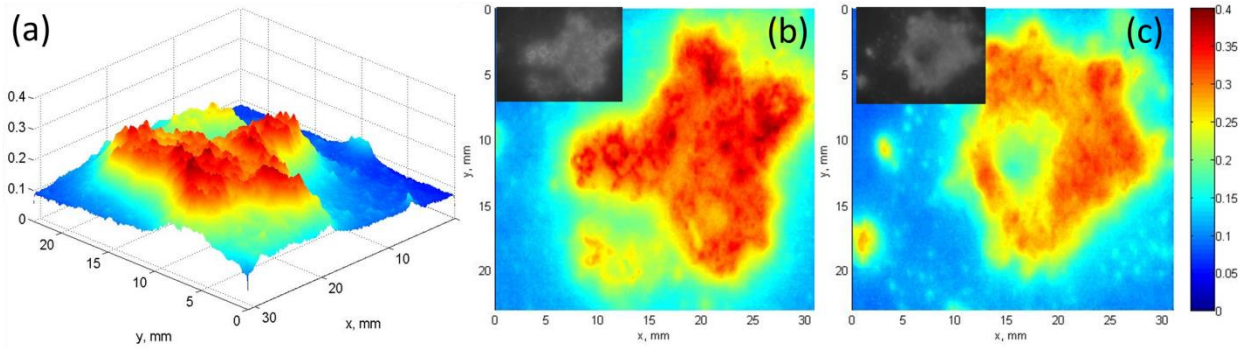

Figure 2.12: *Fluorescence before the first and second PDT treatment cycles of P1 patient with Basal Cell Carcinoma (BCC) after three hours of Metvix® application.* **a** *- 3D surface fluorescence calibrated in millimetres in x and y-direction; and on z-axis there is fluorescence intensity normalised on the camera maximum (on false colour scale).* **b** *– 2D plot of the fluorescence before the first PDT treatment.* **c** *– 2D fluorescence intensity before the second PDT treatment.*

As fluorescence greatly varies from subject to subject[53], in order to confirm the settings for the camera (0.1 ms exposure, x1 gain for normal images without the filter, 16 ms exposure, x11 gain for fluorescence images at 60 fps with fully open aperture) second subject was recruited in the study. This patient P2 had multiple lesions: one BCC lesion and two AK. Metvix® PDT was administered for all three diagnoses. All three lesions were treated on the same day. Analogous to the previous measurents on P1, PpIX fluorescence from patient P2 was imaged after three hours of Metvix® application (**Figure 2.13**).

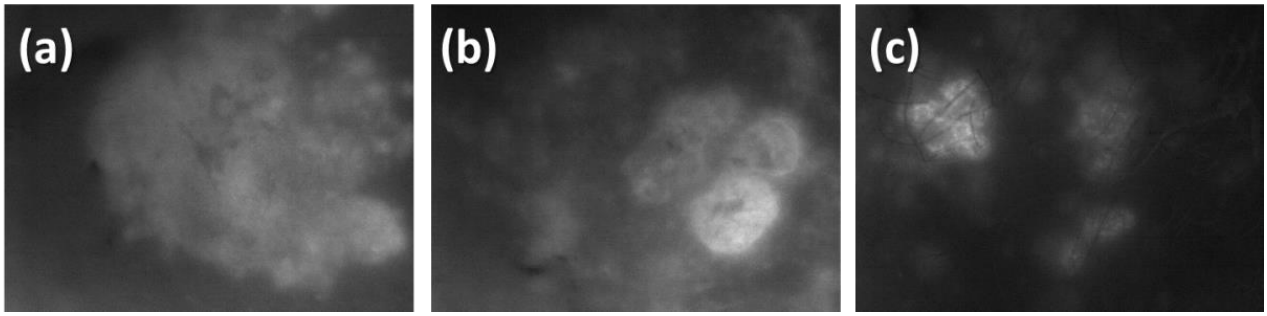

Figure 2.13: *PpIX fluorescence images taken with the camera from P2 patient after three hours of Metvix® application before PDT treatment.* **a** *–Actinic Keratosis (AK).* **b, c** *– BCC lesions. The images were taken to confirm the choice of the settings of the camera and finalised the design of the clinical study.*

All of the fluorescence readings were clear which confirmed the choice for the settings for the camera and allowed to finalise the design for the clinical study which is described in the next chapter.

2.4 Conclusion

The developed instrument and the method introduce a few advantages in PpIX fluorescence imaging compared to existing devices. The illumination light in the device has low irradiance. In addition to this it is pulsed and synchronised with image acquisition. So the total light dose delivered during the measurements is orders of magnitude lower than PDT treatment dose. Because of this low dose the device was not expected to induce PpIX photobleaching or pain during the measurements. Another advantage of pulsed light was reduced sensitivity to ambient light and background noise.

Developed measurement procedure and image processing algorithms enable good referencing of the fluorescent images to the study area, and enable analysing identical regions in time course images. This makes the device appealing for fluorescence time course imaging. Fluorescence time course imaging will provide spatial information on PpIX fluorescence. Different areas on the fluorescent images can be integrated for the time course analysis which is a more accurate method compared to the conventional one point measurement using optical fibre based spectroscopy techniques.

The results during the camera validation demonstrated that it was suitable for monitoring and quantitative PpIX fluorescence display in clinical setting. The camera was selective to the 635 nm peak wavelength in *ex-vivo* measurements on fluorescent solutions and PpIX phantoms, and *in-vivo* experiments on the skin of a healthy volunteer after three hours of ALA application, and PpIX fluorescence developed in AK and BCC tumours of two patients after three hours of Metvix® application. The fluorescence developed in the BCC tumour of the first patient (P1) was imaged before the first and the second PDT treatment cycle which were performed with an interval of one week. The fluorescence images from the first week and the second week showed how the tumour responded to the first PDT treatment. This was of interest and promoted finalising a clinical study which aimed to answering important questions about PpIX metabolises in different lesions using two different creams.

2.5 References

1. Goldsmith LA, Katz SI, Wolff K. *Fitzpatrick's Dermatology in General Medicine*. 8th ed. The McGraw-Hill Companies, Inc; 2012.

2. Grossman D, Leffell DJ. The molecular basis of nonmelanoma skin cancer: new understanding. *Arch Dermatol*. 1997;133(10):1263-1270. doi:10.1001/archderm.1997.03890460087010.

3. Martinez MAR, Et.all. Molecular genetics of non-melanoma skin cancer* Genética molecular aplicada ao câncer cutâneo não melanoma. *An Bras Dermatol*. 2006;81(5):405-419.

4. Kim I, He Y-Y. Ultraviolet radiation-induced non-melanoma skin cancer: Regulation of DNA damage repair and inflammation. *Genes Dis*. 2014;1(2):188-198. doi:10.1016/j.gendis.2014.08.005.

5. Pleasance ED, Cheetham RK, Stephens PJ, et al. A comprehensive catalogue of somatic mutations from a human cancer genome. *Nature*. 2010;463(7278):191-196. doi:10.1038/nature08658.

6. Genomic Classification of Cutaneous Melanoma. *Cell*. 2015;161(7):1681-1696. doi:10.1016/j.cell.2015.05.044.

7. Dunn DS, Inoko H, Kulski JK. The association between non-melanoma skin cancer and a young dimorphic Alu element within the major histocompatibility complex class I genomic region. *Tissue Antigens*. 2006;68(2):127-134. doi:10.1111/j.1399-0039.2006.00631.x.

8. Boukamp P. Non-melanoma skin cancer: what drives tumor development and progression? *Carcinogenesis*. 2005;26(10):1657-1667. doi:10.1093/carcin/bgi123.

9. Lomas a., Leonardi-Bee J, Bath-Hextall F. A systematic review of worldwide incidence of nonmelanoma skin cancer. *Br J Dermatol*. 2012;166(5):1069-1080. doi:10.1111/j.1365-2133.2012.10830.x.

10. *Non-Melanoma Skin Cancer / General Practice Consultations, Hospitalisation and Mortality*. Canberra doi:Cat. no. CAN 39.

11. Non-melanoma skin cancer incidence. *Cancer Res UK*. http://www.cancerresearchuk.org/health-professional/cancer-statistics/statistics-by-cancer-type/skin-cancer/incidence#heading-Ten.

12. Quirk C, Gebauer K, De'Ambrosis B, Slade HB, Meng T-C. Progression of Actinic Keratosis to Squamous Cell Carcinoma Revisited: Clinical and Treatment Implications. *Cutis*. 2010;85(April):318-324. http://www.amjorthopedics.com/fileadmin/qhi_archive/ArticlePDF/CT/085060318.pdf\nhttp://www.medapharma.cz/pdf/aldara/sbbc/Aldara-Quirk-C-2011-sBCC.pdf.

13. Sidoroff a, Thaler P. Taking treatment decisions in non-melanoma skin cancer--the place for topical photodynamic therapy (PDT). *Photodiagnosis Photodyn Ther*. 2010;7(1):24-32. doi:10.1016/j.pdpdt.2009.12.004.

14. Braathen LR, Szeimies R-M, Basset-Seguin N, et al. Guidelines on the use of photodynamic therapy for nonmelanoma skin cancer: an international consensus. International Society for

Photodynamic Therapy in Dermatology, 2005. *J Am Acad Dermatol*. 2007;56:125-143. doi:10.1016/j.jaad.2006.06.006.

15. Morton C a., McKenna KE, Rhodes LE. Guidelines for topical photodynamic therapy: Update. *Br J Dermatol*. 2008;159:1245-1266. doi:10.1111/j.1365-2133.2008.08882.x.

16. Ibbotson SH, Dawe RS, Morton C a. A survey of photodynamic therapy services in dermatology departments across Scotland. *Clin Exp Dermatol*. 2013;38:511-516. doi:10.1111/ced.12051.

17. I.D.W. Samuel JF and AM. OLEDS: Next generation photodynamic therapy of skin cancer. In: *PDT Book Chapter*.; :1-6.

18. Ibbotson S, Moseley H, Brancaleon L, et al. Photodynamic therapy in dermatology: Dundee clinical and research experience. *Photodiagnosis Photodyn Ther*. 2004;1(3):211-223. doi:10.1016/S1572-1000(04)00045-6.

19. Idris NM, Gnanasammandhan MK, Zhang J, Ho PC, Mahendran R, Zhang Y. In vivo photodynamic therapy using upconversion nanoparticles as remote-controlled nanotransducers. *Nat Med*. 2012;18(10):1580-1585. doi:10.1038/nm.2933.

20. Luo G-F, Chen W-H, Liu Y, Lei Q, Zhuo R-X, Zhang X-Z. Multifunctional Enveloped Mesoporous Silica Nanoparticles for Subcellular Co-delivery of Drug and Therapeutic Peptide. *Sci Rep*. 2014;4:6064. doi:10.1038/srep06064.

21. Lucky SS, Muhammad Idris N, Li Z, Huang K, Soo KC, Zhang Y. Titania Coated Upconversion Nanoparticles for Near-Infrared Light Triggered Photodynamic Therapy. *ACS Nano*. 2015;9(1):191-205. doi:10.1021/nn503450t.

22. Morton C a, McKenna KE, Rhodes LE. Guidelines for topical photodynamic therapy: update. *Br J Dermatol*. 2008;159(6):1245-1266. doi:10.1111/j.1365-2133.2008.08882.x.

23. Svanberg K, Andersson T, Killander D, et al. Photodynamic therapy of non-melanoma malignant tumours of the skin using topical ??-amino levulinic acid sensitization and laser irradiation. *Br J Dermatol*. 1994;130(6):743-751. doi:10.1111/j.1365-2133.1994.tb03412.x.

24. Kennedy JC, Pottier RH, Pross DC. *Photodynamic Therapy with Endogenous Protoporphyrin IX: Basic Principles and Present Clinical Experience.*; 1990. doi:10.1016/1011-1344(90)85083-9.

25. Ibbotson SH. An overview of topical photodynamic therapy in dermatology. *Photodiagnosis Photodyn Ther*. 2010;7(1):16-23. doi:10.1016/j.pdpdt.2009.12.001.

26. Molnár a., Dědic R, Kořínek M, Svoboda A, Hála J. Protoporphyrin IX and hematoporphyrin derivatives interactions with oxygen studied by time and spectral resolved phosphorescence. *J Mol Struct*. 2005;744-747(SPEC. ISS.):723-726. doi:10.1016/j.molstruc.2004.10.087.

27. Jockusch S, Bonda C, Hu S. Photostabilization of endogenous porphyrins: excited state quenching by fused ring cyanoacrylates. *Photochem Photobiol Sci*. 2014:1180-1184. doi:10.1039/c4pp00090k.

28. Исаева ОГ, Осипов ВА. Влияние фотодинамического воздействия на противораковый иммунитет. In: Тучина ВВ, Симоненко ГВ, eds. *ПРОБЛЕМЫ ОПТИЧЕСКОЙ ФИЗИКИ И БИФОТОНИКИ*. Саратов: «Новый ветер»; 2009:10-13. doi:УДК 535(068) ББК 22.343.43.

29. Buytaert E, Dewaele M, Agostinis P. Molecular effectors of multiple cell death pathways initiated by photodynamic therapy. *Biochim Biophys Acta - Rev Cancer*. 2007;1776:86-107. doi:10.1016/j.bbcan.2007.07.001.

30. Weishaupt KR, Gomer CJ, Dougherty TJ. Identification of singlet oxygen as the cytotoxic agent in photoinactivation of a murine tumor. *Cancer Res*. 1976;36(7 PT 1):2326-2329.

31. Jarvi MT, Niedre MJ, Patterson MS, Wilson BC. The Influence of Oxygen Depletion and Photosensitizer Triplet-state Dynamics During Photodynamic Therapy on Accurate Singlet Oxygen Luminescence Monitoring and Analysis of Treatment Dose Response. *Photochem Photobiol*. 2011;87(1):223-234. doi:10.1111/j.1751-1097.2010.00851.x.

32. Chen L, Lin L, Li Y, et al. Effect of oxygen concentration on singlet oxygen luminescence detection. *J Lumin*. 2014;152:98-102. doi:10.1016/j.jlumin.2013.10.034.

33. Niedre M, Patterson MS, Wilson BC. Direct near-infrared luminescence detection of singlet oxygen generated by photodynamic therapy in cells in vitro and tissues in vivo. *Photochem Photobiol*. 2002;75(4):382-391. http://www.ncbi.nlm.nih.gov/pubmed/12003128.

34. Tanner MG, Natarajan CM, Pottapenjara VK, et al. Enhanced telecom wavelength single-photon detection with NbTiN superconducting nanowires on oxidized silicon. *Appl Phys Lett*. 2010;96(22):221109. doi:10.1063/1.3428960.

35. Gemmell NR, McCarthy A, Liu B, et al. Singlet oxygen luminescence detection with a fiber-coupled superconducting nanowire single-photon detector. *Opt Express*. 2013;21(4):5005. doi:10.1364/OE.21.005005.

36. Scholz M, Dědic R, Valenta J, Breitenbach T, Hála J. Real-time luminescence microspectroscopy monitoring of singlet oxygen in individual cells. *Photochem Photobiol Sci*. 2014;13(8):1203. doi:10.1039/C4PP00121D.

37. Russell JA, Diamond KR, Collins TJ, et al. Characterization of Fluorescence Lifetime of Photofrin and Delta-Aminolevulinic Acid Induced Protoporphyrin IX in Living Cells Using Single- and Two-Photon Excitation. *IEEE J Sel Top Quantum Electron*. 2008;14(1):158-166. doi:10.1109/JSTQE.2007.912896.

38. De Leeuw J, Van der Beek N, Neugebauer WD, Bjerring P, Neumann H a M. Fluorescence detection and diagnosis of non-Melanoma skin cancer at an early stage. *Lasers Surg Med*. 2009;41(2):96-103. doi:10.1002/lsm.20739.

39. Hewett J, McKechnie T, Sibbett W, Ferguson J, Clark C, Padgett M. Fluorescence detection of superficial skin cancers. *J Mod Opt*. 2000;47(11):2021-2027. doi:10.1080/095003400417179.

40. Mogensen M, Jemec GBE. Diagnosis of nonmelanoma skin cancer/keratinocyte carcinoma: A review of diagnostic accuracy of nonmelanoma skin cancer diagnostic tests and technologies. *Dermatologic Surg*. 2007;33(10):1158-1174. doi:10.1111/j.1524-4725.2007.33251.x.

41. Hetzel F, Brahmavar S, Chen Q, et al. Photodynamic Therapy Dosimetry. *AAPM*. 2005;Report(88):30.

42. Wang KKH, Finlay JC, Busch TM, Hahn SM, Zhu TC. Explicit dosimetry for photodynamic therapy: Macroscopic singlet oxygen modeling. *J Biophotonics*. 2010;3(5):304-318. doi:10.1002/jbio.200900101.

43. Zhu TC, Liu B, Penjweini R. Study of tissue oxygen supply rate in a macroscopic photodynamic therapy singlet oxygen model. *J Biomed Opt*. 2015;20(3):038001. doi:10.1117/1.JBO.20.3.038001.

44. Chaves YN, Torezan LA, Niwa ABM, Sanches Junior JA, Festa Neto C. Pain in photodynamic therapy: mechanism of action and management strategies. *An Bras Dermatol*. 2012;87(4):521-529. doi:10.1590/S0365-05962012000400001.

45. Sandberg C, Stenquist B, Rosdahl I, et al. Important Factors for Pain during Photodynamic Therapy for Actinic Keratosis. *Acta Derm Venereol*. 2006;86(5):404-408. doi:10.2340/00015555-0098.

46. Arits a HMM, van de Weert MM, Nelemans PJ, Kelleners-Smeets NWJ. Pain during topical photodynamic therapy: uncomfortable and unpredictable. *J Eur Acad Dermatol Venereol*. 2010;24(12):1452-1457. doi:10.1111/j.1468-3083.2010.03670.x.

47. Ibbotson SH. Adverse effects of topical photodynamic therapy. *Photodermatol Photoimmunol Photomed*. 2011;27(3):116-130. doi:10.1111/j.1600-0781.2010.00560.x.

48. Wiegell SR, Haedersdal M, Wulf HC. Cold water and pauses in illumination reduces pain during photodynamic therapy: a randomized clinical study. *Acta Derm Venereol*. 2009;89(2):145-149. doi:10.2340/00015555-0568.

49. Moseley H, Allen JW, Ibbotson S, et al. Ambulatory photodynamic therapy: a new concept in delivering photodynamic therapy. *Br J Dermatol*. 2006;154(4):747-750. doi:10.1111/j.1365-2133.2006.07145.x.

50. Attili SK, Lesar A, McNeill A, et al. An open pilot study of ambulatory photodynamic therapy using a wearable low-irradiance organic light-emitting diode light source in the treatment of nonmelanoma skin cancer. *Br J Dermatol*. 2009;161(1):170-173. doi:10.1111/j.1365-2133.2009.09096.x.

51. Lerche CM, Fabricius S, Philipsen PA, Wulf HC. Correlation between treatment time, photobleaching, inflammation and pain after photodynamic therapy with methyl aminolevulinate on tape-stripped skin in healthy volunteers. *Photochem Photobiol Sci*. 2015;14(5):875-882. doi:10.1039/C5PP00069F.

52. Wiegell SR, Petersen B, Wulf HC. Topical corticosteroid reduces inflammation without compromising the efficacy of photodynamic therapy for actinic keratoses: a randomized clinical trial. *Br J Dermatol*. 2014;171(6):1487-1492. doi:10.1111/bjd.13284.

53. Fernández-Guarino M, Harto A, Pérez-García B, Royuela A, Jaén P. Six Years of Experience in Photodynamic Therapy for Basal Cell Carcinoma: Results and Fluorescence Diagnosis from 191 Lesions. *J Skin Cancer*. 2014;2014:1-7. doi:10.1155/2014/849248.

54. Sandberg C, Paoli J, Halldin CB, et al. Photodynamic therapy for “difficult-to-treat” basal cell carcinomas. Do poorly responding BCCs lack accumulation of protoporphyrin IX after ALA/MAL application? *Proc SPIE*. 2009;7380:73805K - 73805K - 8. doi:10.1117/12.822981.

55. Sandberg C, Paoli J, Gillstedt M, et al. Fluorescence diagnostics of basal cell carcinomas comparing methyl-aminolaevulinate and aminolaevulinic acid and correlation with visual clinical tumour size. *Acta Derm Venereol*. 2011;91:398-403. doi:10.2340/00015555-1068.

56. Fritsch C, Lehmann P, Stahl W, et al. Optimum porphyrin accumulation in epithelial skin tumours and psoriatic lesions after topical application of delta-aminolaevulinic acid. *Br J Cancer*. 1999;79(9-10):1603-1608. doi:10.1038/sj.bjc.6690255.

57. Angell-Petersen E, Sørensen R, Warloe T, et al. Porphyrin formation in actinic keratosis and basal cell carcinoma after topical application of methyl 5-aminolevulinate. *J Invest Dermatol*. 2006;126(2):265-271. doi:10.1038/sj.jid.5700048.

58. Kanick SC, Davis SC, Zhao Y, et al. Dual-channel red/blue fluorescence dosimetry with broadband reflectance spectroscopic correction measures protoporphyrin IX production during photodynamic therapy of actinic keratosis. *J Biomed Opt*. 2014;19:075002. doi:10.1117/1.JBO.19.7.075002.

59. Sunar U, Rohrbach DJ, Morgan J, Zeitouni N, Henderson BW. Quantification of PpIX concentration in basal cell carcinoma and squamous cell carcinoma models using spatial frequency domain imaging. *Biomed Opt Express*. 2013;4(4):531-537. doi:10.1364/BOE.4.000531.

60. Tyrrell J, Campbell S, Curnow A. Validation of a non-invasive fluorescence imaging system to monitor dermatological PDT. *Photodiagnosis Photodyn Ther*. 2010;7(2):86-97. doi:10.1016/j.pdpdt.2010.03.002.

61. Georgakoudi I, Jacobson BC, Müller MG, et al. NAD(P)H and collagen as in vivo quantitative fluorescent biomarkers of epithelial precancerous changes. *Cancer Res*. 2002;62(3):682-687.

62. Borisova E, Zhelyazkova A, Genova T, Avramov L, Pavlova E, Troyanova P. Using spectroscopy to diagnose skin cancer. *SPIE Newsroom*. 2014. doi:10.1117/2.1201405.005509.

63. Pires L, Nogueira MS, Pratavieira S, Moriyama LT, Kurachi C. Time-resolved fluorescence lifetime for cutaneous melanoma detection. *Biomed Opt Express*. 2014;5(9):3080. doi:10.1364/BOE.5.003080.

64. MathWorks. *Image Acquisition Toolbox. Acquire Images and Video from Industry-Standard Hardware*. http://www.mathworks.com/products/imaq/.

65. MathWorks. Image Processing Toolbox. Perform image processing, analysis, and algorithm development. http://www.mathworks.com/products/image/.

66. MathWorks. Computer Vision System Toolbox. Design and simulate computer vision and video processing systems. http://www.mathworks.com/products/computer-vision/.

67. Bays R, Wagnières G, Robert D, et al. Three-dimensional optical phantom and its application in photodynamic therapy. *Lasers Surg Med*. 1997;21(3):227-234. http://www.ncbi.nlm.nih.gov/pubmed/9291079.

68. Pogue BW, Patterson MS. Review of tissue simulating phantoms for optical spectroscopy, imaging and dosimetry. *J Biomed Opt*. 2015;11(August 2006):041102-1 - 16. doi:10.1117/1.2335429.

69. Ibbotson SH, Moseley H, Brancaleon L, et al. Photodynamic therapy in dermatology: Dundee clinical and research experience. *Photodiagnosis Photodyn Ther*. 2004;1:211-223. doi:10.1016/S1572-1000(04)00045-6.

70. Valentine RM, Ibbotson SH, Wood K, Brown CT a, Moseley H. Modelling Fluorescence in Clinical Photodynamic Therapy. *Photochem Photobiol Sci*. 2012:203-213. doi:10.1039/c2pp25271f.

71. Valentine RM. Biophysical Aspects of Photodynamic Therapy. *PhD Thesis*. 2011. http://hdl.handle.net/10023/2471.

72. Valentine RM, Brown CT a, Moseley H, Ibbotson S, Wood K. Monte Carlo modeling of in vivo protoporphyrin IX fluorescence and singlet oxygen production during photodynamic therapy for patients presenting with superficial basal cell carcinomas. *J Biomed Opt*. 2011;16:048002. doi:10.1117/1.3562540.

73. ISO 14155:2011 Clinical investigation of medical devices for human subjects -Good clinical practice. :58. http://www.iso.org/iso/home/store/catalogue_ics/catalogue_detail_ics.htm?csnumber=45557.

74. Moseley H. Light distribution and calibration of commercial PDT LED arrays. *Photochem Photobiol Sci*. 2005;4(11):911-914. doi:10.1039/b507325a.

75. *Ambulight PDT Therapy in Motion / Instructions for Use*.; 2007.

76. International Standard. Safety of laser products – Part 1: Equipment, classification, requirements and user's guide / Edition 1.2 consolidated with amendments 1:1997 and 2:2001, p 115, 2001-08, - Ref # IEC 60825-1:1993+A1:1997+A2:2001(E).

77. The University of St Andrews local rules for work with lasers. http://www.st-andrews.ac.uk/staff/policy/healthandsafety/localrulesforlasers/.

78. MathWorks. Using RANSAC for estimating geometric transforms in computer vision. 2014. http://www.mathworks.com/discovery/ransac.html.

Chapter 3

Fluorescence time course imaging: clinical study of Protoporphyrin IX formation in healthy and diseased skin

We went down into the silent garden. Dawn is the time when nothing breathes, the hour of silence. Everything is transfixed, only the light moves.

The task of the right eye is to peer into the telescope, while the left eye peers into the microscope.

— Leonora Carrington (1917 – 2011),

Surrealist artist

3.1 Introduction

The general background about PDT treatment covering the metabolic reactions involved in uptaking the pro-drug from the dermatological creams and converting it into PpIX photosensitizer, the photophysical processes related to the excitation of PpIX and resulting in phototoxic reactions were covered in the previous chapter. This chapter will focus on the clinical aspects relevant for PDT treatment, in particular the treatment procedures at the Photobiology unit (PBU), Ninewells Hospital; and PpIX fluorescence diagnostics. The study will discuss PpIX metabolism with respect to different creams, diagnoses, body sites, correlation to pain and tumours response.

Topical PDT is an effective treatment of NMSC and dysplasia with excellent cosmetic outcome and healing[1,2,3,4,5]. PDT is administered for the treatment of superficial basal cell carcinoma (sBCC), Bowen's disease (BD), and actinic keratosis (AK) in Europe, Asia, Australia,

South America[1,2,3,6,7]. In the US it is only used for treating AK which is a pre-malignant skin condition occurring due to chronic sun damage[8]. If left untreated AK can progress to squamous cell carcinoma (SCC)[9]. BD is carcinoma in situ, similar to AK it can progress to invasive SCC. BCC is the most common skin cancer. NMSC and dysplasia are often multiple with low risk. PDT is one of the best choices for large multiple superficial lesions, field carcinogenesis or dysplasia. It is also a good choice in cases where repeated treatments are needed[3] often in immunosuppressed patients, including organ transplant recipients[10].

At the PBU PDT is administered for sBCC, nodular BCC, BD and AK. A typical procedure is shown in ***Figure 3.1***. White light photographs were taken by a medical photographer before the treatment, and the lesions were prepared with a curette to remove all crust and help the creams to diffuse better in the skin. A thin layer of cream (5-aminolaevulinic acid (ALA), Ameluz or methyl aminolevulinate (MAL), Metvix®) was applied to the lesion and covered with Tegaderm™ film and Mepore™ occlusive dressing for three hours to metabolise into PpIX. The amount of the cream should be sufficient (between 0.01-0.09 ml) to cover the whole area of the lesion[11]. After three hours the dressing is removed, the surplus cream is cleaned up with a cotton wipe, PpIX fluorescence is visually accessed using a Wood's lamp, and 635 nm centre wavelength PDT lamps are used for conventional treatment. The total treatment dose is 75 J/cm^2. In the other centres total dose varies between 37 and 150 J/cm^2. Topically 65-75 mW/cm^2 irradiance is used[12]. The treatment lasts for approximately 19 minutes (the regime is chosen for each PDT lamp to deliver 75 J/cm^2). After the treatment pain is assessed on the visual time scale from 0 points which corresponds to no pain to 10 points which is the worst pain one can imagine. Only in 16% of the cases the treatment is accompanied by severe pain and in some of the cases it has to be terminated or paused, cooling air is typically used for pain relief during the treatment[13,14]. However, there are reports in the literature that cooling air reduces the rate of sucessful outcomes[15]. It is not clear what causes the pain during the PDT[16,17]; there are controversial reports questioning whether PpIX concentration (fluorescence) has any correlation to the pain experienced[8,18].

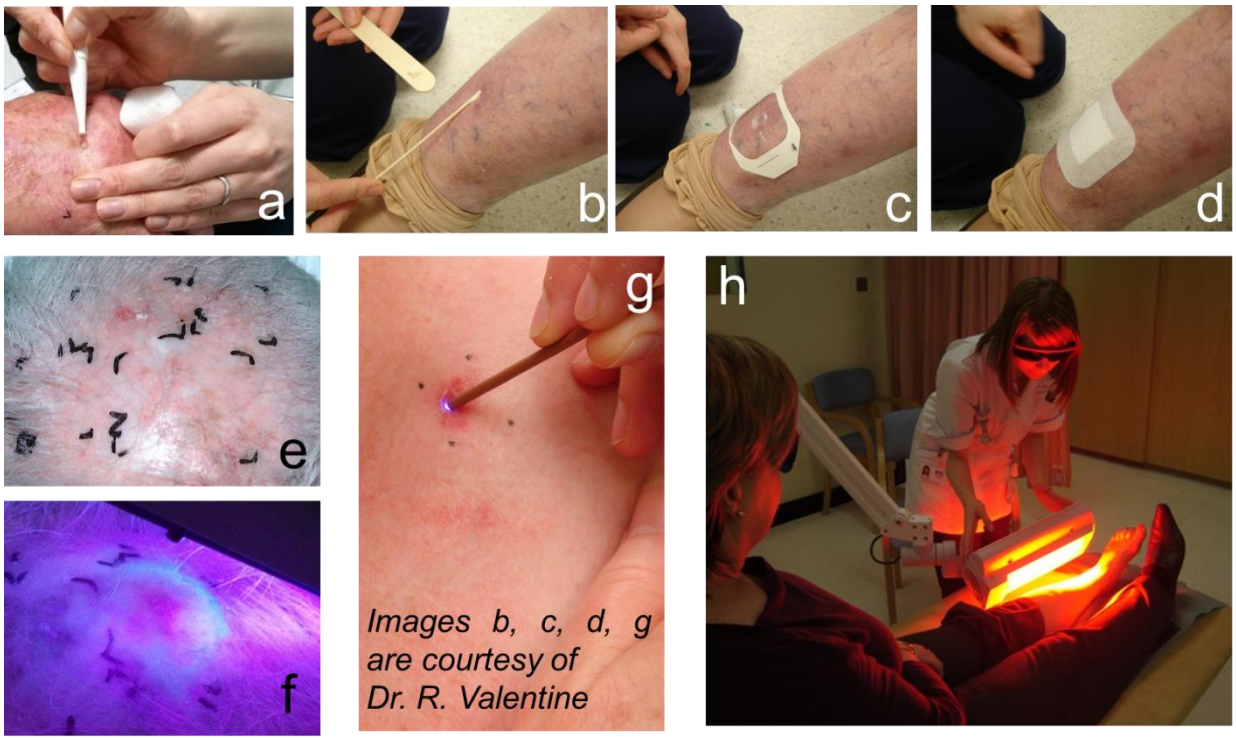

Figure 3.1*: PDT procedure for treating a skin cancer at the Photobiology Unit, Ninewells Hospital (***a - d –** *lesion's preparation).* **a –** *the surface of the lesion is prepared by a curette.* **b –** *Ameluz gel or Metvix® is applied with a wooden spatula at the surface of the lesion.* **c, d –** *Tegaderm™ film and Mepore™ occlusive dressing are covering the cream for three hours.* **e –** *a white light medical photograph.* **f –** *PpIX fluorescence visual assessment using a Wood's lamp;* **g –** *PpIX fluorescence measurements using an optical biopsy system* [19,20,21]*.* **h –** *Aktilite CL128 lamp is used for the conventional PDT treatment. Typically, 75 mJ/cm*^{2} *total dose is delivered during 18-20 min with 65-75 mW/cm2 irradiance at 8.5 cm distance from the lamp. After the treatment pain is assessed on the visual pain score (from 0 to 10 points).*

Although topical PDT is an effective and widely used treatment, the response to the treatment could yet be improved. AK and sBCC have better response to the treatment, 94 % compared to 74 % for nodular BCC[22]. Morton et al (2007) in the Guidelines on the use of photodynamic therapy[4] report the clearance rates. AK at 3 month follow up was cleared in 90% of the cases, sBCC at a 3 month follow up was cleared in 80-97%, BCC at 48 month was clear in 78% cases. A median clearance was 73% at a 6 months median follow-up (range 2–12) in 382 lesions (BCC: n = 126, BD: n = 104, AK: n = 135, nodular BCC: n = 7) across 10 PDT centres in Scotland[3]. 26% of lesions require more than one cycle of PDT treatment[3]; routinely BCC diagnoses administered two cycles treatment separated one week apart. A possible explanation why BCC is more difficult to treat with PDT could be that PpIX metabolises better in superficial layers than in deeper layers[23]. BCC develops in basal cells which are deeper in the

skin than keratinocytes cells. AK develops in keratinocytes. PpIX distribution is one of the key treatment factors. Surface fluorescence is a powerful way of studying the formation of PpIX.

There have been many studies on PpIX fluorescence for PDT[24,25,18,23,26,27,22,8,28,29,30,31], however, there are still many gaps in our knowledge of how PDT works and conflicting reports on PpIX metabolism. One of the arguments is whether or not PpIX fluorescence can be useful for PDT diagnostics. In [29] 54 lesions (21 BCCs, 22 AK, and 11 seborrheic keratosis SK) were used in the study to establish if auto-fluorescence combined with PpIX assisted fluorescence can be used for optical detection of NMSC. ALA solution was applied to the lesions and the fluorescence was imaged at 15, 30, 45 and 60 min in a dark room. They found a noticeable difference between the autofluorescence in healthy and diseased skin; PpIX fluorescence increased the contrast at the lesion margins. In the following study [30] 8 BCC lesions on different anatomical sites were studied using MAL as PpIX precursor. PpIX fluorescence was imaged after 3 hours of MAL application before PDT treatment and immediately after for the first and the second PDT treatment which were separated one week apart. They found that the fluorescence was different at different anatomical sites of the lesions; it was higher on the lip of one subject compared to the eye lid on another subject. The fluorescence was higher before the second PDT session. In both studies relative fluorescence was measured by a portable fluorescence imaging camera integrated with a treatment light source. The dressing and the cream was removed between the images. But it is not clear what the procedure was to make sure that the identical area was analysed between the time course images. Our experience showed that marker pen is not a stable reference as it was dissolved in creams and blurred over the surface of the skin, or removed during the cleaning between the images. The fluorescence was integrated from the images using the values of red pixels. Again, it is not clear what area was integrated and if it was identical between the images. The illumination light was not synchronised with the image acquisition; and the irradiance was 50 mW/cm^2 which is comparable with the treatment PDT lamps. The excitation wavelength of the device was 405 nm; PpIX absorption at this wavelength is more than 10 times higher that at 635 nm treatment wavelength. There was a high probability of PpIX photobleaching during the measurements.

There are other reports which support the facts that PpIX fluorescence can be an indicator of pre-clinical changes in the tissue [27,24,32]. On the other hand there are contradictory studies which show that PpIX fluorescence does not correlate to PDT responses[22,25] therefore can not be ultimately and solely used for PDT diagnostics or optical detection of skin cancer. In these studies fluorescence was not quantified, but visually analysed and correlated to the lesion response.

Another controversial point is the correlation of PpIX fluorescence and pain[8,18]; and the differences in PpIX time course formed from ALA and MAL precursors. There was one study which reported higher PpIX metabolism from ALA precursor than from MAL[18]. From previous experience at PBU there was no difference in ALA and MAL induced fluorescence after 3 hours from the application of the creams in BCC and BD[11], the fluorescence was not significantly different in healthy skin after application of ALA precursor than MAL at 4 hours from the application of the creams, but it became higher for ALA precursor at longer metabolism times[33]. Typically PpIX concentration reaches plateau in 6 hours after the application of ALA precursor[34] and 13 hours after the application of MAL precursor[35]. The full time course for ALA precursor is 24 h[34] and 18 hours for MAL precursor[35]. It is worth noting that the specificity in PpIX metabolism in healthy and diseased skin decreases substantially with time. The most recent reports show that pulsing and shorter metabolism times increase specificity of PpIX accumulation in the malignant cells and reduce pain[36].

In order to address all the above open questions, this study aimed to gather fluorescent images from different diagnoses using two types of creams looking at specific fluorescence patterns and differences between the creams, to learn about PpIX time course at small time steps during the recommended three hours for PpIX metabolism before the treatment, gather information on fluorescence correlation to pain, and to investigate how the improved device and fluorescence diagnostics in general can be helpful in predicting the lesions' response and the reccurence.

3.2 Methods

3.2.1 The Good Clinical Practice (GCP) regulations for a clinical study using a prototype device

The University of St Andrews Teaching and Research Ethics Committee (UTREC) is responsible for evaluating ethical considerations for conducting any studies involving study biological materials or *in-vivo* measurements on healthy volunteers. The Medicines for Human Use (Clinical Trials) regulations 2006 No. 1928 for good clinical practice (GCP) stipulates the requirements for conducting any studies on healthy volunteers and patients. Among the most important requirements laid down in both regulations there are the following points. The

participants have to be informed at least one day before the study and be able to discuss the study, an informed written consent for taking part in the study has to be obtained before the study, the data handling has to be anonymous, only the members of the research team should be able to identify the participants, the data has to be stored on a computer in a special locked room, the participants should be able to withdraw from the study at any point without providing any reasons, the participation in the study should not have any impact on the treatment, clinical procedures have to be conducted only by trained clinical personnel, and health and safety regulations have to be met.

In order to eliminate any possibility for the patients to feel uncomfortable giving a negative response or having concerns about the outcomes of the treatment in cases of negative response the recruitment procedure was designed in the following way. The patients' referrals were screened by the Chief investigator. In case the diagnoses met the exclusion and the inclusion criteria the patients received an opt-in slip at the bottom of the Patient Information Sheets (PIS) together with their appointment letter for the PDT treatment. The opt-in slip asked them to respond by phone, mail or email in case they were interested in taking part in the study instead of being approached by a clinician. The patients did not need to take any actions if they were not interested in taking part in the study. These considerations did not concern the cohort of the healthy volunteers as they were recruited from the database of the Photobiology unit by the research coordinator.

Both the patients and the healthy volunteers had a chance to discuss the study prior to their visit to the PBU with a member of the research team: the chief investigator, the research coordinator or the investigator, or with an independent person at Ninewells hospital with relevant expertise. On the day of the experiment they were briefed about the study and had a chance to ask any questions. There were no personal benefits for participating in the study and the experiment could be terminated at any point if it was uncomfortable. The patients were provided lunch and refreshments, and the volunteers were provided with a small compensation for their expense and inconvenience. All of the data was kept as confidential and the access to the identity of the participants was only available to the members of the research team. The participants agreed that their unidentifiable data could be used for scientific reports, journal papers, conferences and the thesis.

The patients had their standard PDT treatment after the measurements. For the healthy volunteers the area on the skin used in the study was cleaned with alcohol wipes and covered with an occlusive dressing for 24 h to prevent photosensitivity. After that the volunteers would have completed the study.

The application in the Integrated Research Approval System IRAS has Project ID 136393, and Tayside medical science Centre TACS R&D, REC Ref # 2013DS03. The application received approval by the East of Scotland Research Ethics Service EoSRES committee at the TACS, Ref # 13/ES/0151, and the UTREC commettee Ref No: PA10783.

All of the required documents: the study protocol, patient (PIS) and volunteer information sheets, letter of invitation, travel expense forms, patient and volunteer consent forms, a letter of Sponsorship Insurance (Ref 2013DS03) can be found in the Appendix II- XIII:

Appendix II: Capturing fluorescence – Protocol v.1 21.10.2013;

Appendix III: Capturing fluorescence – Device assessment for clinical trials;

Appendix IV: Capturing fluorescence – Standard Operating Procedure (SOP);

Appendix V: Capturing fluorescence – Healthy Volunteer Participant Information Sheet PIS v.2 17.12.2013PIS;

Appendix VI: Capturing fluorescence – Patients Participant Information Sheet PIS v.2 17.12.2013;

Appendix VII: Capturing fluorescence – Healthy Volunteer Consent Form 21.10.2013 V.1;

Appendix VIII: Capturing fluorescence – Patient Consent Form 21.10.2013 V.1;

Appendix IX: Capturing fluorescence – Patient Consent Form 21.10.2013 V.1;

Appendix X: Capturing fluorescence – Participant Travel Expenses Form 2013 V.1;

Appendix XI: Capturing fluorescence – Sponsor Letter Insurance Note 2013DS03;

Appendix XII: Capturing fluorescence – East of Scotland Research Ethics Service EoSRES Favourable Opinion Letter;

Appendix XIII: Capturing fluorescence – University of St Andrews Teaching and Research Ethics Committee UTREC Approval Letter 10.02.2014.

3.2.2 Statistical data analysis

In order to compare the results of PpIX time course between the groups – the diagnoses, the creams, etc. two-sample t-test with unequal variances was calculated in excel between different groups. P-values were analysed at each time step to identify the statistical significance between the groups. The groups are statistically significantly different if p-value > 0.05.

3.3 Results

3.3.1 The set up

The full experimental setup for clinical experiments is shown in the ***Figure 3.2***. It fits on top of a small hospital trolley. The consumables for the study such as cotton wipes, the dressings and the creams are normally kept in a handy location on a small hospital tray.

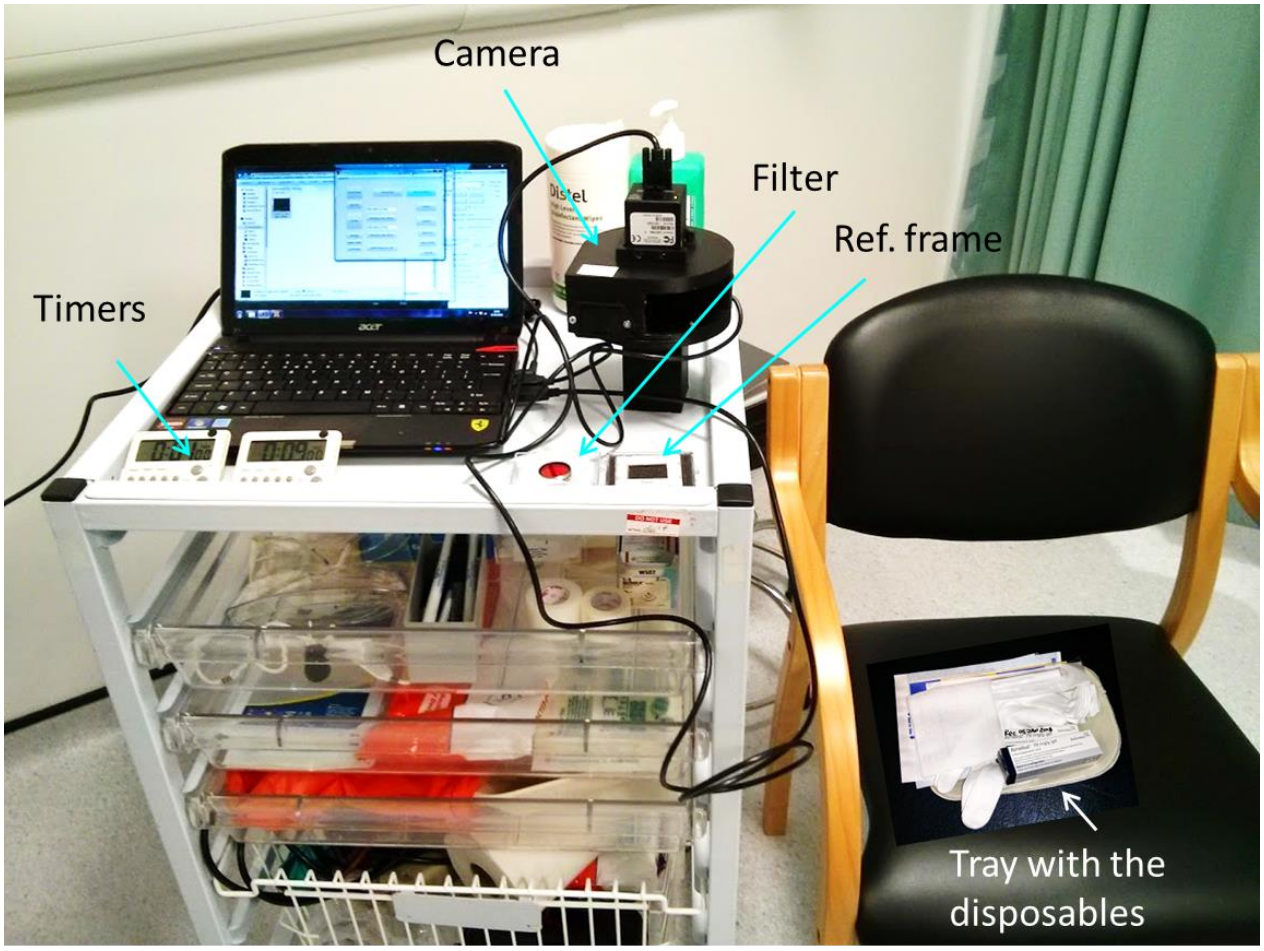

Figure 3.2*: Fluorescence measurements setup. The camera was connected to a laptop via a USB cable and can move around the patient; two timers control the time step of the measurement, one was used to time the waiting and another the duration of the imaging procedure which is re-applying the cream and taking an image. The disposable reference frame is fixed at the study area after the lesion is curetted. The filter is fixed at the camera lens after normal images of the skin are taken. All of the disposables such as the creams, the spatulas, the dressings, a dermatological tape, gloves, and cotton wipes are placed in a carton hospital tray and are on the patient's chair on this image.*

3.3.2 Study design

For the patient cohort, the study was designed to avoid an extra visit to the hospital and be compatible with the routine PDT treatment at the PBU (***Figure 3.1***). The fluorescence was imaged during the three hours of what is called “waiting” time, i.e. the time between the application of the cream and the start of the treatment. A clinical technician was present to apply the cream and prepare the lesions.

The measurement procedure is shown in ***Figure 3.3***. The measurements were taken at 10 minute intervals. The healthy volunteers’ skin was cleaned with ethanol wipes, and left for a few minutes to dry. After that the reference frame was fixed and the study area was ready for the measurements. Patients’ lesions were photographed by a medical photographer then the lesions were prepared with a curette to remove all crust; the reference frame was fixed and the study area was ready for the measurements.

The first iteration of the measurements was different from the rest of the measurements: a normal image under 405 nm illumination was taken with the camera in addition to white light medical photographs. Then the emission filter was inserted and the settings for the camera were changed to image the fluorescence. Background fluorescence was recorded. The cream was applied and covered with an occlusive dressing. The cream was removed before each fluorescence measurement, re-applied after an image was taken, and covered with the dressing again. The cream had to be removed due to Metvix® is being opaque. Regardless that Ameluz gel is transparent and did not affect the imaging, the procedure had to be consistent for the comparison. Re-application of the cream should not have made any difference as long as the quantity is in the range of 0.01-0.09 ml[11]. Two timers were used to control the time step. One was set to 9 minutes and another one for 1 minute. After the first application of the cream the 9 minute timer was started. When it had lapsed, the one minute timer was started. During this minute the dressing was lifted up, the cream was removed with a wooden spatula, cleaned up with a cotton wipe, a fluorescence image taken, the same cream from the spatula was put back on (a small amount of fresh cream was added each time when the cream was used up during the measurements to keep the area covered), and the dressing was put back on. After the minute timer had lapsed (normally it was enough for the procedure), the 9 minute timer was started; and the measurements were repeated 18 times during the three hours.

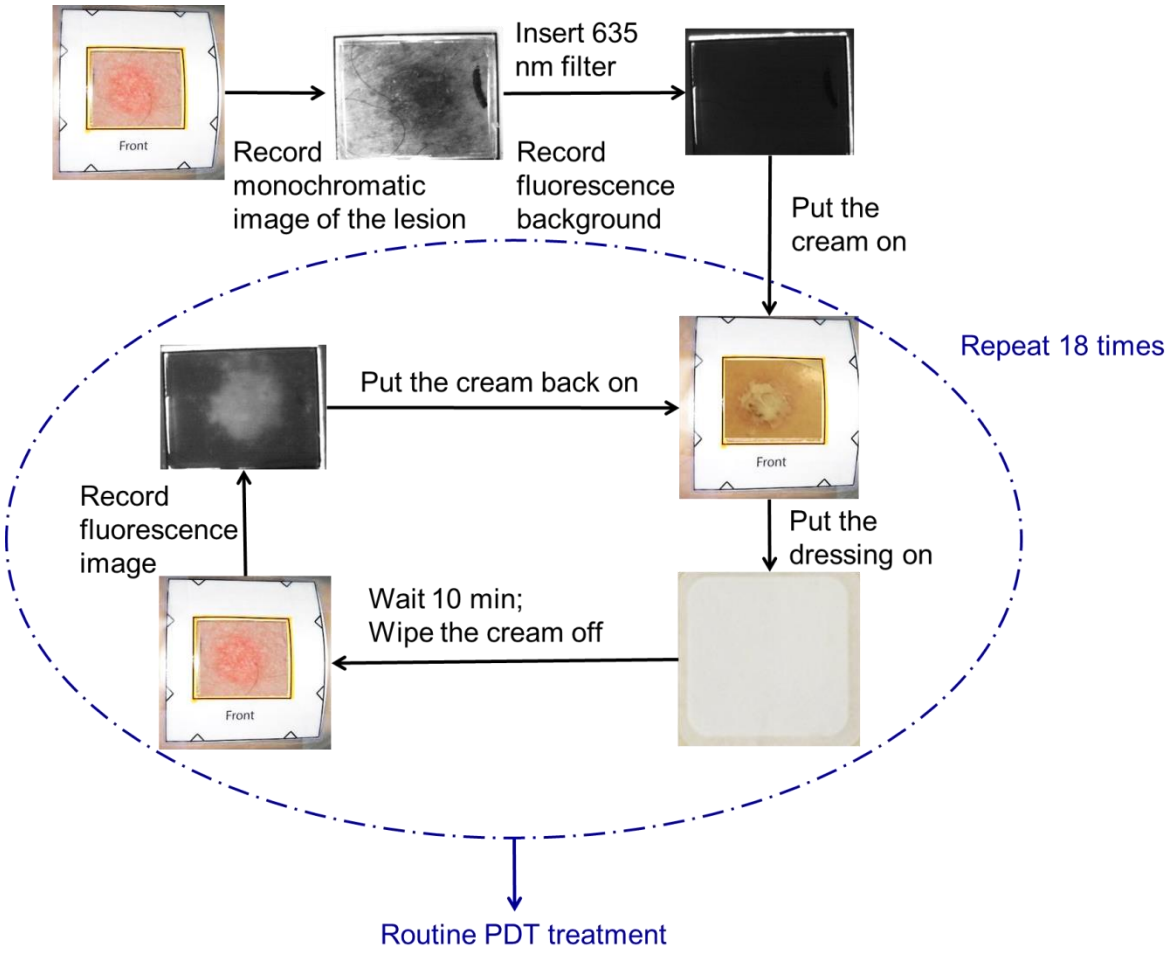

Figure 3.3: *The procedure for the fluorescence time course imaging.*

The size of the initial images were cropped from 640x480 pixels (3.1 mm x 2.4 mm). They were cropped to remove the fluorescent reference contour to 540x380 pixels which corresponded to 2.6 mm x 1.9 mm.

3.3.3 Study population

Healthy volunteers' cohort, inclusion/exclusion criteria

The study protocol included 10 healthy volunteers, a half of them were administered Metvix® and the other half Ameluz. However, one of the volunteers did not express much fluorescence and one extra volunteer was added to the Metvix group in order to have a better baseline. So in total there were 11 volunteers recruited for the study. A previous study at the PBU showed that PpIX fluorescence varies with the body site[37,38]. It was higher on the forearm,

lower on the lower leg and in between on the trunk. Considering this and the fact that the skin on the back is the most uniform, the middle back avoiding the paravertebral regions was the best choice for the base line and was imaged in all the volunteers.

The inclusion criteria for the healthy volunteer cohort were: males and females 18 years old and over (age matched to patient cohort as far as is practicably possible) capable of giving informed consent and able to understand and adhere to protocol requirements. The exclusion criteria were: individuals who are not able to give informed consent, anyone with known allergy to Metvix or Ameluz and known to have a light sensitivity disorder.

Patients' cohort, inclusion/exclusion criteria

There were 15 patients planned in the protocol: 5 patients diagnosed with AK and administered Ameluz PDT, 5 with AK and administered Metvix® PDT and 5 with biopsy confirmed BCC and administered Metvix® PDT. Due to the time scale of the project the study was terminated after 13 patients, meaning that two patients with AK and Ameluz PDT were lacking from the study population.

Inclusion criteria for the patients cohort was males and females 18 years old and over presenting with superficial NMSC and dysplasia, capable of giving informed consent and able to understand and adhere to protocol requirements. The exclusion criteria were: patients who had had previous treatment within the last four months, unable to give informed consent and with known allergy to Metvix or Ameluz or with a light sensitivity disorder.

Neither the body site nor the lesion size were specified. In cases when the size of the lesions were larger than the field of view of the camera, a small area was selected for the study and marked with a marker pen. The area outside was routinely prepared for PDT treatment and covered with an occlusive dressing. An opening in the dressing was cut out to leave the study area accessible. The reference frame was fixed on top of the dressing and the area was ready for the measurements (***Figure 3.4***).

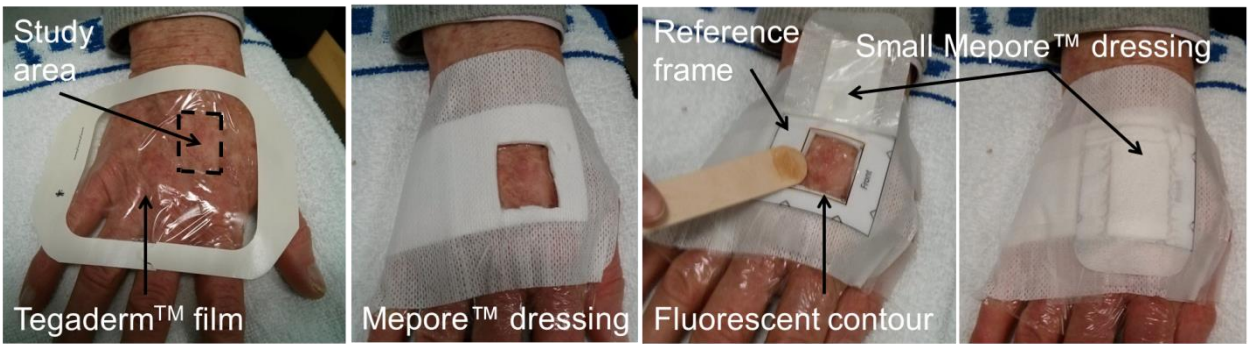

Figure 3.4: *measurements on large lesions. The area outside of the field of view of the camera was prepared and covered for the routine PDT treatment; a small area was left accessible for the study.*

3.3.4 PpIX fluorescence time course in healthy volunteers

The fluorescence imaged in healthy volunteers was mostly uniform in 8 out of 10 cases. Two volunteers had a slightly spotted pattern, such as show in ***Figure 3.5***.

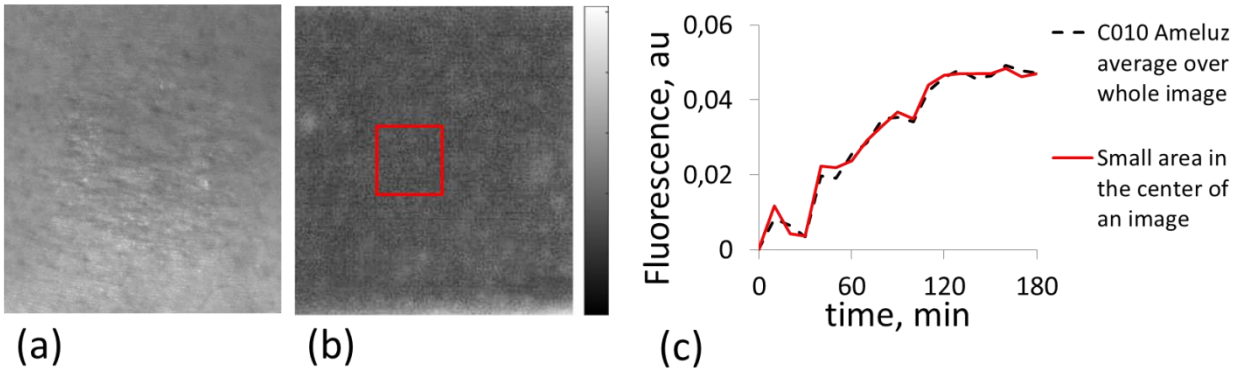

Figure 3.5: *Fluorescence patterns on healthy skin and an integrated PpIX time course.* **a –** *a monochromatic image of the skin under 405 nm illumination taken with the camera.* **b –** *PpIX fluorescence image after 180 min of Ameluz gel application. Red rectangle shows a small area which was used in the comparison to the whole area of the image.* **c –** *an integrated PpIX fluorescence time course from the small area and the whole area normalised on the camera maximum.*

There was no obvious correlation between the fluorescence pattern and the skin in either visual assessment or calculations. The correlation coefficient between the image of the skin and the fluorescence image was below 0.3 for all the subjects. The fluorescence time course from a

small area on the images was almost identical to the time course calculated by integrating the fluorescence over the whole area of the images (***Figure 3.5***, c).

The fluorescence time courses from six healthy volunteers in Metvix® group are shown in ***Figure 3.8***. Background fluorescence was subtracted and the result normalised to the maximum pixel intensity of the camera (which was equal to 255). The time course varied between the individuals; the fluorescence continued to grow over the three hours of the measurement in all subjects. The fluorescence was averaged for the six subjects and is shown in ***Figure 3.8***, (b).

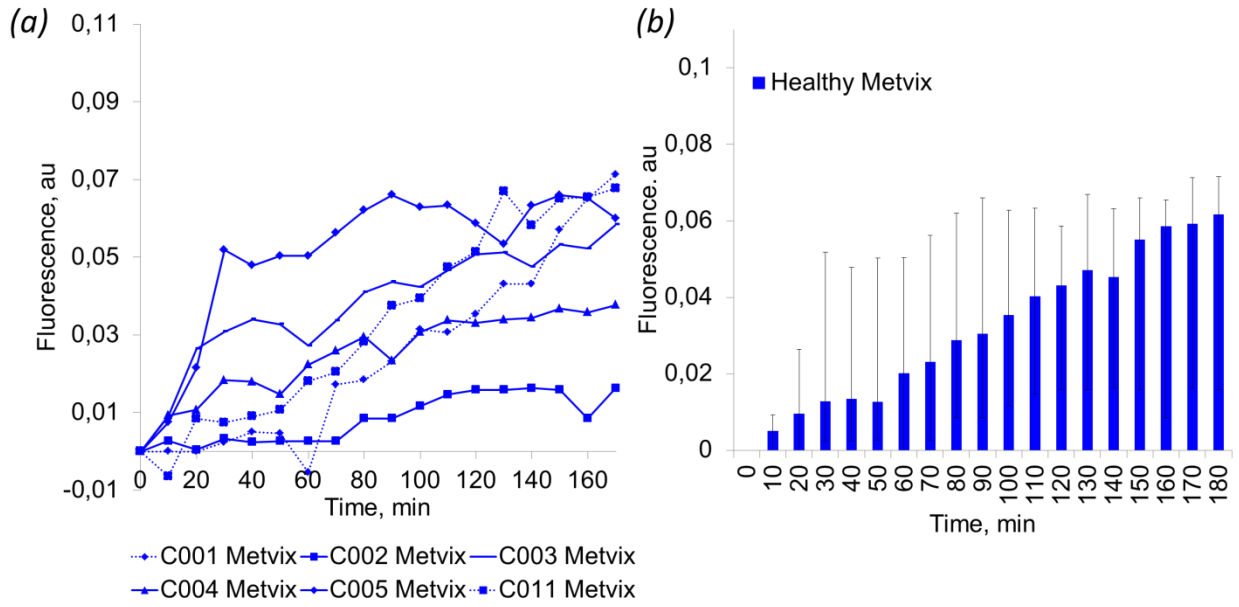

Figure 3.6: *PpIX fluorescence time course in Metvix® healthy volunteers group.* **a –** *fluorescence for six individual subjects in the group.* **b –** *an average fluorescence time course for the group.*

The PpIX fluorescence time course for the Ameluz group is shown in ***Figure 3.7***. The same dynamics were found for this group: the fluorescence continued to grow over three hours of the measurement time and varied among the individuals.

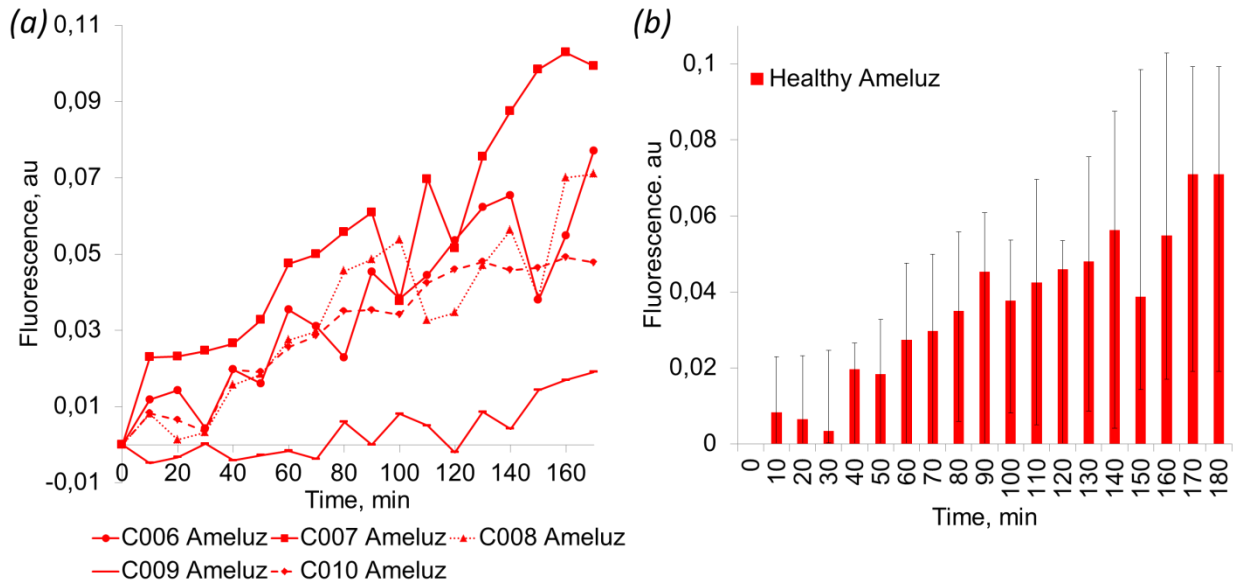

Figure 3.7: *PpIX fluroescence time course in Ameluz healthy volunteers group.* **a –** *fluorescence for five individual subjects in the group.* **b –** *an average fluorescence time course for the group.*

The results from the two groups are shown in ***Figure 3.8***. The two groups were analysed for statistical significance in order to establish if there was any difference between the creams. A two sample t-test with unequal variances was used to calculate the p-values for the groups. The p-values for six volunteers in Metvix® group V.S. five volunteers in Ameluz group at each time step were larger than 0.05, p-value (the average for the time course and at the last time step) was equal to 0.3. The extra volunteer did not change the statistical significance. P-values for the group of 5 Metvix V.S. 5 Ameluz volunteers were similar: average p-value was 0.3 > 0.05 and p-value at 180 min was 0.45 > 0.05. This shows that the groups were statistically insignificant, there was no obvious difference for the Ameluz gel or Metvix® cream. This was concurrent with the previous studies conducted at the PBU[11,37,38].The previous studies [11,37,38] showed that there was no substantial difference in the fluorescence formed from ALA and MAL precursors at 4 hours after the application of the creams, but at longer times the fluorescence was substantially higher after the application of ALA precursor.

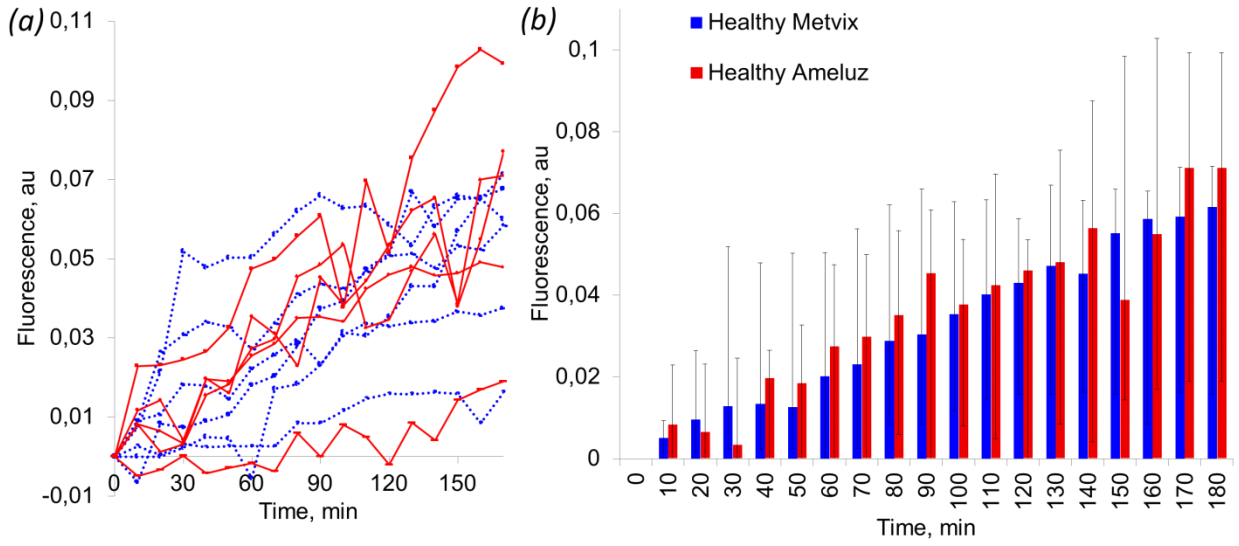

Figure 3.8: *PpIX fluorescence time course in both (Ameluz and Metvix®) healthy volunteers groups.*

3.3.5 PpIX fluorescence patterns in different diagnoses

The fluorescence patterns of the lesions were analysed with respect to the skin structure. The findings agree with the previous reports[27,24,32,39,18] that in some patients the fluorescence develops over an area of the visible tumours forming a rim at the margins (***Figure 3.9***). Sometimes it spreads outside the visible tumour or develops in areas without any evidence of the diseased skin to the naked eye which may be an indication of early stages malignant changes. There findings support the studies showing that PpIX fluorescence is an effective method for detecting pre-clinical diseased skin and assisting with identifying tumours' margins for the surgery[27,24,32].

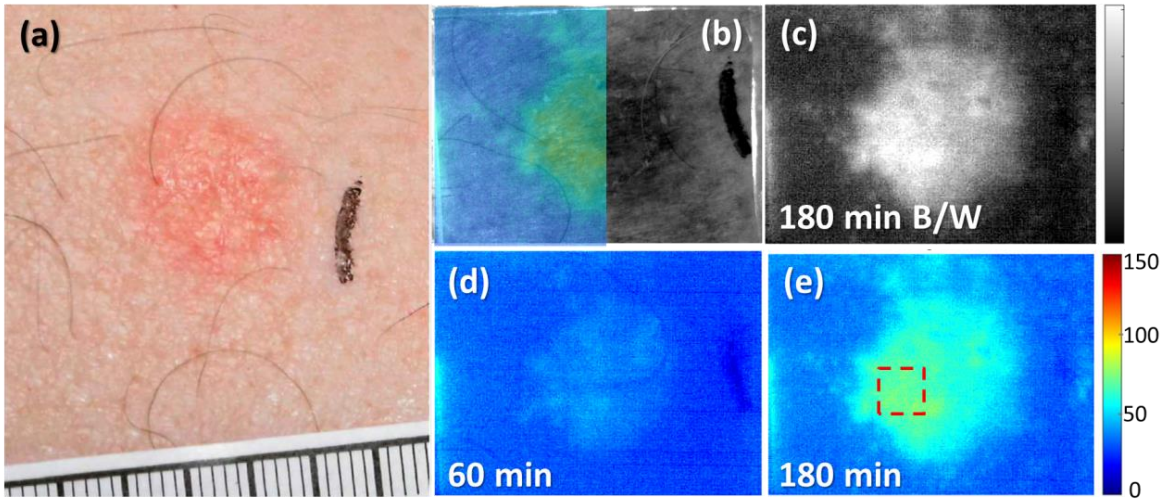

Figure 3.9: *Biopsy confirmed BCC lesion of P010 patient administered Metvix® PDT.* **a –** *a white light image of the tumour taken by a medical photographer.* **b –** *a monochromatic image of the tumour taken by the camera under 405 nm illumination. A half of the image is overlapped with a semi-transparent fluorescence image on a false colour scale taken at 180 min from the application of the cream. It shows that the shape of the lesion is similar to the developed fluorescence pattern. Although, the fluorescence area is larger than the visible tumour; and there is a rim at the margins which may be an indicator of early stages malignancies.* **c, e –** *a monochromatic image and a false colour image of PpIX fluorescence at 180 min from the application of the cream. The red dashed rectangle shows an area on the tumour with the highest PpIX metabolism. This area was used in the time course calculations of peak fluorescence.* **d –** *a false colour fluorescence image taken at 60 min from the application of the cream. The fluorescence starts to develop over the area within the visible tumour and then spreads to the area outwith the tumour.*

The fluorescence time course was analysed by integrating regions of interest (ROIs) which developed the strongest fluorescence. The red dashed line in ***Figure 3.9*** (e) shows such a ROI. The size of the ROIs varied depending on the size of the uniform peak fluorescence region. The smallest ROI was 25 x 38 pixels for P004 subject and the largest was 73 x 86 pixels for P013.

Another example was patient P005 who had two AK lesions treated with Metvix® PDT. The lesions were located on the same foot close to each other; they were similar in shape and size and threated on the same day. Lesion #1 developed almost twice as much PpIX fluorescence over the area corresponding to the lesion compared to only partial fluorescence at the lesion #4 (***Figure 3.10***). The intensity of the fluorescence was also lower in lesion #1. The fluorescence distribution in lesion #4 showed the formation of two halves which may suggest that there were two centres of the malignant growth which merged together in one lesion.

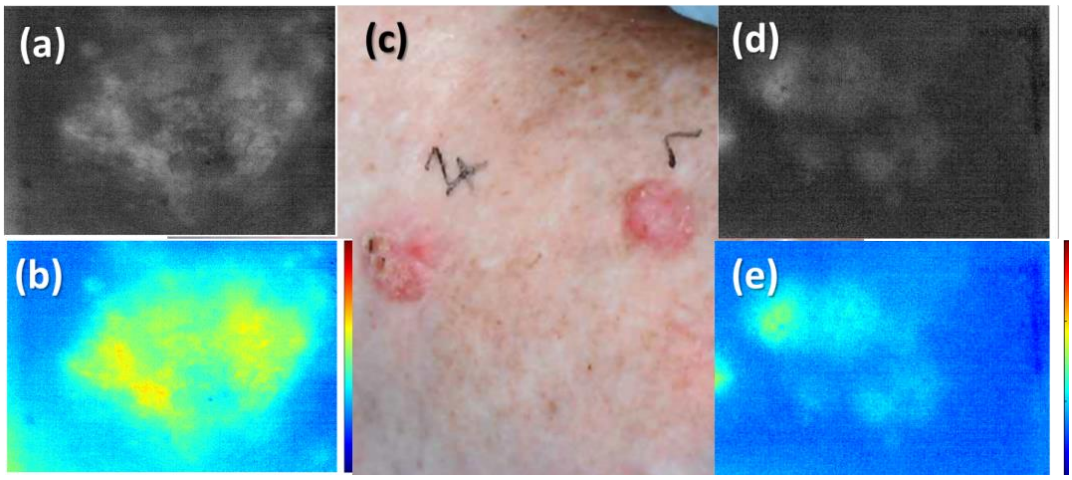

Figure 3.10: *Two AK lesions of subject P005 subject who was administered Metvix® PDT. The lesions were located on the same foot; they were similar in shape and size and treated on the same day. However, the fluorescence from the left lesion (marked as #4 on the image) is almost twice as high and larger in area than the fluorescence from the lesion on the right, marked as #1 on the image.* **a, b –** *a monochromatic and a false colour fluorescence image of lesion #4 taken at 180 min after the application of the cream.* **c –** *a white light image taken by a medical photographer.* **d, e –** *a monochromatic and a false colour fluorescence image of lesion #1 taken at 180 min after the application of the cream. Although the fluorescence was much higher in one lesion than in the other the pain after the treatment was evaluated as the same.*

Surprisingly the pain experienced during PDT was the same for both lesions. Another interesting finding was that both lesions were clear at 3 month follow up. This supports the reports that PpIX fluorescence does not always correlate with PDT outcomes, the fluorescence can be poor yet there is a response to PDT or *vice versa*[22,25].

Fluorescence imaging becomes more challenging in the cases of crusted and eroded lesions, and when there is any bleeding after the curettage. ***Figure 3.11*** shows the fluorescence of a crusted AK lesion treated with Ameluz gel which was bleeding after the preparation. Crust and blood blocked some of the fluorescence signal. However, it was still possible to select areas with a clear surface for the analysis. In this case the fluorescence spreads beyond the visible lesion (***Figure 3.11***, c) and it grows with different speeds over different regions (***Figure 3.11***, d).

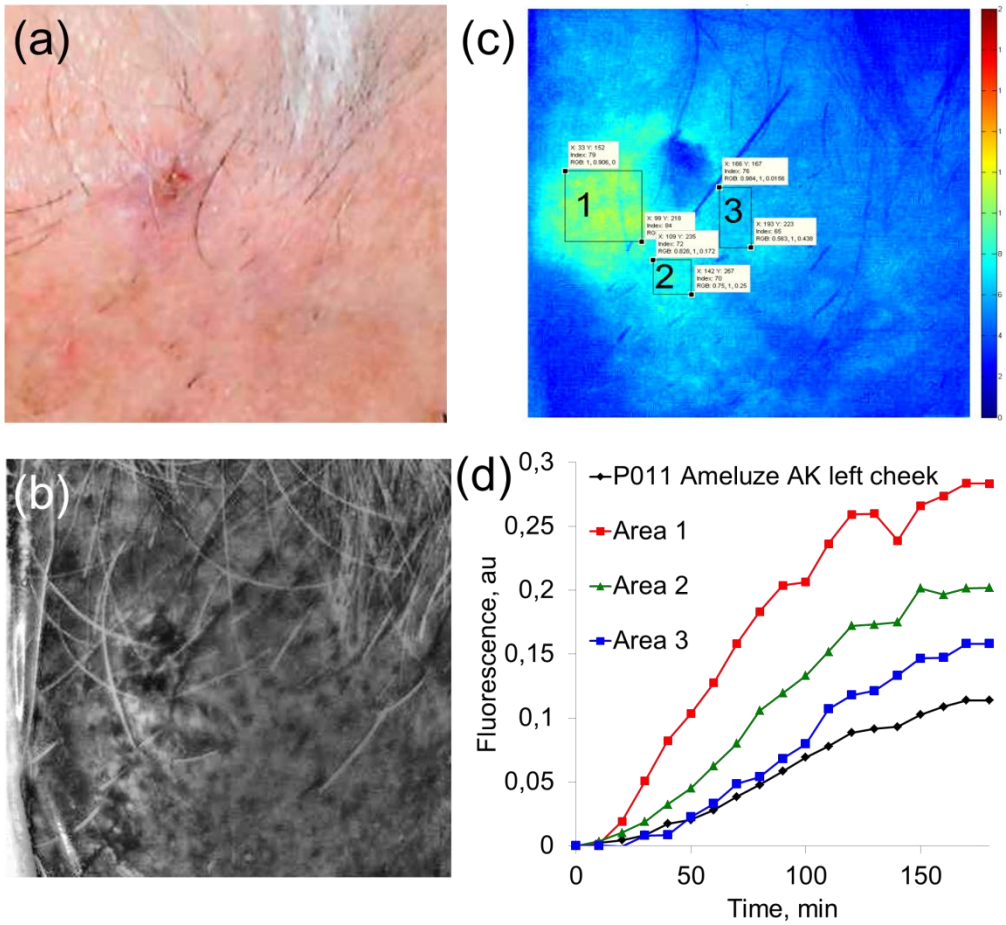

Figure 3.11: *AK lesion of P011 subject administered Ameluz PDT. The surface of the lesion was crusted and there was some bleeding after the curettage. The crust, erosion and bleeding can block some of the fluorescence signal and make the imaging mode difficult. However, it was still possible to analyse the fluorescence in the clear surface around the crusted and bleeding part.* **a –** *a white light medical image of the lesion.* **b –** *a monochromatic image of the lesion taken with the camera under 405 nm illumination. The size of the images taken with the camera were cropped from 640x480 pixels (3.1 mm x 2.4 mm) to 540x380 pixels corresponding to 2.6 mm x 1.9 mm to remove the reference contour used for the alignment.* **c –** *a false colour fluorescence image taken with the camera at 180 min after the application of the gel.* **d –** *PpIX fluorescence time course was integrated over different regions on the image. The black line shows fluorescence integrated over the whole image, three different areas correspond to the areas on the fluorescent image (c).The fluorescence develops with different speeds over different areas.*

There was a case with a blurred fluorescence pattern in a BCC tumour treated with Metvix® PDT (***Figure 3.12***). The margins of the tumour were not clear and it developed a random spotted pattern which did not correlate to the lesion or the skin. Dense sebaceous glands on the neck could be one of the explanations of such patterns. Treating this tumour with PDT would be the best choice as surgery would be quite challenging.

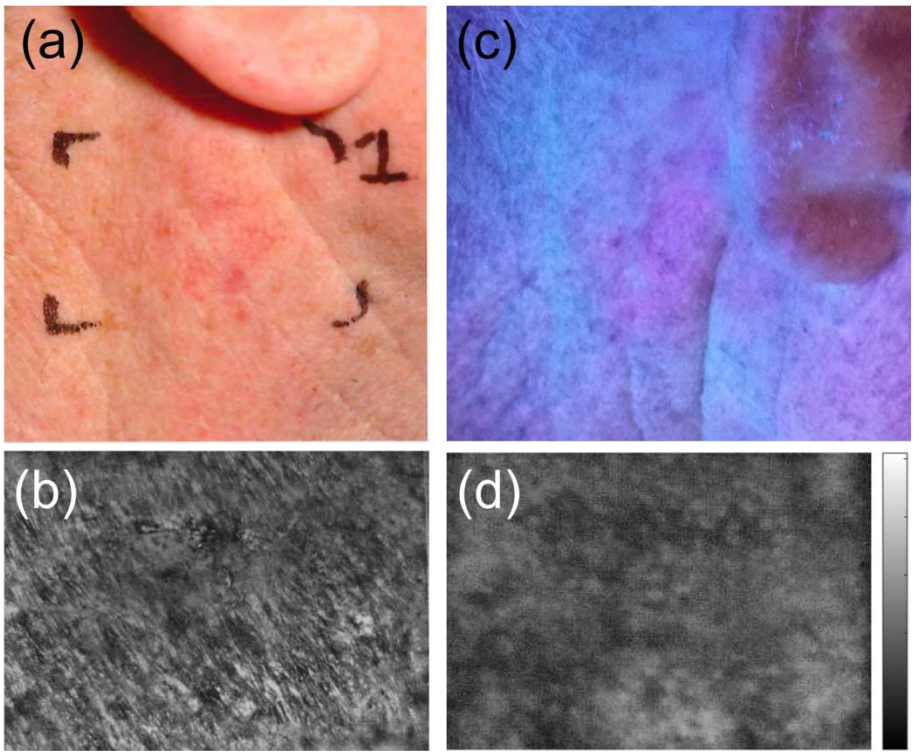

Figure 3.12: *Biopsy confirmed BCC tumour of P008 patient administered Metvix® PDT.* **a –** *a white light medical image of the tumour.* **b –** *a fluorescence image taken with a colour digital camera under Wood's lamp.* **c –** *a monochromatic image of the tumour taken with the camera under 405 nm illumination.* **d –** *a monochromatic fluorescence images taken with the camera at 180 min after the application of the cream. The margins of the tumour are not very clear to the naked eye; the fluorescence has blurred random spotted pattern which may be caused by the activity of sebaceous glands which are quite dense on the neck.*

Fluorescence homogeneity was calculated in the ROIs and over the whole image at 180 min from the application of the creams. The fluorescence value and pixel indices for local minimum and local maximum for ROI and global minimum and global maximum for the whole image were identified. In order to reduce numerical noise 5 pixel values were averaged at the minima and maximuma. The homogeneity was calculated as 1-({global, local} max- {global, local} min) / local_mean, %.

On average for 12 patients the fluorescence of the lesion was homogeneous with more than 75 % homogeneity in the ROIs; and for one patient it was heterogeneous with homogeneity equal to 25 %. Over the whole image the fluorescence was heterogeneous with homogeneity less than 21 % on average for 12 patients which indicated the contrast between the peak fluorescence in ROI and the rest of the image including healthy parts of the skin in cases for well-defined fluorescence patterns; the fluorescence was 54 % homogeneous for one patient with poorly defined weak fluorescence.

3.3.6 PpIX fluorescence correlation to pain

The possibility of correlation between PpIX fluorescence and pain was investigated by calculating correlation coefficient between the pain scores and the peak fluorescence measured at 180 min. The correlation coefficient was calculated in excel using the formula $Correl\,(Fluorescence, Pain) = \frac{\sum(Fluorescence-\overline{Fluorescence})\cdot(Pain-\overline{Pain})}{\sqrt{[\sum(Fluorescence-\overline{Fluorescence})^2\sum(Pain-\overline{Pain})^2]}}$. The pain was scored by the visual pain score from 0 corresponding to no pain to 10 corresponding to the worst pain one could imagine. The patients were asked to score the pain which they experienced during the PDT treatment straight after the treatment. The patients' data including the type of cream, lesion, body site, peak fluorescence at 180 min, pain scores, and lesion clearance at follow up is collected in ***Table 3.1***.

Figure 3.13 shows fluorescence correlation of fluorescence to pain. The data points on the figure represent two values for each patient: the peak fluorescence on the horizontal axis and to the pain experienced during the PDT treatment on the vertical axis. The graph shows random distribution of the data points suggesting that there was no obvious dependence between the fluorescence and the pain.

Table 3.1: *Patients' data. The skin temperature was not measured during the experiment, but was estimated from IR thermograms of healthy skin taken from the literature; paragraph 3.4 explains how it was evaluated.*

Patient	Lesion	Body site	Cream	Pain score, 0-10	Peak Fluorescence at 180 min, au	Temperature, °C	Clearance clear "1" partial "0" no response "-1
P001	AK	Left hand	Ameluz	5.6	0.18	34	0 1 year follow up
P002	AK	Right foot	Metvix	7.9	0.06	31	Not followed
P003	BCC	Right leg	Metvix	6	0.08	32	0 1 year follow up
P004	BCC	Back, right side	Metvix	5.4	0.2	32	1 1 year follow up
P005 #1 lesion #4 lesion	AK	Right foot	Metvix	 1.1 1.1	 0.18 0.26	 33 34	 1 1 year follow up
P006	BCC	Left leg	Metvix	1.1	0.05	31	1 1 year follow up
P007	AK	Forehead	Ameluz	0	0.3	36	1 1 year follow up
P008	BCC	Neck	Metvix	1.5	0.28	35	1 3 month follow up
P009	AK	Top scalp	Ameluz	3.7	0.24	35	0 3 month follow up
P010	BCC	Right shoulder	Metvix	1.6	0.18	34	1 3 month follow up
P011	AK	Left cheek near the ear	Ameluz	9.2	0.28	35	0 3 month follow up
P012	AK	Right hand	Ameluz	8,5	0,13	32	0 3 month follow up
P013	AK	Right hand	Metvix	3,4	0,047	31	1 3 month follow up

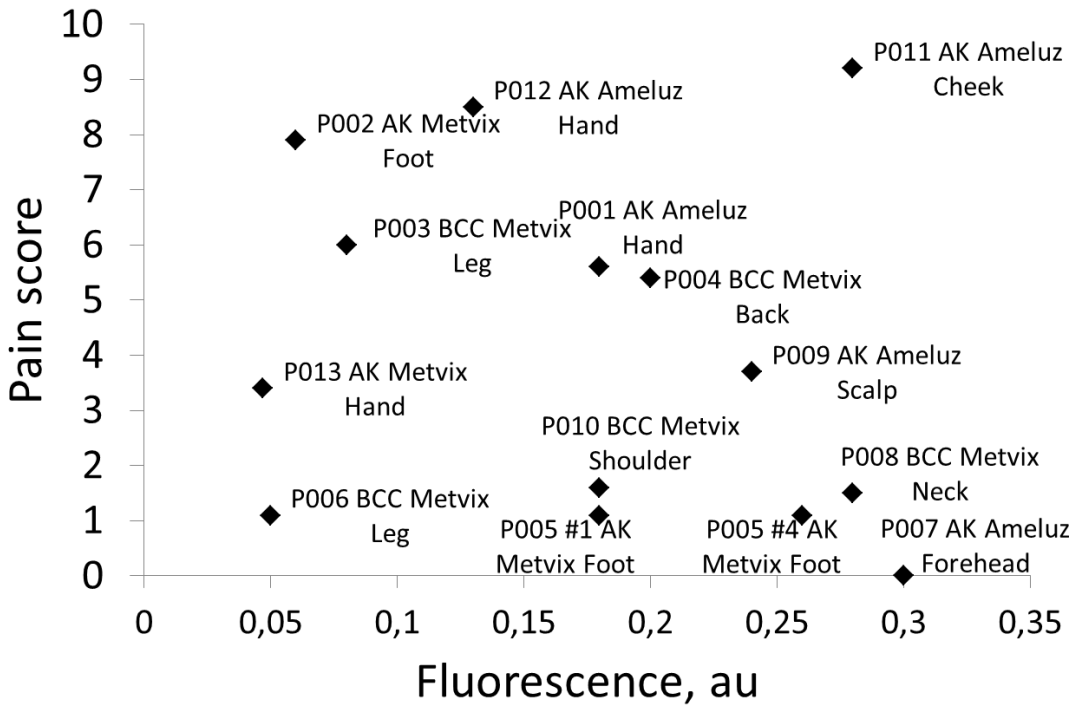

Figure 3.13: *PpIX fluorescence correlation to pain*

There was a small negative correlation coefficient found which was equal to -0.24 (p-value=0.0005). This means that the pain and fluorescence are statistically dependent (p-value<0.001), but the correlation was too small and could be neglected. This agrees with the previous reports which did not see the correlation between the fluorescence and the pain[18], including one study conducted at the PBU on PpIX fluorescence decay (photobleaching) during PDT treatment for BD and sBCC[33]. These findings contradict to the previous reports which showed positive correlation of PpIX fluorescence to pain and erythema[40,8,36]

3.3.7 PpIX correlation to the creams and the diagnoses

The fluorescence time course was calculated by integrating regions of interest with the same intensity (ROI) which developed the highest fluorescence. The background fluorescence was subtracted and the result normalised on the maximum pixel intensity of the camera.

Figure 3.14 shows the results from the three groups AK Ameluz V.S. AK Metvix V.S. BCC Metvix. The results showed that the fluorescence continued to grow over three hours in all subjects. It varied between the diagnoses and the individuals.

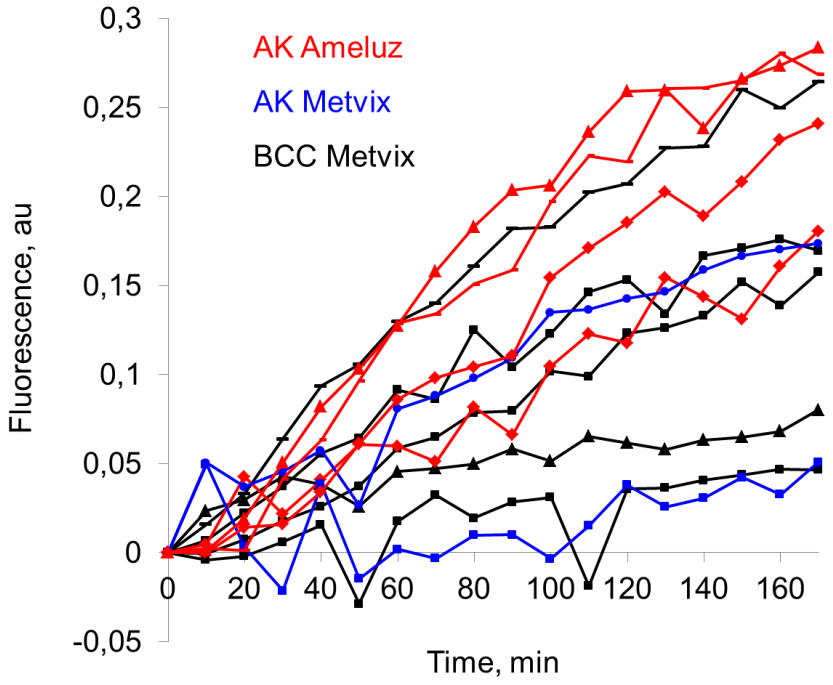

Figure 3.14: *PpIX fluorescence time course in three groups of patients*

The fluorescence was averaged for the three groups and the average fluorescence time course is shown in ***Figure 3.15***. The difference in the time course between the groups was analysed by calculating the p-values which identifies statistical significance. P-values for all cases were larger than 0.05 at each time step (though in AK Ameluz group vs AK Metvix group after 130 min p-value was approaching 0.02). P-values were averaged for all time steps measurements; the statistical difference between the groups AK Ameluz group vs AK Metvix (p-values=0.16), and AK Metvix group vs BCC Metvix (p-value=0.18) was insignificant. This agrees with the previous study at the PBU which showed no difference in the fluorescence developed from ALA or MAL precursors in sBCC and BD measured after three hours from the application of the creams, and during the treatment[33]. One study reported that fluorescence developed form ALA precursor was higher than from MAL precursor[18]. However, averaging peak fluorescence from an area is a more robust method compared to one point measurement. The results in ***Figure 3.11*** demonstrate that the fluorescence can vary three times between three different regions. The distance between areas 1, 2, 3 on that image is less than 3 mm. So for one point measurement using a standard optical fibre with 2 mm diameter gives a high probability of inaccuracies. An integrated fluorescence in that image is much lower than the fluorescence at high intensity regions. So even by measuring the fluorescence over a few points and averaging

it, fluorescence imaging is superior to one point spectroscopic measurements as it gives control over the areas of interest.

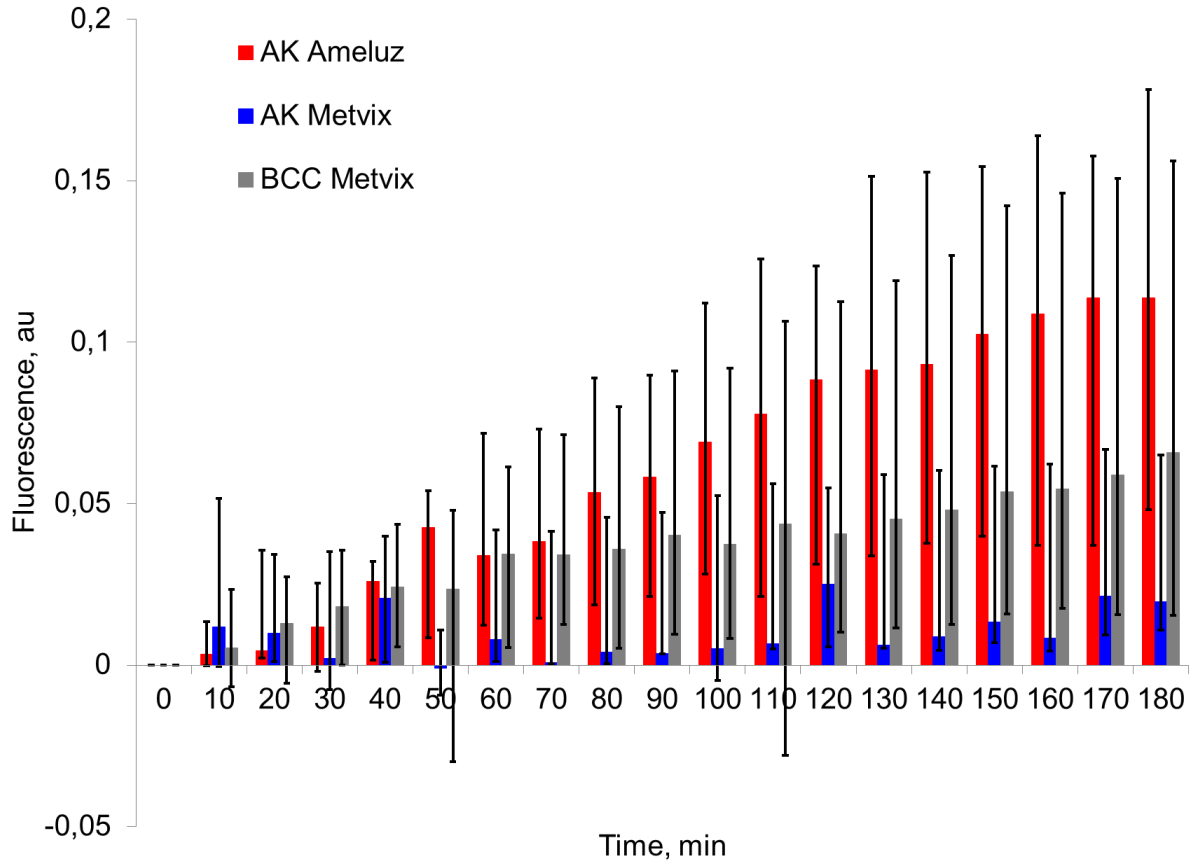

Figure 3.15: *PpIX fluorescence time course in AK Ameluz V.S. AK Metvix® V.S. BCC Metvix® groups. The variation shows that there is no obvious difference between the three groups.*

This concludes that there was no obvious difference between the diagnoses or the creams. However, analysis of fluorescence with respect to the body sites shows that the fluorescence developed in the lesions on the head and the neck was much higher than the fluorescence on the lower leg (***Figure 3.16***). The fluorescence on the shoulders, the hands and the feet is in the middle.

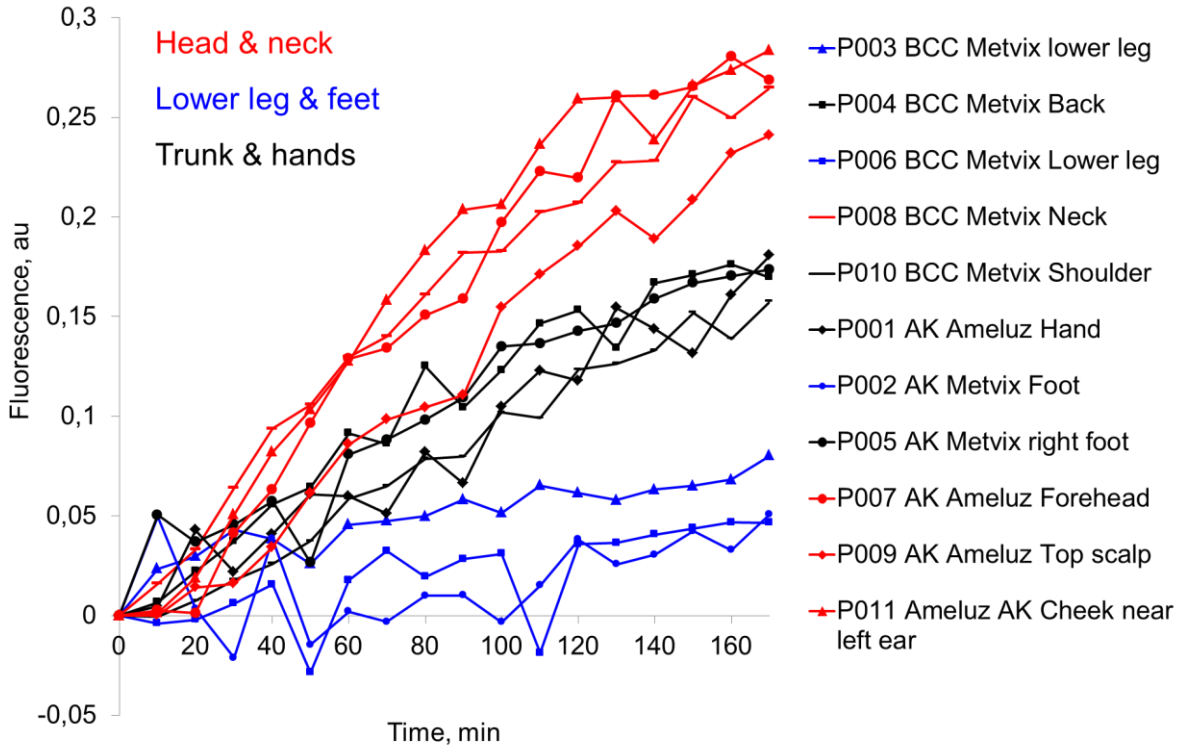

Figure 3.16: *PpIX fluorescence time course in three body sites groups of patients with AK and BCC: Head & neck V.S. Lower leg & feet V.S. Trunk & hands*

The fluorescence was averaged in these body sites groups (***Figure 3.17***). The error bars in the figure which correspond to the variation of the fluorescence in each group are already much smaller than the error bars in ***Figure 3.15***, also the dependence is already obvious to the naked eye. Statistical calculations proof this observation. The groups Head & neck V.S. Lower leg & feet were statistically different (p-value=0.0003 << 0.05); so were the groups Head & neck V.S. Trunk & Hands (p-value=0.001<0.05). However, there is no statistical difference between the group Lower leg &feet V.S. Trunk & Hands (p-value>0.005). The dependence concurs with the previous study conducted at PBU on the skin of healthy volunteers which discovered that the fluorescence on the forearm is higher than the fluorescence on the lower leg[37,38].

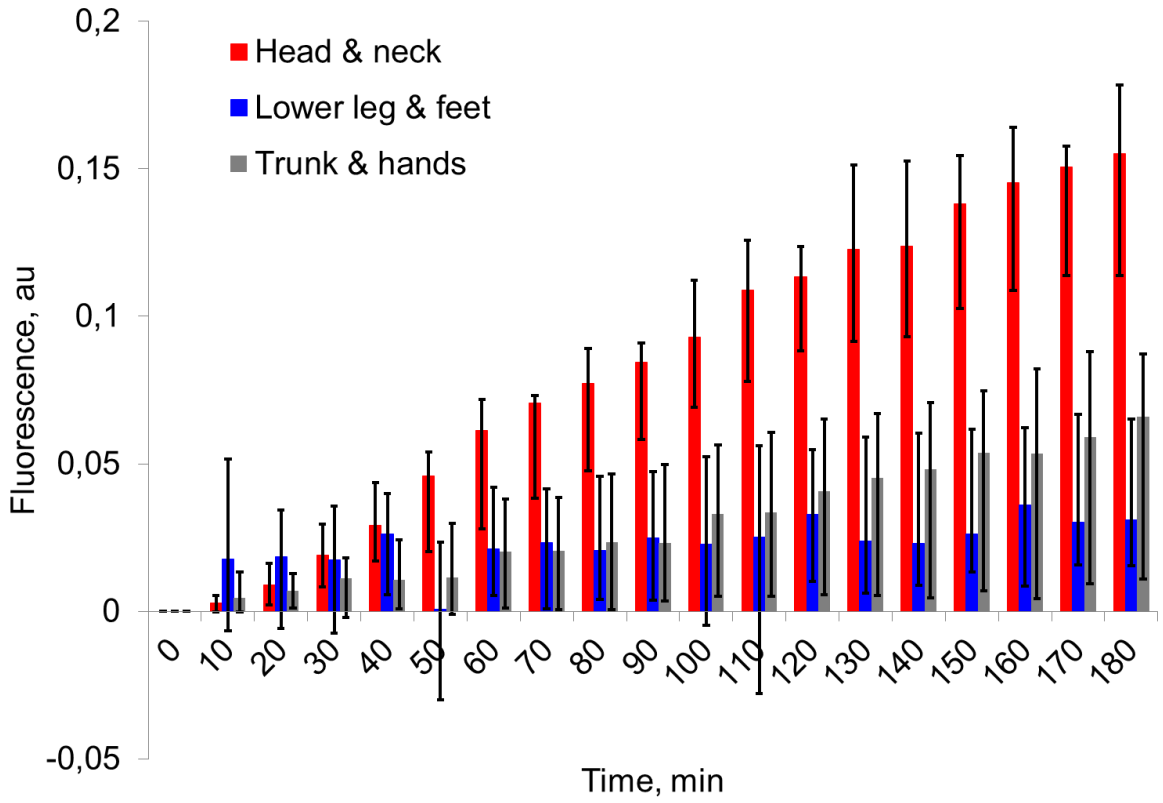

Figure 3.17: *PpIX fluorescence time course in Head & neck group V.S. Lower leg & feet V.S. Trunk & hands groups. The variation shows that the fluorescence is much higher in the group of Head & neck compared to the other two groups.*

3.3.8 Lesion clearance and correlation to the fluorescence

The results of three month and one year follow ups for lesion clearance are shown in ***Table 3.1***. P002 was lost to follow up. The correlation coefficient between PpIX fluorescence form the peak region and the clearance was not significant, -0.0285 (caution should be taken as the sampling population is small and the results should not be over interpreted). Although PpIX metabolism is one of the most important treatment factors and PpIX fluorescence helps to optimise treatment protocols, PpIX fluorescence did not correlate to PDT response in this study, similar to what was reported in the six year study on BCC treatment [22].

3.4 Discussion

3.4.1 PpIX fluorescence correlation to the skin temperature

In order to explain the dependence of PpIX metabolism on the body site, the skin thickness could have been the reason, thicker skin could have had less cream diffusion than thinner skin; for instance PpIX fluorescence is higher when the surface of the skin stripped off with an adhesive tape before the application of the cream [37, 38]. However, the fluorescence is higher on the head and the neck compared to the lower leg, and the skin on the neck is thicker than lower leg[41,42,43]. So the skin thickness could not be the main reason for such fluorescence dependence.

Another possible explanation was the temperature variation across the body. The temperature variation of the skin can be displayed with infrared imaging cameras[44] [http://www.rnhrd.nhs.uk/page/92]. It was shown that local perfusion and temperature of the lesions increases during PDT as a response to the treatment (but not because of thermal hearing induced by PDT lamps)[45]. Average lesional temperature in that study was 34.8±1.2 °C. Lesional temperature measurement was not included in the protocol of the fluorescence study described in this thesis. In order to evaluate the temperatures at the lesions sites, thermograms of healthy skin were collected from the literature[44,46,47]. Typical temperatures for the lesion sites were estimated from the thermograms. For better estimates the temperatures were averaged from a few thermograms where possible; also, considering that healthy individuals have symmetrical temperature distribution across the body[48] the temperatures were taken from symmetric sites and averaged (***Figure 3.18***).

Typical thermograms of the hands and the back are shown in ***Figure 3.18***. The areas over the back and the trunk have similar temperatures to the hands. The areas of the hands show large temperature variations; there are many hot and cooler regions. The lesion of subject P001 was located over the thumb metacarpal section which is one of the hottest regions on the hands. The lesion of P012 was located over the middle of the outer palm (over the four fingers metacarpal bones) which has middle temperatures. And the lesion of P013 was located over the third metacarpophalangeal joint, the area over the four metacarpophalangeal joints is the coldest on the hands. P013 P001 and P012 were treated with Ameluz PDT and P013 was treated with

Metvix PDT. The fluorescence varied significantly in all three subjects with the highest in subject P001 and the lowest in subject P013 which correlated with the temperatures.

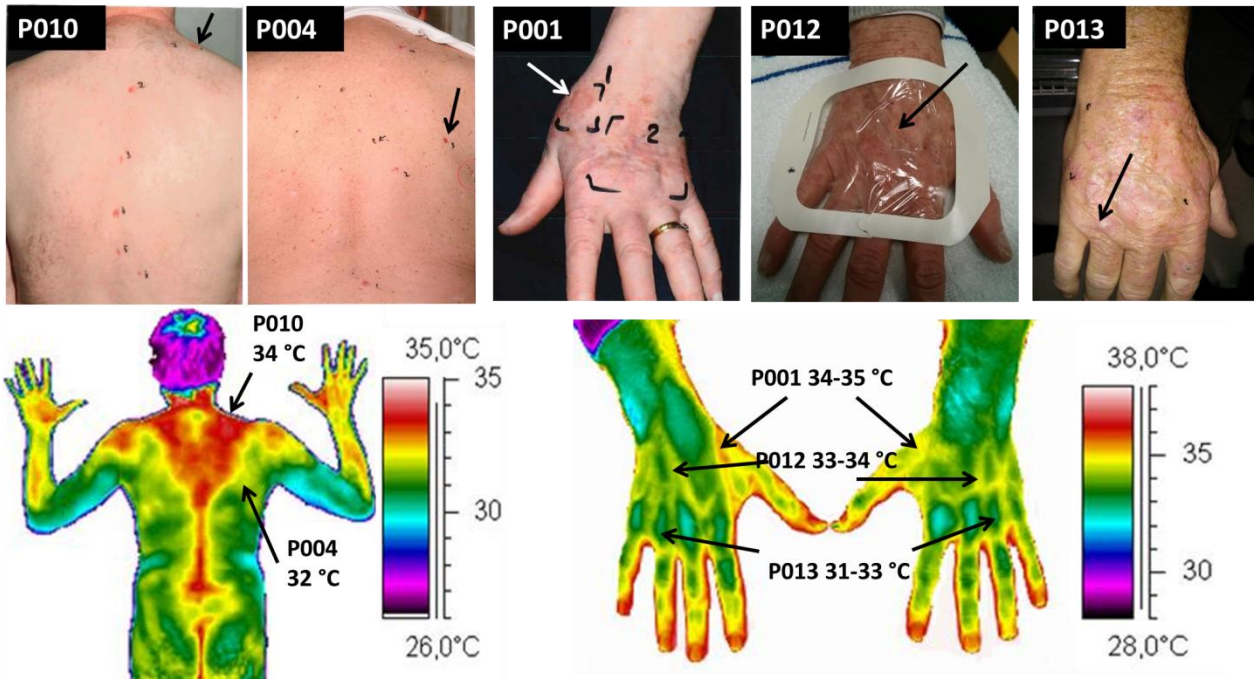

Figure 3.18: *Medical photographs of the patients' hands and the thermograms. The arrows on the images indicate the location of the lesions. The arrows on the thermograms indicate typical temperatures of healthy skin at those locations. The fluorescence varied in all three subjects with the highest fluorescence in P001 and the lowest in P013. There are many small "hot" and "cold" areas, large and rapid variation of the temperature which could be responsible for the variation in the fluorescence time course. The thermogram was taken from a medical thermography course at the website of I.Ya. Horbachevsky Ternopil State Medical University, Ukraine*[48]

The head and the neck have the highest skin temperatures across the body typically reaching 35-37°C[46,47], the lower leg and the cold areas of the feet and the hands have lower temperatures of 30-33°C. The estimated temperatures for all lesions are shown in (***Table 3.1***). PpIX fluroescence was found to depend on the skin temperatures (***Figure 3.19***). This hypothesis concurs with the reports that increased skin temperatures have higher PpIX metabolism rates[49,50,51,52].

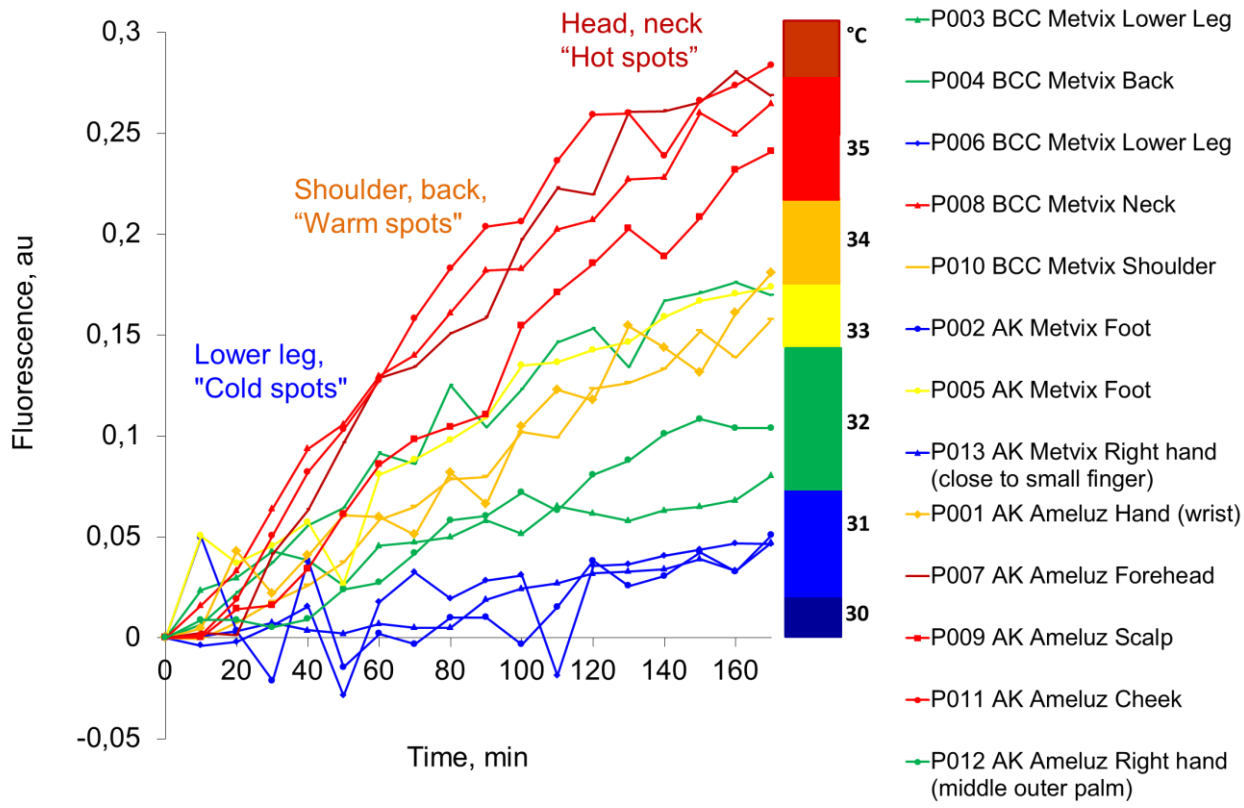

Figure 3.19: *PpIX fluorescence time course and its correlation to the body site and the skin temperature. The temperatures at the lesions were evaluated from the thermograms of healthy skin found in the literature*[48,47,44,46]*. PpIX metabolism seems to be faster on the hotter areas such as the head and the neck compared to the lower leg which supports the findings that PpIX metabolism is higher for higher temperatures*[50,52,49]*.*

The correlation coefficient for these temperatures and the fluorescence at 180 min was 0.93 (p-value = $2.7 \cdot 10^{-18}$ << 0.005). This means that the temperature and fluorescence have very strong statistical dependence and very high positive correlation: the fluorescence increases when the temperature increases. The fluorescence at 180 min was averaged among the patients with the same temperatures. The histogram is shown in ***Figure 3.20***.

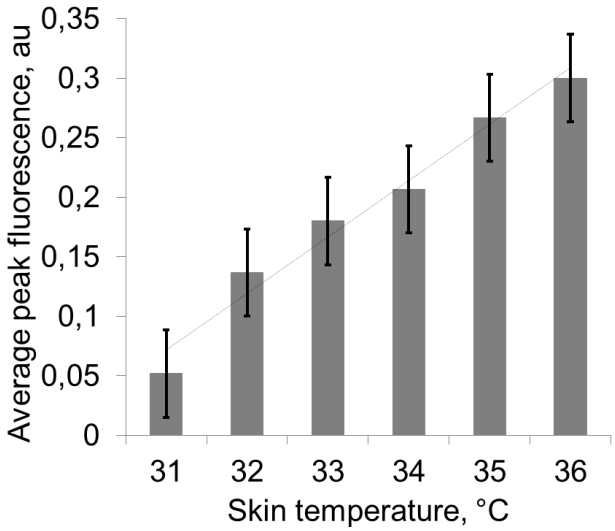

Figure 3.20: *PpIX fluorescence at 180 min in the patients with respect to the skin temperatures at the sites of the lesions. The error bars correspond to the range in fluorescence among patients for the corresponding temperatures.*

If the evaluated temperatures corresponded to the real temperature of patients' lesion and this hypothesis that the skin temperature has such a significant influence on PpIX metabolism is true, then the temperature should be considered in the protocols.

3.5 Conclusions

A time course imaging method was developed and used in a small study on healthy volunteers and patients. The fluorescence continued to grow in both healthy volunteers and patients during the three hours following the application of the cream. Therefore waiting longer before starting the PDT treatment could improve PDT outcome, although care should be taken as the specificity of PpIX metabolism in healthy and diseased skin decreases with time[36].

There was no significant difference in the time courses between the creams (for both volunteers and patients) or among the diagnoses (p-values>0.05 for all groups). However, there was variation among the lesions, the patients and the volunteers; the PpIX fluorescence time course was found to be dependent on the body site (p-values<0.01 between the body sites groups). Temperature variation across the body was explored as one of the possible explanations. There is a positive correlation to temperature (correlation coefficient was 0.93, p-value < 0.001): the fluorescence on the head and the neck was much higher than the lower leg

which coincides with the temperature variation. If this hypothesis is true then this finding could have significant impact on changing the treatment protocol – increasing the skin temperature by thermal dressing for improving PpIX metabolism, taking care when using cooling fans as pain management. After the reports that cooling fans reduce PDT outcomes[2,15] in some PDT centres this pain relief method is not administered anymore. PBU at Ninewells hospital is one such centre. The ambient temperature for daylight PDT should also be considered for administering PDT[53,54]. Also increasing skin temperature by simple thermal dressing could speed up PpIX metabolism and reduce the waiting time before commencing PDT treatment.

There is conflicting evidence about PpIX fluorescence correlation to the pain experienced during the PDT treatment. No correlation was found in this study (correlation coefficient was -0.24, p-value<0.01).

The outcomes of this study should be treated with caution in order not to over-interpret the results in this small population; however, it is a first clinical attempt to undertake time course fluorescence imaging in measuring PpIX fluorescence. The findings address some of the gaps in understanding of PpIX metabolism in different lesions at different body sites, using different pro-drugs. The results of the study demonstrate the effectiveness of the apparatus and the potential of time course imaging to advance our understanding of the biosynthesis PpIX and its effects on the treatment. This may lead on to further studies, with a view to optimisation of treatment regimes.

In the subsequent studies it would be desirable to implement a multi-band imaging experiment in a time course study. Considering the availability and simplicity of fast prototyping equipment such as 3D printing it would be relatively easy to upgrade the current device by adding extra LEDs with different wavelengths in the illuminator PCB and a few different band pass filters which could be easily changed during the imaging. Wide filed thermal images of skin could be obtained with an additional thermal camera. It would be useful to include the following: white light colour imaging to study the development of erythema (skin reddening due to inflammation as a response to PDT); auto-fluoresce which could provide additional information on the malignant changes in the skin; excitation of PpIX in blue and red bands for extracting information about PpIX accumulation at different depth in skin; imaging two peaks of PpIX emission at 635 nm and 710 nm; and most importantly include infrared thermal imaging of skin temperature to investigate the hypothesis on body site temperatures on PpIX metabolism. It would be sufficient to do one measurement before and after PDT. Monitoring the change in skin temperature, erythema and PpIX fluorescence would be useful during and after PDT.

3.6 References

1. Ibbotson, S. H. An overview of topical photodynamic therapy in dermatology. *Photodiagnosis Photodyn. Ther.* **7,** 16–23 (2010).

2. Ibbotson, S. H. *et al.* Photodynamic therapy in dermatology: Dundee clinical and research experience. *Photodiagnosis and Photodynamic Therapy* **1,** 211–223 (2004).

3. Ibbotson, S. H., Dawe, R. S. & Morton, C. a. A survey of photodynamic therapy services in dermatology departments across Scotland. *Clin. Exp. Dermatol.* **38,** 511–516 (2013).

4. Braathen, L. R. *et al.* Guidelines on the use of photodynamic therapy for nonmelanoma skin cancer: an international consensus. International Society for Photodynamic Therapy in Dermatology, 2005. *J. Am. Acad. Dermatol.* **56,** 125–143 (2007).

5. Morton, C. a., McKenna, K. E. & Rhodes, L. E. Guidelines for topical photodynamic therapy: Update. *Br. J. Dermatol.* **159,** 1245–1266 (2008).

6. Ramirez, D. P. *et al.* Experience and BCC subtypes as determinants of MAL-PDT response: Preliminary results of a national Brazilian project. *Photodiagnosis Photodyn. Ther.* **11,** 22–26 (2014).

7. Bagnato, V. S. *et al.* PDT experience in Brazil: A regional profile. *Photodiagnosis Photodyn. Ther.* **2,** 107–118 (2005).

8. Kanick, S. C. *et al.* Dual-channel red/blue fluorescence dosimetry with broadband reflectance spectroscopic correction measures protoporphyrin IX production during photodynamic therapy of actinic keratosis. *J. Biomed. Opt.* **19,** 075002 (2014).

9. Quirk, C., Gebauer, K., De'Ambrosis, B., Slade, H. B. & Meng, T.-C. Progression of Actinic Keratosis to Squamous Cell Carcinoma Revisited: Clinical and Treatment Implications. *Cutis* **85,** 318–324 (2010).

10. Wennberg, A.-M. *et al.* Photodynamic Therapy With Methyl Aminolevulinate for Prevention of New Skin Lesions in Transplant Recipients: A Randomized Study. *Transplantation* **86,** (2008).

11. Lesar, A., Padgett, M., O'Dwyer, M., Ferguson, J. & Moseley, H. Fluorescence induced by aminolevulinic acid and methyl aminolevulinate on normal skin. *Photodiagnosis Photodyn. Ther.* **4,** 224–229 (2007).

12. Moseley, H. Light distribution and calibration of commercial PDT LED arrays. *Photochem. Photobiol. Sci.* **4,** 911–914 (2005).

13. Ibbotson, S. H. An overview of topical photodynamic therapy in dermatology. *Photodiagnosis Photodyn. Ther.* **7,** 16–23 (2010).

14. Ibbotson, S. H. Irradiance is an important determinant of pain experienced during topical photodynamic therapy. *J. Am. Acad. Dermatol.* **65,** 201–2 (2011).

15. Tyrrell, J., Campbell, S. M. & Curnow, a. The effect of air cooling pain relief on protoporphyrin IX photobleaching and clinical efficacy during dermatological photodynamic therapy. *J. Photochem. Photobiol. B Biol.* **103,** 1–7 (2011).

16. Arits, a H. M. M., van de Weert, M. M., Nelemans, P. J. & Kelleners-Smeets, N. W. J. Pain during topical photodynamic therapy: uncomfortable and unpredictable. *J. Eur. Acad. Dermatol. Venereol.* **24,** 1452–7 (2010).

17. Ibbotson, S. H. Adverse effects of topical photodynamic therapy. *Photodermatol. Photoimmunol. Photomed.* **27,** 116–30 (2011).

18. Sandberg, C. *et al.* Fluorescence diagnostics of basal cell carcinomas comparing methyl-aminolaevulinate and aminolaevulinic acid and correlation with visual clinical tumour size. *Acta Derm. Venereol.* **91,** 398–403 (2011).

19. Valentine, R. M., Ibbotson, S. H., Wood, K., Brown, C. T. a & Moseley, H. Modelling Fluorescence in Clinical Photodynamic Therapy. *Photochem. Photobiol. Sci.* 203–213 (2012). doi:10.1039/c2pp25271f

20. Valentine, R. M., Brown, C. T. a, Moseley, H., Ibbotson, S. & Wood, K. Monte Carlo modeling of in vivo protoporphyrin IX fluorescence and singlet oxygen production during photodynamic therapy for patients presenting with superficial basal cell carcinomas. *J. Biomed. Opt.* **16,** 048002 (2011).

21. Valentine, R. M. Biophysical Aspects of Photodynamic Therapy. *PhD Thesis* (The University of St Andrews, 2011). at <http://hdl.handle.net/10023/2471>

22. Fernández-Guarino, M., Harto, A., Pérez-García, B., Royuela, A. & Jaén, P. Six Years of Experience in Photodynamic Therapy for Basal Cell Carcinoma: Results and Fluorescence Diagnosis from 191 Lesions. *J. Skin Cancer* **2014,** 1–7 (2014).

23. Togsverd-Bo, K., Idorn, L. W., Philipsen, P. A., Wulf, H. C. & Hædersdal, M. Protoporphyrin IX formation and photobleaching in different layers of normal human skin: Methyl-and hexylaminolevulinate and different light sources. *Exp. Dermatol.* **21,** 745–750 (2012).

24. Hewett, J. *et al.* Fluorescence detection of superficial skin cancers. *J. Mod. Opt.* **47,** 2021–2027 (2000).

25. Sandberg, C. *et al.* Photodynamic therapy for 'difficult-to-treat' basal cell carcinomas. Do poorly responding BCCs lack accumulation of protoporphyrin IX after ALA/MAL application? *Proc. SPIE* **7380,** 73805K–73805K–8 (2009).

26. Tyrrell, J., Campbell, S. & Curnow, A. Validation of a non-invasive fluorescence imaging system to monitor dermatological PDT. *Photodiagnosis Photodyn. Ther.* **7,** 86–97 (2010).

27. De Leeuw, J., Van der Beek, N., Neugebauer, W. D., Bjerring, P. & Neumann, H. a M. Fluorescence detection and diagnosis of non-Melanoma skin cancer at an early stage. *Lasers Surg. Med.* **41,** 96–103 (2009).

28. Saager, R. B., Cuccia, D. J., Saggese, S., Kelly, K. M. & Durkin, A. J. Quantitative fluorescence imaging of protoporphyrin IX through determination of tissue optical properties in the spatial frequency domain. *J. Biomed. Opt.* **16,** 126013 (2011).

29. Andrade, C. T., Vollet-Filho, J. D., Salvio, a. G., Bagnato, V. S. & Kurachi, C. Identification of skin lesions through aminolaevulinic acid-mediated photodynamic detection. *Photodiagnosis Photodyn. Ther.* **11,** 409–415 (2014).

30. Blanco, K. C. *et al.* Fluorescence guided PDT for optimization of the outcome of skin cancer treatment. *Front. Phys.* **3,** 1–7 (2015).

31. Hempstead, J. *et al.* Low-cost photodynamic therapy devices for global health settings: Characterization of battery-powered LED performance and smartphone imaging in 3D tumor models. *Sci. Rep.* **5,** 10093 (2015).

32. Mogensen, M. & Jemec, G. B. E. Diagnosis of nonmelanoma skin cancer/keratinocyte carcinoma: A review of diagnostic accuracy of nonmelanoma skin cancer diagnostic tests and technologies. *Dermatologic Surg.* **33,** 1158–1174 (2007).

33. Valentine, R. M., Ibbotson, S. H., Brown, C. T. A., Wood, K. & Moseley, H. A Quantitative Comparison of 5-Aminolaevulinic Acid- and Methyl Aminolevulinate-Induced Fluorescence, Photobleaching and Pain During Photodynamic Therapy. *Photochem. Photobiol.* **87,** 242–249 (2011).

34. Fritsch, C. *et al.* Optimum porphyrin accumulation in epithelial skin tumours and psoriatic lesions after topical application of delta-aminolaevulinic acid. *Br. J. Cancer* **79,** 1603–1608 (1999).

35. Angell-Petersen, E. *et al.* Porphyrin formation in actinic keratosis and basal cell carcinoma after topical application of methyl 5-aminolevulinate. *J. Invest. Dermatol.* **126,** 265–271 (2006).

36. Lerche, C. M., Fabricius, S., Philipsen, P. A. & Wulf, H. C. Correlation between treatment time, photobleaching, inflammation and pain after photodynamic therapy with methyl aminolevulinate on tape-stripped skin in healthy volunteers. *Photochem. Photobiol. Sci.* **14,** 875–882 (2015).

37. Lesar, A., Ferguson, J. & Moseley, H. An investigation of the fluorescence induced by topical application of 5-aminolaevulinic acid and methyl aminolaevulinate at different s on normal human skin. *Photodiagnosis Photodyn. Ther.* **8,** 97–103 (2011).

38. Ibbotson, S. H. *et al.* Characteristics of 5-aminolaevulinic acid-induced protoporphyrin IXfluorescence in human skin in vivo. *Photodermatol. Photoimmunol. Photomed.* **22,** 105–110 (2006).

39. Sunar, U., Rohrbach, D. J., Morgan, J., Zeitouni, N. & Henderson, B. W. Quantification of PpIX concentration in basal cell carcinoma and squamous cell carcinoma models using spatial frequency domain imaging. *Biomed. Opt. Express* **4,** 531–7 (2013).

40. Wiegell, S. R., Skiveren, J., Philipsen, P. A. & Wulf, H. C. Pain during photodynamic therapy is associated with protoporphyrin IX fluorescence and fluence rate. *Br. J. Dermatol.* **158,** 727–733 (2008).

41. Y., L. & K., H. Skin thickness of Korean adults. *Surg. Radiol. Anat.* **24,** 183–189 (2002).

42. BARKER, D. E. SKIN THICKNESS IN THE HUMAN. *Plast. Reconstr. Surg.* **7,** ppg 115–116 (1951).

43. Sandby-Møller, J., Poulsen, T. & Wulf, H. C. Epidermal Thickness at Different s: Relationship to Age, Gender, Pigmentation, Blood Content, Skin Type and Smoking Habits. *Acta Derm. Venereol.* **83,** 410–413 (2003).

44. Lahiri, B. B., Bagavathiappan, S., Jayakumar, T. & Philip, J. Medical applications of infrared thermography: A review. *Infrared Phys. Technol.* **55,** 221–235 (2012).

45. Pålsson, S. *et al.* Kinetics of the superficial perfusion and temperature in connection with photodynamic therapy of basal cell carcinomas using esterified and non-esterified 5-aminolaevulinic acid. *Br. J. Dermatol.* **148,** 1179–1188 (2003).

46. Živčák, J., Hudák, R., Madarász, L. & Rudas, I. J. *Methodology, Models and Algorithms in Thermographic Diagnostics*. **5,** (Springer Heidelberg New York Dordrecht London, 2013).

47. Ring, E. F. J. & Ammer, K. Infrared thermal imaging in medicine. *Physiol. Meas.* **33,** R33–R46 (2012).

48. http://www.tdmu.edu.ua. Medical Thermography / I.Ya. Horbachevsky Ternopil State Medical University, Ukraine. at <http://intranet.tdmu.edu.ua/data/kafedra/internal/klinpat/classes_stud/en/med/lik/ptn/Functional diagnostics_2 course/2/04. Diagnostics Methods pathology of internal organs.htm>

49. Mordon, S. A commentary on the role of skin temperature on the effectiveness of ALA-PDT in Dermatology. *Photodiagnosis Photodyn. Ther.* **11,** 416–419 (2014).

50. Juzenas, P., Sørensen, R., Iani, V. & Moan, J. Uptake of topically applied 5-aminolevulinic acid and production of protoporphyrin IX in normal mouse skin: dependence on skin temperature. *Photochem. Photobiol.* **69,** 478–481 (1999).

51. Van den Akker, J. T. H. M. *et al.* Effect of elevating the skin temperature during topical ALA application on in vitro ALA penetration through mouse skin and in vivo PpIX production in human skin. *Photochem. Photobiol. Sci.* **3,** 263–267 (2004).

52. Juzeniene, A., Juzenas, P., Kaalhus, O., Iani, V. & Moan, J. Temperature Effect on Accumulation of Protoporphyrin IX After Topical Application of 5-Aminolevulinic Acid and its Methylester and Hexylester Derivatives in Normal Mouse Skin. *Photochem. Photobiol.* **74,** 452–456 (2002).

53. Wiegell, S. R. *et al.* Daylight photodynamic therapy for actinic keratosis: an international consensus. *J. Eur. Acad. Dermatology Venereol.* **26,** 673–679 (2012).

54. Campbell, C. L., Wood, K., Valentine, R. M., Brown, C. T. A. & Moseley, H. Monte Carlo modelling of daylight activated photodynamic therapy. *Phys. Med. Biol.* **60,** 4059–4073 (2015).

Chapter 4

Towards improving ambulatory light sources for topical Photodynamic Therapy

Old ideas can sometimes use new buildings. New ideas must use old buildings

— Steven Johnson,

Where Good Ideas Come From: The Natural History of Innovation, 2010

4.1 Introduction

Previous chapters covered general background of PDT treatment for NMSC. Chapter 3 was dedicated to a clinical study of photosensitiser PpIX formation from the pro-drugs. PpIX concentration is one of the three key treatment factors. There are two other crucial parameters which are needed for a good clinical response. They are light delivery and molecular oxygen. So PDT dosimetry considers all three factors with respect to each[1,2,3,4]. This chapter will concentrate on the importance of low irradiance PDT light sources and diffusion of molecular oxygen to the lesions. It will then describe the development of an optical apparatus to design and test wearable light sources for future devices. The application of optical modelling will mostly concern optimisation of the uniformity of the light output from the devices and diffusion in skin as a helper to equalizing non-uniform irradiance. It will also compare an OLED treatment device to the current LED-based device. At the end, the chapter will raise a question about the significance of directional emission for potential improvements of light transmission in skin.

Clinically relevant concentrations of singlet oxygen which induce oxidative stress and cell death can only be produced when the concentration of molecular oxygen is above a certain threshold. It is known that molecular oxygen diffuses to the lesions from subcutaneous vessels[5]. If tissue oxygenation is below the threshold any delivery of excitation light will no longer be efficient; it will only result in photobleaching of PpIX without the clinical effect[6]. In fact, an optimal

light source should deliver as much energy at a time as is needed to excite as much PpIX as there is molecular oxygen. In reality the irradiance should be just enough to excite as much PpIX as is needed to generate the treatment threshold amount of singlet oxygen. If the irradiance is too high with respect to the oxygen supply rate it would result in PpIX photobleaching instead of generating singlet oxygen[7].

The formation of singlet oxygen can be predicted by a dynamic microscopic model which takes into account oxygen supply rate, diffusion of oxyhaemoglobin and irradiance of light sources. In this model the specifics of the photosensitizer formation, the concentration and inhomogeneous distribution were not taken into account; the photosensitizer was assumed to be infinite and uniform in the model. In animal studies the photosensitizer was metabolised in the tumours after injections of the precursors. There was good agreement between the simulated and PDT induced necrotic diameter of the skin cancer in mice[2,3,8]. These studies also reported that the lowest irradiance which was equal to 15 mW/cm^2 (the other irradiances were equal to 50, 75 and 150 mW/cm^2) resulted in much higher singlet oxygen production and better tumour response[2,8]. These findings play in favour of choosing low irradiance ambulatory PDT devices such as Ambulight PDT (7 mW/cm^2)[9] as a better alternative to the conventional PDT lamps with irradiance equal to 65-75 mW/cm^2.

Initial motivation for developing wearable PDT light sources was that it would reduce hospital load and improve quality of treatment by cutting down the time which patients spend in hospital by three hours. Also, there was an assumption that pain during conventional PDT treatment could be reduced at lower irradiances. Ambulatory PDT was first explored in a Proof and Concept project beginning in 2002 at the Photobiology Unit, Ninewells hospital, Dundee; the results were published in 2006[10].

The proof of concept project led to prototypes of a new generation of ambulatory devices which consisted of a low-irradiance OLED with a 550–750 nm emission spectrum and a peak wavelength at 620 nm. They were potentially disposable, lightweight, with a 2 cm emitting area. A study was performed using the devices for the treatment of histologically confirmed BD in 8 patients and sBCC in 4 patients with lesions smaller than 2 cm in diameter were administered aminolaevulinic acid for 4 hours and treated with a 45–60 J/cm^2 light dose at irradiance equal to 5 mW cm^2. 60% of tumours were cured at a 12 month follow up. The rest of the tumours had peripheral margin failure which could have been caused by mismatch between the size of the treated area and the light emitting area. The patients were scored for pain during and immediately after the treatment using the numerical rating scale (NRS; 1–10); 100% of the

patients scored the pain as less than 2[11,12]. In subsequent studies the light source was always larger than the lesion to avoid peripheral margin failure.

Although OLEDs have very attractive features for PDT, a suitable OLED manufacturer was not available at the time of the next stage of development and so commercialisation has so far proceeded using inorganic LEDs, leading to Ambulight PDT (***Figure 4.1***) receiving a CE mark and has become a key choice for lesions under 2.4 cm in diameter in many countries.

Figure 4.1: *Ambulight PDT device. The emitting head has a diameter of 30 mm but the treated area can be up to 24 mm to prevent any marginal failure due to misalignment of the area or intensity drop at the edges. The battery pack shows information on the display about remaining time and the treatment mode. The pictures were taken from Ambulight PDT product information video.*

The device consists of an array of 42 LEDs emitting at 640 nm with a diffuser on a flexible substrate with a dermatological tape which is fixed to the lesion's site. The area of the lesion is measured and an alignment contour is drawn with the help of a paper reference contour which comes with the Ambulight PDT device. The lesion is prepared with a curette, dermatological cream is applied and covered with a Tegaderm™ dressing film as for conventional PDT. After that the battery pack for the device is fixed on a belt on the patient or placed in a pocket, the light emitting head of the device is fixed with sticky plaster and the timer is activated. The patient is free to leave. The light will be automatically turned on after three hours; a 75 J/cm^2 treatment dose at irradiance of 7 mW/cm^2 will then be delivered over the following 3 hours. The patient then can remove and dispose of the device at home or place it in a casing and return it at the follow up visit in cases where rechargeable batteries are used (***Figure 4.2***). The responses to Ambulight PDT PDT in 53 patients with 61 lesion sBCC (n=30), BD (n=30), and AK (n=1) was 84%. 23 of these 53 patients received conventional PDT to separate lesions. The median pain score was compared between the conventional PDT and

Ambulatory PDT using a pain scale from 0 (no pain) to 10 (the worst pain one could imagine). The median pain score for Ambulight PDT was found to be 1 compared to 5 for conventional PDT[13].

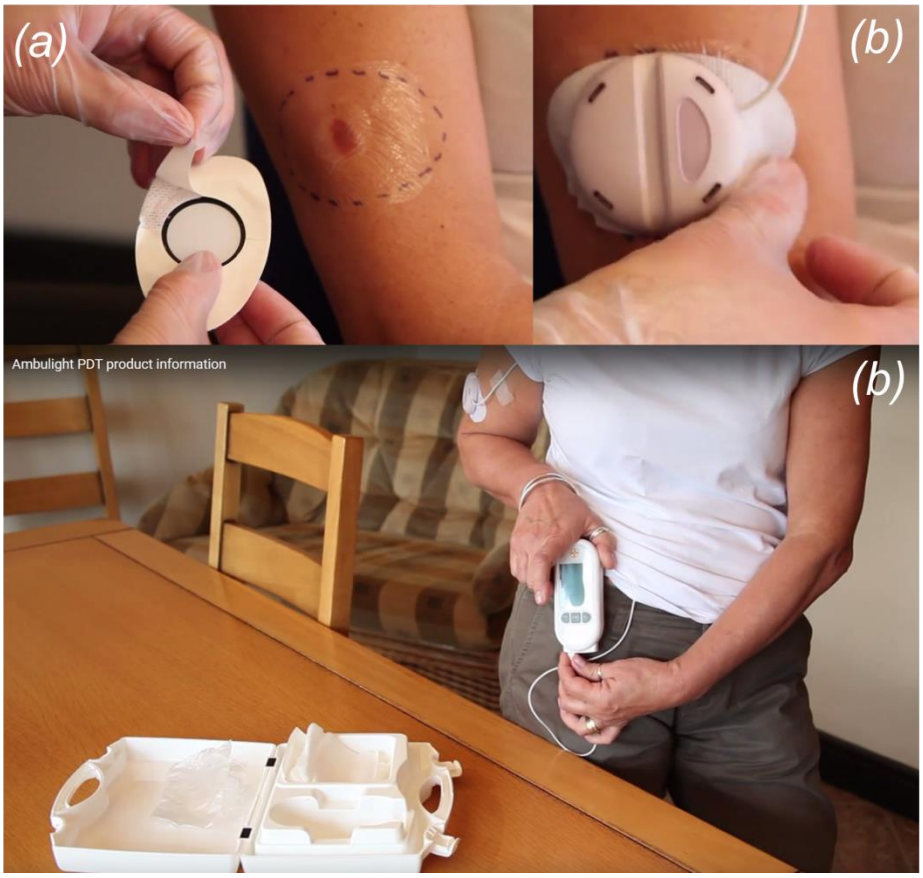

Figure 4.2: *Procedure for ambulatory treatment with Ambulight PDT.* **a –** *the size of the lesion is confirmed to fit in the treated area, the contours are marked with the help of a carton disposable card, the cream is applied, the lesion is covered with Tegaderm™ film dressing; after this the device was fixed with a self-adhesive tape.* **b –** *the device is fixed at the lesion and timer is activated.* **c –** *after 6 hours the treatment is complete (3 for metabolism of the cream, and 3 for light delivery) the device can be removed and the battery pack disposed of or returned to the hospital at next visit. The pictures were taken from Ambulight PDT product information video.*

Although Ambulight PDT is already a big advance in PDT treatment, the response could be better still. One aim of this thesis was to explore the propagation of light from the current Ambulight PDT in the skin and identify ways to optimise the design. The uniformity of the irradiance, intensity drop at the edges, the significance of distribution of LED in the array and the diffusers were studied. This chapter will describe the modelling and measurement approaches for light propagation in tissue, including the brain and the skin for proof of concept studies and PDT device design and will conclude on the optimisation routes for future ambulatory devices.

4.1.1 Light propagation through the skin

Light propagation in tissue is a statistical process. An incident ray of light which consists of a packet of photons can be randomly reflected, refracted, scattered, absorbed or propagated without any change at the interfaces or interaction points in tissue where there is a variation in optical properties (scattering at membranes, absorbing in heme and melanin molecules, etc.). How much and how far certain photons will penetrate in tissue is governed by wavelength-dependent optical properties.

(a) Absorption in tissue

There are many chromophores in tissue which absorb light via different mechanisms. For instance porphyrin and pyrrole molecules, heme and melanin cells absorb by electronic transitions via p-orbitals, water absorbs via vibrational states[14]. Absorption is defined by the effective cross-section of absorbing chromophores σ_a, $[cm^2]$[15]:

$$\sigma_a = Q_a A, \qquad \textit{Eq. 4.1}$$

where A, cm^2 is the geometrical area of the chromophore, and Q_a is the absorption efficiency. The absorption coefficient μ_a for the bulk tissue is then calculated as:

$$\mu_a = \rho_a \, \sigma_a \; [cm^{-1}] \qquad \textit{Eq. 4.2}$$

where ρ_a is the density of chromophores in units of cm^{-3}.
Light transmission T through tissue with thickness equal to $L, [cm]$ is defined by:

$$T = e^{-\mu_a L} \qquad \textit{Eq. 4.3}$$

Total absorption in the skin is a sum from contributions from all chromophores[16]:

$$\mu_a(\lambda) = log_{10} \sum_i C_i \varepsilon_i \, , cm^{-1} \qquad \textit{Eq. 4.4}$$

where C, [mol/L or M] is the concentration and ε, $[cm^{-1}M^{-1}]$ is the extinction coefficient. Blood and water are one of the strongest chromophores in skin and considering that they are present in high concentration, they will typically dictate the overall absorption[16]:

$$\mu_a(\lambda) = f_{Hb}\left[S \, \mu_a^{oxyHb}(\lambda) + \, (1 - S \,)\mu_a^{deoxyHb}(\lambda)\right] + W \mu_a^{water}(\lambda), \; [cm^{-1}], \qquad \textit{Eq. 4.5}$$

f_{Hb} - fraction of blood or haemoglobin concentration with units of g/L.

S – tissue oxygen saturation (oxygenation fraction),

$\mu_a^{oxyHb}(\lambda)$, $cm^{-1}\frac{L}{g}$ and $\mu_a^{deoxyHb}(\lambda)$, $cm^{-1}\frac{L}{g}$ - wavelength-dependent absorption coefficients of oxygenated haemoglobin and deoxygenated haemoglobin,

W - water content,

$\mu_a^{water}(\lambda)$, $cm^{-1}\frac{L}{g}$ - absorption coefficients of water.

The absorption spectra have been measured by many groups and reviewed by Steven Jacques (***Figure 4.3***).

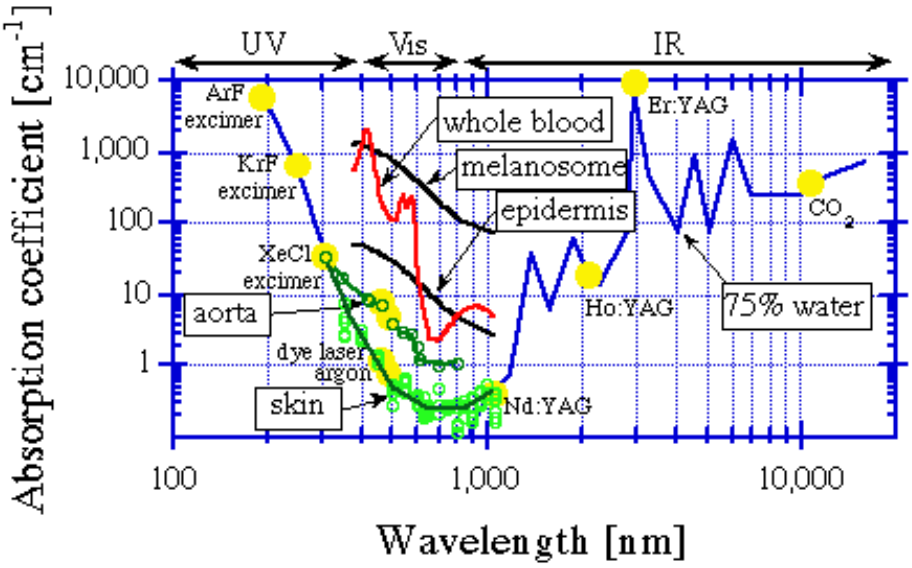

Figure 4.3: *Absorption properties of biological tissue. The figure was taken from Oregon Medical Laser Centre (OMLC) website*[17]

The resulting absorption of skin consists of the contribution of many chromophores. Skin is layered; each layer contains different chromophores. The concentration of the chromophores and the thickness of the layers vary between the individuals, body site and the skin types. This makes it very challenging to measure and model real absorption in skin.

(b) Scattering in tissue

Scattering in tissue occurs due to fluctuation of refractive index n which mostly takes place at the interface of membranes of mitochondria, nuclei and cells, myosin protein and collagen fibrils, macromolecular aggregates, lysosomes and vesicles. Lipids are some of the strongest scatterers; they play the most significant role in defining the refractive index and scattering properties of tissue[18]. Similar to how absorption was described, scattering is defined by the effective cross-section of the scatterers[19]:

$$\sigma_s = Q_s A, \qquad \textit{Eq. 4.6}$$

where $A, [cm^2]$ is the geometrical area of the scattering particle, Q_a is the scattering efficiency.

When the size of the scatterers is comparable to the wavelength of the photon the scattering is described by Mie theory. When the scatterer is much smaller than the wavelength it is described by Rayleigh theory.

The scattering coefficient μ_s is:

$$\mu_s = \rho_s \sigma_s \qquad \textit{Eq. 4.7}$$

where ρ_s is the density of scattering particles.

The probability of light scattering at certain angles in tissue can be approximated by the Henyey-Greenstein angular dependence function[20]:

$$P(cos\,\theta) = \frac{1}{4\pi}\frac{1-g^2}{(1+g^2-2\,cos\,\theta)^{3/2}} \qquad \textit{Eq. 4.8}$$

θ – the angle of the scattered ray with respect to the specular ray,

g – anisotropy parameter defined by the media; it varies from “-1” to “1”. “-1” corresponds to total backward scattering, “0” to isotropic (Rayleigh) scattering and “+1” to forward scattering. For biological tissue typical values are 0.7-0.9 which means that the tissue strongly scatters light in a forward direction.

The integral of the probability density function is equal to one:

$$\int_0^{2\pi}\int_0^{\pi} P(cos\,\theta)\,sin\,\theta\,\mathrm{d}\,\theta\mathrm{d}\varphi = 1 \qquad \textit{Eq. 4.9}$$

In some of the modelling algorithms reduced scattering coefficient μ_s' is used instead of the regular scattering coefficient μ_s. Reduced scattering coefficient is calculated from the scattering coefficient μ_s and the g parameter as[19]:

$$\mu_s' = \mu_s(1-g) \qquad \textit{Eq. 4.10}$$

There are many reported values for optical properties of tissue; the most up to date collection can be found in the Handbook of Biophotonics by V. Tuchin[21]. However, there is a huge variation among the values from different groups especially for the scattering coefficients, for instance there is an order of magnitude variation of the reduced scattering coefficient for both the brain and the skin tissue[16]. In [16] Steven Jacques et al. developed fit models for approximating and extracting a wavelength dependent reduced scattering coefficient using

experimental data from seven different groups for different types of tissues. They also presented a number of values for fit parameters to their model together with some values for the optical properties and examples of fitting curves for a few types of tissue cultures, the rest of the optical properties can be taken, for instance, from the Handbook of Biophotonics by V. Tuchin [21]. The fit model for the reduced scattering coefficient is[16]:

$$\mu_s'(\lambda) = a\left(\frac{\lambda}{500\,nm}\right)^{-b}, cm^{-1}, \qquad \textit{Eq. 4.11}$$

where a and b are fit parameters, λ is the wavelength. Scattering coefficient is calculated:

$$\mu_s = \frac{\mu_s'}{1-g}, cm^{-1} \qquad \textit{Eq. 4.12}$$

Later in the chapter there will be measurements and simulations presented for the skin and the brain at 840 nm and 633 nm. Here there is an example of the calculations of the reduced scattering coefficient which will be used in the simulations for brain white matter at 840 nm. The fit parameters and g value were taken from the paper [16] $a_{brain} = 40.8$, $b_{brain} = 3.089$, $g_{brain} = 0.8$. From Eq. 4.11: $\mu_s'^{\text{brain}}(\lambda) = 40.8\left(\frac{840}{500\,\text{nm}}\right)^{-3.089} = 8.216, \text{cm}^{-1}$. From Eq. 4.12: $\mu_s^{brain} = \frac{0.8216\,mm^{-1}}{1-0.8} = 4.108\,mm^{-1}$.

Transmission through L, cm path length of tissue can be calculated as:

$$T = e^{-\mu_s L} \qquad \textit{Eq. 4.13}$$

Scattering in tissue is approximated by the Henyey-Greeinstein probability density function. Fortunately, there are many reports from different groups on measurements and modelling for combinations of scattering coefficients and the g value of the probability function for different tissue cultures. Unfortunately, there are big differences among the reports. This can be explained by the variation of optical properties between subjects for the same tissue culture. S. Jacques developed an approximation based on the data from 8 groups which allows for calculations of wavelength dependent scattering properties for many types of human tissue and gives a more accurate prediction.

(c) Monte Carlo approach for modelling light propagation through tissue

The gold standard for modelling light propagation in tissue is the Monte Carlo algorithm. It was first introduced by Nicolas Metropolis and Ulam in 1949 for solving a class of mathematical problems which occurs in natural sciences and deals with a class of particles[22].

The Monte Carlo approach was pioneered to describe light propagation in tissue by B Wilson and G Adam in 1983[23]. And since then the method has been improved and widely used to describe light propagation at many wavelengths in many biological tissues by the pioneers in the field B. Wilson[24], S. Prahl[25,26] and S. Jacques,[27], and others [28,29,30].

The Monte Carlo algorithm records the history of photon packets as they travel through the tissue. Once a parent packet is launched at a source at (x, y, z) position with initial power P it is moved for a step Δs (or $\Delta s' = \frac{1}{\mu_t} = \frac{1}{\mu_a + \mu_s'}$ in cases when reduced scattering coefficient is used in the simulations). At the end of each step the energy of the parent ray can be split into child rays, the rays can be reflected, scattered, absorbed or transmitted. The probability for each scattering or absorption events is defined by the scattering and the absorption coefficients. New coordinates $(\mathrm{x}', \mathrm{y}', \mathrm{z}')$of the ray are calculated:

$$x' = x + cos\theta_x \Delta s,\ y' = y + cos\theta_y \Delta s,\ z' = z + cos\theta_z \Delta s, \qquad \textit{Eq. 4.14}$$

where $cos\theta_x, cos\theta_y, cos\theta_z$ are directional cosines which define the angle for the child ray after the parent ray underwent reflection, refraction or scattering. If the ray is absorbed or terminated the parameters (position and absorbed energy) are recorded and stored in ray history files for the analysis after the simulation has been completed. The ray is propagated many times until it escapes from the tissue, is absorbed or has an energy which is below the simulation threshold. In theory when the number of simulated events approaches infinity, light distribution (reflection, transmission, scattering and absorption profiles) will approach true values[26]. However for real simulations 1,000,000 generated rays with reasonable threshold energies for terminating propagation of the rays with low energy can predict light distribution in tissue with sufficient accuracy[29,30].

Monte Carlo modelling has been used as a tool to predict light propagation in tissue for sensing applications and to calculate light doses for treatment applications. Also in a combination with diffuse reflectance measurements regression Monte Carlo modelling allows for extraction of optical properties. Using real values of optical properties allows for more accurate modelling of light transport in tissue.

4.1.1 Optical phantoms and measurements for studying light propagation in skin and tissue

Tissue phantoms emulate optical properties of tissue. They are commonly used for measurements to test proof-of-principle concepts, develop devices and validate theoretical models. There are many choices for fabricating phantoms. The most common ones are made of silicone, gelatine, gel, Intralipid, and water matrixes with addition of scattering, absorbing and fluorescent particles[31,32,33].

There are a few liquid and gel phantoms. For instance, water with milk is the simplest liquid phantom with scattering similar to tissue. Intralipid is another liquid phantom which intrinsically has scattering properties close to tissue. It can be mixed with blood which will provide a very good match to absorption in tissue. Fluorescence can be added by mixing up fluorescence compounds with Intralipid. Such liquid fluorescence suspension was used to test and calibrate fluorescence measurements devices for PDT[34]. Water, gel and gelatine are other possibilities for fabricating liquid and gel phantoms.

The most common solid phantoms are made of silicone polymer which has a rubber-like texture, it is flexible, and can be moulded in any shape to represent body parts and organs[33]. So in addition to optical properties, silicone can mimic the natural shape of the body; it also to some extent matches mechanical properties of skin.

Silicone is almost transparent in visible and near IR, it has a refractive index similar to some layers of the skin and brain tissue. Absorption or fluorescence can be added by mixing absorptive inks, dyes, or blood cells. Fluorescence can be incorporated by dissolving fluorescent agents in ethanol, methanol or DMSO solutions and mixing it up with the silicone. The solutions evaporate from silicone under a fume hood and the phantom is vulcanised over 72 hours[33].

The most common additives to mimic scattering in silicone (and also in gel and gelatine) are TiO_2 and Al_2O_3 powders. The prediction of the ultimate scattering properties of the phantom is made based on the size, shape and volume percentage of alumina (or TiO_2) powder in the phantom. However, the powders vary in particle size and shapes from manufacturer to manufacturer. Also, when mixed to the silicone the particles can form sediment and form aggregates. The aggregates of the particles will have different scattering cross-sections compared to individually dispersed particles. The most common sources of discrepancy between the predicted ultimate scattering properties of the phantoms and the real vales are: the size and shape of the particles, the aggregates, non-uniformly distributed particles in the phantom, sedimentation of the particles during vulcanization and air bubbles[33].

Reported values for the scattering coefficient of the silicone phantom with alumina powder was in a range from $2.37\,mm^{-1}$ to $3.73\,mm^{-1}$. In [33] a phantom with 4% of alumina with 2.5 μm particles was predicted to have $n = 1.4$, $\mu_s = 2.46\,mm^{-1}$, $g = 0.88$ at 633 nm. Study [29] reported that for the phantom with 1% alumina powder with 4 μm particles size the predicted anisotropy parameter was $g = 0.89$, reduced scattering coefficient was $\mu_s = 0.41mm^{-1}$ (from Eq. 4.12 scattering coefficient is $\mu_s = \frac{0.41\ \mathrm{mm^{-1}}}{1-0.89} = 3.73\ \mathrm{mm^{-1}}$), refractive index was confirmed with the elipsometry measurements and was equal to 1.41. After the regression modelling using a custom Monte Carlo program written in C programming language and fitting to the diffuse reflectance measurements at 660 nm the scattering coefficient was adjusted to $\mu_s = 2.37\,mm^{-1}$[29]. The size, the shape and the aggregation of the particles was not studied in that work.

Optical properties of the silicone phantoms are representative of the optical properties of tissues, such as skin and brain. For instance $\mu_s^{phantom} = 2.46\,mm^{-1}$ [33] compared to $\mu_s^{brain} = 4.108\,mm^{-1}$. μ_s^{brain} was calculated using Eq. 4.11 and Eq. 4.12 on page 91. The refractive index of silicone was also matched to tissue, it is equal to 1.4 for the phatnom[33] compared to 1.35 for the brain, 1.5 for epidermis, 1.31 for dermis[21]. Scattering coefficients in skin vary from layer to layer, typical values for μ_s^{skin} range from 10 to $53\,mm^{-1}$[V. Tuchin[21]].

Silicone phantoms have optical properties which are close to biological tissue, the phantoms can incorporate absorbing, scattering and fluorescent particles, it can be used for years, it is not toxic, easy to handle, it does not degrade, and scattering particles do not sediment after the phantom solidifies; the only caution needed is to keep it clean as the surface is very susceptible to dirt and is difficult to clean when contaminated. Rubber-like texture allows for fabricating phantoms of any shape and using it in various types of optical measurements. The phantom is a good choice for optical measurements for PDT and OCT devices.

(a) Diffuse reflectance and transmission measurements

Optical properties can be measured and extracted from the data using regression Monte Carlo modelling[34,35]. Diffuse reflectance measurements is one of the most common types for both *in-vivo* and *ex-vivo* data collection. In this case the source and the detector are placed on the same surface; diffuse backscattering is measured as a function of distance between the source and the detector. The most common set up is based on optical fibres: the source is coupled to one fibre and the backscattered light is out-coupled to the detector's fibre[35]. The read out of such measurements can be quite demanding due to weak and noisy signals, but the

advantage is that it allows for measuring of backscattering at very small distances which are only limited by the thickness of the fibres; measurements at small steps are important to extract optical properties from the modelling. Another possibility is to use an LED and photodetectors without coupling them into optical fibres [29,30]. The level of measured signals increases which allows simplifying the read-out. However, this set up is limited to the step sizes by the size of the detectors and the LED.

Another type of measurement which can only be used on phantoms or in *ex-vivo* experiments on tissue is transmission measurement. Optical power is measured as a function of thicknesses of the tissue or phantom placed between the source and the detector. The advantage of this mode is that the signals can be much higher and simple meters can be used for readout; this may allow direct power comparison between measurements and the modelling (for weak signals the power is typically normalised). The diagram on ***Figure 4.4*** demonstrates the concepts for both types of measurements.

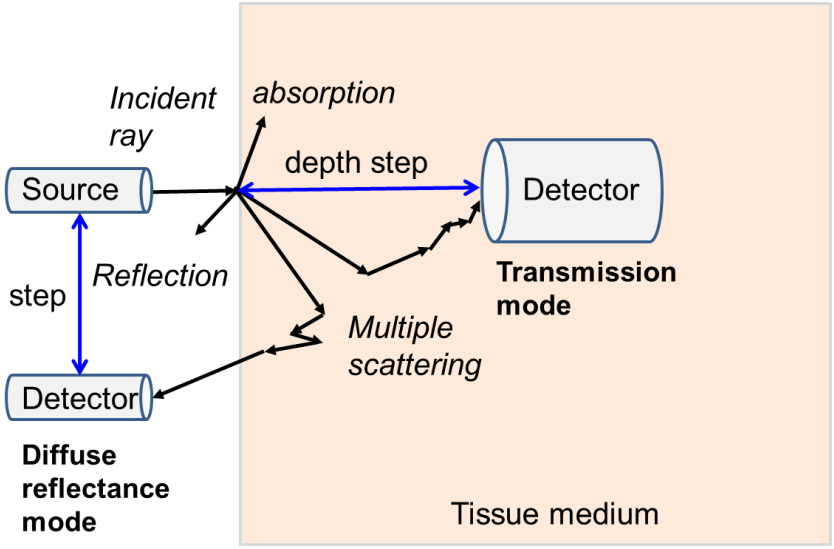

Figure 4.4: *Optical processes in tissue and measurements of diffuse reflectance and light transmission.*

Absorption and scattering in tissue, especially in skin are the most challenging optical properties to measure and model. There are many layers with the variation in thickness and concentration of chromophores and light scatterers between the individuals.

There are custom made optical probes which can measure optical properties[34,35]. They are normally calibrated on a number of in-house made phantoms with different concentration of scatterers, absorbers and fluorophores. Monte Carlo modelling is used to simulate diffuse backscattering for many combinations of the properties and look-up tables are generated. These

look-up tables contain modelled values of the diffuse backscattering at distances together with a combination of optical properties which were used for this simulation run. The measurements are compared with the simulated values and the combination of the properties is taken from the best fit. The same method can be applied to characterise optical phantoms. In this case Monte Carlo simulations are done for one set of predicted properties. By trial and error the initial set of properties are adjusted until the simulated results are in the best agreement with the measurements.

4.2 Methods

4.2.1 Choice of optical software for light transport in tissue

During the first year of the PhD project Zemax optical software was evaluated for the ability to model light transport in tissue. A library extension (Tissue.dll) was compiled in Visual C++ programming language and added to Zemax. Tissue.dll extension contained an implementation of Henyey-Greenstein scattering approximation and a Monte Carlo roulette algorithm. The simulations of diffuse reflectance in tissue phantom in Zemax agreed well with the previous Monte Carlo simulations in a custom C program[29,36]; Zemax results also agreed well with the following diffuse reflectance measurements. However, software called FRED v.12.107.0/14.40.0 from Photon Engineering was found to be more suitable for light transport in tissue. In this chapter only the results obtained with FRED will be discussed.

FRED software is a ray tracing suit optimised for non-sequential biomedical applications. It has an intrinsic Monte Carlo ray tracing algorithm and a model of Henyey – Greenstein scattering volume. These two capabilities can be activated for ray tracing in tissue. In addition there is a small library of optical properties of human tissues taken from V. Tuchin Handbook of Biophotonics[21].

A description of how a random generator is set for Henyey – Greenstein angular probability function (Eq. 4.8) is available in FRED help documentation[37]. The substitutions are made to solve the integral in Eq. 4.9: $x = \cos\theta,\ \mathrm{d}x = -\sin\theta\,\mathrm{d}\,\theta,\ a = 1 + g^2,\ b = -2g$. The integral is manipulated: $r = \frac{1-g^2}{2}\int_1^{\cos\theta} \frac{\mathrm{d}x}{(a+bx)^{\frac{3}{2}}}$, where r is a random number in the range between 0 and 1. The solution of the last equation: $\cos\theta = \mathrm{t} + \frac{\mathrm{t}}{2}(1-\mathrm{t}^2),\ \mathrm{t} = \frac{2\mathrm{r}-1+\mathrm{g}}{1+\mathrm{g}(2\mathrm{r}-1)}$. New

coordinates for the ray in Eq. 4.14 are calculated using the directional sines and cosines. When new material is created to describe tissue this model can be selected from a drop down list of scattering volumes; wavelength dependent absorption, scattering and g values can be entered in dialog windows.

Simulations are multi-threaded which increases the speed. One simulation of light distribution in a cubic tissue model with 10 cm^3 size would take from a few seconds to a few minutes (for power of a source equal to 1 W with 1,000,000 rays randomly generated at the source and cut off energies equal to half the energy of a photon). Simulations are slower for a larger number of rays, more complicated geometries of optical components and tissue, larger number of objects and optical surfaces in the system, higher scattering in tissue and lower or zero absorption. Still, for the most computation intense simulation performed to simulate light transport in fibrous muscle tissue containing 1457 optical surfaces, 400,000 rays generated at the source, the simulation of light propagation in 121 x 101 x 21 mm^3 scattering volume with 53 mm^{-1} scattering coefficient was less than an hour (this work will be described in the next chapter). FRED system units are millimetres and Watts. So all the values for scattering and absorption coefficients will be converted and discussed in mm^{-1}. However, the irradiance will be discussed in mW/cm^2 as this unit is used by the medical community.

Creating, changing and debugging optical designs are easy in a user-friendly graphical interface. Different analysis and visualisation tools allow for more flexible optimisation of the devices.

The possibility of running Monte Carlo ray tracing, the Henyey-Greenstein scattering model, the library of optical properties of tissue, many analysis and optimisation tools, a friendly user interface and fast multithreaded simulations made this software the best choice for modelling of light transport in tissue and developing of the optical device for bio-medical application.

4.2.2 Fabrication of optical phantoms

(a) Solid silicone phantoms

The protocol for fabricating silicone phantoms was adapted from[33]. Two parts, A and B of RHODORSIL RTV 141 silicone were used in a 1:10 ratio, 4% of alumina powder was thoroughly mixed to the polymer and left at room temperature to vulcanise. The phantoms normally vulcanise and develop resin-like texture after 72 hours. They can be moulded in any shape and

easily come off the mould after the silicone vulcanisation. A simple rectangular-shape phantom was made for diffuse reflectance measurements.

(b) Absorption properties of silicone pigments and dyes

Various inks from Silc Pig® Silicone Pigments (Smooth-On, Macungie USA) and Cirius Urethane Resin Dye (ArtMolds, Summit, NJ USA) were mixed with the silicone to explore the absorption properties with the view to potentially mix different dyes and pigments in the phantom to match the complex absorption spectrum of the skin. In order to place the phantoms in an absorption spectrometer, 1 mm thick phantom layers were prepared in a sandwich-like container formed from 1 mm thick microscope glass slides. When silicone vulcanises it does not stick to any of the surfaces but forms quite a tight contact as it pushes out all the air trapped at the interface with the container. It is easy to use a spatula to lift up and peel off the phantom from the container, but in the case of small tight containers such as a regular glass cuvette taking the phantom out would become a challenge without damaging the cuvette. So cheap disposable glass slides were used as phantom holders in the film holder of an absorption spectrometer. Two 1/4 pieces of the glass slide were placed as side walls and two full glass slides were used as top and bottom base of the container. A few drops of the silicone mixture were dropped in the middle of the semi-open cavity, and then the phantom was covered from the top with another slide. The Silicone is viscous enough to stay in the cavity and vulcanise on the slides almost without leaking out from the two open sides. Different colour phantoms in the glass semi-open containers are shown in ***Figure 4.5***, a. A LAMBDA 950 UV/Vis/NIR spectrometer was used to measure the absorption spectrum. A broad range of wavelengths from 400 nm up to 2 μm was investigated for potential use in many applications, including PDT, OCT and other devices. A glass container with air and also one with pure silicone were measured for the baseline. The absorption spectra are shown in ***Figure 4.5***, b.

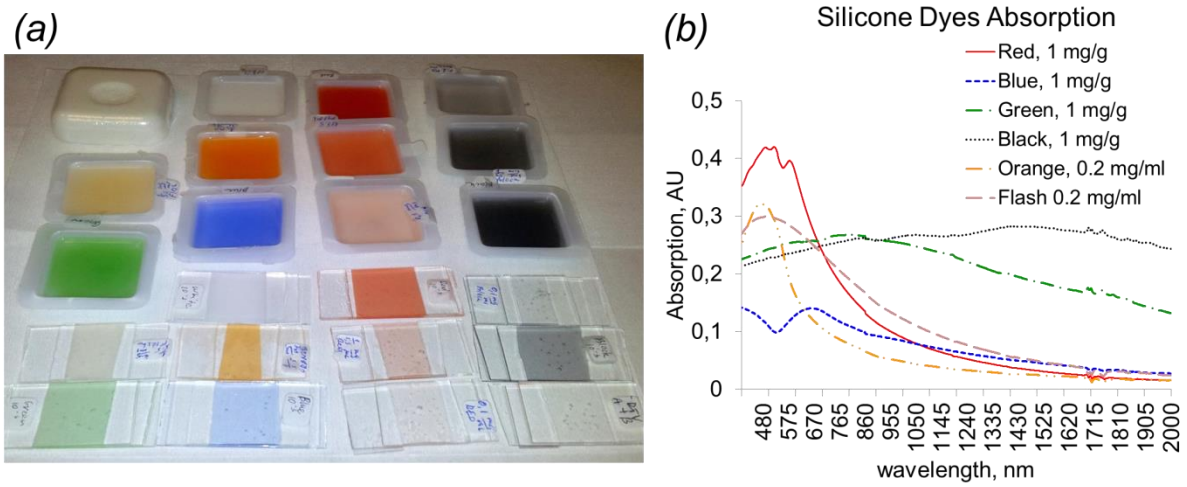

Figure 4.5: *Absorption in phantoms using of Silicone dyes.* **a** *–.phantoms with the dyes.* **b** *–.absorption spectrums.*

Considering that there are many chromophores in skin with complex spectra (***Figure 4.3***) the task of imitating the ultimate absorption in skin is quite challenging. Necessary ink or dye or a combination of them can be selected to meet specific measurement requirements. However, for the purposes of the work in this chapter the ultimate phantoms did not have any absorbers.

(c) Incorporating PpIX fluorescence in silicone phantoms

Fluorescent phantoms mentioned in the previous chapter for testing the fluorescence imaging camera were made by incorporating fluorescent powder of PpIX in a similar way to that mentioned in [33]. Protoporphyrin IX P8293 - ≥95% from SIGMA-ALDRICH was dissolved in methanol. The methanol solution of PpIX was mixed with alumina powder to provide a more uniform suspension of alumina particles and PpIX fluorophores. This suspension was then thoroughly mixed to the silicone polymer. Methanol evaporated under a fume hood and the silicone vulcanised after three days. If kept in the dark the phantoms retain their fluorescence properties for months.

(d) Gel synthetic silicate Laponite® RD phantoms

Gel scattering phantoms for depth-dependent transmission measurements were made of a Laponite® RD[38] aqueous suspension. The protocol for this phantom was developed by Dr Mario Giardini, former research fellow at the School of Medicine, the University of St Andrews. In addition to the optical properties this phantom mimics the mechanical properties of the brain

which enables various opto-mechanical manipulations in a brain-like medium. Laponite® RD is a synthetic layered silicate which is insoluble but hydrates and swells in water to give clear and colourless colloidal dispersions[39]. It stays in gel phase for as long as the water does not evaporate. 3% of Laponite® RD was mixed with water and 4% of alumina powder. Gel-like phantoms were thoroughly mixed in a plastic container and left overnight to swell and jellify. Before the measurement the phantoms were mixed up again to obtain a uniform gel structure. Optical properties of this phantom were dictated by all the components. Laponite® does not absorb in visible and near IR, so the only absorber in IR was water[40]. The refractive index of Laponite® RD powder is 1.54, in water suspensions it changes depending on the concentration Laponite® RD and ambient temperature[41,42,43]. Due to the fact that only 3% of the powder was added in the phantom, the refractive index of the ultimate phantom was only slightly increased to 1.35 compared to 1.33 refractive index of water (this value was not confirmed by measurements). Scattering properties of the phantom were the same as in silicone phantoms with alumina powder[33,29] as the same quantities were added.

Two types of phantoms - gel and solid - enabled measurements to be conducted inside phantoms and on the surface. Gel Laponite® RD phantom had similar mechanical and optical properties of brain; solid silicone phantom had a flexible resin-like texture similar to the mechanical properties of skin and was close in optical properties. It was demonstrated that these phantoms could be mixed with any combination of absorbers or fluorophores depending on the requirements of the measurement.

4.2.3 Diffuse reflectance and optical transmission measurements in tissue phantoms

Two modes of measurements (diffuse reflectance and transmission) were used to validate optical modelling and adjust the predicted properties of the phantoms to the real values. The diffuse reflectance set up consisted of two optical probes: an IR LED source was coupled to one fibre and another fibre was out coupled into a silicon detector which was connected to a lock-in amplifier. The voltage signal was measured and converted to optical power taking into account the response of the detector and the detector's gain at 50 Ohm load:

$$P, W = \frac{V\ [Volts]}{50\ [Ohm] \cdot Gain} \cdot response\ [\frac{W}{A}]. \qquad \textit{Eq. 4.15}$$

The power was normalised on the maxima for the comparison with modelling.

A transmission measurement set up was built and the data collected by Phen Toh, from the School of Medicine, the University of St Andrews under the supervision of Dr Mario Giardini. It was based on an IR LED and photodiodes without optical fibres. The LED was emitting light directly onto the gel phantom and a series of photodiodes detected the power transmitted though the phantom. The signal levels were sufficiently high, there was no need to use any advanced sensitive noise reduction equipment such a lock-in amplifier. This allowed use of a simple multimeter as a readout to perform a direct power comparison with the modelling. Short circuit currents from Phen Toh' measurements were converted to optical power using the response of the photodetectors:

$$P, W = I\ [A] \cdot response\ [\frac{W}{A}]. \qquad \textit{Eq. 4.16}$$

Both transmission and diffuse reflectance measurements can be used to study light transport in tissue and extract optical properties in regression modelling. If the distance resolution is important then the detector and the light source could be coupled to optical fibres, this however significantly reduces the intensity of the signal and would require a more expensive readout. Another option is to use simple LEDs and photodetectors which will allow for detecting strong signals and could enable the use of real power values for the modelling

.

4.3 Results

4.3.1 FRED software validation with the work of previous groups on Monte Carlo modelling and diffuse reflectance measurements

The results of the predecessors using Monte Carlo simulations written in C programming language and diffuse reflectance measurements on silicone scattering phantoms are available in [30, page 57]. [30] follows the work described in [29]. The only difference between [30] and [29] was that the volume part of alumina powder in the phantoms was increased from 1% to 4%. The initial properties of the phantoms were assumed to be the same as in [29]: $n = 1.41$, $\mu_s = 2.37\ mm^{-1}$, $g = 0.89$, $\mu_a = 0\ mm^{-1}$. The measurements set up consisted of a 5 mm in diameter IR LED SFH 487 with 880 nm central wavelength and series of 0,265 x 0,265 cm^2 BPW34 silicone photodiodes placed at 6, 10, 15, 20, 25, 30 mm centre to centre distances from the

source. Due to the sizes of the LED and the photodiodes the smallest distance which could be resolved at the first step was 6 mm.

An optical model equivalent to the one in [30] was created in FRED. A light source had 880 nm central wavelength. The actual power was not important as only the normalised power comparison was reported in that work; so the LED power was set to 1 W. The phantom had the same refractive index and scattering properties $n = 1.41$, $\mu_s = 2.37\, mm^{-1}$, $g = 0.89$; however, considering the absorption measurements of pure silicone (***Figure 4.5***), an absorption coefficient equal to $\mu_a = 0.0072\, mm^{-1}$ was added in FRED model. 1,000,000 rays were generated at the source. Ray tracing cut off energies were 10^{-19} W which was a little bit less than half of the energy of a 880 nm photon: $E_{photon} = \frac{hc}{\lambda} = 2.25 \cdot 10^{-19}\, J$. Diffuse reflectance signals were calculated at the photodetectors placed at 6, 10, 15, 20, 25, 30 mm centre to centre distances from the LED.

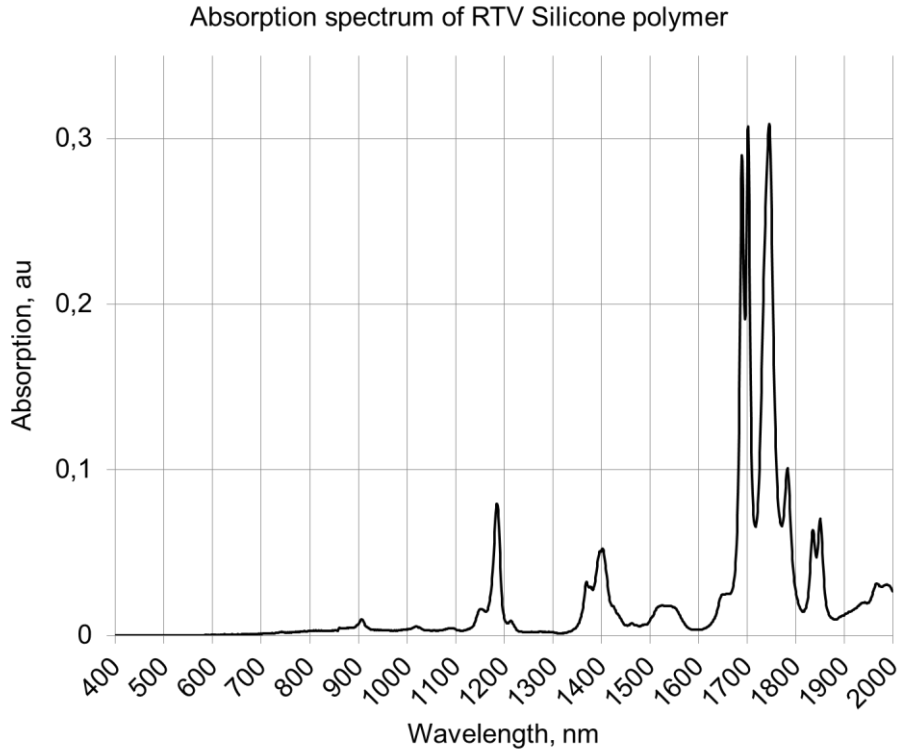

Figure 4.6: *Absorption spectrum of pure RTV silicone phantom. It is almost transparent in the visible range and starts absorbing in near IR; at 840-880 nm the absorption coefficient is 0.0072.*

FRED simulations agreed well with the results in [30] (***Figure 4.8***).

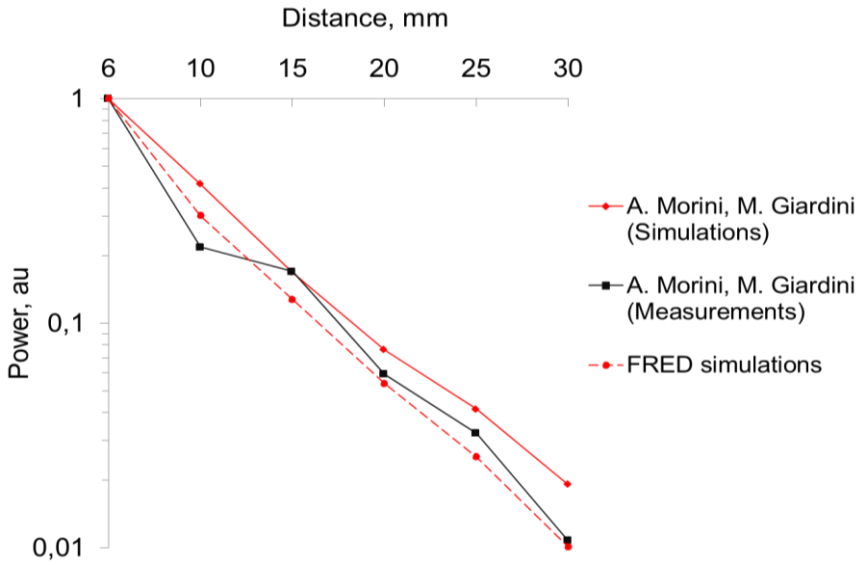

Figure 4.7: *FRED validation on Monte Carlo simulations and diffuse reflectance measurements on silicone phantoms with alumina powder. The values for the comparison were taken from [30, page 57].*

FRED fit to the diffuse reflectance measurement of the predecessors was even better than their original Monte Carlo modelling possibly due to the fact that in the FRED model the real value for absorption in silicone was taken into account. This gave confidence in using FRED for the further studies of light transport in tissue.

4.3.2 Fibre optics diffuse reflectance measurement set up to study light propagation in solid tissue phantoms

After the validation of FRED, the optical measurements apparatus was developed. The measurement set up was built using a SFH4740 IR LED with 860 nm central wavelength which was coupled in 1 mm in diameter core optical fibre with 2 mm in diameter cladding. Signals were collected by the same type of fibre and coupled to a PDA36A silicon photodetector which was then connected to a lock-in amplifier (***Figure 4.8***, a). Output power from the source fibre was 59 μW. In order to have a distance reference between the source and the signal fibre a fibre spacer was cut from 6 mm thick PMMA plastic sheet using a CO_2 laser cutter (CTR Lasers, UK) described in in chapter 2. An array of 2 mm in diameter (plus a small tolerance) holes at 2 mm centre to centre distances provided a 2 mm step between the source and the signal fibres. A sheet of beam blocking paper was placed between the phantom and the fibre spacer to prevent any feedback on the interface between PMMA plastic and the phantom. The detector was set to

70 dB mode at 50 Ohm load which corresponded to 2.38 MV/A detector's gain. The response of the photodetector was 0.65 A/W. The integration time of the lock-in amplifier was 1 s. Voltage measurements were taken at 3, 7; 11; 15; 19; 23; 27 mm. Optical power was calculated from the voltage, the photodetector's gain and the response using Eq. 4.15. The power was normalised at the maxima. The results can be found in Appendix XIX.

The optical model was equivalent to the measurement set up: the source with 1 mm in diameter emission area and the detectors with 1 mm in diameter sensitive area were placed at 3, 7; 11; 15; 19; 23; 27 mm centre to centre distances. The light divergence from the source and acceptance angle of the detectors was set to ±12.7° which was due to 0.22 NA of the optical fibres. The LED spectrum and the directional emission were imported from the manufacturers' datasheets. The source and the detector fibre had a 1 μm gap from the phantom. The model is shown in ***Figure 4.8***, b, c.

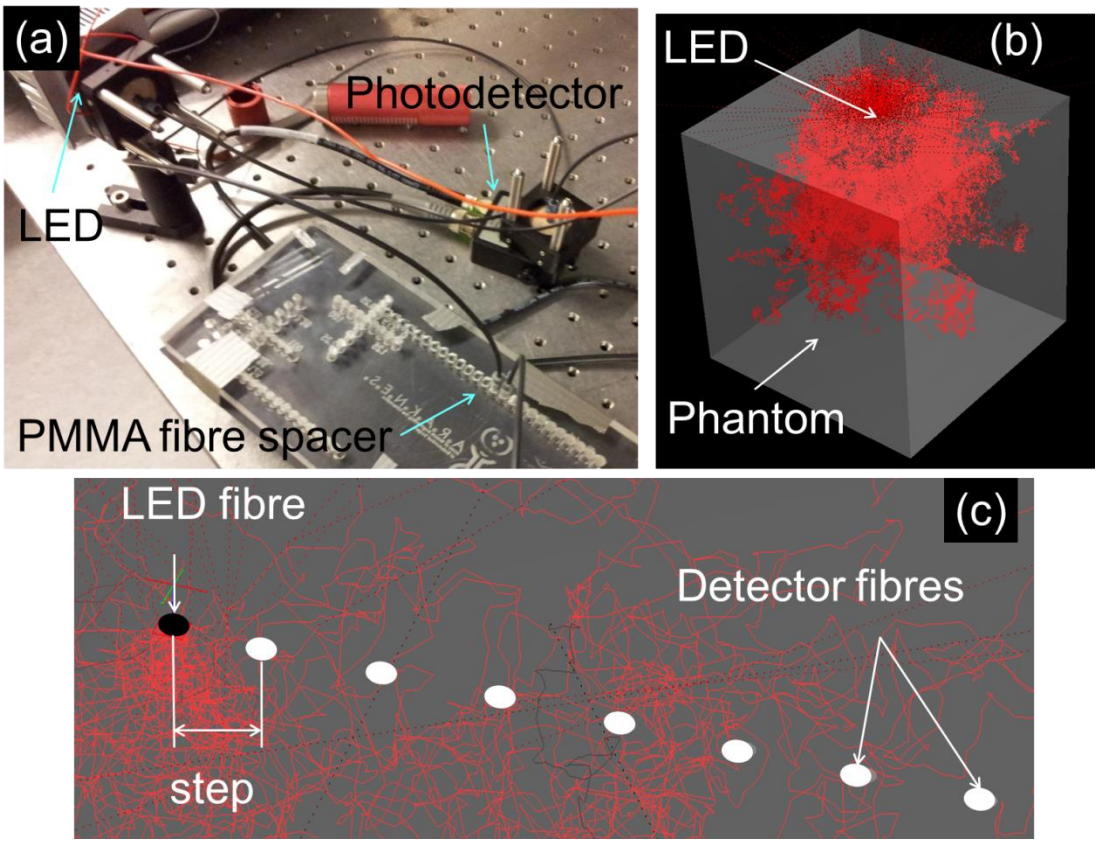

Figure 4.8: *Measurements and modelling of diffuse reflectance in scattering tissue phantom.* **a** *– measurements set up. Two optical fibres (one source fibre coupled to LED on aluminium heat sink and signal fibre coupled to a photodetector) were placed in the holes of the plastic fibre holder for distance reference. A sheet of black beam blocking paper was fixed with a duct tape to the fibre spacer and then it was placed on top of the phantom.* **b** *–.modelling of light scattering in the phantom,* **c** *– the arrangements of the source and the detectors in the model which corresponded to the arrangements in the measurement set up.*

The initial properties of the phantom and ray tracing properties were set the same as in the validation tests described above. The simulation for the initial properties of the phantom did not have a very good fit to the measurements. This could be explained by the fact that the properties of alumina powder were not measured in this work - the scattering coefficient used was based on previous reports. The aggregation state, sedimentation and bubbles could be the other possible reason for the discrepancies. In order to adjust the initial scattering coefficient in the phantom to the real value, regression modelling was done and the best fit was found to be for the value equal to $\mu_s^{phantom} = 4.1\ mm^{-1}$ (***Figure 4.9***).

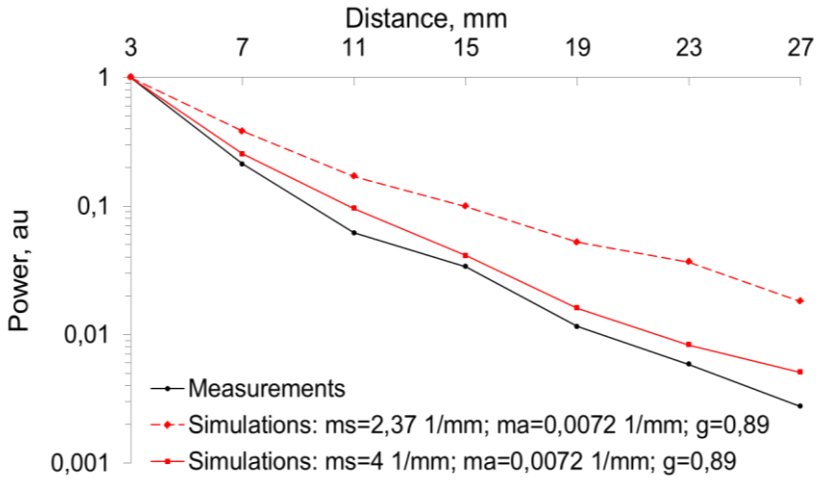

Figure 4.9: *Light propagation in silicone phantoms. The powers are normalised on maxima. The scattering coefficient was adjusted after regression modelling from 2.37 mm^{-1} predicted value to 4.1 mm^{-1} real value in the phantom.*

Fabricated and measured silicone phantoms, fibre optics set up and FRED modelling completed the development of the optical apparatus for design and testing of devices for PDT and other applications.

4.3.3 Measurements in gel phantoms and FRED Monte Carlo modelling to study optical power transmission in brain

FRED modelling was used to explore the possibility of powering a small portable robot implanted in a brain phantom from a solar panel using an IR LED. In addition to optimising the design of the solar panel, the aim of the modelling was to perform direct power comparisons with the measurements. The measurements were done by Toh Pheng Shiew under supervision of Mario Giardini and the description of the project can be found in the Bachelor of Science

(Honours) in Medicine thesis, 2013, candidate number 10023[38]. The measurements set up consisted of an SFH4740 LED, Laponite® RD gel scattering phantom and two types of solar panels made in-house. The solar panels were moved through the phantom; the optical power transmitted from the LED was detected with the solar panels. The panel was connected to a variable load and a multimeter. The aim of this measurement was to find an optimal load which for which the robot could generate maximum power from the LED. The project report[38] describes the voltage measurements as a function of variable load and the calculations of the peak power. However, this method brings extra inaccuracies in power measurements, so for the aim of the simulations a direct short circuit current was provided and this can be found in Appendix XX. The power was calculated from this current and the response of the photodiodes using Eq. 4.16.

The first solar panel consisted of six silicone BPW34 photodiodes with the response equal to 0.48 A/W and another one was made of four silicone SLSD-71N300 photodiodes with the response equal to 0.55 A/W (***Figure 4.10***). The solar panels were made on a rigid probe which was then immersed in the Laponite® RD gel phantom and moved with a 5-20 mm depth step. The depth step was measured with a calliper as a distance between the front panel of the probe and the front wall of the aluminium heat sink where the LED was fixed.

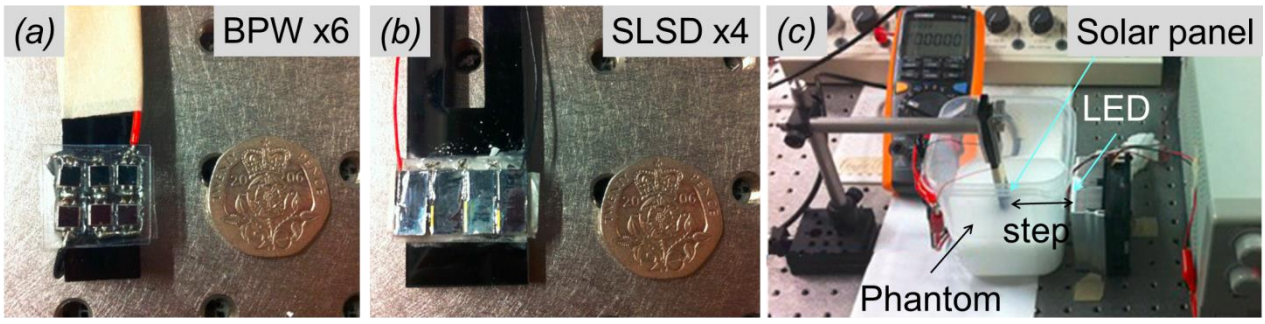

Figure 4.10: *Solar panels and measurement set up for power transmission in brain phantom.* **a** *– BPW x6 solar panel probe.* **b** *– SLSD x4 solar panel probe.* **c** *– depth dependence measurements in gel phantom. (The photographs were kindly provided by Toh Pheng Shiew, graduate of the School of Medicine, the University of St Andrews).*

The optical model of the setup is shown in ***Figure 4.11***. . The LED power was set to 0.685 W (the same power was used for the short circuit current measurements). The LED emission spectrum and directional diagram were imported from the datasheets.

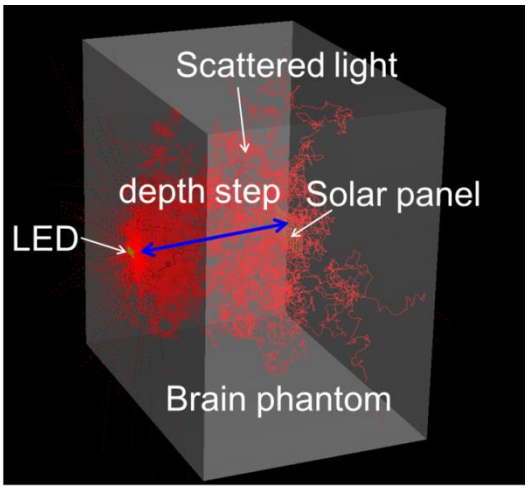

Figure 4.11: *FRED model of IR light transmission in scattering brain phantom*

The arrangements and the properties of the solar panels corresponded to the fabricated solar panels in the experiment. Six silicon BPW34 photodetectors were placed in two rows, three detectors in each. The spacing between the edges of the detectors in a row was 1.2 mm, the spacing between the edges of the top and bottom rows was 2.4 mm. The radiant sensitive area of each BPW34 photodiode was 2.74 mm x 2.74 mm = 7.5 mm^2, and 45 mm^2 for the whole solar panel.

The second panel was made of one row of four silicon SLSD-71N300 photodiodes with a radiant sensitive area equal to 10.16 mm x 5.08 mm = 51.61 mm^2 per one photodiode and 206.45 mm^2 per whole solar panel. The detectors were placed as close as possible - with 0.2 mm spacing between the edges. From the datasheet for both photodiodes BPW34 and SLSD-71N300 the acceptance angle was equal to 60°.

The consideration for the optical properties of Laponite ® RD phantom were described in paragraph 4.2.2: $n = 1.35$, $\mu_s = 4.1\ mm^{-1}$, $g = 0.89$, $\mu_a = 0.0039\ mm^{-1}$.

1,000,000 rays were simulated at the source and propagated with the same ray tracing properties as in the previous simulations. Irradiance and total power at each photodetector was calculated using an irradiance detector from the analysis tools. The resulting power was summed from all the detectors and compared with the measurements (***Figure 4.12***), Appendix XX.

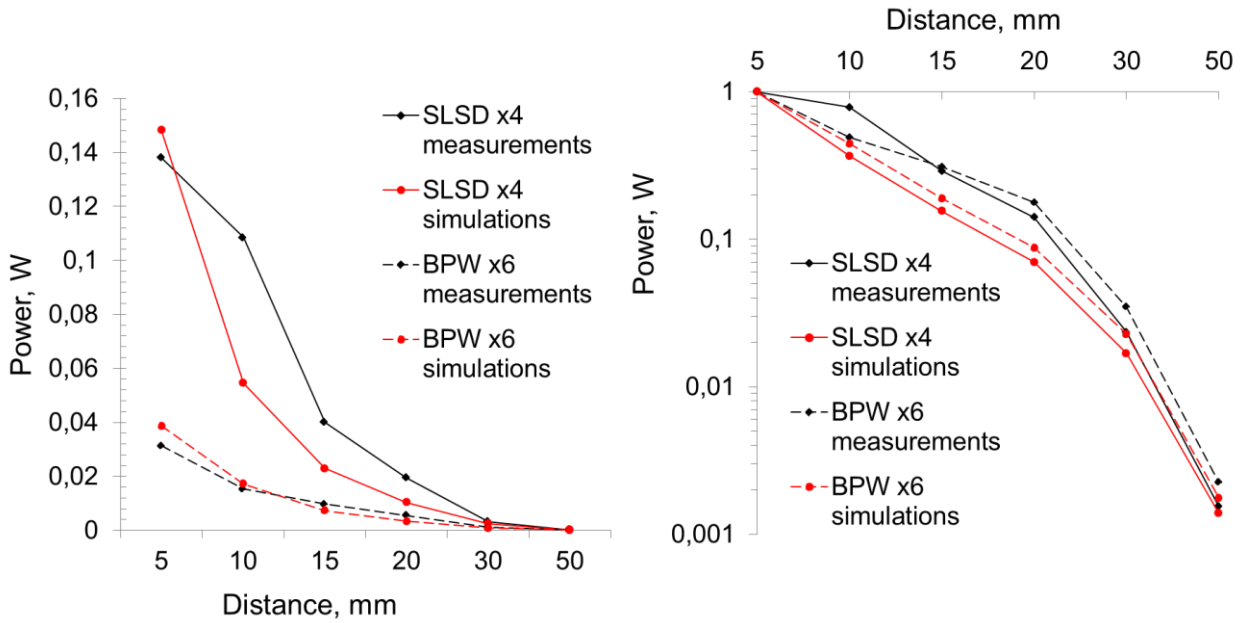

Figure 4.12: *Absolute power comparison in brain phantom transmitted from an IR LED and measured by two solar panels BPW x6 and SLSD x4. The power on the right graph was normalised on the maxima.*

For the initial set of optical properties there was an acceptable agreement between the measurements and the modelling. There is a small discrepancy, but it is still a good fit considering all the sources of possible inaccuracies which could have introduced a much bigger mismatch. Such sources could be possible aggregation or sedimentation of alumina particles with time, formation of air bubbles in the phantoms, especially during the movements of the probe in the gel; the model did not take into account optical properties of the 1.57 mm thick walls of the plastic container where the phantom was kept or slight tilt.

The simulations of the irradiance distribution at each photodiode in BPW x6 and SLSD x4 solar panels submerged in brain phantom at 5 mm depth are shown in ***Figure 4.12*** and ***Figure 4.14***. The results showed that the arrangement of photodiodes in SLSD x4 panel was more effective than in BPW x6. Regardless of strong diffusing properties of the phantom the transmission of optical power is still directional even at large distances. If the LED and solar panel are cantered with respect to each other then most of the power will be detected in the central region of the panel. Big gaps in the centre of BPW x6 result in missing most of the transmitted power and collecting it only at the edges. SLSD x4 has very good coverage of the central area. The edge detectors contribute seven times less in collecting optical power than the middle detectors. The design of the panel could be improved by reducing the area and removing the edge detectors without significant loss in the efficiency.

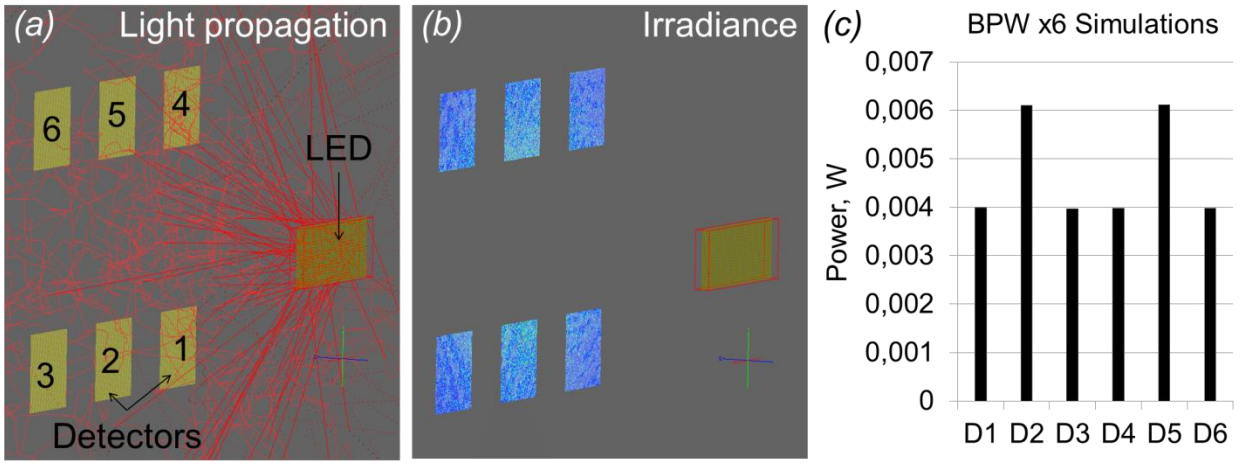

Figure 4.13: *BPW x6 solar panel in brain phantom irradiated by SFH4740 IR LED.* **a** *– light propagation.* **b** *–irradiance on the detectors 5 mm deep in phantom.* **c** *– total power at each detector. Central detectors detect much more power indicating that the arrangements of the photodetectors with the respect to the light source is very important regardless of the light diffusion in the phantom.*

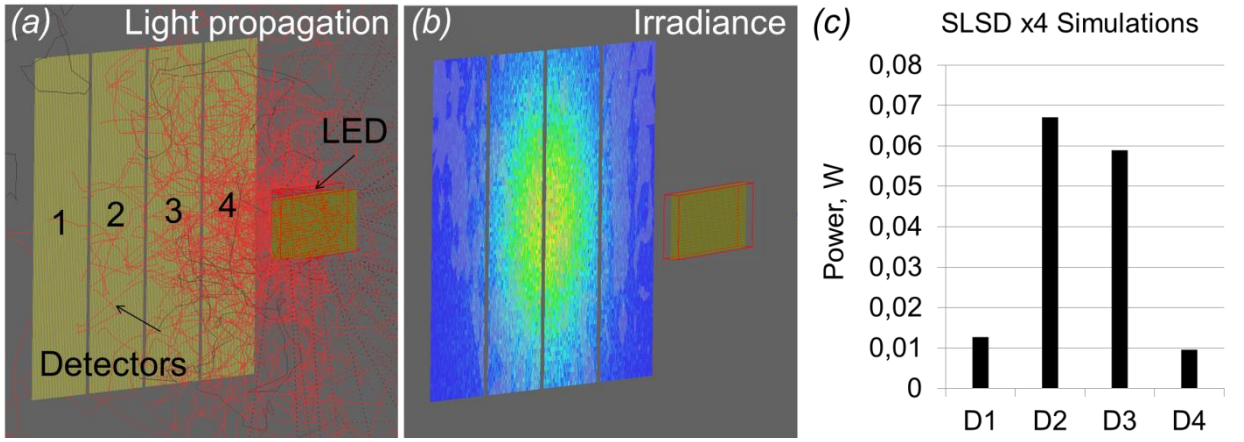

Figure 4.14: *SLSD x4 solar panel in brain phantom irradiated by SFH4740 IR LED.* **a** *– light propagation.* **b** *–irradiance on the detectors 5 mm deep in phantom.* **c** *– total power at each detector. The design is very efficient in collecting optical power by well covered central area. Two edge photodetectors collect much less power and could be removed from the design reducing the size.*

These results gave the confidence in the capabilities of the software to model absolute powers and real optical components for light transport applications. Regression tests from the previous paragraph and direct power measurements in this paragraph established scattering properties in phantoms for 4% alumina powder.

The modelling also helped to better understand the most efficient placement of the photodiodes in the solar panels for wireless power collection in the brain for the potential

application in implanted robots. Big gaps in the first solar panel BPWx6 particularly playing the role in the centre resulted in poor power collection; the second solar panel SLSDx4 had good coverage of the central area and was much more efficient. The size of the SLSDx4 panel could be reduced without adverse effects to the efficiency. One monolithic photodiode and coordination between positioning of the LED and the panel would be an optimal approach for this application.

The solar panel SLSD x4 detected approximately 2% of the transmitted power in 30 mm brain phantom. For the current LED with the wireless charging power equal to 0.685 W the SLSD x4 solar panel was able to generate 12.6 mW.

One of the examples of miniature robots of high importance to this project was reported in [44], where a robot was able to perform *in vivo* natural orifice surgery. The robot was powered through wires but the group was aiming for developing wireless powering. However, there was no information about the power consumption for the robot available. Another work which reports power consumption of a miniature robot was published in [45]. The robot was able to move with the speed equal to 40 mm/s and was controlled by IR signals. It had dimensions equal to 20 mm x 8 mm x 15 mm and was powered from a battery. The power consumption was equal to 6 mW. So by detecting 12.6 mW with the SLSD x4 solar panel from the wireless IR power transmitter the SFH4740 LED at 30 mm in depth of the brain phantom it would be possible to wirelessly power this robot deeper than 30 mm in the phantom.

4.3.4 Modelling of Ambulight PDT device and an investigation of ways for potential improvements in the design

Declaration of Interests

Ambulight PDT is an ambulatory device for PDT developed and commercialised by Ambicare Health Ltd. a spin-out company of the University of St Andrews. The supervisor of this research project is one of the founders of Ambicare Health Ltd and one of the inventors of Ambulight PDT.

This section aimed to address the following questions:

- how uniform was the output illumination in the current device;

- would it be possible to reduce the number of LEDs in the array without significant loss of the optical output or having adverse effects on the uniformity of the light field;
- how much diffusion in skin could help to equalise non-uniformities of the illumination;
- could the skin itself provide enough diffusion to allow the diffusers to be completely removed from the design;
- investigate the potential of OLED light sources for future Ambulight PDT devices.

(a) Geometrical arrangements

The optical model of Ambulight PDT corresponded as closely as possible to the real device. The current device has an emission area with the diameter equal to 30 mm and consists of an array of 42 Kingbright Hyper Red KPD-3224SEC-J3 LEDs with 640 nm central wavelength built on a hybrid flexible printed circuit board (PCB) and two paper-based diffusers. The PCB and the diffusers are placed in a semi-flexible plastic-resin casing. The coordinates of the LEDs in the array can be found in Appendix XXI; the arrangements are shown in ***Figure 4.15*** in the optical model and in ***Figure 4.16*** (a) in real device.

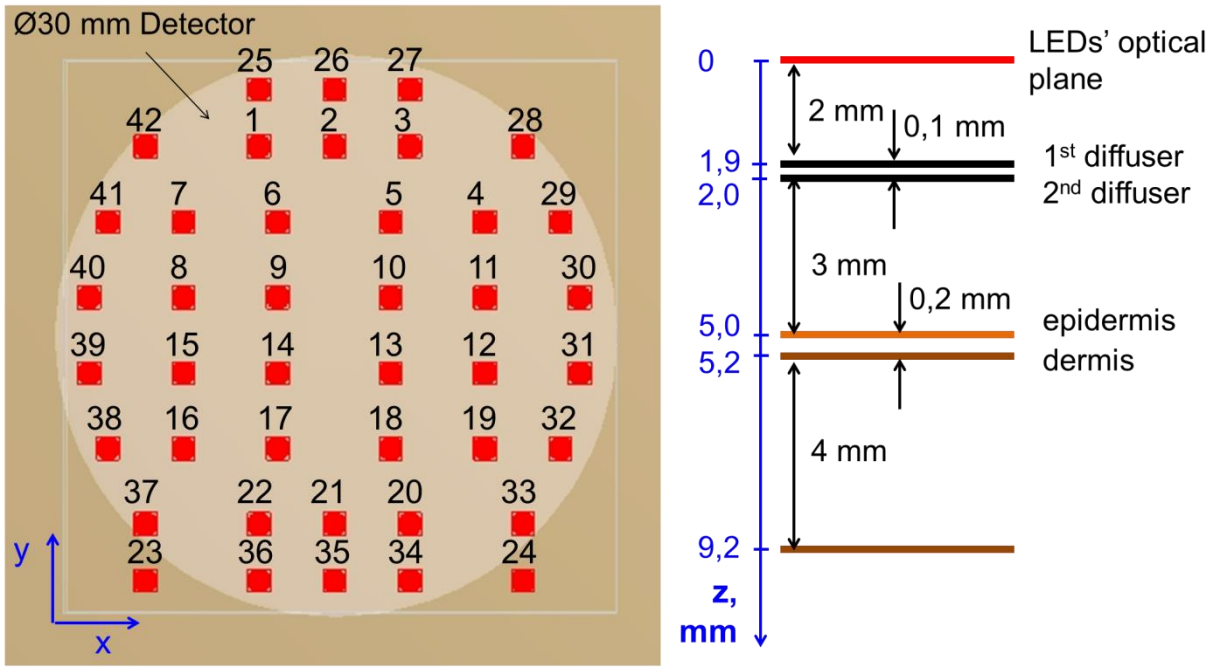

Figure 4.15: *Optical model of Ambulight PDT. The numbers and the coordinates of the LEDs in the array correspond to the schematics of Ambulight PDT device; the heights of the optical planes on z-axis were selected as close as possible to the real values (however, the device is flexible so the values should be treated with caution).*

(b) LED properties

Each LED has a 1.2 mm in diameter dome-shaped microlens and ±10° emission divergence. The spectrum and the directional emission were imported to FRED from the datasheet. The optical output in the datasheet was given in photometric units and had to be converted to radiometric quantities which were required to characterise light sources in FRED. The calculations are as follows[46].

$Power = Irradiance \cdot Area$

$Area = \pi \cdot r^2, mm^2$

$$Irradiance = \frac{Luminance \cdot Solid\ angle}{Eye\ response \cdot Multiplicative\ constant}$$

$$Solid\ angle = \pi \cdot 2 \cdot \left(1 - \cos\left(\frac{\pi \cdot 20°}{180°}\right)\right) = 0.378$$

$Eye\ response\ (at\ 640\ nm) = 0.185$ [47]

$Multiplicative\ constant = 638.002\ \frac{lm}{W}$

$Brightness\ (at\ 20\ mA) = 1\ cd$ (from the datasheet)

$$Luminance = \frac{Brightness}{Area} = \frac{1\ cd}{\pi \cdot 0.0006^2 mm^2} = 884642{,}6044\ \frac{cd}{m^2}$$

$$Irradiance = \frac{884642{,}6044 \cdot 0.378}{0.185 \cdot 638.002} = 2835{,}751771 \frac{W}{m^2}$$

$$Power = 2835{,}751771\ \frac{W}{m^2} \cdot \pi \cdot 0.0006^2 mm^2 = 3.2\ mW$$

(c) Ray tracing properties

There were 22,500 rays from each LED, the total number of rays for 42 LEDs was 945,000. Power apodization was according to the directional diagram. Average energy for each parent ray was $3.2 \cdot 10^{-3}\ W/22500 = 1.42 \cdot 10^{-7}\ W$. The energy of the 640 nm red photon was $3.1 \cdot 10^{-19}\ J$. So one ray consisted of $4.5 \cdot 10^{11}$ photons. Cut off energy for the ray tracing was $3 \cdot 10^{-19}\ W$ which is less than the energy of one photon. One simulation run with these ray tracing parameters took about 30 seconds.

(d) Diffusers' properties and power output

To guide the modelling, light emission from Ambulight PDT with and without diffusers was imaged with a colour digital camera and a monochromatic Lumenera 075 CCD camera with 635±10 nm band pass filter (***Figure 4.16***). The diffusers in the device were placed with a very

small gap between them at 2 mm distance from the LEDs' optical plane (***Figure 4.15***)..

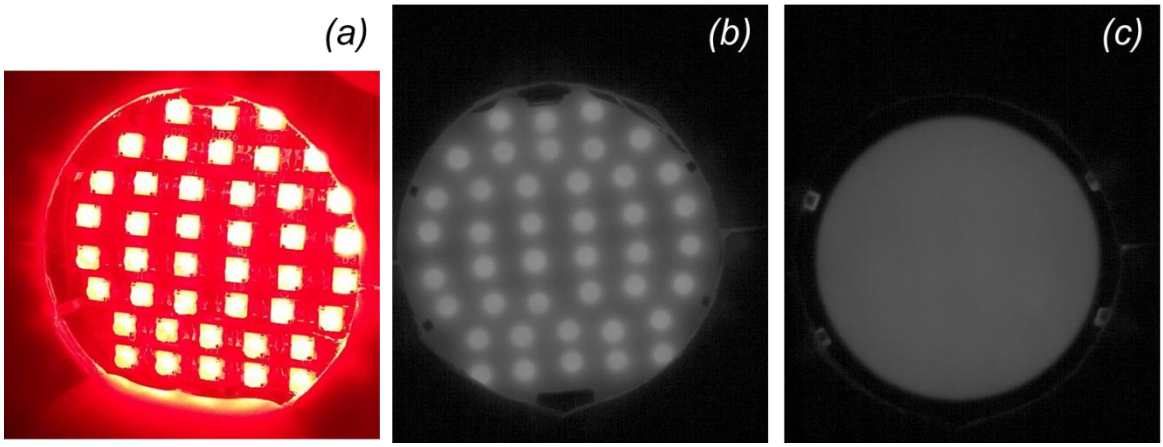

Figure 4.16: *Ambulight PDT emission.* **a –** *an image of LED array without diffusers taken with a digital colour camera* **b, c –** *monochromatic images of the emission through one and two diffusers correspondingly. The images were taken with a CCD camera and red band pass filter.*

In the model the diffusers were set to diffuse 80 % of the light with Lambertian profile and had 40% reflection. The distance from the second diffuser to the skin was 3 mm. According to the specification of Ambulight PDT the irradiance output at the surface of the skin is equal to 7 mW/cm^2.

(e) Skin model

The Skin model consisted of two layers: epidermis and dermis. Layers which follow after dermis are not treated with PDT and were not considered in the model. Typical thickness of epidermis varies from 50 μm to 1.5 mm, the thickness of dermis can be from 0.3 to 3 mm[48]. The thickness of epidermis was set to 200 μm in the model. The thickness of dermis was set to 4 mm for modelling purposes, but the results were analysed only up to 2 mm as PDT is only recommended for superficial lesions.

Scattering coefficients for epidermis and dermis were calculated for 633 nm using Eq. 4.11 and Eq. 4.12. The fit parameters were taken from [16]. For epidermis $a_{epi} = 68.7$, $b_{epi} = 1.161$, $g_{epi} = 0.79$, $n_{epi} = 1.5$, $\mu_a^{epi} = 0.43\, mm^{-1}$ and for the dermis $a_{derm} = 45.3$, $b_{derm} = 1.292$, $g_{derm} = 0.75$, $n_{derm} = 1.31$, $\mu_a^{derm} = 0.27\, mm^{-1}$ $(at\ 633\, nm)$. Values for n, g, μ_a were taken from V. Tuchin Handbook of Biophotonics[21]. Resulting scattering coefficients were found to be $\mu_s^{epi} = 25.011\, mm^{-1}, \mu_s^{derm} = 16.7\, mm^{-1}$ $(633\, nm)$.

(f) Detectors and data analysis

An irradiance and a power flux detectors in the model were used to analyse the transmitted light. A 30 mm in diameter 2D irradiance detector had pixel resolution equal to 300 μm x 300 μm. The power flux detector had the same diameter, but with higher voxels resolution, equal to 50 μm x 50 μm x 50 μm. The model of Ambulight PDT with the skin is shown in ***Figure 4.17***.

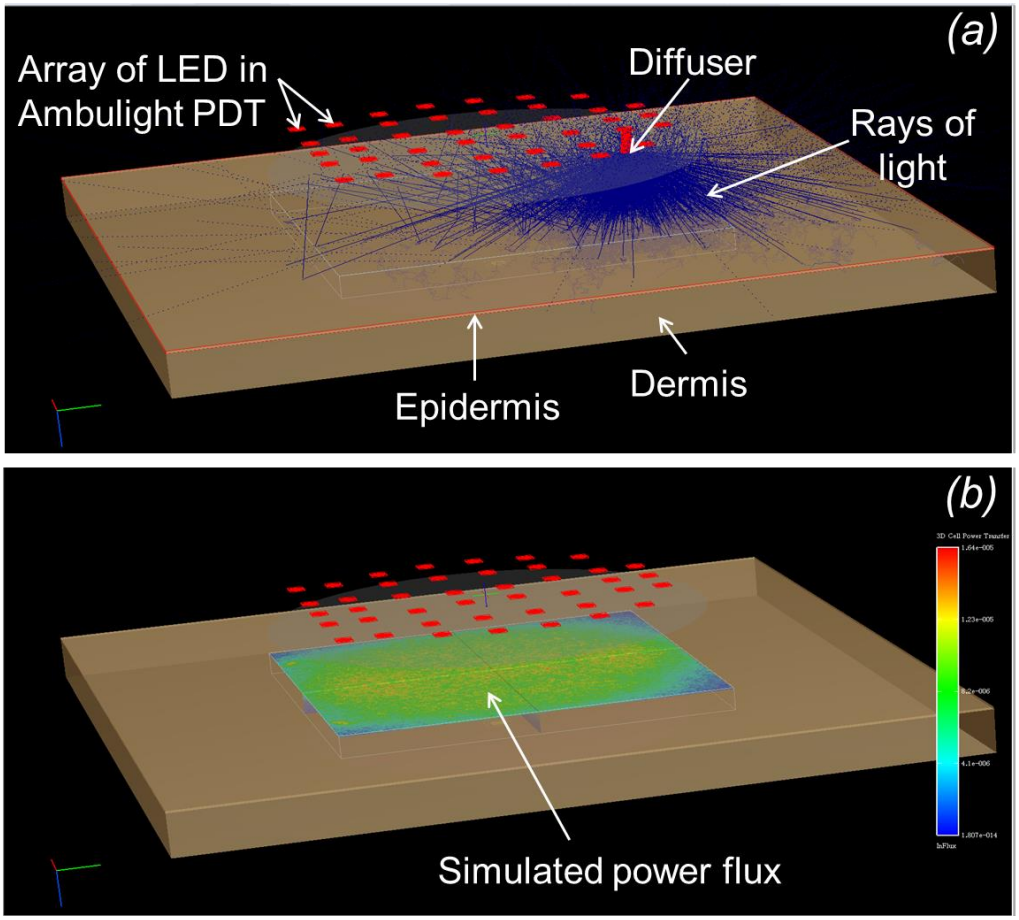

Figure 4.17: *Optical model of Ambulight PDT with skin.* **a –** *simulations of light propagation in skin from one LED (red rays) through the diffuser (blue rays).* **b –** *light influx at the power flux detector at 100 μm cross-section in epidermis.*

(g) Test simulations

The test run of the simulations was done for calculating the irradiance at 1 μm from the LED (***Figure 4.18***). Average irradiance at each LED was equal to $0.0029\,W/mm^2$ and is shown on the cross-section of the irradiance simulations (***Figure 4.18***, b). Power was calculated from an emitting area of one LED with the diameter equal to 1.2 mm: $\mathrm{P} = 0.0029\,W/mm^2 \cdot$

$\left(\left(\frac{1.2}{2}\right)^2 \cdot 3.14\ \mathrm{mm}^2\right) = 3.2\ \mathrm{mW}$ which corresponded to $3.2\ \mathrm{mW}$ defined at the start of the simulations.

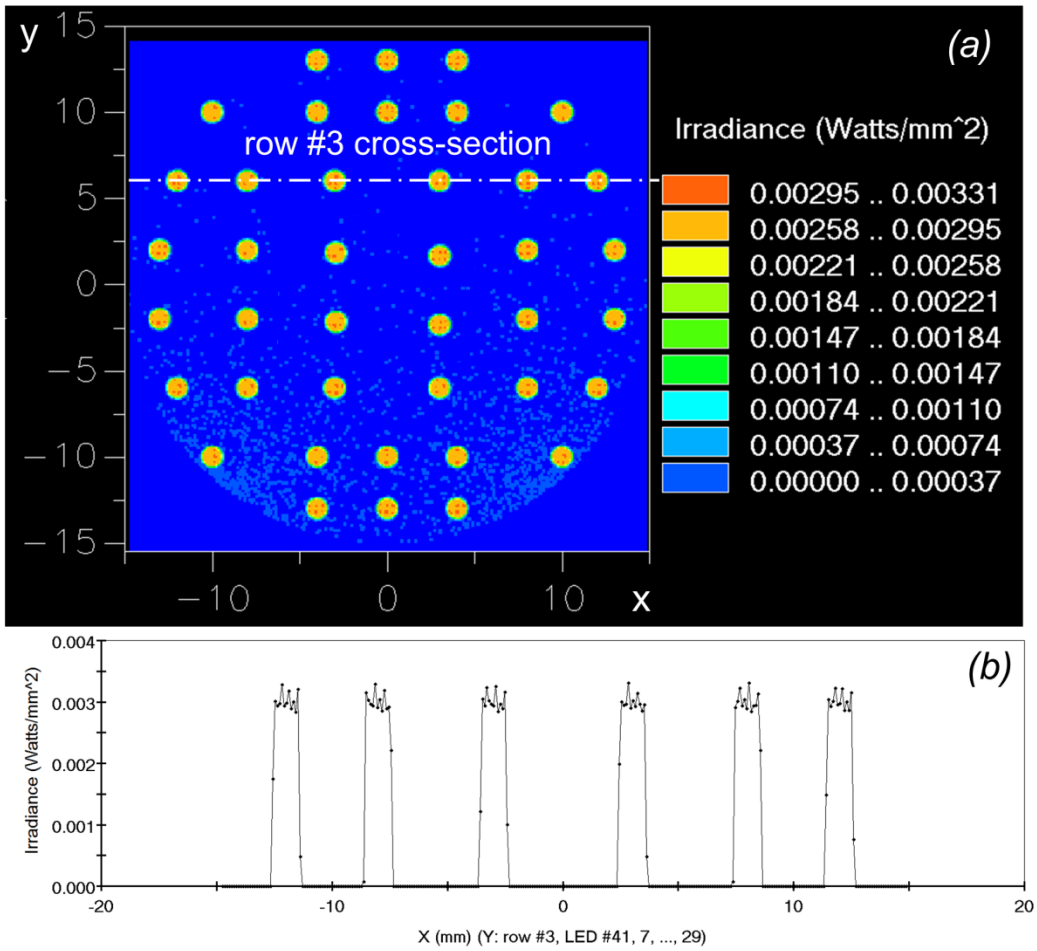

Figure 4.18: *Simulations test.* **a –** *simulated irradiance at 1 µm distance from the LEDs' array plane.* **b –** *2D cross-section of the irradiance simulation at the centre of the third row from the top of the LEDs array.*

Output irradiance at the optical plane of the skin (epidermis layer) was 7.3 mW/cm^2 which corresponded to the specification of the Ambulight PDT device.

(h) Uniformity of the illumination from Ambulight PDT and optimising the diffusers

According to the modelling after the diffuser the minimum irradiance was 6 mW/cm^2 and average was 7.3 mW/cm^2 (***Figure 4.19***). If non-uniformity is estimated as

$$non\_uniformity = \frac{average\ -minimum}{average} \cdot 100\% \qquad \textit{Eq. 4.17}$$

output irradiance of Ambulight PDT is 18 % non-uniform which is better than in conventional PDT lamps with non-uniformity up to 38 %[49].

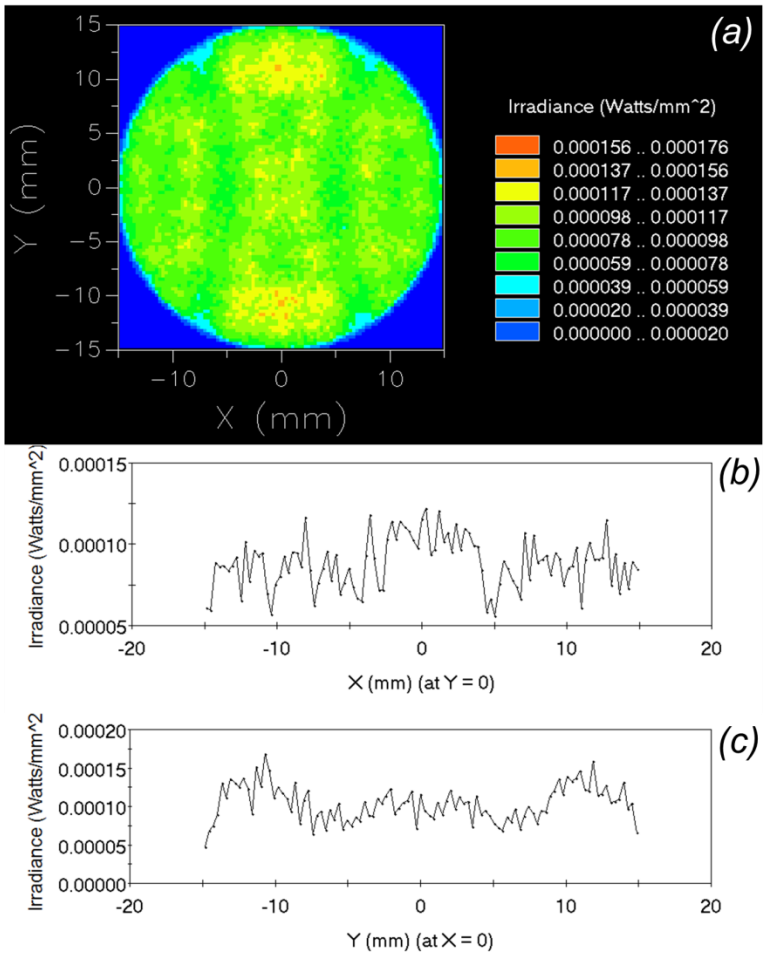

Figure 4.19:*Detector at 5 mm from the source after two diffusers in air.* **a –** *irradiance distribution.* **b, c –** *1D irradiance cross sections along x- and y-axis correspondingly.*

However, considering that the gap between two diffusers is very small the contribution from the second diffuser at this small distance may be much less significant than increasing the distance to the skin. Irradiance was simulated at 7 mm distance for one diffuser. The results demonstrated improvements in irradiance even with one diffuser (***Figure 4.20***).

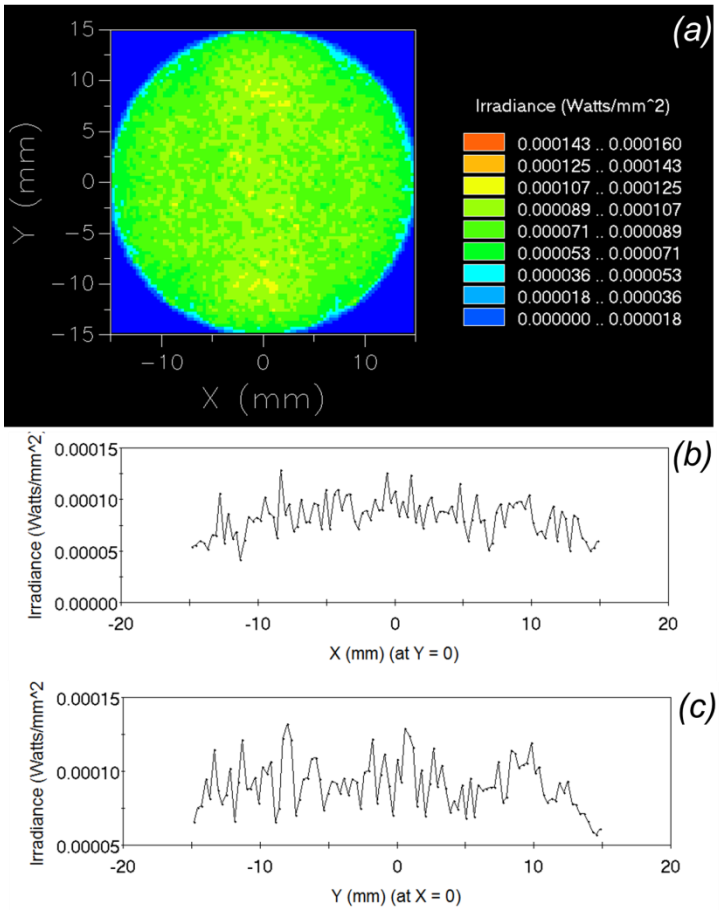

Figure 4.20: *Optimisation of the position and number of diffusers in Ambuligth PDT. If the diffuser is placed 2 mm more from the skin, the diffusion is more uniform even with one diffuser.* **a –** *irradiance distribution.* **b, c –** *1D irradiance cross section along x- and y-axis correspondingly.*

(i) Optimisation of number of LEDs

In order to find the optimal number of LEDs and the best configuration in the array, LEDs were taken out one by one from different locations in different combinations and the change in the output irradiance and the uniformity of the illumination was analysed. The positions of the LEDs in the array are shown in ***Figure 4.15***. ***Figure 4.21*** shows two irradiance plots for two cases. The left plot shows an irradiance when four LEDs were removed from the central locations from the positions numbers were #25, #27, #23, and #24. The right plot shows irradiance for the case when four different LEDs were removed from the edge locations from the positions #9, #13, #4, and #16. The irradiance formed non-uniform spots in both cases which demonstrated that removing central and edges LEDs would result in adverse effects to the design. However, taking out LEDs from the position #2 and #21 did not introduce any non-

iformity. At the furthest edges LEDs #23 and #24 did not change the uniformity either. So it was safe to remove LEDs from the positions #2, #21, #23 and #24.

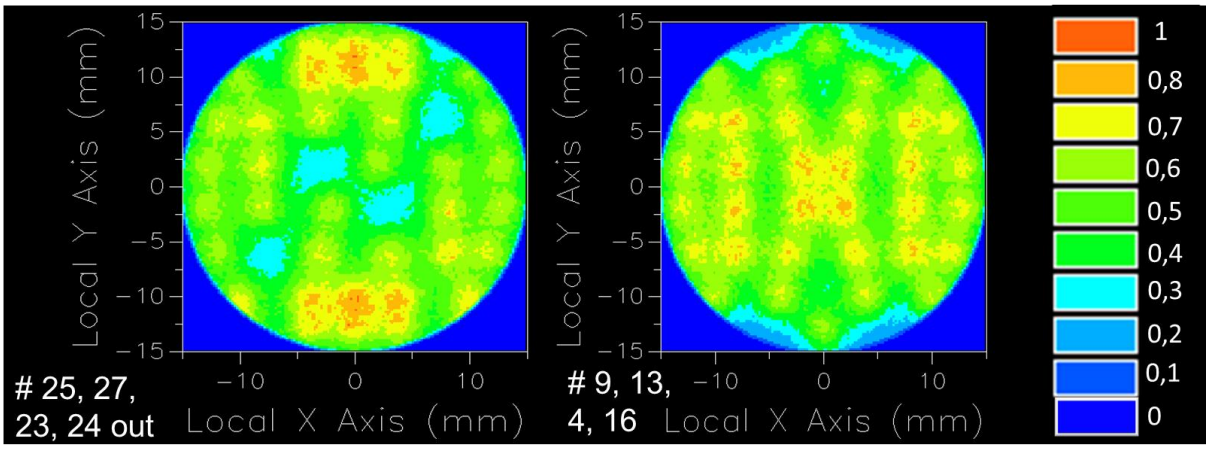

Figure 4.21: *The effect of removing a few LEDs from Ambulight array. The numbers on the images followed by # correspond to the positions of LEDs (***Figure 4.15***) which were taken out from the array. The most dramatic effect was observed from taking out edge LEDs. Illumination at the edges could play a role in marginal tumour response failure, so regardless that the emission area is larger than the treated area, illumination at the edges should stay as uniform as possible.*

Figure 4.22 shows the drop of average and minimum irradiance as a function of reduced number of LEDs. Average irradiance was integrated over the area of 30 mm in the diameter of the irradiance detector. The distance from the LED array to the detector was 5 mm. There was a diffuser placed at 2 mm distance from the LED array. Minimum irradiance was calculated from the pixel(s) at the detector with minimal incident power and integrated over the area of the pixels. The dots on the graph correspond to the calculated output irradiance from the Ambulight model at the detector for the scenario when one LED from the position #1 was removed, then for the case when one LED from the position #2 was removed, and so on. The results showed that the average irradiance was not affected by removing up to four LEDs, hower there were large drops in the minimal irradiance. As it was demonstrated in ***Figure 4.12***, some of the locations have a more pronounced contribution to the uniformity than the other. So care should be taken when changing the distribution of LED in the array.

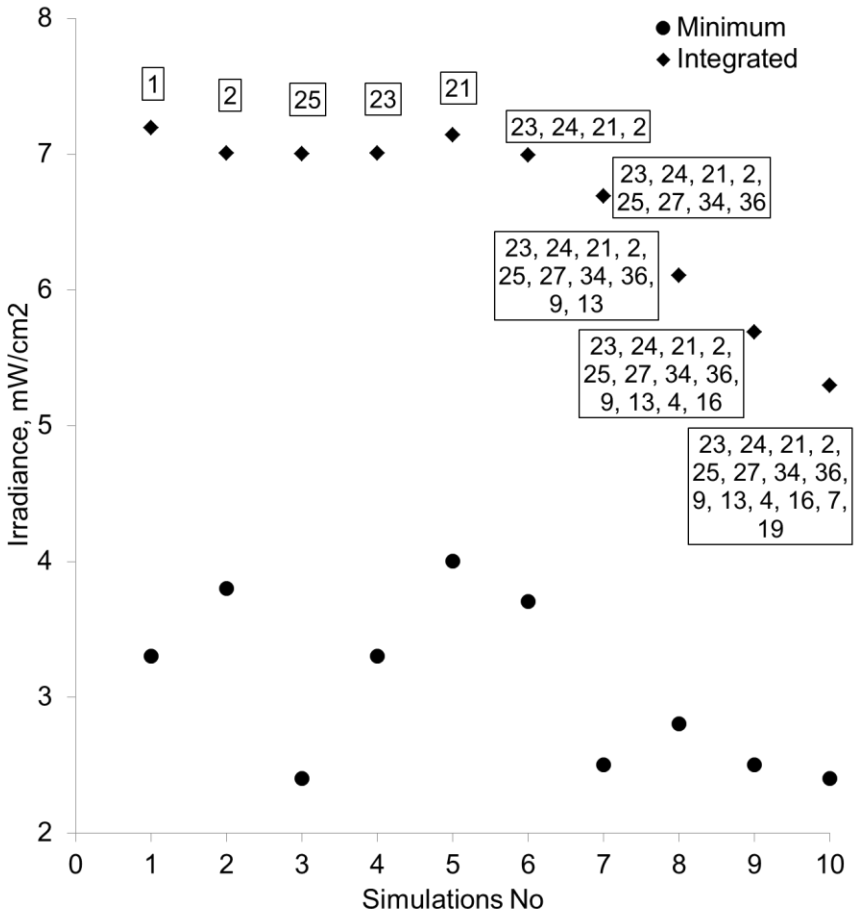

Figure 4.22: *Optimisation of number and position of LEDs in Ambulight PDT array. The numbers in the boxes correspond to the # of LEDs which were taken out of the array.*

The irradiance distribution, average and minimal values could help in making a decision about changing the number of LEDs and to identify the least significant LEDs in the array. Average irradiance was still above 7mW/cm^2 for more than 38 LED in the array which means that four LED could be safely removed from the current design.

(j) Can the design of Ambulight PDT benefit from light diffusion in the skin?

The aim of the work in this paragraph was to investigate how much natural diffusing process in skin can equalize non-uniform illumination delivered from treatment light sources. If it was discovered that at shallow thicknesses of skin equal to 100-200 μm the skin can compensate large fluctuations in the illumination field, it would enable simplifying the requirement for the uniformity of the illumination field in the treatment light sources. The modelling in this paragraph aimed to investigate whether a 100-200 μm or 1 mm thick layers of the skin could diffuse the light enough to enable removing the diffusers from the current model of

Ambulight PDT. This simplification of the design would make the device cheaper and the fabrication processes easier. The approaches taken to study the diffusion in skin was by modelling light distribution form the Ambulight LED array without the diffusers on the surface of the skin, and in depth of the skin. Two cases were studied with thicknesses of the skin relevant for PDT treatment. The first case was focused to investigate the diffusion at 100 μm depth in epidermis which is the depth relevant to AK where malignant keratinocytes proliferate. The other case was to study the diffusion at 1 mm depth in skin which consisted of two layers, a 200 μm thick layer of epidermis and an 800 μm thick layer of dermis layers. The emission from the LED array was modelled in air first at distances equal to 5 mm from the LEDs (the distance to the surface of the skin), at 5.1 mm from the LEDs (the distance when a layer of 100 μm thick epidermis would be added to the model), and at 6 mm from the LEDs (the distance when a layer of 1 mm thick skin would be added in the model). Then the skin was added in the model and the simulations of light distribution were repeated for the previous distances, but now with the skin. The diffusion in skin was evaluated by calculating the emission spot size from the LED in air and the change in the spot size introduced by adding the skin in the model. The uniformity of the illumination was evaluated by the percentage difference between the minimal and average irradiance. The ultimate result of the modelling was to estimate the improvements of the uniformity of the illumination of the treatment light sources by adding the skin in the model.

In this paragraph the first case with a 100 μm thick epidermis layer will be investigated. First the irradiance at 5 mm and 5.1 mm from the LED array was simulated in air and the emission spot size from one LED was calculated. The irradiance simulations at 5 mm distance from the LED array in air is show in ***Figure 4.23***. The spot size of one LED at this distance was found to be 3 mm. It is interesting to note that the emission spot size diverged from 1.2 mm at zero distance (***Figure 4.18***) to 3 mm at 5 mm distance. This may be useful to keep in mind when designing the light sources, at sufficient distances to the skin the divergence from the LED light sources may eliminate the need to introduce any diffusive components.

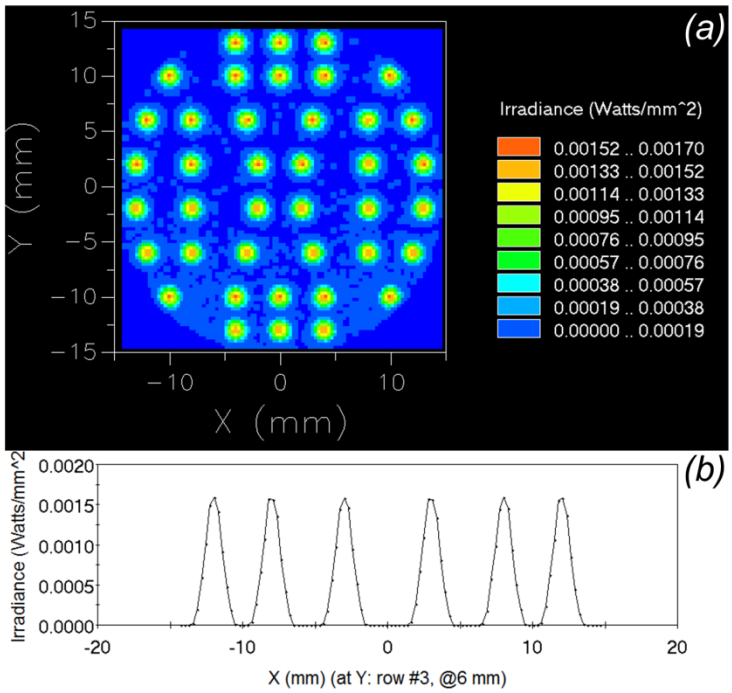

Figure 4.23: *Irradiance at 5 mm distance from the Ambulight LED array in air.* **a** *– irradiance distribution.* **b** *– 1D irradiance cross section along x-axis at the third row of LED form the top*

Then the irradiance was simulated at 5.1 mm distance in air and is shown in ***Figure 4.24***. The emission spot size from one LED did not increase much compared to the previous simulations (***Figure 4.23***). The spot size was found to be approximately 3.12±10 mm. So additional 100 μm distance from the LED array in air expands the spot for only 0.12±10 mm.

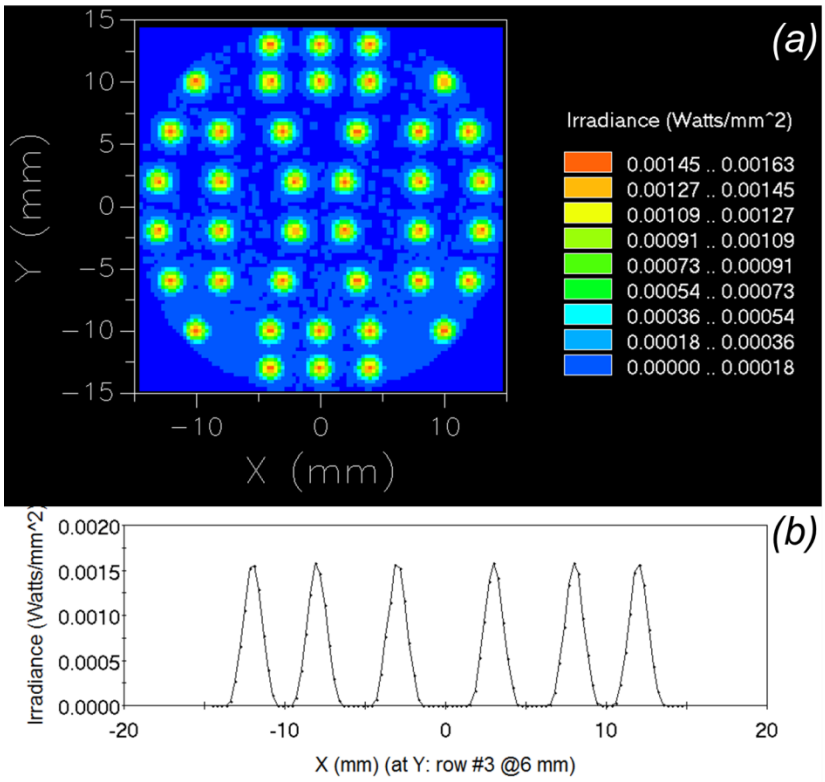

Figure 4.24: *Irradiance at 5.1 mm distance from the Ambulight LED array in air.* **a** *– irradiance distribution.* **b** *– 1D irradiance cross section along x-axis at the third row of LED form the top*

Then the skin was added to the model. Light propagation was simulated from the LED through 5 mm air and a 100 µm thick layer of epidermis. The detector was placed at 5.1 mm distance and the irradiance simulations are shown in ***Figure 4.25***. The emission spot size of one LED increased to 3.25±10 mm compared to 3.12±10 mm emission spot size the LED in air at this distance (***Figure 4.24***). So 100 µm of epidermis can only compensate non-uniformities in the illumination field by 4%.

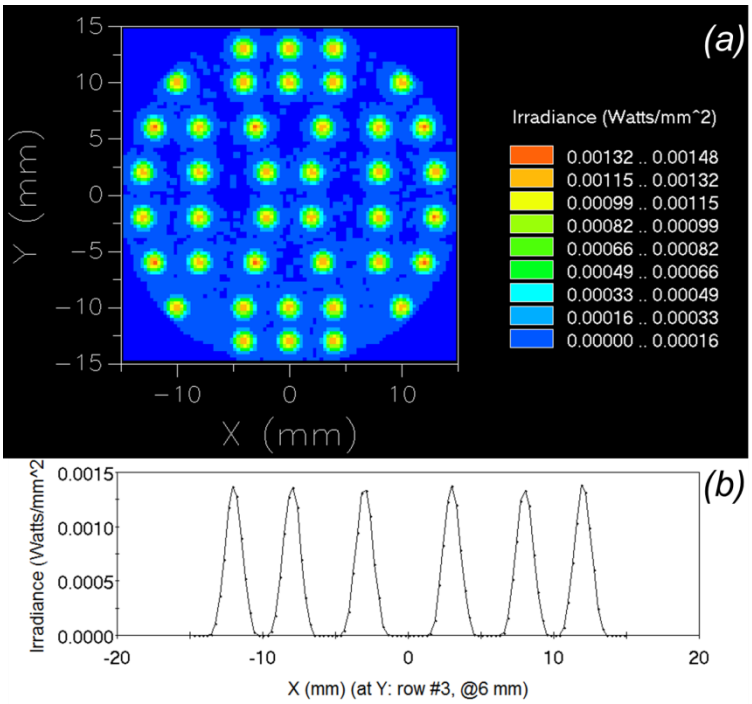

Figure 4.25: *Irradiance at 5.1 mm distance from the Ambulight LED array in 100 μm of epidermis.* **a** *– irradiance distribution.* **b** *– 1D irradiance cross section along x-axis at the third row of LED form the top*

Even light distribution at larger thicknesses is more clinically relevant though as the intensity of light is very high at the surface and small depths, so even lower intensity at the minimum of non-uniform spots will be enough to achieve clinical effect.

The second case studied the irradiance uniformity at 1 mm in depth of skin which consisted of a 200 μm thick layer of epidermis and an 800 μm thick layer of dermis. Similarly to the previous case, the irradiance was simulated in air at 6 mm and the skin was added to the models; the irradiance was simulated at 6 mm distance with light propagation through 1 mm of the skin. The irradiance at 6 mm distance from the LED array in air is shown in ***Figure 4.26***. The emission spot size from one LED at this distance was found to be 3.5 mm

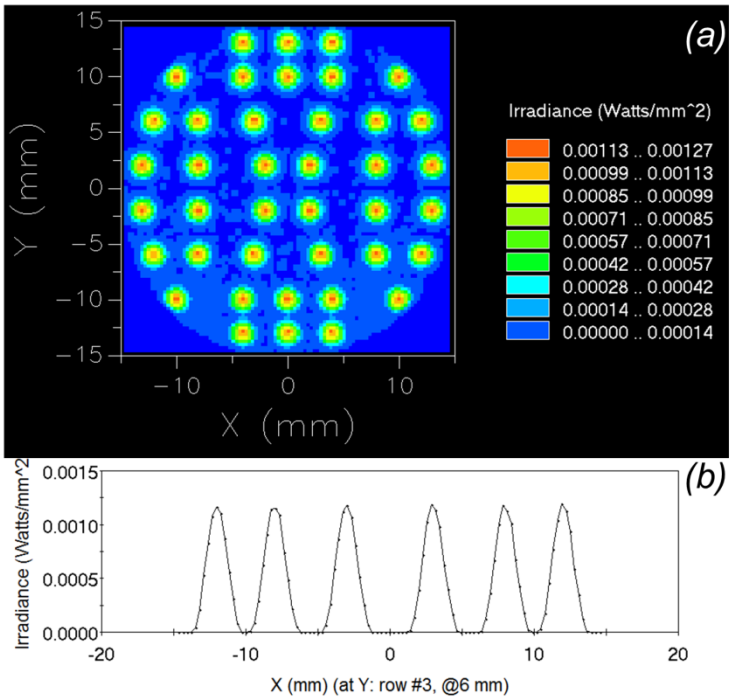

Figure 4.26: *Irradiance at 6 mm distance from the Ambulight LED array in air.* **a** *– irradiance distribution.* **b** *– 1D irradiance cross section along x-axis at the third row of LED form the top*

Then the skin was added to the model. The irradiance was simulated at 6 mm distance from the LED array, which means that the light propagated though a 200 μm thick layer of epidermis and an 800 μm thick layer of dermis. The irradiance distribution at 1 mm depth in the skin is shown in ***Figure 4.27***. The emission spot size from one LED was found to be 10 mm. This means that 1 mm of skin expanded the emission spot size from 3.5 mm at this distance in air (***Figure 4.26***) to 10 mm. The expansion of the spot size was $\Delta spot_{size} = \frac{spot_{size2} - spot_{size1}}{spot_{size2}} \cdot 100\% = \frac{10-3.5}{10} \cdot 100\% = 65\%$.

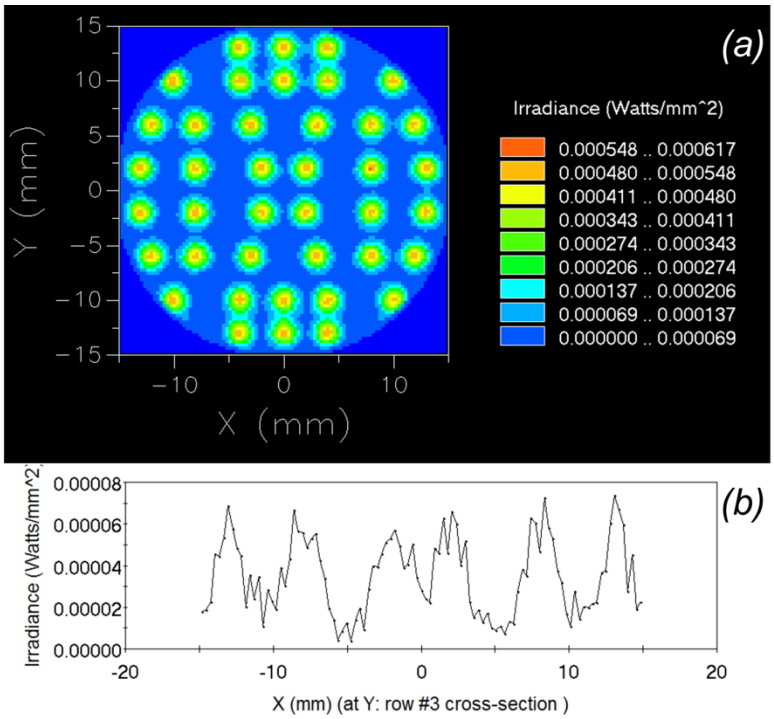

Figure 4.27: *Irradiance at 6 mm distance from the Ambulight LED array in 1 mm of the skin which consisted of a 200 μm thick layer of epidermis and followed by a 800 μm thick layer of dermis.* **a –** *irradiance distribution.* **b –** *1D irradiance cross section along x-axis at the third row of LED form the top (@Y=6 mm).*

This demonstrates that the skin can substantially reduce non-uniformities but if non-uniform areas are far away from each other, the field will still remain highly non-uniform. For the current 4 mm centre to centre average distance between the LEDs with 3.5 mm emission spot size this diffusion is not sufficient to equalise the field.

The following simulations aimed to investigate how much the skin could compensate smaller non-uniformities. A few extra LEDs were added to the second row of the Ambulight LED array; the LEDs became denser in this row. The the LEDs in this row were placed at 2 mm distance from centre to centre with 0.8 mm separation between the edges of the LEDs. The irradiance simulation in the air is shown in ***Figure 4.28***. The emission spot size from eacn LED in the second row overlapped decreasing the fluctuation of the emission. Non-uniformity of illumination in this row was calculated as a percentage difference between the minimal and average irradiance at the irradiance cross-section of the second row (***Figure 4.28***, (b)) and was found to be $non\_uniformity = \frac{0.8-0.6}{0.8} \cdot 100\% = 25\,\%$. 25 % non-uniform illumination is already within an acceptable non-uniformity range (non-uniformity from the conventional PDT lamps is up to 38 %[49]).

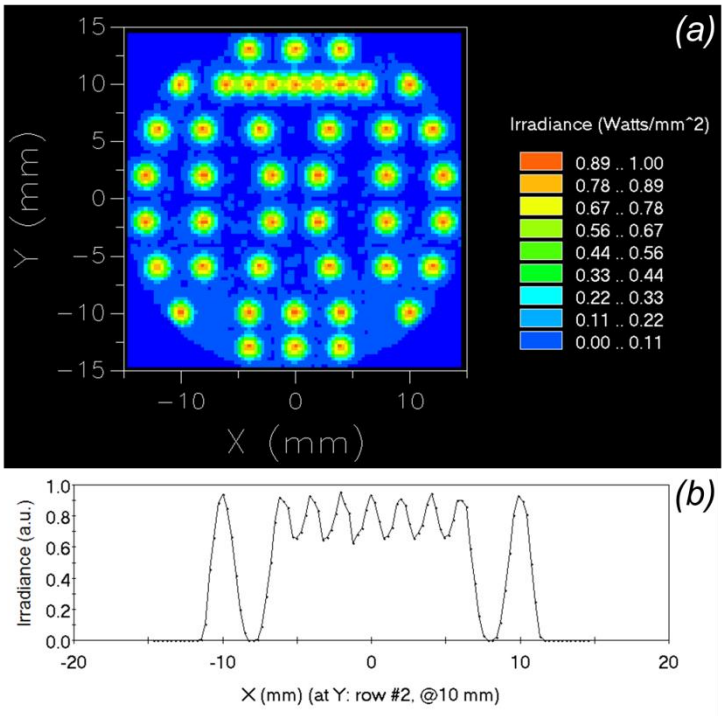

Figure 4.28: *Irradiance at 6 mm distance from the modified Ambulight LED array in air (the LEDs in the second row were placed denser).*

Then the skin was added to the model and the irradiance was simulated at 6 mm distance from the LEDs while light was propagated through 200 μm thick layer of epidermis and 800 μm thick layer of dermis. The irradiance simulations are shown in ***Figure 4.29***. The non-uniformity was calculated in the same way as in the previous paragraph $non\_uniformity = \frac{0.52-0.45}{0.52} \cdot 100\% = 15\ \%$ This means that the non-uniformity was reduced from 25 % in air (***Figure 4.28***) to 15 % in 1 mm of skin at the same distance.

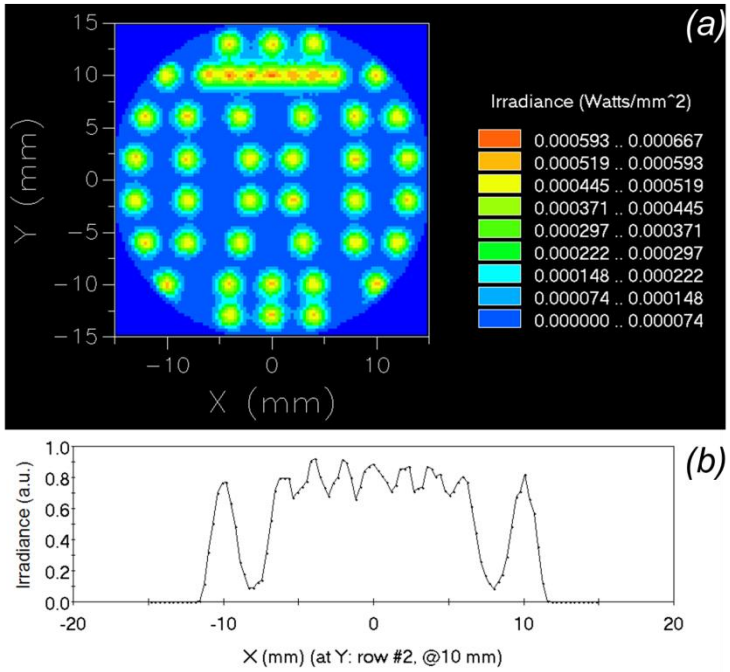

Figure 4.29: *Irradiance at 6 mm distance from the modified Ambulight LED array (the LEDs in the second row were placed denser) in 1 mm of the skin which consisted of a 200 μm thick layer of epidermis and followed by an 800 μm thick layer of dermis.* **a** *– irradiance distribution.* **b** *– 1D irradiance cross section along x-axis at the second row of the LEDs form the top.*

A small separation between the LEDs over 6 mm distance resulted in 25 % non-uniform illumination which is already better compared to the conventional PDT lamps. Light diffusion though a 1 mm thick layer of skin compensated this non-uniform illumination by 10 % bringing the ultimate non-uniformity down to only 15 %. Thin layers of skin such as a 100 μm thick layer of epidermis diffuses non-uniform illumination but can only compensate 4 % of non-uniformities. Diffusion in skin on its own is not sufficient to compensate large fluctuations in the illumination field and will not allow for removing the diffusers from Ambulight PDT devices. However, the design of the device can benefit from the divergence of the emission from each LED in the array if they are placed at sufficient distances and close to each other.

(k) Potential of OLED light sources for a new generation of Ambulight PDT devices

OLEDs are very promising candidates for future Ambulight PDT devices. They are thin, will not require complex PCB and clever design with the diffusers. The technology readiness is already at a substantial level to deliver stable devices in mass production. A test OLED device from a potential supplier was measured and characterised for potential application in Ambulight

PDT. The power measurements and directional emission can be found in Appendix XXII. The emission is very close to Lambertian. The emission spectrum is quite broad, half width at half maximum (HWHM) is from 590 nm to 675 nm with peak wavelength at 612 nm which would be perfectly suited for application in PDT treatment (in the guidance for PDT the spectrum of the light sources should be within 570-670 nm[7,9,51]). At 370 mA driving current the irradiance was 11.7 mW/cm^2 which, if necessary, leaves enough room to compensate for the irradiance to take into account the spectral difference in this OLED compared to Kingbright Hyper Red. Kingbright Hyper Red is better centred to PpIX absorption so in order to keep the same treatment protocol as in the current Ambulight PDT irradiance in the test OLED would have to be higher; however, the decision upon treatment protocols and the irradiance levels is always a call for biomedical physics experts.

The test OLED model was created in FRED based on the measured spectrum, power and directional emission from the test devices. The irradiance at the surface of the skin is shown in ***Figure 4.30***. It is very uniform in the central area; the intensity drops down beyond the circle with a diameter equal to 16 mm towards the edges of the LED because of Lambertian emission. So the size of the treated area should be compensated to take into account the intensity distribution.

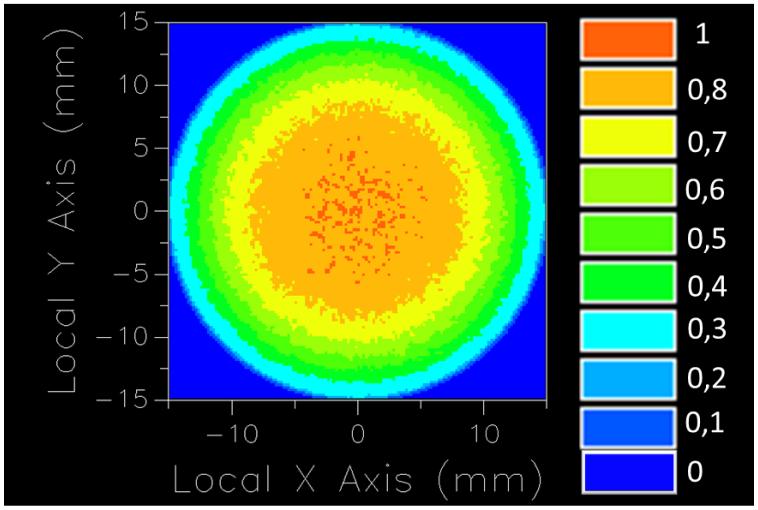

Figure 4.30: *Simulations of OLED irradiance at the surface of the skin as an alternative light source for next generation of Ambulight PDT devices.*

4.4 Discussion

4.4.1 Can treatment devices benefit from forward scattering in skin and structured illumination?

One interesting observation was made during the simulations and that is that the probability of rays backscattering and escaping from the skin is much higher for large incidence angles (***Figure 4.31***). Conversely if the incidence angles are normal to the skin the rays are much more likely to propagate further in the skin. This is obvious due to the forward-scattering nature of the skin. The question is how much more light is it possible to deliver when the incidence is structured to normal incidence. Our group achieved less than 15° directional emission from OLED devices by introducing gratings which make the emission close to laser-like[52]. The investigation of the potential of such structured OLED devices will be described in the next chapter.

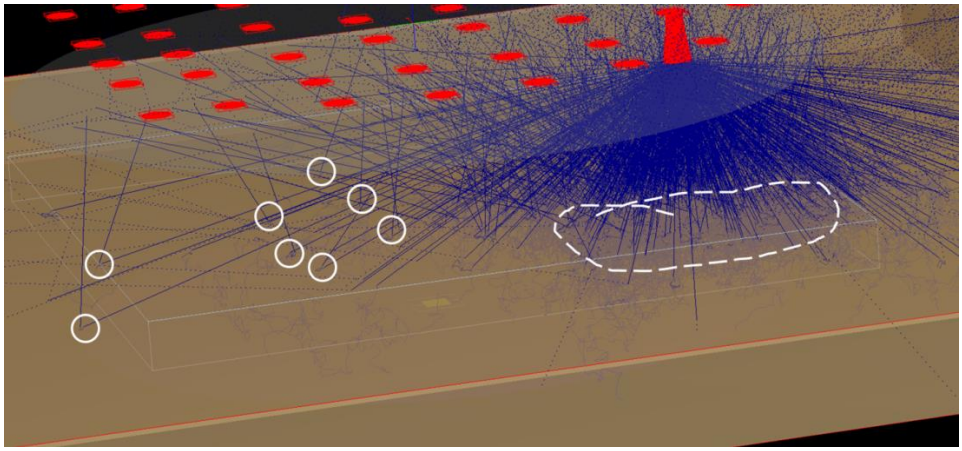

Figure 4.31: *Modelling of light propagation through layered skin. White circles indicate rays which penetrate very small distances and quickly backscatter from the skin. White dashed line highlights the region of smaller incidence angles; in this region there is less backscattering and more forward scattering which suggests that the structuring of light sources could favour better light penetration for PDT treatment*

.

4.5 Conclusions

The optical apparatus developed in this chapter enabled modelling and measuring of light transport and optical properties of tissue phantoms. The modelling approach based on commercial software allowed for flexibility in manipulating different parameters of optical systems to improve the design and learn about light transport in different tissue types. In addition to similar optical properties, two types of phantom gel and solid had textures close to brain and skin which enabled testing the proof of concept devices. This modelling approach was used to optimise current ambulatory devices Ambulight PDT. Although Ambulight PDT already has good uniformity, the design could be more efficient. The modelling demonstrated that natural diffusion processes in the skin do not fully compensate non-uniform illumination from an LED array such as in the Ambulight PDT device. For instance, if the distance between non-uniform illumination spots is smaller than the size of the spots, then at 1 mm depth in skin the diffusion of light can lead to smoothing the non-uniform illumination for only 10-15 %. Therefore it is necessary to keep at least one diffuser after the LED array. Though, it is possible to improve the illumination field of the device by removing one diffuser from the current device (there are two in the current model) and increase the spacer distance between the diffuser and the LED array. .

Another improvement would be to shorten the distance between the LEDs to 2 mm from the current 4 mm which will result in 25% non-uniformity without any diffusers; 1 mm of skin will compensate it to 15%. In this design the diffuser could be removed from the device, but it will then be necessary to double the number of LEDs which on the other hand could be operated at lower current keeping the battery consumption at the same level. This would be an alternative solution for the design if the cost of placing the diffusers were larger than the cost of increasing the number of LEDs in the device – an unlikely scenario.

Up to four LEDs can be removed from the array without a significant change to the average irradiance, and then the irradiance drops down below 7 mW/cm^2. Care should be taken about the position, as by removing LEDs form the least dense areas or from the edges (#4, #9, #13, #16, #25, #27) there was a dramatic drop in minimum irradiance. So LEDs in the array should remain evenly spaced with taking care of good coverage at the edges. Drop of the intensities at the edges when LEDs are removed from these locations can be particularly dangerous as there is a possibility of misalignment of the device with respect to the treated area; this could lead to poor tumour response at the margins.

The test OLEDs were tested for potential application in future ambulatory devices and an optical model was developed based on the measured characteristics. According to the modelling, the OLED had less than 5 % non-uniformity of the illumination. However, due to Lambertian emission the size of the OLED has to be substantially bigger than the treated area as the intensity rapidly drops towards the edges. For instance for an area equal to 2 cm in diameter the OLED has to be at least 3.5 cm in diameter. However, being thin and flexible they would allow treatment of areas with large curvatures. This in addition to excellent light output makes them good candidates for light sources for Ambulatory PDT.

4.6 References

1. Hetzel F, Brahmavar S, Chen Q, et al. Photodynamic Therapy Dosimetry. *AAPM*. 2005;Report(88):30.

2. Wang KKH, Finlay JC, Busch TM, Hahn SM, Zhu TC. Explicit dosimetry for photodynamic therapy: Macroscopic singlet oxygen modeling. *J Biophotonics*. 2010;3(5):304-318. doi:10.1002/jbio.200900101.

3. Zhu TC, Kim MM, Busch TM. In-vivo singlet oxygen threshold doses for PDT Timothy. *Photonics Lasers Med*. 2015;4(1):59-71. doi:10.1515/plm-2014-0037.In-vivo.

4. Ibbotson SH. Adverse effects of topical photodynamic therapy. *Photodermatol Photoimmunol Photomed*. 2011;27(3):116-130. doi:10.1111/j.1600-0781.2010.00560.x.

5. Giuseppe Argenziano. Vascular Structures in Skin Tumors. *Arch Dermtol*. 2004;140:1485-189.

6. Wilson B, Tuchin V. Advances in biophotonics. *NATO Sci Ser Ser I Life Behav Sci*. 2005;369:283.

7. Zhu TC, Bonnerup C, Colussi VC, et al. Absolute calibration of optical power for PDT: report of AAPM TG140. *Med Phys*. 2013;40(8):081501. doi:10.1118/1.4813897.

8. Zhu TC, Liu B, Penjweini R. Study of tissue oxygen supply rate in a macroscopic photodynamic therapy singlet oxygen model. *J Biomed Opt*. 2015;20(3):038001. doi:10.1117/1.JBO.20.3.038001.

9. Morton C a, McKenna KE, Rhodes LE. Guidelines for topical photodynamic therapy: update. *Br J Dermatol*. 2008;159(6):1245-1266. doi:10.1111/j.1365-2133.2008.08882.x.

10. Moseley H, Allen JW, Ibbotson S, et al. Ambulatory photodynamic therapy: a new concept in delivering photodynamic therapy. *Br J Dermatol*. 2006;154(4):747-750. doi:10.1111/j.1365-2133.2006.07145.x.

11. Attili SK, Lesar A, McNeill A, et al. An open pilot study of ambulatory photodynamic therapy using a wearable low-irradiance organic light-emitting diode light source in the treatment of nonmelanoma skin cancer. *Br J Dermatol*. 2009;161(1):170-173. doi:10.1111/j.1365-2133.2009.09096.x.

12. Ibbotson SH. An overview of topical photodynamic therapy in dermatology. *Photodiagnosis Photodyn Ther*. 2010;7(1):16-23. doi:10.1016/j.pdpdt.2009.12.001.

13. Ibbotson SH, Ferguson J. Ambulatory photodynamic therapy using low irradiance inorganic light-emitting diodes for the treatment of non-melanoma skin cancer: An open study. *Photodermatol Photoimmunol Photomed*. 2012;28(5):235-239. doi:10.1111/j.1600-0781.2012.00681.x.

14. Jacques SL, Prahl SA. Some biological chromophores. *ECE532 Biomed Opt Oregon Grad Inst*. 1998. http://omlc.org/classroom/ece532/class3/chromophores.html.

15. Jacques SL, Prahl SA. Definition and units of absorption coefficient μa [cm-1]. *ECE532 Biomed Opt Oregon Grad Inst*. 1998. http://omlc.org/classroom/ece532/class3/muadefinition.html.

16. Jacques SL. Optical Properties of Biological Tissues: A Review. *Phys Med Biol*. 2013;58(11):R37-R61. doi:10.1088/0031-9155/58/11/R37.

17. Jacques SL, Prahl S. Absorption spectra for biological tissues. *ECE532 Biomed Opt Oregon Grad Inst*. 1998. http://omlc.org/classroom/ece532/class3/muaspectra.html.

18. Jacques SL, Prahl SA. Some biological scatterers. *ECE532 Biomed Opt Oregon Grad Inst*. 1998. http://omlc.org/classroom/ece532/class3/scatterers.html.

19. Jacques SL, Prahl SA. Definition and units of scattering coefficient. *ECE532 Biomed Opt Oregon Grad Inst*. 1998. http://omlc.org/classroom/ece532/class3/musdefinition.html.

20. Jacques SL, Prahl SA. Henyey-Greenstein scattering function. *ECE532 Biomed Opt Oregon Grad Inst*. 1998. http://omlc.org/classroom/ece532/class3/hg.html.

21. Popp J, Tuchin V V, Chiou A, Heinemann S. *Handbook of Biophotonics: Volume 1: Basics and Techniques*. Wiley-VCH; 2011. http://eu.wiley.com/WileyCDA/WileyTitle/productCd-3527410473.html.

22. Url S, Archive TJ, Archive T. The Monte Carlo Methd. *J Am Stat Assoc*. 1949;44(247):335-341.

23. Wilson B. A Monte Carlo model for the absorption and flux distributions of light in tissue. *Med Phys*. 1983;10(6). doi:http://dx.doi.org/10.1118/1.595361.

24. Wilson BC. A Monte Carlo model for the absorption and flux distributions of light in tissue. *Med Phys*. 1983;10(6):824-830.

25. PRAHL SA. Light transport in tissue by 3D Monte Carlo: influence of boundary voxelization. *Comput Methods Programs Biomed*. 1988;89(1). doi:10.1016/j.cmpb.2007.10.008.

26. Prahl S, Keijzer M, Jacques S, Welch A. A Monte Carlo model of light propagation in tissue. *Dosim Laser Radiat Med Biol*. 1989;5(5):102-111. http://citeseerx.ist.psu.edu/viewdoc/download?doi=10.1.1.132.5731&rep=rep1&type=pdf. Accessed October 11, 2011.

27. PRAHL SA, Jacques SL. Monte carlo simulation. *omlc*. 2007. http://omlc.ogi.edu/software/mc/. Accessed May 10, 2012.

28. Meglinski I V, Matcher SJ. Quantitative assessment of skin layers absorption and skin reflectance spectra simulation in the visible and near-infrared spectral regions. *Physiol Meas*. 2002;23(4):741-753. http://www.ncbi.nlm.nih.gov/pubmed/12450273.

29. Giardinia ME, Locontet L, Gemetti GGA, et al. Simple instrument for the characterization of diffuse reflectance. *Library (Lond)*. 1998;3568(September):59-63.

30. Morini A. SIMULAZIONE E STUDIO SPERIMENTALE DI SPETTROSCOPIA INFRAROSSA IN TESSUTI Introduzione. 2004.

31. Pogue BW, Patterson MS. Review of tissue simulating phantoms for optical spectroscopy, imaging and dosimetry. *J Biomed Opt*. 2011;11(4):041102. doi:10.1117/1.2335429.

32. Hwang J, Ramella-Roman JC, Nordstrom R. Introduction: Feature Issue on Phantoms for the Performance Evaluation and Validation of Optical Medical Imaging Devices. *Biomed Opt Express*. 2012;3(6):1399. doi:10.1364/BOE.3.001399.

33. Bays R, Wagnières G, Robert D, et al. Three-dimensional optical phantom and its application in photodynamic therapy. *Lasers Surg Med*. 1997;21(3):227-234. http://www.ncbi.nlm.nih.gov/pubmed/9291079.

34. Kanick SC, Davis SC, Zhao Y, et al. Dual-channel red/blue fluorescence dosimetry with broadband reflectance spectroscopic correction measures protoporphyrin IX production during photodynamic therapy of actinic keratosis. *J Biomed Opt*. 2014;19:075002. doi:10.1117/1.JBO.19.7.075002.

35. Kim A, Roy M, Dadani F, Wilson BC. A fiberoptic reflectance probe with multiple source-collector separations to increase the dynamic range of derived tissue optical absorption and scattering coefficients. *Opt Express*. 2010;18(6):5580-5594. http://www.ncbi.nlm.nih.gov/pubmed/20389574.

36. Loconte L. CORSO DI LAUREA IN FISICA TECNICHE OTTICHE PER L ' INDAGINE NON INVASIVA DI SISTEMI BIOLOGICI Relatore interno : (416463).

37. PhotonEngineering. FRED Help documentation. Materials - Scripted Volume Scatter, Application Notes.

38. Toh PS, Giardini ME. Can We Power Optically a Robot or a Radio Transmitter in a Tissue Phantom ? Candidate Number : 2013.

39. ALTANA. LAPONITE-RD. 2015. http://www.byk.com/en/additives/additives-by-name/laponite-rd.php.

40. Kou L, Labrie D, Chylek P. Refractive indices of water and ice in the 065- to 25-μm spectral range. *Appl Opt*. 1993;32(19):3531. doi:10.1364/AO.32.003531.

41. Neumann BS. The Rheological Properties of Dispersions of Laponite, a Synthetic Hectorite-Like Clay, in Electrolyte Solutions. *Clay Miner*. 1971;9(2):231-243. doi:10.1180/claymin.1971.009.2.08.

42. Cenens J, Schoonheydt R a. Visible Spectroscopy of Methylene Blue on Hectorite, Laponite B, and Barasym in Aqueous Suspension. *Clays Clay Miner*. 1988;36(3):214-224. doi:10.1346/CCMN.1988.0360302.

43. Ravi Kumar NVN, Muralidhar K, Joshi YM. On the refractive index of ageing dispersions of Laponite. *Appl Clay Sci*. 2008;42(1-2):326-330. doi:10.1016/j.clay.2007.12.010.

44. Tiwari MM. In vivo miniature robots for natural orifice surgery: State of the art and future perspectives. *World J Gastrointest Surg*. 2010;2(6):217. doi:10.4240/wjgs.v2.i6.217.

45. Büchi R, Rohrer D, Schmid C. A fully autonomous mobile mini-robot. In: *Proceedings of SPIE Photonics East '95. Microrobotics and Micromachanical Systems Symposium Vol. 2593, Philadelphia (PA)*.; 1995. https://www.zhaw.ch/en/research/personen-publikationen-projekte/detailansicht-publikation/publikation/209/.

46. Wyszecki, Günter, Stiles. *Color Science - Concepts and Methods, Quantitative Data and Formulae*. 2nd ed. Wiley-Interscience; 2000.

47. Deane J. *Contributions to Color Science*. Washington D.C. 20234: National Bureau of Standards NBS Special Publication 545; 1979.

48. Bolognia JL, Schaffer J V., Duncan KO, Ko CJ. *Dermatology Essentials*. Elsevier Saunders; 2014. https://books.google.de/books?id=9cY0AwAAQBAJ&source=gbs_navlinks_s.

49. Moseley H. Light distribution and calibration of commercial PDT LED arrays. *Photochem Photobiol Sci*. 2005;4(11):911-914. doi:10.1039/b507325a.

50. McGrath JA, Eady RA, Pope FM. *Rook's Textbook of Dermatology*. 7th ed. Blackwell Publishing; 2004.

51. Braathen LR, Szeimies R-M, Basset-Seguin N, et al. Guidelines on the use of photodynamic therapy for nonmelanoma skin cancer: an international consensus. International Society for Photodynamic Therapy in Dermatology, 2005. *J Am Acad Dermatol*. 2007;56:125-143. doi:10.1016/j.jaad.2006.06.006.

52. Zhang S, Turnbull GA, Samuel IDW. Highly Directional Emission and Beam Steering from Organic Light-Emitting Diodes with a Substrate Diffractive Optical Element. *Adv Opt Mater*. 2014;2(4):343-347. doi:10.1002/adom.201300441.

Chapter 5

The potential of structured light sources for PDT

There is strong shadow where there is much light.

— Johann Wolfgang von Goethe,
Götz von Berlichingen, Act I (1773)

5.1 Introduction

The three previous chapters covered the background of PDT treatment, investigated the metabolism of the drug and the development of low irradiance wearable light sources. Currently most non-laser based PDT light sources have a wide angle emission, close to Lambertian. Much attention was drawn to pulsing light, using coherent light or multiple wavelengths. This chapter presents a theoretical and an experimental investigation on how structured emission could improve light transmission in skin. It will explore the hypothesis that natural forward scattering processes in skin could provide better light transmission from collimated light sources compared to the wide emitting angles light sources.

5.1.1 Current attempts to structure light for optimising light penetration in devices for PDT

There have been many attempts to improve PDT outcomes by optimising light delivery. It is clear that red light penetrates deeper than blue which is preferential for treating deeper lesions; blue light is only used for treating superficial lesions such as AK[1]. Also it was established that different irradiances play a role in tumour response; lower irradiances give a better outcome[2,3]. The situation is less clear about coherence and pulsed regimes.

There is a report which suggests that when coherent laser light penetrates through tissue it does not completely lose its coherence as would be expected in highly scattering tissue; the

coherence is weakened but still present[4]. After a few millimetres in tissue coherent light forms speckles which supposedly improves biological responses to the treatment light[4]. In cell studies for PDT there is a report which shows that non-coherent compared to coherent light sources resulted in better phototoxic effect in L9 cells cultures with a photosensitizer[5]. Also there is a clinical repot which did not show any difference in PDT treatment outcomes using coherent compared to non-coherent light sources[6].

The situation is similar for pulsed light. Some reports show evidence that a pulsed regime is less painful and results in complete lesion response[7]. But others report that continuous wave light sources give better outcomes[8]. There is a report which suggests that sequential pulses of blue and red wavelength give the best outcome[9].

The previous chapter gave a hint that structuring the emission could be beneficial for improving the penetration of the treatment light and set a scene to investigate the potential improvements of light propagation from directional light sources compared to broad Lambertian emitters. Forward scattering in skin suggests that if light is incident at normal angles it will penetrate further. Conversely there should be a bigger chance of light backscattering from the skin if the angle of incidence is large. It was demonstrated in our group that it is possible to achieve a narrow directional surface emission from OLEDs light sources[10] which means that the incident angles from such light sources can be very small, less than 15°. If the hypothesis that directionality could provide substantial improvement in light propagation in skin is true, it will make directional OLEDs excellent candidates for a new generation of structured light sources for PDT treatment.

The hypothesis was first evaluated by modelling and this was followed an experimental investigation. Although phantoms have representative properties of tissue and are commonly used to test devices, they do not fully mimic the complex layered structure of skin. In order to demonstrate clinically significant differences in the performance of one light source compared to the other, the results have to be obtained from real skin samples. One of the possible options which were considered for the experiment was chicken skin; however it is too thin, at approximately 0.5 mm, and would not allow for depth-dependent measurements. Porcine skin is thick enough for the measurements and is the closest analogue to human skin.

Pig skin has been commonly used by pharmaceutical, biomedical and aesthetics communities. Goettingen mini pig skin was used in a drug study for pre-clinical assessment of Ameluz gel[11]. Another drug study used pig skin to demonstrate improvements in PpIX formation by applying a microneedle array for better penetration of ALA-precursor[12]. Pig skin was used for optical clearing for tattoo removal[13], for sun screen lotion studies[14], for measuring a change in

temperature induced by IR radiation for wound healing[15,16], and for wireless power transmission of millimetre wavelength[17]. So measurement results on porcine skin have credibility in the medical and bio-engineering community. That is why it was identified as a good candidate for the measurements.

For the purpose of modelling and measurements in this chapter, the data on optical properties and transmission of porcine skin were investigated in the literature. A small list of optical properties of porcine skin is reported by S. Chung et al (2011)[18]. Results on optical measurements in porcine skin were only available from few groups where they used different skin (piglet and pigs), different wavelength ranges and set ups. The results varied between groups: and the groups even reported big variations in the properties within their own measurements.

Du et al[19] measured optical properties in the range of 700 nm to 1500 nm using an integrating sphere for diffuse reflectance; a spatial filtering set up for measuring collimated transmittance; and reverse Monte Carlo calculations to extract the measured optical properties. They also studied the cellular change by microscopy imaging when the samples were stored at room temperature and in ice buckets. There was moderate change in optical properties stored at room temperatures compared to stable measurements when the samples were stored in ice buckets over 30 hours. They explain the change of optical properties due to cellular rupture and loss of water. The same results are reported by S. Firdous et al (2005)[20]. Scattering and absorption coefficients were lower for dry samples.

Beek et al[21] measured optical properties of piglet skin in the range from 630 to 1064 nm. They used two integrating spheres with the sample in between the spheres, one integrating sphere measured diffuse reflectance and the other transmittance at 630, 632.8, 790, 850 and 1064 nm. An inverse adding–doubling algorithm was used for extracting properties from the measurements. They report reproducible, but hugely different results when different skin samples or slightly different lasers were used (argon dye pumped laser at 630 nm compared to HeNe laser at 632.8 nm).

In this chapter optical properties were taken for porcine skin from Ma et al[22] as they reported the data for the most appealing wavelength for PDT, 633 nm and adult pigs' skin. They used an integrating sphere for measuring diffuse reflectance and collimated transmittance; and inverse Monte Carlo calculations. For the study in this chapter there was no interest in measuring absolute power transmission or reflectance of pork skin, neither was there intention to study optical properties (although regression Monte Carlo modelling was used to adjust the initial properties closer to the real values).

This chapter was aiming to model and build an experiment to investigate whether there was a difference between light transmission of directional light sources and wide angle light sources through the skin which could be useful to the medical community.

5.2 Methods

5.2.1 Optical modelling

The same modelling approach was used as described in the previous chapter. The model was developed in FRED software and the optical properties of pork skin were taken from the literature.

5.2.2 Fabrication of organic films

Organic films were fabricated by Dr Ashu Bansal and Dr Guohua Xie. . Two identical organic films were fabricated on 25 mm x 25 mm glass substrates. One of the films had 5 gratings of 3 mm x 3 mm size. The gratings provided directional emission. The other film was made of the same emitting material but on a substrate without the gratings. Gratings were nanoimprinted on the substrates by UV-Nanoimprint lithography (UV-NIL) process. The Super Yellow polymer was spin-coated from a Chlorobenzene solution on both substrates, with and without the gratings. The solution concentration was 7.5 mg/ml. The spin-coating speed was 2000 rpm. The thicknesses of the films was 100 nm.

UV-Nanoimprint lithography (UV-NIL)[23] is used to nanopatterned films using a perfluoropolyether soft stamp. The soft stamps (MD700 (Solvay)) were cast on silicon master gratings (patterned by e-beam lithography and reactive ion etching), and hardened by ultraviolet curing. Before transferring a thick layer of perfluoropolyether(PFPE)-urethane dimethacrylate (Fluorolink MD700) as a compliant material onto a clean and bare silicon substrate, an adhesive layer (3-Trimethoxysilyl)propyl acrylate (Sigma-Aldrich) was spin-coated directly onto the glass substrate after oxygen plasma treatment. Another layer of MD700 was spin-coated on the glass substrate after UV exposure for 220 seconds. Through the second UV exposure, the 1D grating patterns with a period of 350 nm on a Si master were transferred onto this glass substrate

(daughter stamp) by adding some droplets of perfluoroalkylpolyether (Fluorolink MD500) mixed with 1-2% of the photo initiator DURACOUR (Sigma-Aldrich).

The daughter stamp was used as a mould for replicating the grating structures onto a photoresist (Micro Resist Technology UVCur06) which was spin-coated atop another bare glass substrate with an additional adhesion promoter (Micro Resist Technology mr-APS1). The UV nanoimprint lithography (UV-NIL) processes were performed using an EVG®620 automated mask alignment system.

The films had a broad emission spectrum with from 520 to 700 nm[24]. The directional emission from the films was measured by an in-house built set up for angular dependent measurement. The film was fixed in a holder and an optical fibre connected to a photodetector was moved with an angle step to measure the angular emission. Full width at half maximum (FWHM) of the directional emission of the film with the grating was found to be less than 15°, the same as was reported for the directional OLED devices[10]. The film without the grating had Lambertian emission. The films were stable; there was no drop in the intensity during the experiment.

5.2.3 Porcine skin samples preparation

Fresh pork skin was kindly provided by Minick of St Andrews butchers shop. Dehaired by hot the water method[25] skin samples were collected post-mortem. The skin had to stay fresh as freezing ruptures the cells, the content leaks out and this results in change to optical properties. Unfortunately, the only option to dissect the skin was by using a surgical scalpel and trying to achieve dissections as uniform as possible.

A special protocol was developed to dissect the skin and protect it from drying. Fresh skin tissue was collected from the butchers shop early in the morning. The samples were prepared and the measurements taken during 8-10 hours on the same day There was no storage protocol followed. The samples were disposed of after the experiment. The skin was handled at the ambient temperature of an optical laboratory at the Department. The skin was kept covered all the time in clean kitchen film between the manipulations. The skin was dissected in 0.5, 1.0, 1.5, 2.0, 2.5, 3.0, 3.5 mm layers parallel to the skin surface (to keep the layered structure). The thickness of the skin was measured by placing the skin dissections between the legs of a digital calliper and sliding the calliper along the sample without introducing

any pressure or stretch. An averaging protocol for the transmission measurements was used to compensate for any non-uniformities in the skin and tolerances of the dissections.

It is a known fact that skin has variation in optical properties among subjects, including which side of the animal is chosen, *in-vivo* or *ex-vivo* samples*;* also any skin processing such as dehairing or exposing postmortem skin samples to air changes the skin properties. In order to keep the variation to a minimum, small slices of the skin of the same animal from the same side of the animal were dissected for one experiment.

In order to provide stable measurements the change in optical properties during the time of the experiment was studied. The samples were exposed to air for a short period of time for one measurement (less than a minute) and covered in kitchen film between the measurements; even with this protocol the optical properties were changing as the skin was drying out.

A special protocol was developed to protect dissected porcine skin samples from drying and losing thier optical properties. The skin was placed in AQUASONIC® 100 ultrasound gel which is used for medical ultrasound scans. After one dissection had been finished it was covered with the gel and sandwiched in two standard 1 mm thick microscope glass slides (***Figure 5.1***). Care was taken to avoid formation of air bubbles. Nonetheless, any present bubbles were visible on the camera during the imaging of light transmission; and this area was avoided.

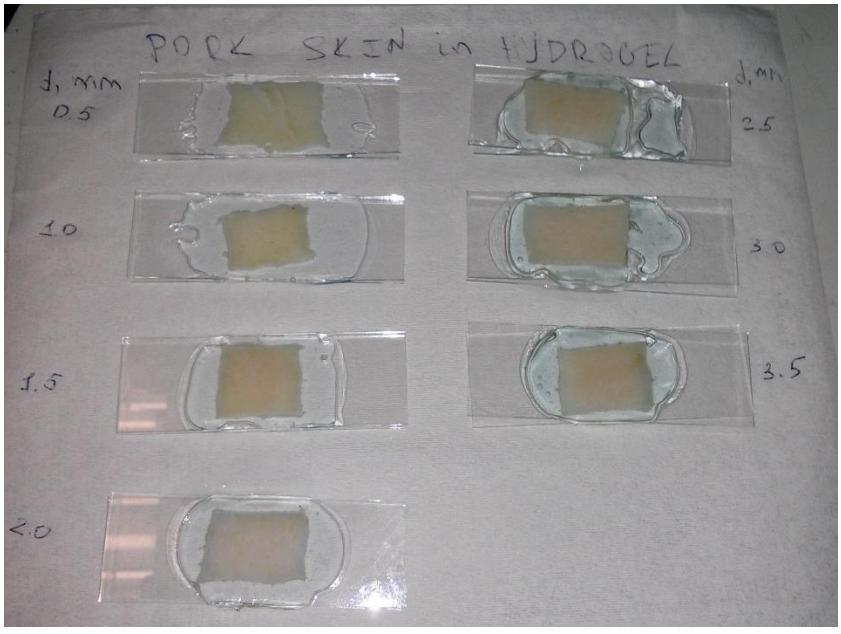

Figure 5.1: *Skin samples in hydrogel*

5.2.4 Image analysis

The transmission images were analysed in Matlab. It was used to outline the emission profiles of the light sources and use their contours for the integration of the intensity in the transmission measurements; and perform any other manipulations with the data such as averaging, removing autofluorescence background and normalising the transmission.

5.3 Results

5.3.1 Theoretical investigation: how much can directional emission improve light propagation in skin?

The optical model for simulating depth dependent light transmission of structured illumination though porcine skin is shown in ***Figure 5.2***. It was very straightforward and consisted of a surface emitting light source, a layer of porcine skin and an irradiance detector. The optical properties of porcine skin were taken from the Handbook of Biomedical optics (Edited by David A. Boas, 2011), p. 78, Tabl. 5.1 “Optical Properties of Human and animal skin and subcutaneous tissue measured in vivo and in vitro”[18], from the group of Ma et. all, the original work was published in [22]. They were as follows: $n = 1.35$, $\mu_s = 5.8\, mm^{-1}$, $g = 0.72$, $\mu_a = 0.07\, mm^{-1}$ for 633 nm wavelength. The thicknesses of the skin were 1.0, 1.5, 2.0, 2.5 mm which are the most relevant thicknesses for PDT treatment.

The light source had properties equivalent to the intended properties of the light emitting organic films and lasers. However, the simulations were performed for one wavelength and perfectly collimated light. The consideration for the wavelength included the consideration for the emission spectrum of the organic films, the laser, the availability of reported optical properties of porcine skin and the relevance to PDT treatment. The emission spectrum of the organic semiconductor films was wide from 530 to 700 nm. The intended laser was a HeNe laser with a spectral line at 632.8 nm. The reported optical properties of the porcine skin were measured at 633 nm. This wavelength is the most relevant for PDT treatment and was chosen for the modelling. In addition there were other choices for light sources at this wavelength or very close to it.

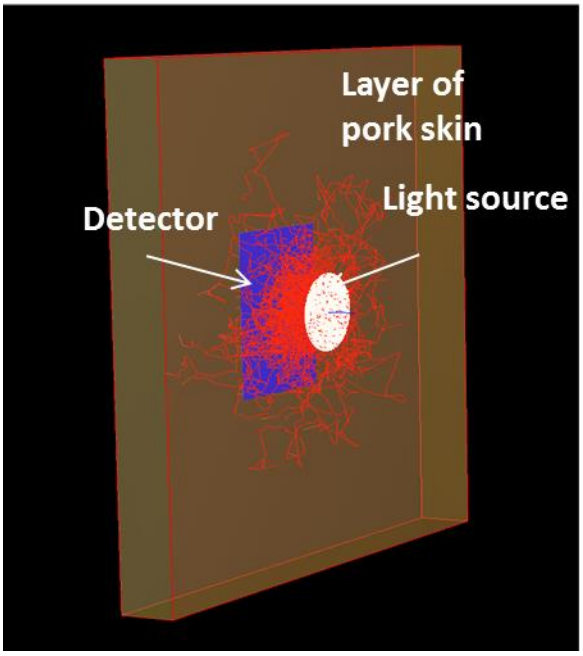

Figure 5.2: *Modelling of light transmission trough porcine skin*

One of the light sources had collimated emission and another one had Lambertian emission. The surface of the skin in the optical model was perfectly flat. The other parameters for both of them were identical. The light sources were 3 mm in diameter and were placed at a small gap equal to 1 μm from the skin for the purpose of modelling and the power was set to 1 W (the results were normalised so the actual power was not important for this simulation). The transmitted power was measured at an irradiance detector with the diameter equal to 2 mm. The detector was smaller than the light source to avoid arguable results at the edges; only the central area was used for the comparison where the intensity profile of the two light sources does not change much but only the directionality of emission is different. The results were normalised to the input power at the front side of the skin sample (***Figure 5.3***).

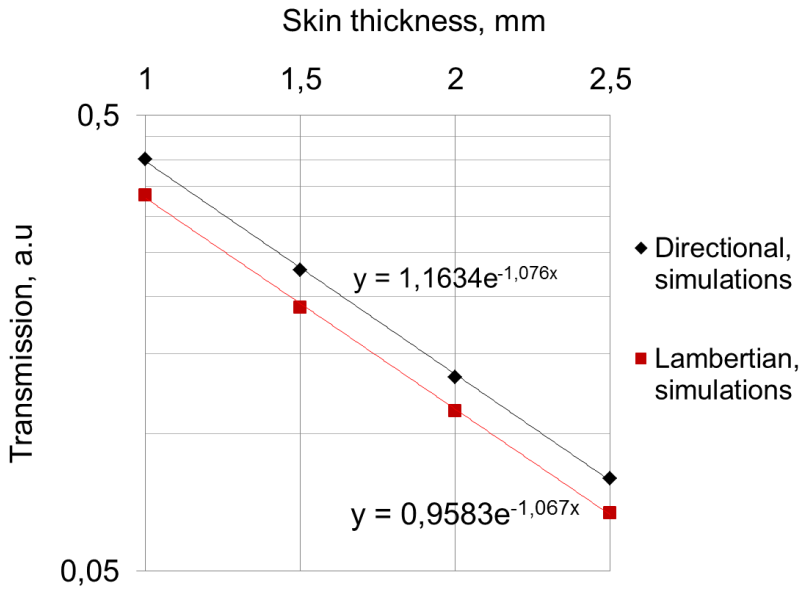

Figure 5.3: *Simulation results of light transmission in porcine skin from directional and Lambertian emittance light sources.*

The results of the modelling showed more than 10 % improvement in light transmission for 633 nm wavelength through the porcine skin from the directional light sources. This gave the motivation to proceed with the measurements.

5.3.2 In-vitro transmission measurements of structured light from organic light emitting films through porcine skin

The first experimental set up was built to study the transmission of light emitted by the organic films. The emission from one of the organic films was structured by the grating to provide narrow angle emission. The other film was made of the same active material but without the gratings. The films were encapsulated to prevent degradation in air. The films were pumped using a 393 nm Picoquant laser with a stripe laser profile driven by a PDL800 laser driver. The beam was expanded using a defocusing lens to provide a larger beam spot for the excitation; the larger study area would give better accuracy during the image analysis. The pump beam was spatially filtered through an aperture to pump only the area corresponding to the size of the grating. The area outside of the grating was also emissive. The active material was spin-coated on the whole substrate. The gratings were fabricated only on five small 3x3 mm patches on the substrate. So the whole substrate was emissive, but only those five areas with the gratings had

directional emission, the rest of the area had Lambertian emission. The pumping of this area (the area outside of the gratings with Lambertian emission) was avoided to prevent wide angle emission from the area outside the grating adding up to the directional emission from the area with the grating. That would reduce the directionality of the emission from the films with the gratings and potentially would make the expected improvements in transmission less distinguishable. A monochromatic Lumenera LM075 CCD camera with a wide angle TV lens and adjustable focal length was used for the measurements. The emission from the films was imaged before and after each experiment to ensure that the films did not degrade. A 530 nm long pass filter was used to cut off the excitation and was placed before the camera lens. The measurement set up is shown on ***Figure 5.4***.

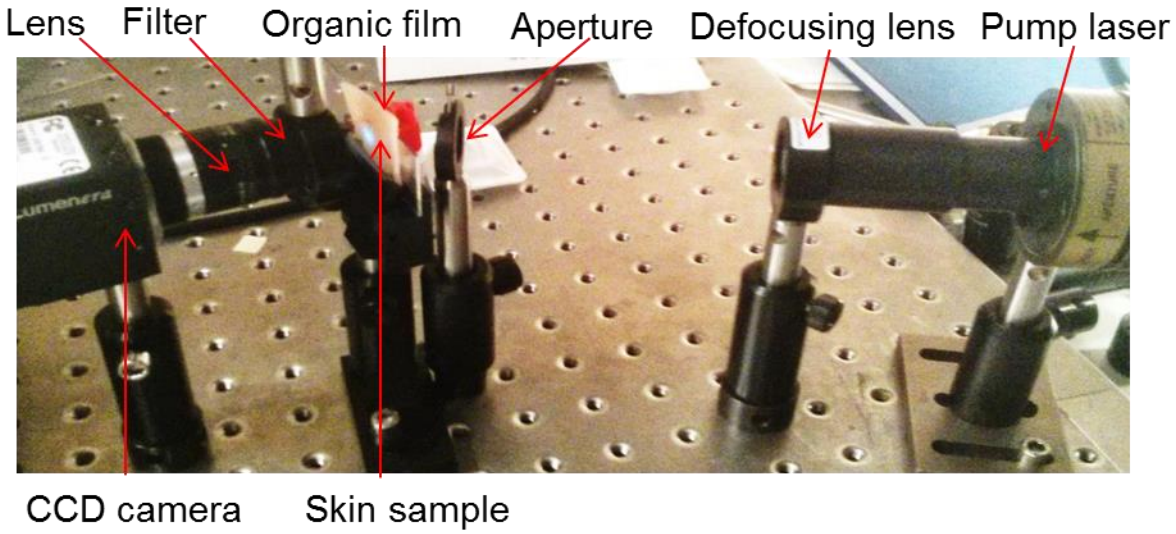

Figure 5.4: *Measurements set up using organic films. The camera with a M118FM08 lens with an adjustable aperture and a focal length was on one optical axis with the filter, the sample plane and the organic film. The laser path was incident under a small angle on the organic films to avoid the lens of the camera. The excitation angle for the organic films was not critical in this experiment. The laser profile was diagnosed once when the camera was placed on one axis with the laser and then for the rest of the measurements the camera was moved to the axis of the films. The distance between the organic film and the camera lens was approximately 40 mm; the length of the camera lens was 27 mm. The diameter of the optics used in the set up was 25 mm; the viewing angle of the lens was 50.8 x 38.6°; the lens aperture was set to 1.4. Defocusing lens in the laser path was used to expand the beam to excite the whole area of the grating in the directional organic light emitting film. The aperture in the laser path was used to match the size of the pump beam to the size of the grating.*

The laser profile and the calibration of the pixel size of the camera are shown in ***Figure 5.5***.

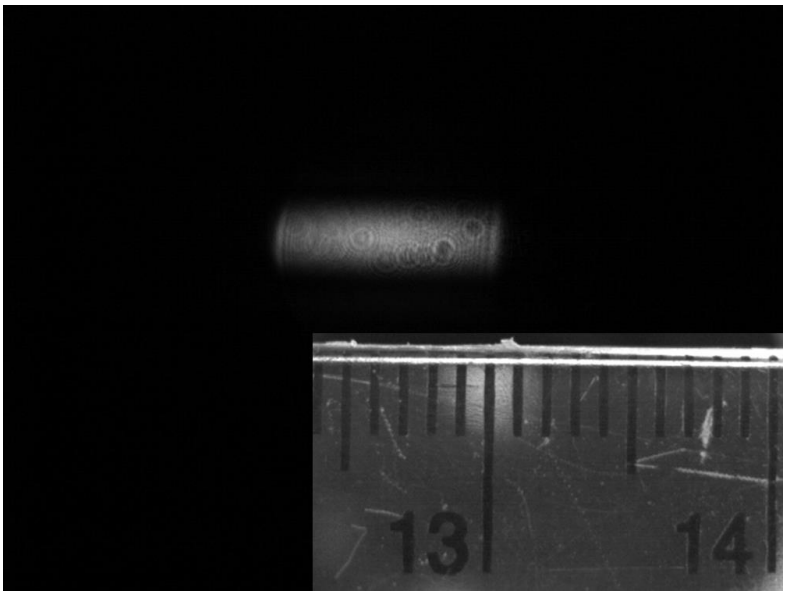

Figure 5.5: *An image of the pump laser beam profile at the sample plane with fully open aperture. The long pass filter was removed from the set up and the camera was placed on one optical axis with the laser path. The camera was moved back to the sample plane axis and the ruler at the sample plane was imaged to calibrate the size of the pixel at the working distance.*

The organic light emitting films were placed after the aperture. The skin samples were put in contact with the organic films. In the first experiment when the skin was exposed to air, the skin was placed directly on the glass substrate of the film. The skin was greasy and sticky which formed a good contact with the film substrate; there was no need to use any additional fixation. The films were encapsulated so the active layer stayed protected from any contamination. The skin samples were covered in kitchen film between the measurements; one measurement took up to one minute.

In all measurements the skin which consists of epidermis as the top layer and dermis as the bottom was oriented such that the epidermis was facing the light source and the dermis was facing the detector, as would be the case during PDT.

Due to the fact that the UV and blue light excite autofluorescence in skin which has a broad spectrum in the green part and that could have had an effect on the red transmission measurements, the first measurement was an autofluorescence measurement. The film was replaced by an empty glass slide and the autofluorescence signal was imaged at six positions on each sample. After each position the sample was randomly shifted for a few millimetres in x-y directions. The ultimate result was averaged. This allowed for compensating any non-uniformities in skin. The autofluorescence signal was compensated in the transmission measurements for each thickness of the skin samples.

After the autofluorescence measurements the organic film was placed in the set up and the camera was then focused to image the film's emission to normalise the transmission measurements. The intensity on the transmission images was analysed in Matlab. A circular area with 2 mm diameter (which is less than the size of the 3 mm x 3 mm grating) was selected for the analysis. The circle was positioned in Matlab Image Processing Toolbox to fit in the middle of the grating. The central position of the circle was defined and saved in a Matlab file for further image analysis. The film was fixed at the same spot during the experiment, so the same pixel coordinates of the circle were used for all images. The intensity was integrated over the area of the circle.

Then the skin was fixed at the film substrate and transmission measurements were taken in the same fashion as autofluorescence measurements: for six random positions on the skin sample and the results were averaged.

Autofluorescence was subtracted from the transmission images; the result was normalised on the film emission.

As the experiment was conducted in air, the change in optical properties was monitored over 3.5 hours. Thinner samples were losing water quicker and the transmission was increasing more rapidly. The change in optical properties for a 1 mm thick skin sample is shown in ***Figure 5.6***. The transmission increased up to 6%. The previous reports also observed increased transmission when the skin was drying out[18,20].

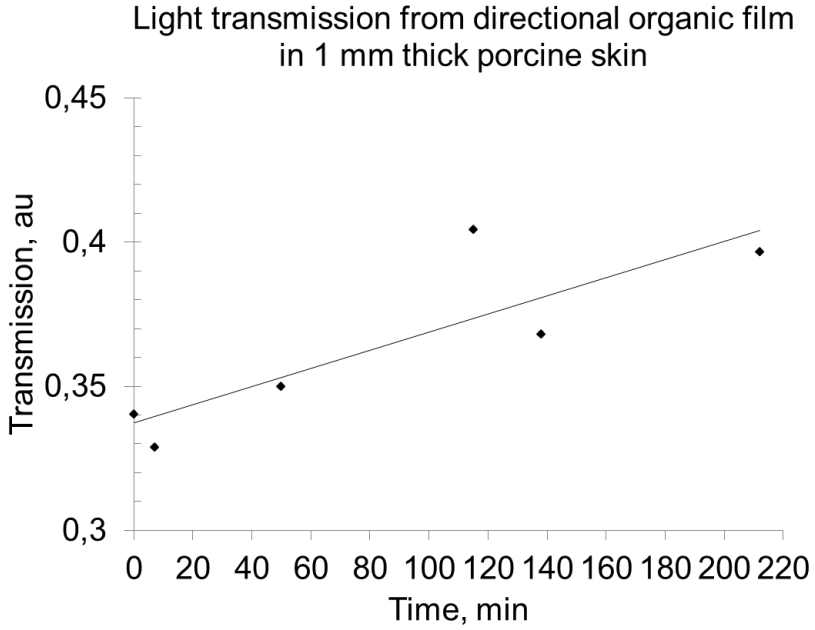

Figure 5.6: *Change in optical properties of porcine skin when it is exposed to air*

During the second experiment when the skin was placed in gel and was sandwiched in between the microscope glass slides, the sample glass slide was put in contact with the organic film. In order to keep the organic film fixed at the same position during the whole experiment and place the sample in contact with the film, a tiny amount of the ultrasonic gel was put at the surface of the film. The gel kept the sample glass slide sticking to the organic film. The same measurement protocol and image analysis were applied:

- autofluorescence was imaged first for the six positions on the skin,
- the film was placed in the set up
- the emission profile of the film was imaged,
- the transmission measurements for six positions on the skin were taken
- the emission of the film was imaged to monitor stability of the film
- the film was replaced by the other one,
- the emission of this film was imaged
- the transmission measurements for six positions on the skin were taken.
- the emission from this film was imaged for stability purposes
- a contour (the circle with 2 mm diameter) was selected to match the centre of the grating, the coordinates of the centre pixel were saved in a Matlab file for the analysis of all images
- the intensity was integrated over this contour in all images
- the results were averaged for 6 positions of one sample thickness
- autofluorescence was subtracted from the measurements
- the ultimate transmission was normalised on the films' emission profile

An example of the images: the emission profiles of the films and the transmission measurements through 0.5 mm skin are shown in ***Figure 5.7***.

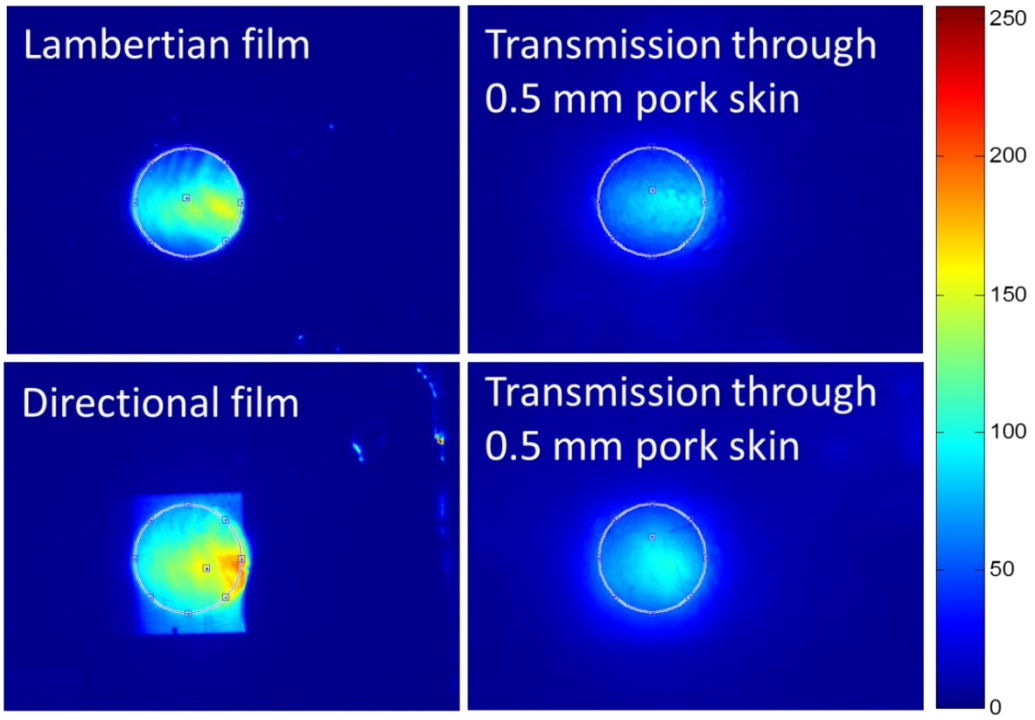

Figure 5.7: *Light transmission through porcine skin on false colour scale from wide emitting angle and directional emittance organic films*

The simulations were repeated for the defined thicknesses of the dissected skin, the emission spectrum and the 15° FWHM angular emission of the Super Yellow polymer films. The simulations are shown in ***Figure 5.8***. Super Yellow polymer has a peak emission wavelength at 580 nm. For this wavelength, the angular range and this porcine skin model the expected improvement was up to 6 % (porcine skin properties were $n = 1.35$, $\mu_s = 5.8\, mm^{-1}$, $g = 0.72$, $\mu_a = 0.07\, mm^{-1}$ [22]). Human skin has more forward scattering than the porcine skin, so it was expected that the directional light sources would have a more pronounced effect on the improvement in the light transmission.

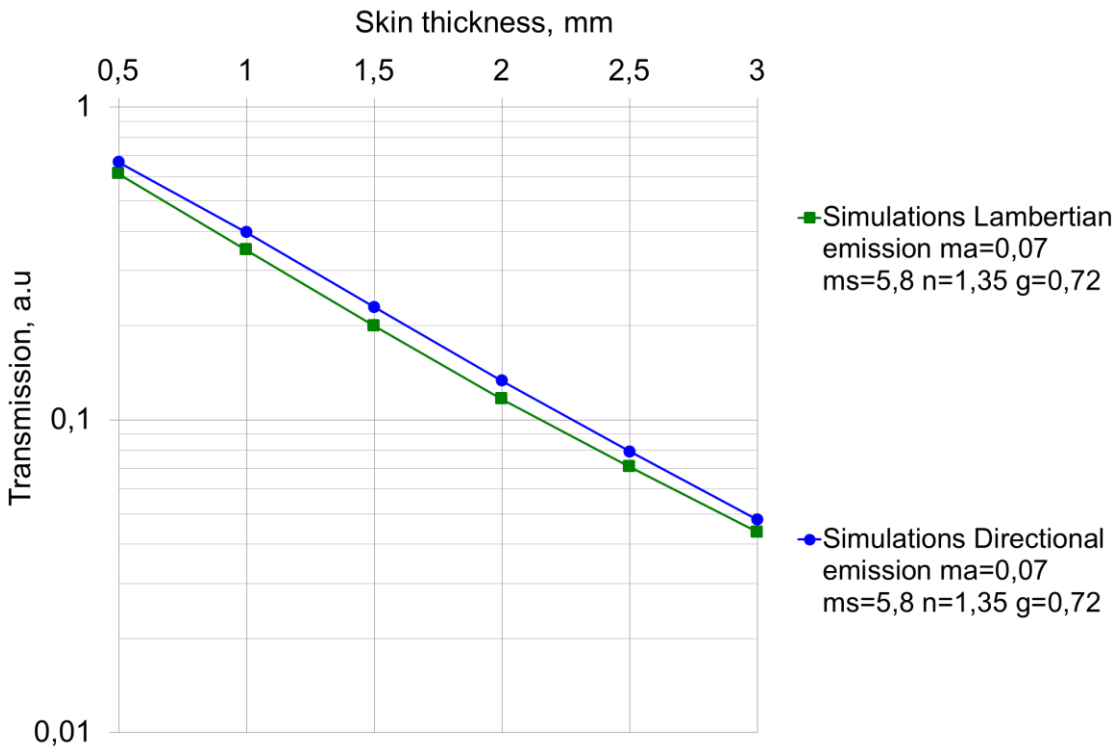

Figure 5.8: *Expected light transmission through porcine skin from directional and Lambertian organic light emitting films*

Both the measurements and the simulations are shown in ***Figure 5.9***.

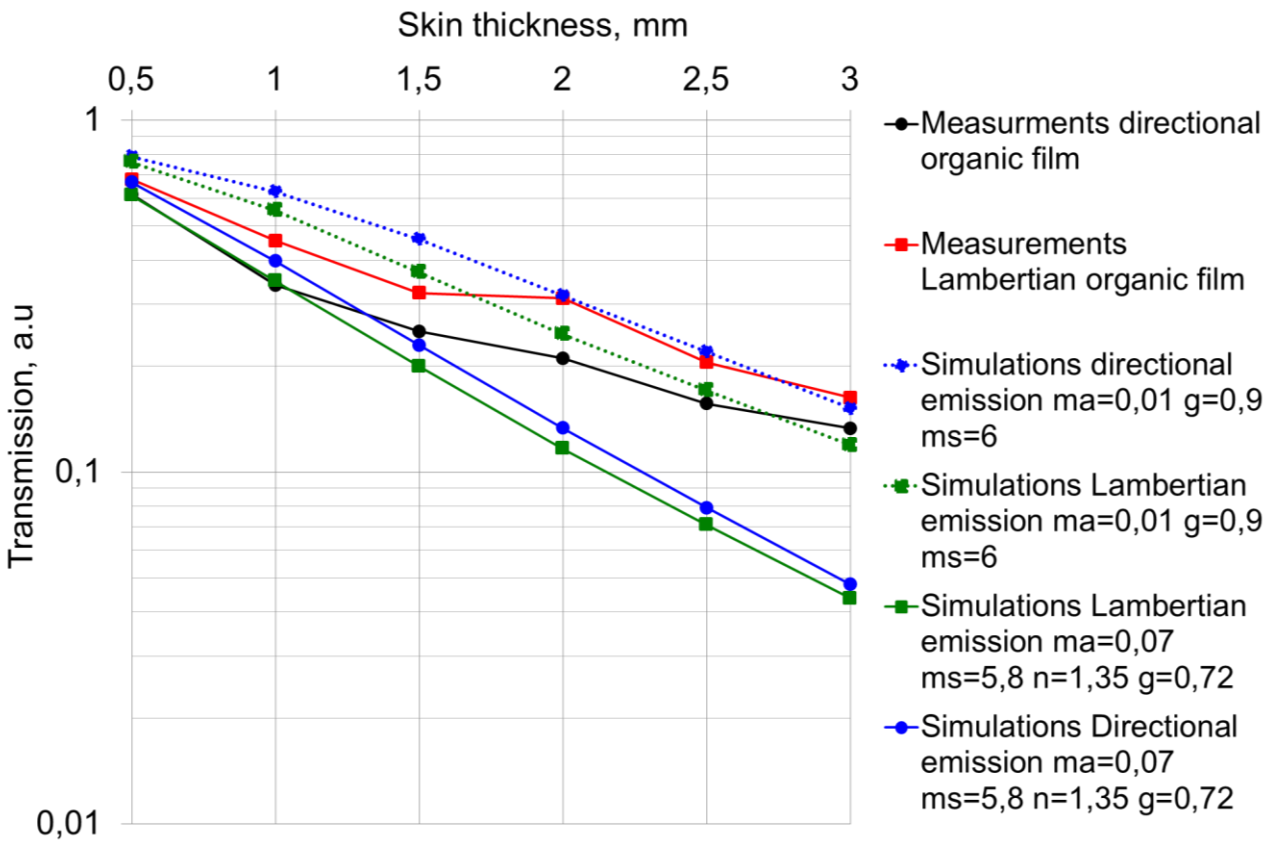

Figure 5.9: *Simulations and measurements of light transmission in porcine skin from wide angle and directional light sources*

These results did not show that directionality can improve light penetration in skin. Regression modelling attempted to adjust optical properties of the skin to have a better fit to the measurements. The initial properties of the skin gave better agreement at small depths. At larger depths increased forward scattering and reduced absorption were in better agreement. This could be explained by the fact that the skin is layered; porcine skin has a substantial amount of fatty tissue in deeper layers which is less absorptive and more scattering. At 1.5-2 mm there seemed to be a different angle in the measured transmission curve, in the skin samples with the thickness starting from 1.5 mm the amount of adipose fat increased substantially. So a better theoretical fit for less scattering and more absorption at shallow layers, and a better fit for more scattering and less absorption at deeper layers could be explained and modelled by layered tissue with different properties and thicknesses. However, the fact that the measurement demonstrated better transmission for Lambertian light sources in contrast to the modelling could not be explained by the discrepancies in real and initial optical properties or layered structure of the skin.

One of the potential explanations of why the measurement did not show the improved transmission from the directional light sources as predicted by the modelling was that the emission from the organic films was not perfectly collimated; 15° divergence and a not very uniform emission profile could result in a very small discrimination between the transmission from the directional and Lambertian films. So a new experiment was planned using a collimated and a diffused laser beam.

5.3.3 Transmission of diffused and collimated HeNe laser light through porcine skin

The measurement set up is shown in ***Figure 5.10***. A HeNe laser (0.5-0.1 mW, model 05-LLR-811) beam was expanded and spatially filtered to have a uniform large beam spot necessary for the image analysis. The input beam was too intense to control with the exposure of the camera, so a set of neutral density (ND) filters was used, the settings of the camera remained the same during the experiment. The skin sample was placed after the aperture. The sample glass slides were gently placed in the sample holder to avoid introducing any excess pressure to deform the sample. A paper diffuser was placed at the exit of the aperture to diffuse the collimated beam. The same camera was used for the measurements.

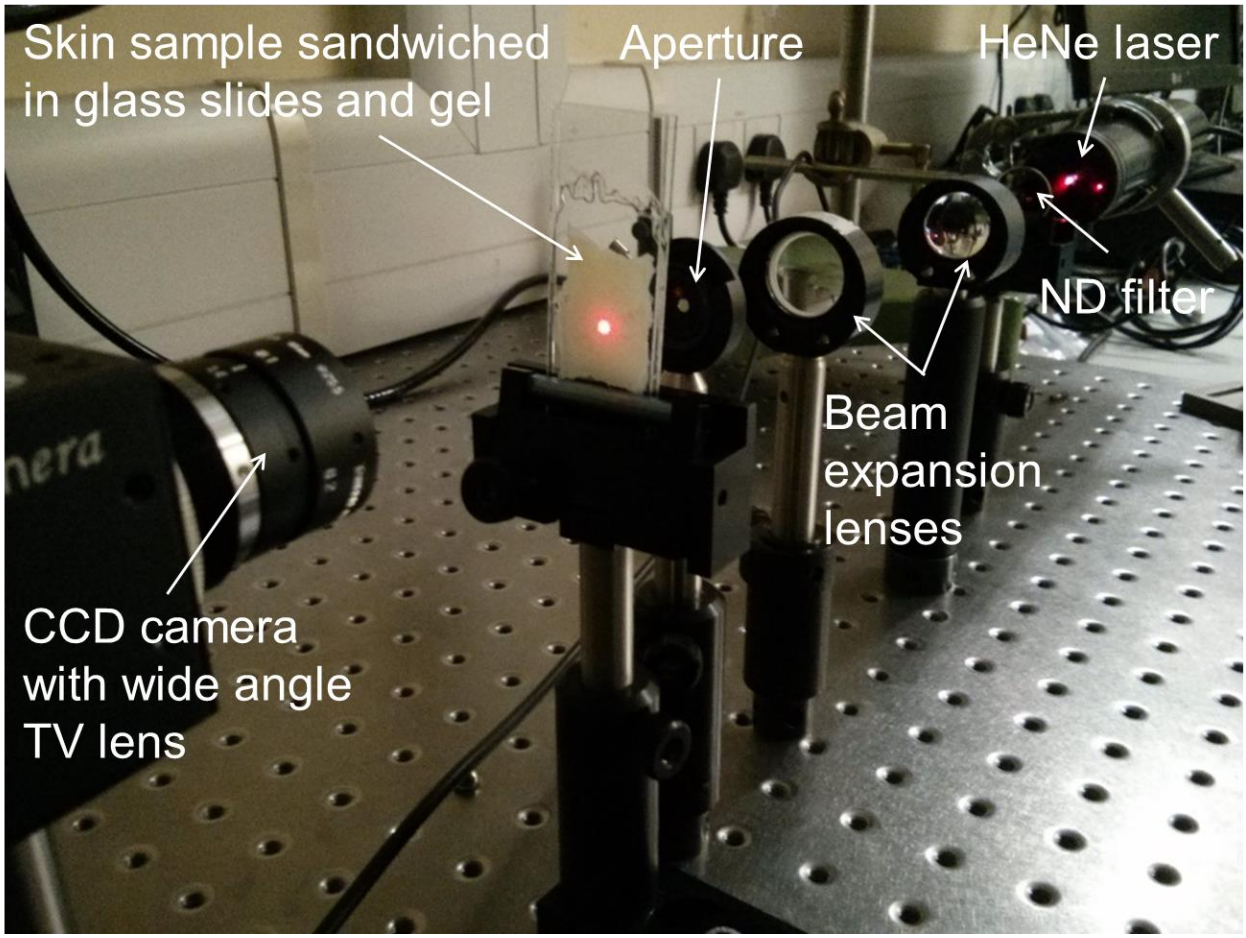

Figure 5.10: *Transmission measurements set up using HeNe laser to study collimated and diffused laser light propagation through pork skin. Two lenses were used to expand the beam spot and an aperture was used to spatially filter the beam. ND filters were placed before the first lens if needed. A diffuser was placed at the aperture.*

The laser profiles (diffused and collimated) were imaged at the microscope glass slides sandwiched with a drop of ultrasound gel and placed at the sample holder. The quality of the incident beam was improved compared to the emission spot from the organic films (***Figure 5.11***, ***Figure 5.12***).

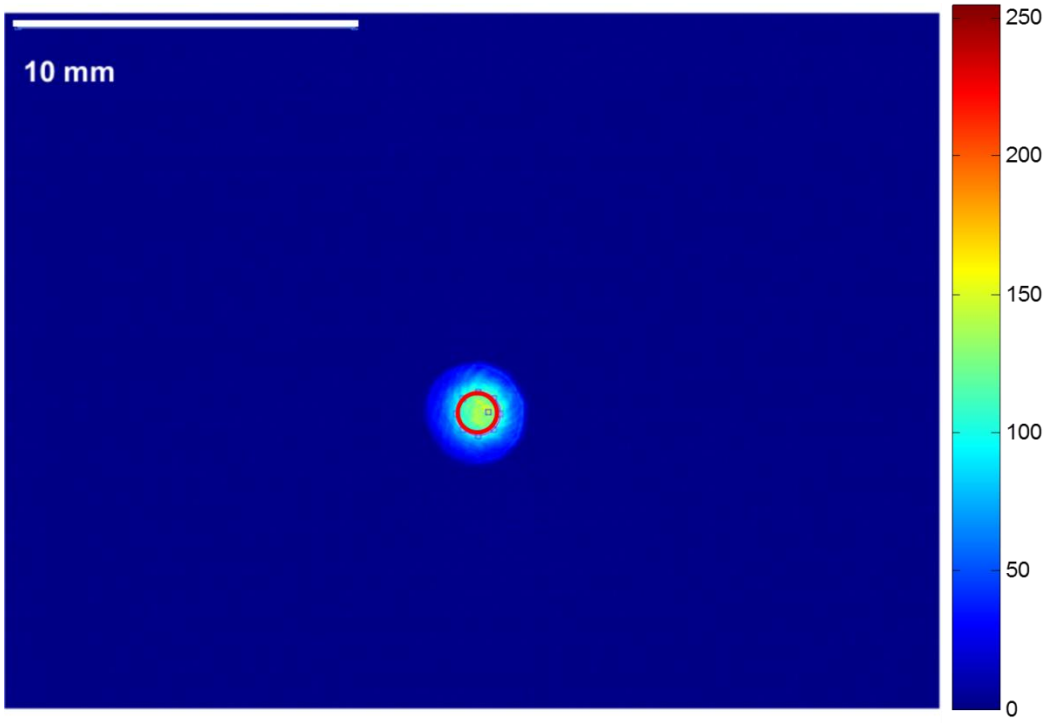

Figure 5.11: *The CCD camera's field of view: HeNe laser profile. The area which was used for integration of the transmission in all images is marked with a small red circle. It corresponds to 30 x 30 pixels area and in calibrated coordinates it has diameter equal to Ø1.28 mm. The position and the size of this circle remained the same for all images and so was the beam spot during the measurements. The combination of ND filters used to obtain this image was OD3.0 and OD1.5*

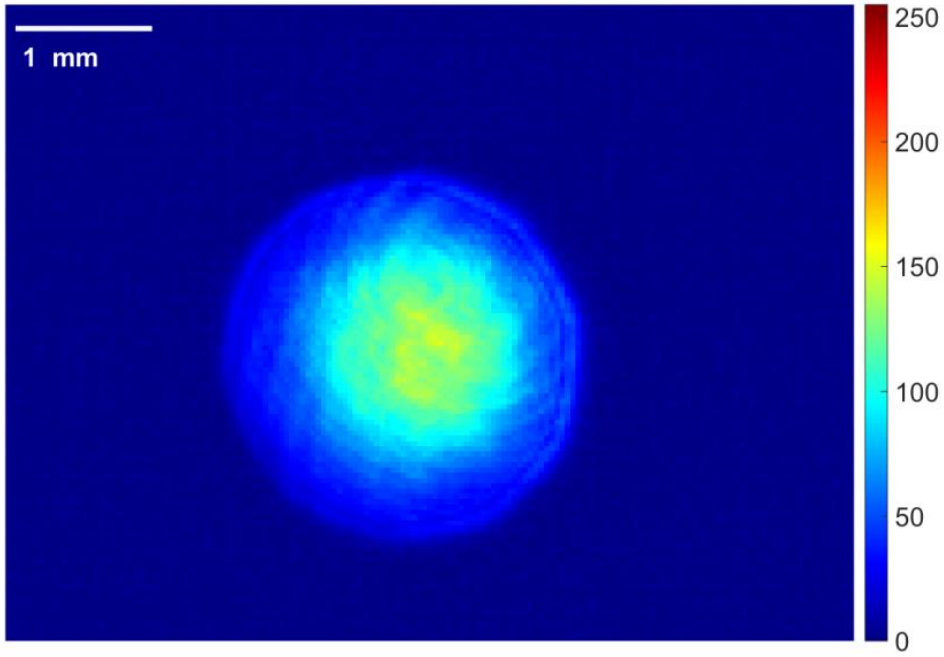

Figure 5.12: *Laser profile zoomed, ND filters OD3 OD1.5*

The measurement protocol and image analysis was the same as for the measurements on the organic films, except there was no need to compensate autofluorescence as it is only excited at shorter wavelength. The examples of the images: the collimated and diffused laser profiles and the transmission through 1 mm of porcine skin are shown in ***Figure 5.13***.

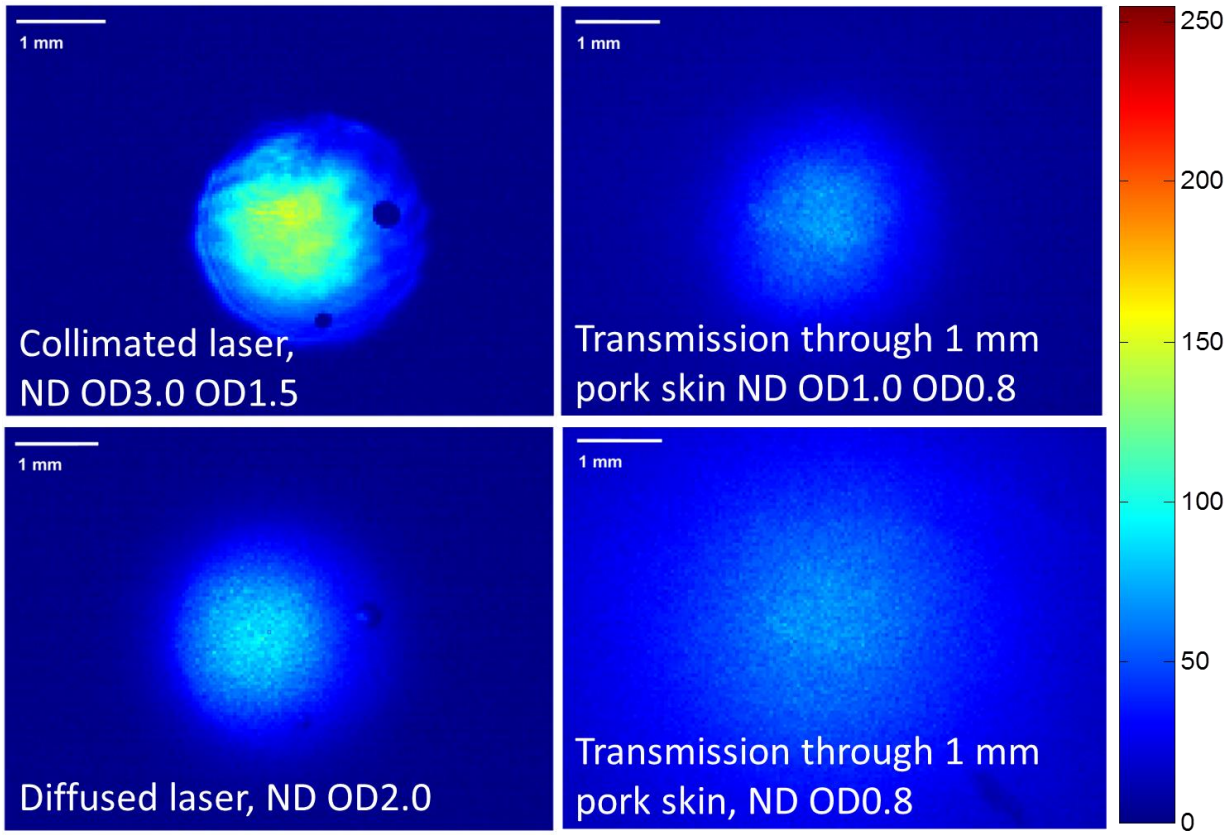

Figure 5.13: *Light transmission of collimated and diffused light thought porcine skin using HeNe laser*

The intensity profiles are shown in ***Figure 5.14***. The collimated beam is 30 pixels in diameter. This area corresponds to a circle with 1.28 mm diameter and was used to analyse the transmission images. The beam was diffused to more than 200 pixels after the diffuser which was six times larger than the collimated beam.

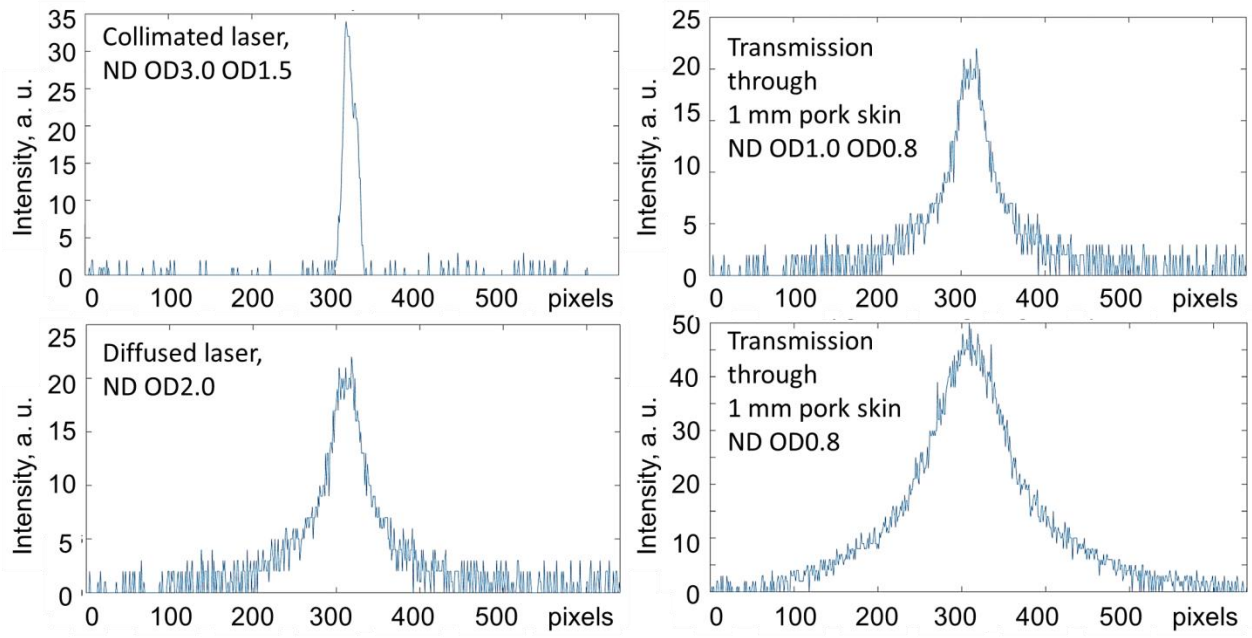

Figure 5.14: *Intensity cross sections of HeNe collimated and diffused laser beams and its transmission through 1 mm of porcine skin. The diffuser was placed at the exit of the aperture, ND filters between the laser and the first beam expansion lens.*

The transmission measurements were averaged and normalised by dividing by the laser profiles (***Figure 5.15***).

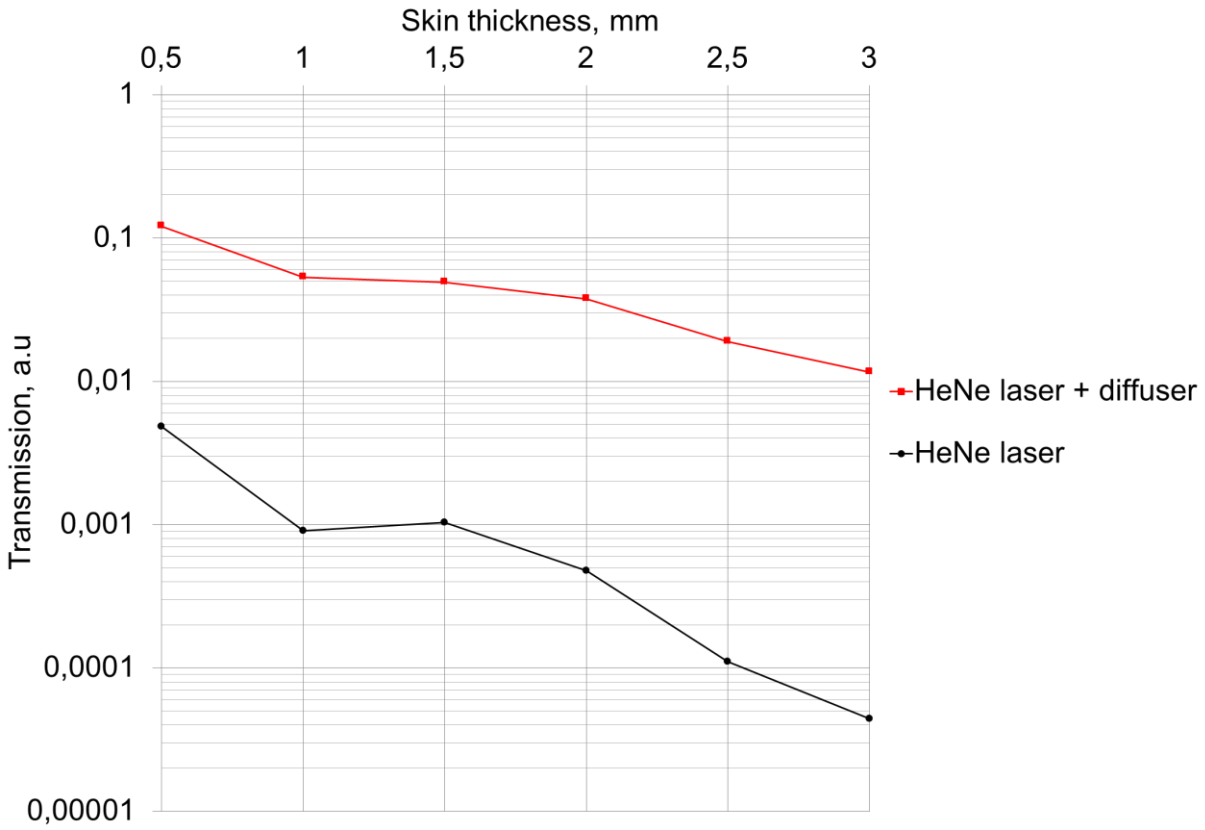

Figure 5.15: *Light transmission through porcine skin from diffused and collimated HeNe laser*

For this experiment a different animal was used and new samples were dissected. Similar to the transmission measurements using the organic film there was a region where the transmission curve changed the angle. In the previous measurement this transition region was at 1.5-2 mm depth, in this measurement this region was at 1-2 mm thicknesses. After 2 mm adipose tissue started to appear which had different optical properties. However, even with the improved experimental settings such as much better collimation of the beam and uniform laser profile, the results of the measurements again showed higher transmission for the diffused light.

5.4 Discussion

One of the possible explanations of the disagreement between the theoretical modelling and the measurements could be the fact that the roughness of the skin was not measured or taken into account in the modelling. The size of stratified ridges of the epidermal thickening is in

a range of 50 – 200 μm which proliferate over many layers[26]. This can form compartments which can play a role in light coupling.

One group reported a big change in the calculations of optical properties when roughness is taken into account[22]. They used a confocal laser scanning microscope (LSM 510, Zeiss) to obtain confocal images of the samples sandwiched between microscope glass slides and obtained surface roughness from statistical analysis of the profile lines.

They demonstrated that the g value, the scattering and the absorption coefficient were lower for the models where roughness of the skin was taken into account. The difference in some cases was more than two times. For instance, g value is equal to 0.4 for the rough skin and 0.8 for the flat skin. This means that in the case with rough skin there is much less forward scattering. This on its own would not explain why Lambertian light sources gave better transmission compared to collimated light, but demonstrates that rough porcine skin loses directionality in the scattering. A possible explanation why Lambertian emitters showed improved transmission could be that the roughness of the skin was also responsible for coupling mechanisms of light; light coming at large incidence angles could have been trapped by the rough surface and have less reflection compared to normal incidence..

The research in this chapter demonstrated that pig skin may not be a good choice for optical investigation as a surrogate representative of human skin. As it turned out, the roughness of the skin changes the optical properties; the roughness of pig skin is very different from human skin, so is the rest of the anatomical structure. Also there are many controversial points in the developed measurement approach such as changing optical properties in the time course of the experiment, non-uniformities of the skin due to dissecting, and when the skin samples are obtained from a regular butcher shop, the skin comes treated with hot water which changes the optical properties of the skin. The best way to improve the experiment attempted by this chapter would be to use a well-studied Intralipid phantom mixed with real blood such as was described by Kanick et al.27 Kanick et al used this mixture with different concentrations of blood and PpIX to perform diffuse reflectance and fluorescence measurements. The measurements results were matched to Monte Carlo modelling of light transmission in those phantoms to generate look-up tables of optical properties of skin and the concentrations of PpIX. These looks-up tables were used to extract optical properties and PpIX concentration from the measurements using the optical probes reported in that paper. Intralipid with blood is a well-studied skin phantom with the most representative scattering and absorption properties. It could be used for the same transmission measurements with a CCD camera, with standard photodiodes or spectroscopes using diffused and collimated laser light, and directional and wide emitting angles OLEDs. Such

a standard phantom would eliminate any possibilities of uncertainty related to measurements in pig skin samples.

However, the structural properties of layered human skin would still be missing from the experiment, so would be the dynamic processes related to oxygen diffusion and PpIX metabolism in skin. Therefore the ultimate resolution in order to confirm the effect of structuring directional emission for PDT light sources would be a randomised controlled double-blind clinical trial with two identical OLED devices, but with directional and wide angle emission. The results from the previous chapter suggested that the area of OLED has to be substantially larger (3.5 cm for 2 cm treatment area in diameter) to compensate for the drop in the intensity due to Lambertian emission. So this should be taken into account in the consideration of the sizes of the treated area and the devices. Considering that there have been a few successful clinical trials of using OLED devices for ambulatory PDT[28,29,30,31] which led to commercialisation of inorganic version of such ambulatory devices (Ambulight PDT), a new trial comparing two OLEDs would follow already established protocols. If the intensity, wavelength and treatment time remained the same for both OLED devices, directional OLED would not be expected to cause any reduction in the efficacy of PDT, but an improvement.

5.5 Conclusions

The developed optical apparatus and modelling approach can distinguish presence of layers in skin tissue by detecting the change in the angle of the transmission curves. This change is due to different optical properties in a new layer. Monte Carlo regression modelling showed that it is possible to extract the properties of each layer by fitting the transmission modelling to the measured curve for each depth.

Unfortunately by the transmission measurements on porcine skin we did not observe the expected 10 % improvements for the directional light sources which were predicted by the modelling. During the investigation of the possible causes which could have prevented measuring the improved transmission in porcine skin, it was discovered that there are too many assumptions about the properties of porcine skin. All of the reported results on the extraction of optical properties differ hugely. One of the most important findings was that taking roughness into account could change all optical properties, reducing the directionality of the scattering to be almost insignificant. This along with the fact that the structure of porcine skin is different from human skin leads to the conclusion that the absolute evidence which could demonstrate the

difference between the two light sources (directional and Lambertian) would be a randomised clinical study on patients using the same light sources but with the only difference being in the directionality of the emission.

.

5.6 References

1. Lin J, Wan MT. Current evidence and applications of photodynamic therapy in dermatology. *Clin Cosmet Investig Dermatol*. 2014:145. doi:10.2147/CCID.S35334.
2. Wang KKH, Finlay JC, Busch TM, Hahn SM, Zhu TC. Explicit dosimetry for photodynamic therapy: Macroscopic singlet oxygen modeling. *J Biophotonics*. 2010;3(5):304-318. doi:10.1002/jbio.200900101.
3. Zhu TC, Liu B, Penjweini R. Study of tissue oxygen supply rate in a macroscopic photodynamic therapy singlet oxygen model. *J Biomed Opt*. 2015;20(3):038001. doi:10.1117/1.JBO.20.3.038001.
4. Liebert MA. Letter to the Editor The Importance of the Coherency. *Photomed Laser Surg*. 2005;23(4):431-434.
5. Reeds KB, Ridgway TD, Higbee RG, Lucroy MD. Non-coherent light for photodynamic therapy of superficial tumours in animals. *Vet Comp Oncol*. 2004;2(3):157-163. doi:10.1111/j.1476-5810.2004.00052.x.
6. Brancaleon L, Moseley H. Laser and non-laser light sources for photodynamic therapy. *Lasers Med Sci*. 2002;17(3):173-186. doi:10.1007/s101030200027.
7. Babilas P, Knobler R, Hummel S, et al. Variable pulsed light is less painful than light-emitting diodes for topical photodynamic therapy of actinic keratosis: A prospective randomized controlled trial. *Br J Dermatol*. 2007;157(1):111-117. doi:10.1111/j.1365-2133.2007.07959.x.
8. Strasswimmer J, Grande DJ. Do pulsed lasers produce an effective photodynamic therapy response? *Lasers Surg Med*. 2006;38(1):22-25. doi:10.1002/lsm.20277.
9. Friedmann DP, Goldman MP, Fabi SG, Guiha I. The Effect of Multiple Sequential Light Sources to Activate Aminolevulinic Acid in the Treatment of Actinic Keratoses : A Retrospective Study. 2014;7(9):20-25.
10. Zhang S, Turnbull GA, Samuel IDW. Highly Directional Emission and Beam Steering from Organic Light-Emitting Diodes with a Substrate Diffractive Optical Element. *Adv Opt Mater*. 2014;2(4):343-347. doi:10.1002/adom.201300441.
11. Committee for Medicinal Products for Human Use (CHMP). *CHMP Assessment Report: Ameluz Ref EMEA/H/C/002204*. 7 Westferry Circus, Canary Wharf, London E14 4HB, United Kingdom; 2012.
12. Rodrigues PGS, Campos de Menezes PF, Fujita AKL, et al. Assessment of ALA-induced PpIX production in porcine skin pretreated with microneedles. *J Biophotonics*. 2015;8(9):723-729. doi:10.1002/jbio.201400081.
13. Genina E a., Bashkatov AN, Gavrilova A a., et al. Skin Optical Clearing for Improvement of Laser Tattoo Removal. *Proc SPIE*. 2007;6734:673419-673419 - 9. doi:10.1117/12.753224.
14. Dlugos JF. In Vitro Method for the Calculation of Sunscreen SPF Values. *Case study 009963B_01, PerkinElmer, Inc*. 2011:4. www.perkinelmer.com.
15. Laffitte J, Denton ML, Thomas RJ, City-base B. Experimental Characterization of Near-Infrared Laser Energy Absorption , Scattering , and Transmittance in Biological Tissue Human

Effectiveness Directorate Optical Radiation Branch. *AFRL-HE-BR-TR-2007-0050; Interim Rep Febr 2004 – March 2007 ; Air Force Res Lab , Hum Eff Dir , Dir Energy Bioeffects Div , Opt Radiat Branch, Brooks City-Base, TX 78235*. 2007.

16. Abdussamad Abbas H, Triplett GE. Infrared Transmission Characteristics and Laser Tissue Interaction of Albino Pigskin Using Pulsed NIR Laser Light. *ISRN Opt*. 2013;2013:1-8. doi:10.1155/2013/451208.
17. Payne J, Song KD, Yang SY, Kim J, Park Y, Choi SH. <title>Wireless power transmission for medical applications</title>. In: Varadan VK, ed.; 2009:72910X - 72910X - 9. doi:10.1117/12.816020.
18. Chung S, Tanamai W, Durkin A. Handbook of Biomedical Optics. *Group*. 2011:0-1. doi:10.1186/1475-925X-11-7.
19. Du Y, Hu XH, Cariveau M, Ma X, Kalmus GW, Lu JQ. Optical properties of porcine skin dermis between 900 nm and 1500 nm. *Phys Med Biol*. 2001;46(1):167-181. doi:10.1088/0031-9155/46/1/312.
20. Firdous S, Aslam M. Measurements of ptical parameters: absorption scattering and auto-fluorescence of skin in vitro. *Int J Cancer Res*. 2005;1(1-2):10-15.
21. Beek JF, Blokland P, Posthumus P, et al. In vitro double-integrating-sphere optical properties of tissues between 630 and 1064 nm. *Phys Med Biol*. 1997;42(11):2255-2261. doi:10.1088/0031-9155/42/11/017.
22. Ma X, Lu JQ, Ding H, Hu X-H. Bulk optical parameters of porcine skin dermis at eight wavelengths from 325 to 1557 nm. *Opt Lett*. 2005;30(4):412-414. doi:10.1364/OL.30.000412.
23. Tsiminis G, Wang Y, Kanibolotsky AL, et al. Nanoimprinted organic semiconductor laser pumped by a light-emitting diode. *Adv Mater*. 2013;25(20):2826-2830. doi:10.1002/adma.201205096.
24. Gambino S, Bansal AK, Samuel IDW. Photophysical and charge-transporting properties of the copolymer SuperYellow. *Org Electron physics, Mater Appl*. 2013;14(8):1980-1987. doi:10.1016/j.orgel.2013.03.038.
25. *FSA Project MO1038: Reduction of Salmonella Contamination of Pig Meat*.; 2007. http://www.grimsby.ac.uk/frperc/documents/frperc/projects/FSA_Project_MO1038.pdf.
26. Bolognia JL, Schaffer J V., Duncan KO, Ko CJ. *Dermatology Essentials*. Elsevier Saunders; 2014. https://books.google.de/books?id=9cY0AwAAQBAJ&source=gbs_navlinks_s.
27. Kanick SC, Davis SC, Zhao Y, et al. Dual-channel red/blue fluorescence dosimetry with broadband reflectance spectroscopic correction measures protoporphyrin IX production during photodynamic therapy of actinic keratosis. *J Biomed Opt*. 2014;19:075002. doi:10.1117/1.JBO.19.7.075002.
28. I.D.W. Samuel JF and AM. OLEDS: Next generation photodynamic therapy of skin cancer. In: *PDT Book Chapter*.; :1-6.
29. Attili SK, Lesar A, McNeill A, et al. An open pilot study of ambulatory photodynamic therapy using a wearable low-irradiance organic light-emitting diode light source in the treatment of nonmelanoma skin cancer. *Br J Dermatol*. 2009;161(1):170-173. doi:10.1111/j.1365-2133.2009.09096.x.
30. Morton C a, McKenna KE, Rhodes LE. Guidelines for topical photodynamic therapy: update. *Br J Dermatol*. 2008;159(6):1245-1266. doi:10.1111/j.1365-2133.2008.08882.x.
31. Ibbotson SH, Ferguson J. Ambulatory photodynamic therapy using low irradiance inorganic light-emitting diodes for the treatment of non-melanoma skin cancer: An open study. *Photodermatol Photoimmunol Photomed*. 2012;28(5):235-239. doi:10.1111/j.1600-0781.2012.00681.x.

Chapter 6

A wearable optoelectronic sensor for muscle contraction

Any sufficiently advanced technology is
indistinguishable from magic.

— Sir Arthur Charles Clarke (1917 – 2008),
British science fiction writer

6.1 Introduction

This chapter will describe how light interaction with tissue was employed for developing a flexible organic optoelectronic sensor suitable for continuous monitoring of tissue conditions. Anisotropic scattering of light by muscle was used for optical sensing of muscle activity. The potential of the sensor to drive active prosthetic devices with improved functionality by reading optical signals from muscle was demonstrated by actuating a robotic arm. Optoelectronic sensors can also be applied for continuous monitoring of other biological changes in the body and point of care diagnostics for risk groups of patients. The sensor was developed by Dr A. Bansal, Dr M. Giardini and Mr S. Hou. My contribution was to perform optical modelling of the device. The implementation of optical modelling of the muscle contraction sensor is the concern of this chapter.

Continuous monitoring of health condition is particularly important for rehabilitation in groups of patients with chronic conditions or risk groups such as elderly people living alone. Monitoring of gradual changes in the mobility of the elderly can be done with the help of telemedicine[1]. The other risk group is patients with diabetes where chronic monitoring of blood pressure could reducing the risks of microvascular disease[2]. Measuring of the blood pressure and the pulse in real time is an important task; new technology is being developed which could be combined with current advances in telemedicine. There was a report on the development of a

wearable and highly sensitive sensor with gold nanowires[3]. Gathering information continuously about different physiological factors is highly relevant for rehabilitation[4].

Another growing field where real time continuous sensing is of great importance, is human-machine interactions. There are reports of flexible and stretchable sensors which can mimic skin functions[5]. These types of sensors were named epidermal electronics and combined two important parameters: the mechanical properties of skin and ability to measure all biologically relevant signals such as surface electromyography sEMG signals from the muscle, temperature, pressure, strain, etc.[6,7]. This area is currently most appealing for the real time gaming industry, however, it has potential for other applications.

Organic optoelectronics has just begun to be applied for treatment, sensing, and manipulations of biological activity[8,9,10]. It introduces many advantages for wearable sensors such as simple fabrication technology by spin-coating from solutions, and it is potentially cheap. The devices can be made flexible to conform to body shapes, they can be incorporated on a wearable bandage, and are low weight[11],[12]. The devices can be made on plastic[13]. From the recent advances, the emission of OLEDs can be structured to make laser-like surface emitters which open new opportunities[14]. In addition to the above advantages, organic electronics can bring benefits such as being non-toxic; also it does not degrade in the biological soup and can be implanted for neuronal photoactivation[15] or in-vivo recording of brain activities[16]. Also organic optoelectronics is not sensitive to electromagnetic noise.

The concept of wearable light sources such as OLEDs for ambulatory PDT treatment[17] was exploited further and resulted in implementation of the wearable organic flexible optoelectronic muscle contraction sensor[18,19]. The principles of how anisotropic scattering of muscle can be used to detect optical changes during muscle contraction and distinguish the degree and the type of the contraction was published in [20] using inorganic LED and photodiodes. This work was developed further: the light sources and the photodetectors were made of organic materials with tuneable properties of flexible substrates. The sensor was placed on a wearable bandage and was used to actuate a robotic arm[18,19]. This chapter will describe how optical modelling was used to understand the optical design of the sensor and get better insights into light interaction with anisotropic muscle in combinations with layered skin and fatty tissue.

6.1.1 Current prosthetic device based on reading electrical signals from the muscles

The most common sensors used to detect muscle activity are based on measuring surface electromyography (sEMG) signals. Those are electrical signals are sent by the brain to the nerves to contract or relax the muscles. They are measured with surface electrodes[21]. However, this sensing technique introduces the need to insert electrodes in tissue which require simple and safe, but nevertheless surgical, intervention; the electrodes degrade due to the immune response and over time require replacement. Another issue is that sEMG is not able to distinguish the two types of muscle contraction (isotonic and isometric[22]) which are responsible for different functionality (flexion/extension and resisting or maintaining pressure). Distinguishing both types is important for the development of a prosthetic device able to mimic natural gaits, and other movements which require resisting or withstanding pressure. There have been a few attempts to distinguish the two types of contraction using sEMG but they have not been very successful so far.

One of the studies attempted to analyse EMG tension and the frequency spectrum of some masticatory muscles at rest, during isotonic and isometric contractions[23]. It showed that the frequency spectrum is different for the two types of contractions. Another study applied adaptive mixture independent component analysis (AMICA) to analyse electro-cortical EEG signals in the lower limb of healthy volunteers and achieved 69-87% accuracy in distinguishing the two types of contractions[24].

Another approach in adding functionality to the prosthetic device which requires distinguishing the two types of contraction was by analysing the dynamics of drive energy consumption in the prosthetic device. It introduced some improvements in mimicking natural gaits when using active prosthetic devices by introducing more advanced models of mechanical motions[25].

We have demonstrated that optoelectronic sensors can successfully detect the two types of contraction and they can be used to drive a robotic arm to mimic the natural motion of limbs using the two types of contraction[18,19]. Another big advantage of this technology is that optical sensing does not require inserting electrodes and eliminates all the problems with degradation of electrodes and the need to replace them over time. The sensor is thin, lightweight and flexible so it can match the body shape which makes it a good candidate for an improved prosthetic device.

6.1.2 Anatomical structure of muscle, physiological and optical changes during muscle contractions

Muscle consists of fibres, the structure of the fibres is shown in ***Figure 6.1***. The first-order fibres are threads of two proteins actin and myosin. They are bundled together in myofibrils which are second-order fibres. Myofibrils are finally bundled in the final third order fibres which are responsible for the physiological function of skeletal muscle – relaxation, flexion, extension and maintaining constant force. The length of third order muscle fibres is 10-12 cm and the diameter is 2-4 mm[22].

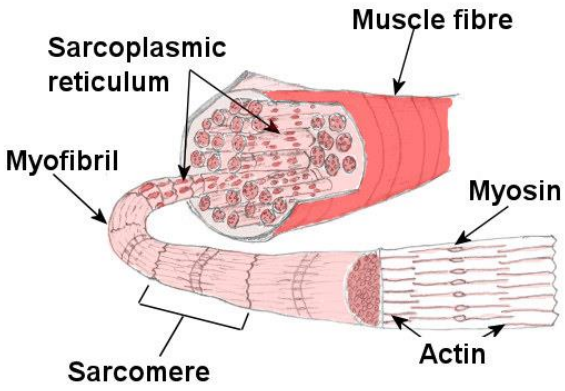

Figure 6.1: *Structure of a third order skeletal muscle fibre*[26]

When muscle contracts actin protein slides along myosin protein making the fibres shorter and thicker. The volume of the fibre remains the same during the contraction[27,28] (***Figure 6.2***). Myosin is optically anisotropic[29]. Therefore the fibrous structure of muscle and anisotropic myosin protein are responsible for transverse and longitudinal anisotropy of light propagation in muscle.

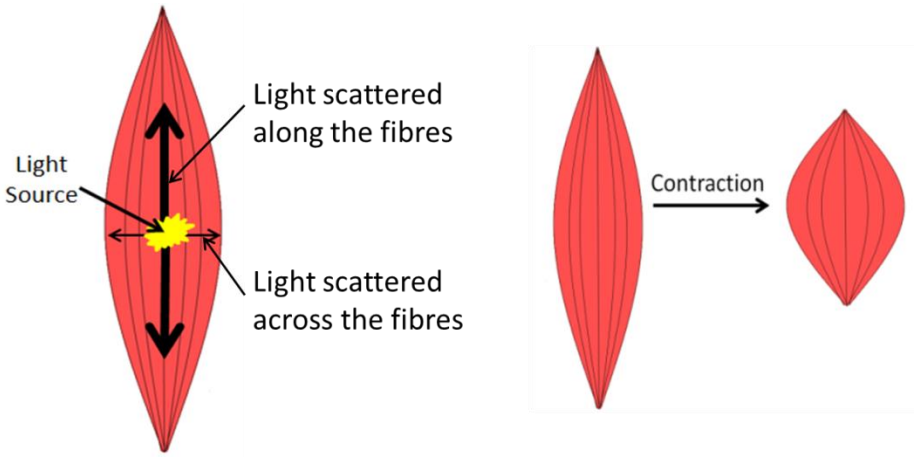

Figure 6.2: *Light scattering in muscles principles (figure credit: Dr Ashu Bansal)*

Light travelling parallel to muscle fibres is scattered differently from light travelling perpendicular to the fibres. This anisotropy can be detected by a surface-mounted light source and detectors positioned along and perpendicular to muscle fibre[20,18,19] (***Figure 6.2***). Physiological change during muscle contraction results in changing the fibres aspect ratio; the fibres become shorter and thicker. It means that for contracted muscle there will be more light scattering perpendicular to the fibres compared to the amount of light scattered in this direction for relaxed muscle. Also, when muscle contracts it changes the oxygenation and blood saturation which affects light absorption. So by measuring the difference in light scattering along and across the muscle it is possible to tell the degree and the type of the contraction[20,18,19].

The challenges which come to play with optical detection of muscle activity are the effect of skin and adipose fatty tissue which cover the muscle. Both of the tissues are very diffusive which blurs the difference in the scattering in two directions. So the questions for the modelling in this chapter were:

- how far it is possible to penetrate in tissue and probe the muscle activity?
- what were the optimal thickness of the skin and fatty tissue where the signal from the muscle could still be resolved?
- what was the optimal distance between the source and the detector in order to achieve the best discrimination in detecting the two different directional scatterings from muscle?

The biggest achievement in this chapter was implementation of a 3D anisotropic scattering model of muscle in the commercial optical software by manipulating the geometrical shape of existing Henyey-Greenstein 1D anisotropic scattering model. This allowed for

optimising the performance of the sensor and learning about the effects of the skin and fatty tissue on the detected signal from the muscle.

6.2 Methods

6.2.1 Optical design software

The same FRED optical design software was used as in the previous chapters. However, it only allows modelling of one dimensional anisotropy of light scattering in tissue by the standard Henyey-Greenstein approximation. This dimension is in-depth of the tissue (muscle). In order to model anisotropic scattering in two other directions – transverse (across the muscle fibres) and longitudinal (along the muscle fibres) some manipulations with the geometry and the Henyey-Greenstein scattering model were done. Special geometrical arrangements of scattering fibres were implemented which corresponded to the anatomical structure of and biophysical processes in muscle.

Optical properties of tissue were taken from[30,31]. The same approach as in the previous chapters was taken for approximating the scattering coefficients of the muscle, the adipose tissue and the skin for the wavelength range of interest[31] (*Eq. 4.11*,*Eq. 4.12*).

6.3 Results

6.3.1 Wearable sensor for detecting muscle contraction

The schematic of the sensor is shown in ***Figure 6.3***. An OLED and four organic photodiodes (OPDs) were placed on a wearable bandage. Two OPDs were placed parallel to the muscle fibres and other two were placed perpendicular to the muscle fibres.

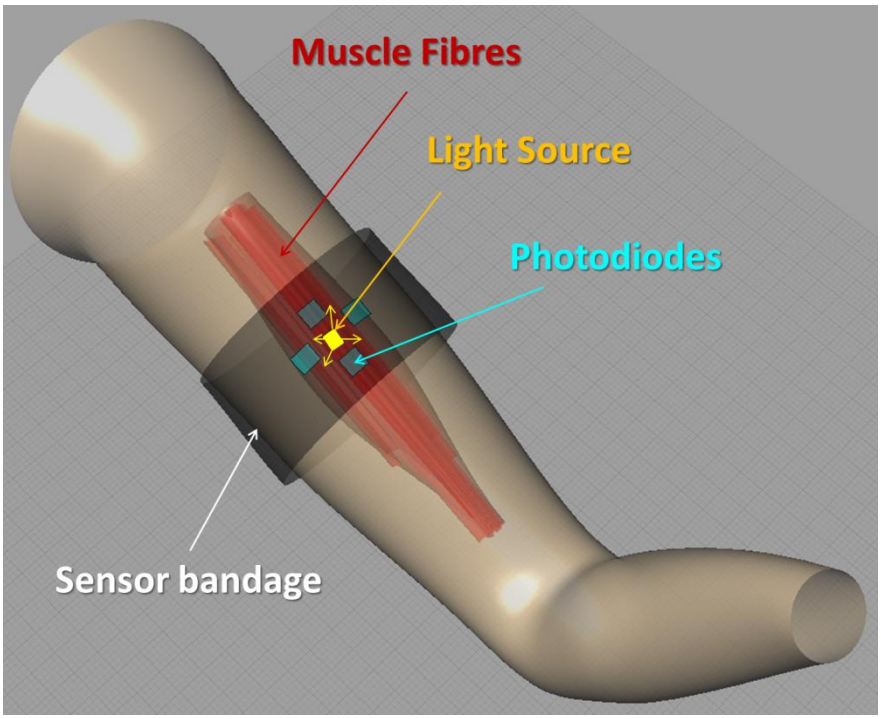

Figure 6.3: *Schematics of the wearable bandage for muscle contraction sensing.*

The implementation of fully flexible sensor (on a flexible substrate with flexible electrodes, the OLED and the OPDs) is shown in ***Figure 6.4, (a)***. The sensor was put on a bandage with Velcro® straps wrapped around bicep muscle and connected to the robotic arm and is shown in ***Figure 6.4, (b)***. The signals from bicep and deltoid muscle of a healthy volunteer were measured by the sensor in real time and used to mimic the motion by the robot arm. This demonstrates the potential of the sensor to read the signals which would come from partial limbs of disabled people to drive a prosthetic device.

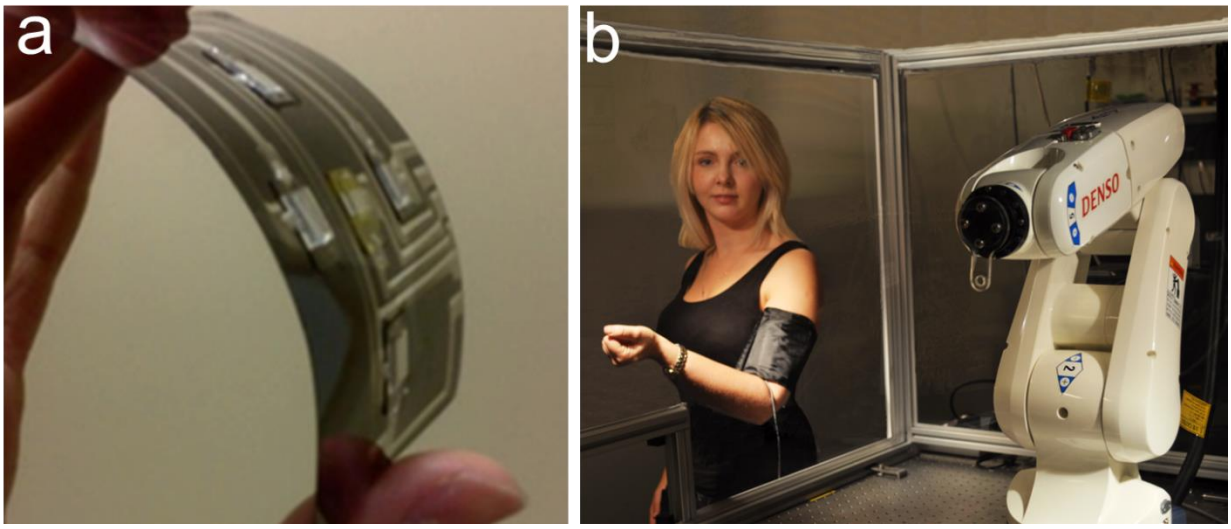

Figure 6.4: *Sensor implementation.* **a** *– a fully organic flexible muscle contraction sensor (figure credit: Shuoben Hou).* **b** *– the sensor on a wearable bandage demonstrating the possibility to actuate a robotic arm using signals from the muscle in real time.*

The sensor was fabricated and applied to drive a robotic arm by Shouben Hou under the supervision of Dr Mario Giardini, Dr Ashu Bansal, and Prof Ifor Samuel. Full description of the fabrication technology, the implementation of the electronics circuits and the manipulation of the robotic arm can be found in the MS thesis of Shouben Hou[32] and in [18, 19]. One pair of the detectors was placed along the muscle fibres (parallel pair) and another pair was placed across the muscle fibres (transverse pair). The signals from the two detectors in each pair were added. The two pairs were connected to a differential amplifier. The difference between the parallel and transverse pair was substrate. This difference was amplified; the signal was measured by an oscilloscope or was used to control the robotic arm. The robotic arm had two degrees of motion: flexion/extension, and rotation which corresponded to two different types of contractions (isotonic and isometric). The measured voltages from the sensor were sent to the robot. The amplitude of the motion of the robotic arm was calibrated using a relaxed muscle and a fully contracted muscle of a volunteer. The robot fully mimicked the motion of the arm of the volunteer in real time [the video can be found in the supplementary information in [33].

6.3.2 Optical model of the sensor

The final optical model of the sensor corresponds to the above implementation of the sensor. The arrangements of the components are shown in ***Figure 6.5***. A 3 mm x 3 mm OLED

was placed in the middle. The output optical power was equal to 0.27 mW, and the irradiance was 3 mW/cm^2. The OLED was made of Super Yellow polymer with a low pass filter. The emission spectrum of the SY was from 530 nm to 700 nm with the peak wavelength at 580 nm[34]. There was a 580 nm long pass filter to cut off shorter wavelengths which did not penetrate at long distances in muscle. Shorter wavelengths would only scatter in the skin not reaching the muscle which would introduce noise in the measurements. The spectrum in the model corresponded to the spectrum of the SY polymer taking into account the transmission of the low pass filter. In the ultimate design four 6 mm x 6 mm OPD detectors were placed at a 20 mm centre-to-centre distance from the OLED. The OLED and the photodetectors were positioned at a small (1 μm distance is needed between two optical surfaces to prevent them overlapping and causing computing errors) distance above the skin for the modelling purposes. The power at the detectors was simulated for 5, 10, 15, 20 mm distances between the OLED and the detectors to find the optimal configuration. The results of the modelling will be shown in the next section after the discussion on the implementation of optical models of the tissue.

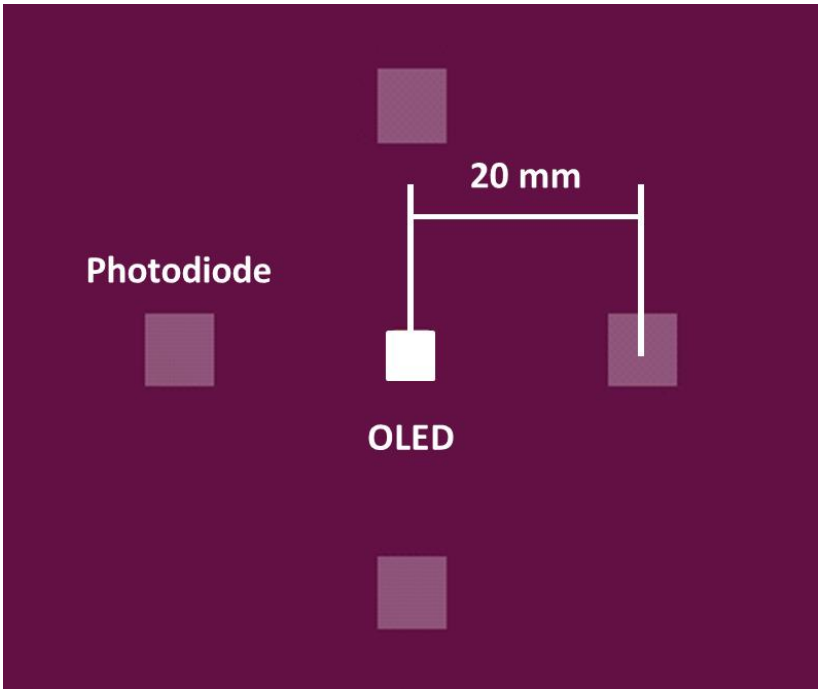

Figure 6.5: *Geometrical arrangements of the components in the sensor*

6.3.3 Optical models of skin, adipose fatty tissue and 1D anisotropic scattering muscle

Although muscle is anisotropic in all three dimensions, the initial model was simplified and did not take into account longitudinal and transverse anisotropy. The scattering in the muscle was modelled by the same Henyey-Greenstein approximation as in the skin or the adipose tissue. It was anisotropic only in the z-direction (in depth). This simplified model was created to evaluate how deep the signal can penetrate and how far the detector can be placed from the source. The skin and the adipose tissue were added to the model to evaluate how much it affects light distribution and signals coming from the muscle.

Optical properties of bulk muscle were only available for two wavelength[35]. The scattering coefficient at 515 nm was 53 mm^{-1}, and for 1024 nm it was 21.5 nm. The approximation of the scattering coefficient averaged over the emission spectrum of the OLED with the filter (580 nm to 700 nm) was calculated using *Eq. 4.11* and *Eq. 4.12*. An example of the calculations for 580 nm is the following. $a_{muscle} = 13.0$, $b_{muscle} = 0.926$, $g_{muscle} = 0.96$. The fitting parameters were taken from [31]. *Eq. 4.11*: $\mu_s'^{\text{muscle}}(\lambda), cm^{-1} = 13.0\left(\frac{580\text{ nm}}{500\text{ nm}}\right)^{-0.926} = 11.3307\text{ cm}^{-1}$. *Eq. 4.12*: $\mu_s^{muscle}(580\,nm) = \frac{11.3307\,mm^{-1}}{1-0.96} = 28.3267\,mm^{-1}$. The refractive index and the absorption coefficient were taken from [35] and were equal to $n_{muscle} = 1.37$, $\mu_a^{muscle} = 1\,mm^{-1}$.

The same calculations were done for the skin and the subcutaneous adipose tissue. The fitting parameters for the adipose fatty tissue were: $a_{adip} = 15.4$, $b_{adip} = 0.68$, $g_{adip} = 0.9$, $n_{adip} = 1.3$, $\mu_a^{adip} = 0.26\,mm^{-1}$, from *Eq. 4.11* and *Eq. 4.12* the scattering coefficient was $\mu_s^{adip}(580\,nm) = 13.92\,mm^{-1}$.

It is known that optical properties of skin differ hugely, so there were 5 different fitting parameters in the range of: $a_{skin} = 29.7 \ldots 48.9$, $b_{skin} = 0.75 \ldots 2.453$, $g_{skin} = 0.5 \ldots 0.82$. The values from Jacques, 1996 measurements (row #2, pageR41[31]) were taken for the simulations: $a_{skin} = 47.8$, $b_{skin} = 2.453, g = 0.8$. Ultimate scattering coefficients were found to be $\mu_s^{skin}(580\,nm). = 16.6\,mm^{-1}$. Values for n, g, μ_a were taken from V. Tuchin Handbook of Biophotonics[35], and were equal to $n_{skin} = 1.31$, $\mu_a^{skin}(633\,nm) = 0.27\,mm^{-1}$.

First, light propagation was modelled for individual layers of skin and adipose fatty tissue with the thicknesses equal to 2 mm each. The muscle was 30 mm (as by initial prediction the light at this wavelength would not penetrate deeper than this). The light propagation in all three layers is shown in ***Figure 6.6***. Due to a very small absorption, and the largest mean free path

($mfp = \frac{1}{\mu_s}$ or $mfp' = \frac{1}{\mu_s'}$[36]) the fat diffuses light more than the other tissue. This diffusion will have an adverse effect on the detection of the difference in directional scattering from the muscle. It will become challenging to detect the signal through large amounts of fat. Similar modelling results were reported in [37]. This showed that strongly scattering adipose tissue impedes with the detection of the oxygenation of the muscles (in terms of both sensitivity and sampling). In cases with thick adipose tissue it was possible to detect oxygen change in muscle when the light source and the detector were placed far away from each other. In this case at 20 mm the light interacted with the muscle at very shallow layers, but still it was possible to detect it.

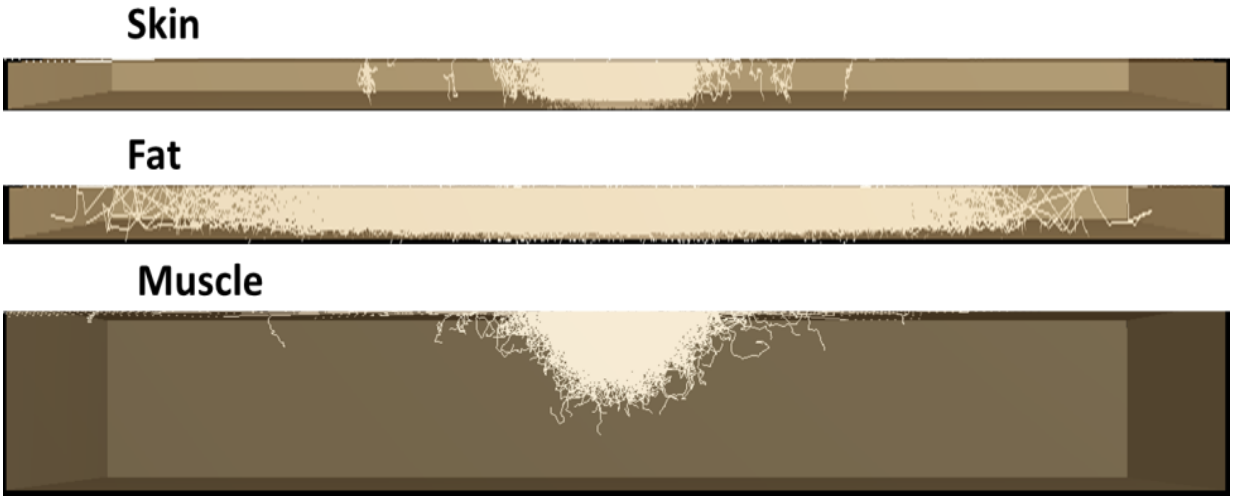

Figure 6.6: *Light propagation from the OLED made from Super Yellow polymer in individual layers of 2 mm thick skin, 2 mm thick adipose fatty tissue and 30 mm thick muscle.*

A distance of 20 mm between the source and the detector was taken for the initial simulations for the muscle contraction sensor. The model consisted of 2 mm thick layer of skin and 30 mm thick layer of muscle. The OLED and the detector were placed at a small gap from the surface of the skin. The model is shown in ***Figure 6.7***.

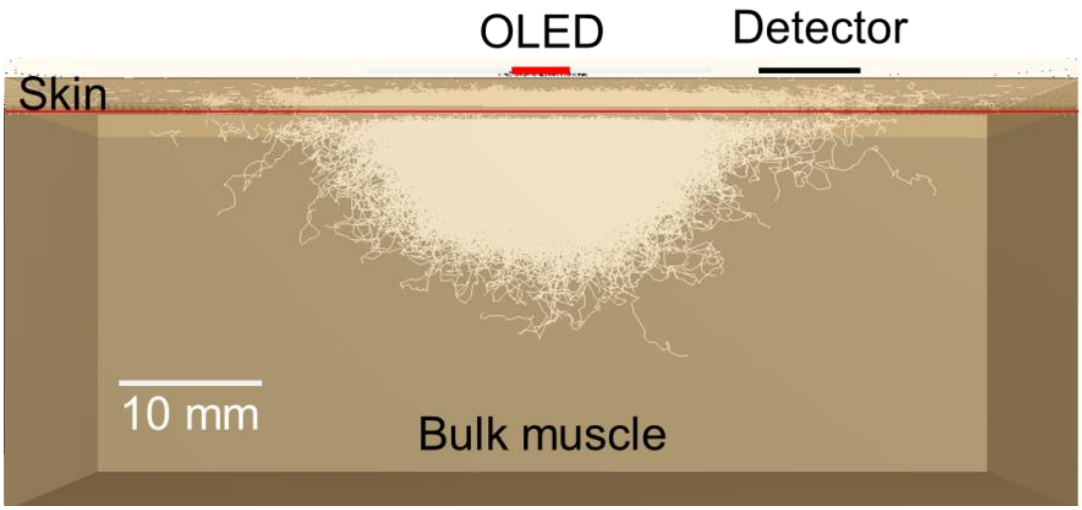

Figure 6.7: *Light propagation from Super Yellow polymer in two-layered tissue model. 2 mm of skin and 30 mm of muscle*

The maximal separation between the source and the detector at which there was still some light backscattered from the muscle and reaching the detectors was 20 mm. For SY emission spectrum the penetration depth was a little bit more than 20 mm.

When a thick, 5 mm layer of fatty tissue is added to the model (***Figure 6.8***), the light is diffused much more. The light penetrates only to a very small depth in the muscle. The overall penetration depth is reduced to 12 mm through all layers; the light penetrates through the 2 mm thick layer of skin, the 5 mm thick layer of fat, and only 3-5 mm thick layer of muscle. The light interacts with deeper layers of muscle in the centre (approx. 5 mm). These results agree with the findings in [37] that at 20 mm there was still some signal reaching the detector, but only from very shallow layers.

Figure 6.8: *Three-layered tissue model: 2 mm skin, 5 mm fat and 30 mm muscle. The light from SY polymer is diffused hugely through the fat, it only penetrates at 5 mm depth in muscle.*

This simplified model of layered tissue allowed for studying the penetration depth, selecting the separation between the source and the detector and estimating the maximum thickness of the fatty tissue at which optical detection of muscle activity was still possible. However, in order to find the optimal configuration for the sensor to discriminate between the two directional backscatterings from the muscle, it was necessary to be able to model anisotropic scattering along and across the muscle fibres.

6.3.4 Optical model of 3D anisotropic muscle and the performance of the sensor

Modelling of anisotropy of light scattering in muscle in two other directions, which were not considered by the simplified model, was implemented by creating the same geometrical arrangements of the scattering fibres as in the anatomical structure of muscle. The scattering was only modelled inside the fibres, the space in between the fibres was not scattering in the model. The integrated scattering in the ultimate muscle model resulted in more scattering events along the muscle fibres than across.

The model consisted of an array of 2 mm in diameter and 10 cm long scattering fibres. There were 480 fibres which formed 8 layers with 60 fibres in each layer. The fibres were placed next to each other (at 1 μm gap). The size of this array was $120.059\,mm \times 100\,mm \times 16.006\,mm$. The small micrometre precisions in the dimensions of the muscle array (59 μm x 0 μm x 6 μm) corresponded to the accumulated 1 μm distances between the 60 fibres next to each other in one layer and the 7 fibre layers stacked one on top of the other. The size of the muscle model corresponded to the anatomical dimensions of a bicep muscle; the size of one fibre corresponded to an average size of human skeletal muscle fibres[22,29]. The array was placed in a box with the same refraction and absorption as in the muscle fibres, except there was no scattering in that box. The size of the box was slightly bigger to accommodate the muscle array: $121\,mm \times 101\,mm \times 17\,mm$.

The scattering in the final version of the muscle model (the box and the fibres) had to correspond to the reported scattering coefficients for muscle tissue. So scattering in the fibres was increased to compensate for the non-scattering volume of the box. The volume of the box was $V_{box} = width \times length \times height = 121\,mm \times 101\,mm \times 17\,mm = 201757\,mm^3$. The volume of one muscle fibre was $V_{one\ muscle\ fibre} = \pi \cdot radius^2 \cdot length = 3.14 \cdot 1 \cdot 100 = 314\,mm^3$. The total scattering volume was $V_{all\ muscle\ fibres} = 60 \cdot 8 \cdot V_{one\ muscle\ fibre} = 156720\,mm^3$. The difference between scattering and non-scattering volumes was $volume\_difference = \frac{V_{box}}{V_{all\ muscle\ fibres}} = 1.378$. So the scattering coefficient in the fibres was increased to $\mu_{s\_compensated}^{muscle} = \mu_s^{muscle} \cdot volume_{difference} = 28.3267 \cdot 1.378 = 39.046\,mm^{-1}$.

The ultimate model of the muscle with a layer of skin and a layer of adipose fatty tissue is shown in ***Figure 6.9***. ***Figure 6.9***, b shows light scattering in one fibre. ***Figure 6.9***, c shows a cross section of power in the muscle model. There are more scattering events along the fibres and a larger power flux inside the fibres. This demonstrates the concept of how such geometrical arrangements of the fibres provide different scattering properties in transverse and longitudinal directions.

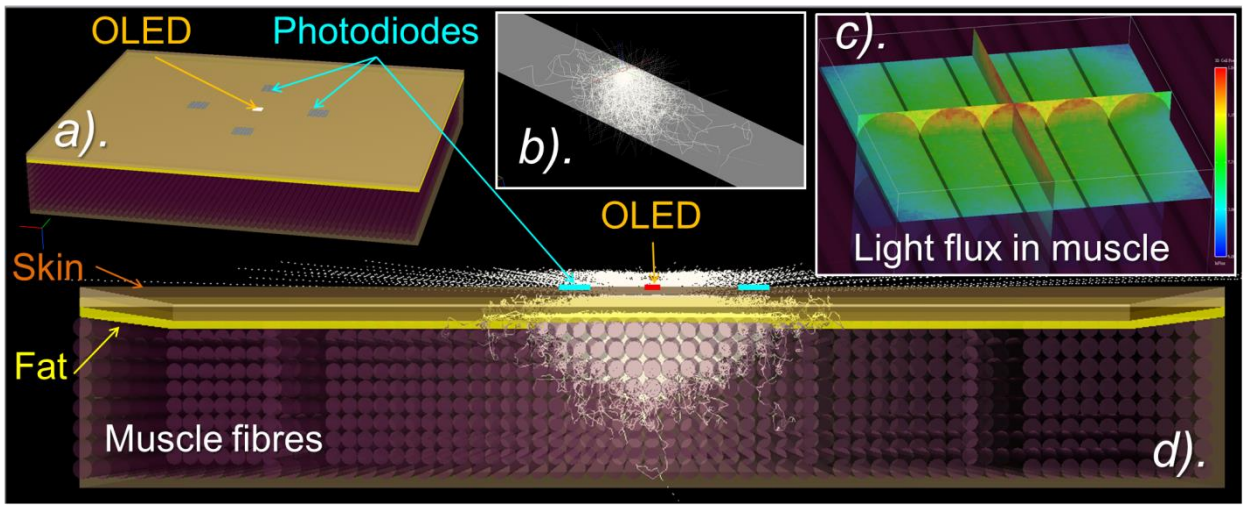

Figure 6.9*: Optical model of 3D anisotropic muscle and the sensor.* **a** *– The arrangements of the OLED and the phtodiodes.* **b** *– modelling of light propagation in one muscle fibre.* **c** *– modelling of power flux in muscle array.* **d** *– light propagation in the skin, adipose tissue and muscle fibres.*

The ultimate light propagation in the muscle is elongated (has a more elliptical profile compared to the simplified model) (***Figure 6.10***). The same simulations were done for two- and three-layered tissue.

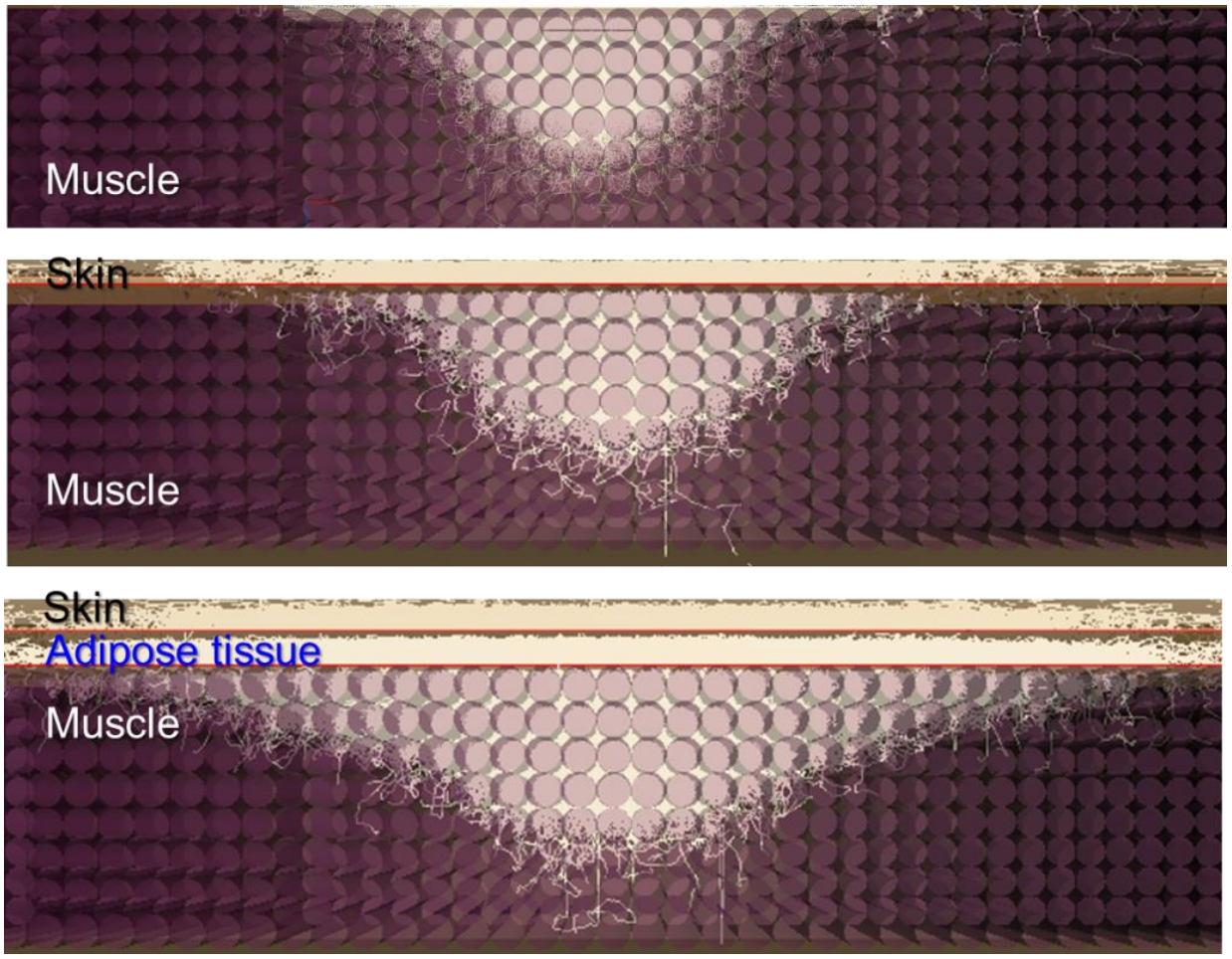

Figure 6.10: *Light propagation from SY polymer in layered tissue.*

Simulated power at two pairs of detectors (parallel and transverse) showed that there was more light backscattering along the fibres than across (***Figure 6.11***). The signal intensity decreased with the distance, however, the discrimination between the two directional scatterings increased. So the optimal separation of the source and the detectors was a trade-off between the signal intensity and the sensitivity.

When a 2 mm thick layer of skin and a 2 mm thick layer of adipose fatty tissue was placed on top of the muscle, the difference in the two directional scatterings decreases dramatically. At small distances between the source and the detector the signal was far too diffused and the difference between the two direction backscatterings was almost insignificant. At larger distances such as 20 mm the signal was very weak, but still allowed for discrimination between the two directional scatterings. At 20 mm distance the powers at the parallel and transverse detectors $P_{\times 2\ detectors\ along\ the\ muscle} = 8.08 \cdot 10^{-12}\ W$, and the power at left and right detectors was $P_{\times 2\ detectors\ across\ the\ muscle} = 2.94 \cdot 10^{-12}\ W$. The energy of one orange photon

from the SY polymer $E_{photon}(580\,nm) = \frac{hc}{\lambda} = 3.43 \cdot 10^{-19}\,J$. There were $\frac{2.94 \cdot 10^{-12}\,J}{3.43 \cdot 10^{-19}\,J} = 8.5 \cdot 10^{6}$ photons detected at the detectors across the muscle in this model.

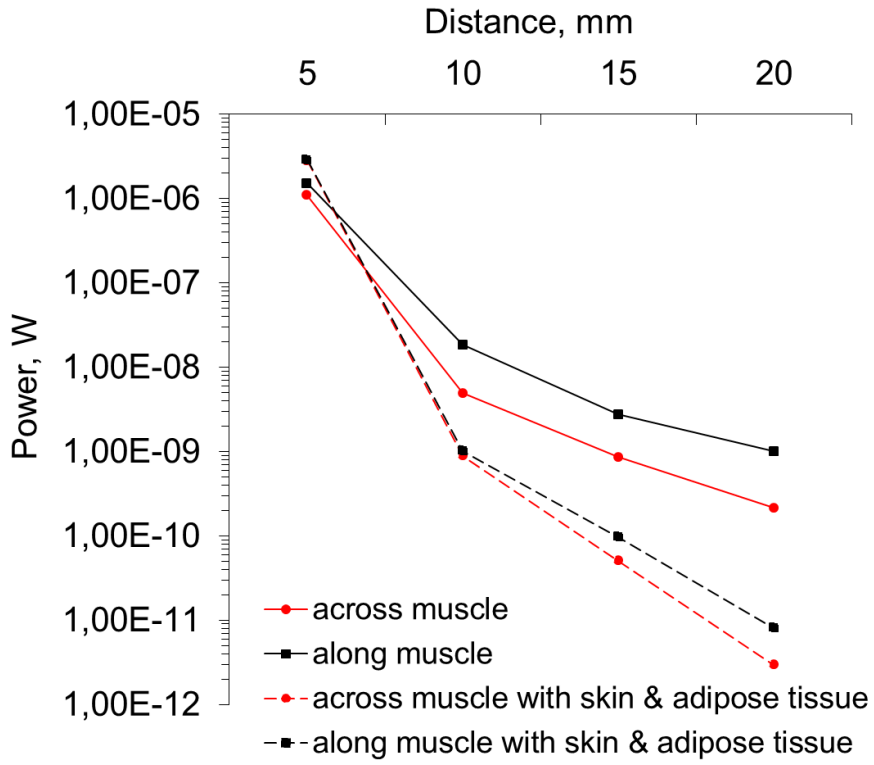

Figure 6.11: *Simulated power at the detectors along and across the muscle. The selectivity of the sensor increases with the distance between the source and the detector; however, the power drops down substantially. In the model with 2 mm layer of skin and 1 mm adipose tissue the discrimination between the two direction backscattering decreases; it becomes more difficult to measure muscle activity.*

6.4 Conclusion

My own work in the development of the optical organic muscle contraction sensor included optical modelling of light propagation in muscle at the wavelength of interest. This modelling helped to establish the design of the sensor, in particular to define and justify optimal distances between the light source and the detectors. Also it helped with understanding important processes such as how far light penetrates in muscle and at what depth the sensor is capable of probing the muscle activity. In addition the chapter investigated adverse effects of skin and fat in the operation of the sensor and helped to establish the limitations and ways to

optimise the performance. In particular it was shown that although the signal drops in intensity with the increase in the separation between the source and the detectors, the discrimination between the two directions of the scattering increases. This is crucial for optical sensing of the contractions. A two directional (longitudinal and transverse with respect to muscle fibres) anisotropic scattering model was implemented together with the standard one dimensional (in depth of muscle) anisotropic Henyey-Greenstein scattering model to describe light propagation in muscle in three dimensions. The model was applied to understand the operation of a muscle contraction sensor. The fully flexible organic muscle contraction sensor was demonstrated as a good candidate for application in improved functionality prosthetic devices. Not only can it add ability to better mimic the motion by distinguishing isotonic and isometric contractions, but is also insensitive to electromagnetic interference and immune responses. Implementation of the muscle contraction sensor using organic optoelectronics demonstrated the potential of using this appealing technology for a new generation of wearable devices which can revolutionize ambulatory healthcare, strengthen telemedicine, and find application in the gaming industry and other human-machine interactions.

Developed optical modelling approaches allowed for evaluating the performance of biomedical sensors using optical models of tissue. The modelling demonstrated that the choice of the optimal distance between the source and the detectors in the muscle contraction sensor was based on the drop of intensity at large distances but increased sensitivity for two directional scattering; it was chosen to be 20 mm. The light emitted by the Super Yellow polymer allowed for sensing the signals at approximately 20 mm in depth of the tissue.

Skin and adipose tissue have very strong diffusing properties. At short distances between the source and the detectors the sensor becomes insensitive to two directional scattering. For thick adipose tissue the signal penetrates only at shallow layers and requires at least 20 mm of separation between the source and the detectors.

In future the simulations could help to calibrate the sensor for each skin type to compensate for the differences in absorption. The absorption in skin type I is much lower than in skin type VI (by Fitzpatrick scale). When the sensor was tested, there was two orders of magnitude difference in the voltage measured on a bicep muscle for skin type II (white) and skin type V (dark brown). This means that if the prosthetic limb was calibrated to move as if the person wearing it had skin type V, but in fact the person wearing the limb had skin type II, the limb would hugely over respond to the measured signals; for intended small motion the limb would generate maximum range of the motion. In the opposite scenario, the limb intended to work for skin type II placed on skin type V would not be responsive to the low levels of signals.

So the modelling could give a guidance of the expected levels of the signals and help to adjust the calibration to each individual.

6.5 Reference

1. Scanaill CN, Carew S, Barralon P, Noury N, Lyons D, Lyons GM. A Review of Approaches to Mobility Telemonitoring of the Elderly in Their Living Environment. *Ann Biomed Eng*. 2006;34(4):547-563. doi:10.1007/s10439-005-9068-2.

2. Holman RR, Paul SK, Bethel MA, Neil HAW, Matthews DR. Long-Term Follow-up after Tight Control of Blood Pressure in Type 2 Diabetes. *N Engl J Med*. 2008;359(15):1565-1576. doi:10.1056/NEJMoa0806359.

3. Gong S, Schwalb W, Wang Y, et al. A wearable and highly sensitive pressure sensor with ultrathin gold nanowires. *Nat Commun*. 2014;5. doi:10.1038/ncomms4132.

4. Bonato P. No Title. *J Neuroeng Rehabil*. 2005;2(1):2. doi:10.1186/1743-0003-2-2.

5. Pang C, Lee G-Y, Kim T, et al. A flexible and highly sensitive strain-gauge sensor using reversible interlocking of nanofibres. *Nat Mater*. 2012;11(9):795-801. doi:10.1038/nmat3380.

6. Kim D-H, Lu N, Ma R, et al. Epidermal Electronics. *Science (80-)*. 2011;333(6044):838-843. doi:10.1126/science.1206157.

7. Jeong J-W, Yeo W-H, Akhtar A, et al. Materials and Optimized Designs for Human-Machine Interfaces Via Epidermal Electronics. *Adv Mater*. 2013;25(47):6839-6846. doi:10.1002/adma.201301921.

8. Shinar J, Shinar R. Organic light-emitting devices (OLEDs) and OLED-based chemical and biological sensors: an overview. *J Phys D Appl Phys*. 2008;41(13):133001. doi:10.1088/0022-3727/41/13/133001.

9. Bernards DA, Malliaras GG, Owens RM, eds. *Organic Semiconductors in Sensor Applications*. Berlin, Heidelberg: Springer Berlin Heidelberg; 2008. doi:10.1007/978-3-540-76314-7.

10. Attili SK, Lesar A, McNeill A, et al. An open pilot study of ambulatory photodynamic therapy using a wearable low-irradiance organic light-emitting diode light source in the treatment of nonmelanoma skin cancer. *Br J Dermatol*. 2009;161(1):170-173. doi:10.1111/j.1365-2133.2009.09096.x.

11. Forrest SR. The path to ubiquitous and low-cost organic electronic appliances on plastic. *Nature*. 2004;428(6986):911-918. doi:10.1038/nature02498.

12. Li G, Zhu R, Yang Y. Polymer solar cells. *Nat Photonics*. 2012;6(3):153-161. doi:10.1038/nphoton.2012.11.

13. Sessolo M, Khodagholy D, Rivnay J, et al. Easy-to-Fabricate Conducting Polymer Microelectrode Arrays. *Adv Mater*. 2013;25(15):2135-2139. doi:10.1002/adma.201204322.

14. Zhang S, Turnbull GA, Samuel IDW. Highly Directional Emission and Beam Steering from Organic Light-Emitting Diodes with a Substrate Diffractive Optical Element. *Adv Opt Mater*. 2014;2(4):343-347. doi:10.1002/adom.201300441.

15. Ghezzi D, Antognazza MR, Dal Maschio M, Lanzarini E, Benfenati F, Lanzani G. A hybrid bioorganic interface for neuronal photoactivation. *Nat Commun*. 2011;2:166. doi:10.1038/ncomms1164.

16. Khodagholy D, Doublet T, Quilichini P, et al. In vivo recordings of brain activity using organic transistors. *Nat Commun*. 2013;4:1575. doi:10.1038/ncomms2573.

17. Attili SK, Lesar A, McNeill A, et al. An open pilot study of ambulatory photodynamic therapy using a wearable low-irradiance organic light-emitting diode light source in the treatment of nonmelanoma skin cancer. *Br J Dermatol*. 2009;161(1):170-173. doi:10.1111/j.1365-2133.2009.09096.x.

18. Bansal AK, Hou S, Kulyk O, Bowman EM, Samuel IDW. Wearable Organic Optoelectronic Sensors for Medicine. *Adv Mater*. 2014. doi:10.1002/adma.201403560.

19. Samuel I, Bansal AK, Hou S, Kulyk O. An organic optoelectronic muscle contraction sensor for prosthetics. *SPIE Newsroom*. 2015. doi:10.1117/2.1201503.005812.

20. Chianura A, Giardini ME. An electrooptical muscle contraction sensor. *Med Biol Eng Comput*. 2010;48(7):731-734. doi:10.1007/s11517-010-0626-x.

21. López NM, di Sciascio F, Soria CM, Valentinuzzi ME. Robust EMG sensing system based on data fusion for myoelectric control of a robotic arm. *Biomed Eng Online*. 2009;8(1):5. doi:10.1186/1475-925X-8-5.

22. Guyton AC, Hall JE. *Textbook of Medical Physiology*. 11th ed. (Belfus L, Schmitt W, eds.). Elsevier Saunders; 2006.

23. Bazzotti L. Electromyography tension and frequency spectrum analysis of some masticatory muscles at rest, isotonic and isometric contractions. *Electromyogr Clin Neurophysiol*. 39(7):421-434.

24. Gwin JT, Ferris DP. An EEG-based study of discrete isometric and isotonic human lower limb muscle contractions. *J Neuroeng Rehabil*. 2012;9(1):35. doi:10.1186/1743-0003-9-35.

25. Li J, Li W, Hu H, Sha H, Sun L. Dynamics analysis and optimization for prosthesis based on drive energy consumption. In: *The 7th IEEE International Conference on Nano/Molecular Medicine and Engineering*. IEEE; 2013:18-21. doi:10.1109/NANOMED.2013.6766308.

26. TeachPE. Skeletal Muscle Cell Structure. *Anat Physiol*. 2015. http://www.teachpe.com/anatomy/structure_skeletal_muscle.php.

27. HUXLEY AF, NIEDERGERKE R. Structural Changes in Muscle During Contraction: Interference Microscopy of Living Muscle Fibres. *Nature*. 1954;173(4412):971-973. doi:10.1038/173971a0.

28. Huxley a. F, Niedergerke R. Measurement of the striations of isolated muscle fibres with the interference microscope. *J Physiol*. 1958;144(3):403-425.

29. М.В. ВОЛЬКЕНШТЕЙН. *ОБЩАЯ БИОФИЗИКА / § 5.2. Структура Мышцы И Мышечных Белков (с. 219-226)*. Москва: Наука; 1978.

30. Prahl S a. A Review of the Optical Properties of Biological Tissues. *IEEE J Quantum Electron*. 1990;26(12):2166-2185. doi:10.1109/3.64354.

31. Jacques SL. Optical Properties of Biological Tissues: A Review. *Phys Med Biol*. 2013;58(11):R37-R61. doi:10.1088/0031-9155/58/11/R37.

32. Hou S. Optical Detection of Muscle Contraction for Prosthesis Actuation. 2014.

33. Bansal AK, Hou S, Kulyk O, Bowman EM, Samuel IDW. Wearable Organic Optoelectronic Sensors for Medicine. *Adv Mater*. 2014:1-7. doi:10.1002/adma.201403560.

34. Gambino S, Bansal AK, Samuel IDW. Photophysical and charge-transporting properties of the copolymer SuperYellow. *Org Electron*. 2013;14(8):1980-1987. doi:10.1016/j.orgel.2013.03.038.

35. Popp J, Tuchin V V, Chiou A, Heinemann S. *Handbook of Biophotonics: Volume 1: Basics and Techniques*. Wiley-VCH; 2011. http://eu.wiley.com/WileyCDA/WileyTitle/productCd-3527410473.html.

36. Jacques SL, Prahl SA. Reduced scattering coefficient. *ECE532 Biomed Opt Oregon Grad Inst*. 1998. http://omlc.org/classroom/ece532/class3/musp.html.

37. Matsushita K, Homma S, Okada E. Influence of adipose tissue on muscle oxygenation measurement with an NIRS instrument. Benaron DA, Chance B, Ferrari M, eds. *SPIE*. 1998;3194:159-165. doi:10.1117/12.301048.

Chapter 7

Conclusion

Science never solves a problem without creating ten more.

— George Bernard Shaw (1856-19550),
Irish playwright, critic, political activist

The energy and the wavelength of visible light are comparable to the energy transitions and the sizes of living cells, large proteins and organelles. This makes it possible to use the energy of light to trigger many processes in cells and tissue, and also to visualize and sense many biological parameters. But if we go to shorter wavelengths (XUV-UV) the photons are already too energetic; their energy is absorbed by proteins, molecules and viruses. If we go even shorter wavelengths, X-rays and gamma rays, the energy of these photons is even more energetic; these rays mostly break the bonds in proteins and molecules. An example is radiotherapy, proton or ion-beam therapy for cancer where the energy of the beams is used to destroy the DNA in cancer cells[1]. Then if we go to the other side of the visible spectrum, to the far IR region, the energies of these photons are too low; the wavelengths are too long; so they are only absorbed by water and dissipate into heat. Beyond IR, in the millimetre range we, humans, are already transparent to this energy. So there is a so called optical window from 400 nm to 1.3 μm with little absorption, and mostly scattering in tissue[2]. This window allows penetration and interaction with tissue for sensing and treatment.

This thesis explored a few processes in the area of light-tissue interactions which were important for improvements in the Photodynamic therapy (PDT) of non-melanoma skin cancer (NMSC), developing new light sources for ambulatory treatment and other optical wearable devices such as for muscle contraction sensing.

PDT is a well-established treatment modality for NMSC with excellent cosmetic outcome, yet the response is only up to 80 % on average among the reports (a median clearance was 73% at a 6 months median follow-up, Ibbotson et al[3]; Morton et al[4] reported 90% clearance for actinic keratosis (AK) at a 3 month follow up, 80-97% clearance for superficial basal cell carcinoma (sBCC) at a 3 month follow up, 78% clearance for basal cell carcinoma (BCC) at a 48

month follow up). So the majority of the work in this thesis was aimed at investigating possible improvements in terms of expanding the knowledge of PpIX metabolism and also studying light transport in tissue with the view to optimise treatment light sources.

One of the key parameters involved in the treatment investigated in this thesis was the metabolism of a photosensitizer Protoporphyrin IX (PpIX) in healthy and diseased skin. The highest concentrations of PpIX formed after continuous application of 5-Aminolevulinic acid (ALA) and Methyl Ester 5-Aminolevulinic acid (MAL) precursors were observed at 24 hours (in BCC and healthy skin)[5] and 13-18 hours (in BCC and AK)[6] correspondingly. The highest specificity of accumulation of PpIX from ALA precursor was 2-4 hours, so the study [[5]] suggested that the optimal time to start ALA PDT treatment was any time after 2 hours from the application of an ALA precursor. In the case of application of the MAL precursor, PpIX concentration continued to increase over 13 hours[6]. The study recommended starting the treatment at 3 hours after the application of MAL. However, the graphs of the lesion to normal skin selectivity ratio did not show any obvious difference in the specificity of PpIX accumulation in lesions compared to healthy skin during 13 hours of MAL application while the fluorescence in lesions continued to grow[6]. So one of the questions investigated was how Ameluz gel (ALA precursor) and Metvix® cream (MAL precursor) are metabolised to PpIX during the three hours of recommended waiting time before commencing treatment. In addition there was interest in seeing if there were any particular fluorescence fingerprints in PpIX metabolic maps between the lesions or if there was any difference between the creams. By correlating the follow up data about the lesions' response to the treatment the hope was to find a positive correlation which could help to predict the PDT outcome on the day of the treatment. ***Chapter 2*** addressed a clinically-driven need to develop a convenient hand-held instrument which allowed for quick measurements of PpIX fluorescence on healthy volunteers and patients following simple protocols. The method developed and image analysis enabled robust referencing of the fluorescence images to the skin, which was important for the study of the formation of PpIX fluorescence patterns in time. The camera was able to visualise fluorescence in standard Coproporphyrin fluorescent solution, in-house made PpIX fluorescent phantoms and *in-vivo* from the skin of a healthy volunteer after administration of Ameluz gel and in AK and BCC lesions administered Ameluz and Metvix® PDT. This simple and handy device and the method demonstrated the potential to answer many clinically relevant questions.

In the future, it would be desirable to upgrade the current device to enable multi-band PpIX imaging. It is a known fact that blue light such as 405 nm wavelength which was used in the current version of the fluorescence camera penetrates only at superficial layers in skin

therefore exciting superficial PpIX fluorescence. Red light such as 632 nm which corresponds to one of the PpIX absorption peaks penetrates deeper in skin. So measuring fluorescence excited with this wavelength would give information about PpIX distribution at a greater depth. Another important imaging modality would be to add imaging of green auto-florescence emission excited by the same 405 nm wavelength. Auto-fluorescence can be helpful to observe structural changes in tissue due to the change in production of collagen, elastin and keratin in malignant cells. White light imaging using a colour camera would be useful to monitor the development of erythema (skin redness condition developed due to an inflammation) which only recently was associated with pain and the response to PDT[7].

In ***Chapter 3*** the prototype device was used in a small study on 11 healthy volunteers and 13 patients. PpIX formation was studied over three hours with a 10 minute interval (three hours is the recommended metabolism time before commencing PDT treatment).

Healthy volunteers were administered Ameluz gel (n=5) and Metvix® cream (n=6). The study area was the middle back avoiding paravertebral regions as the skin is the most uniform here. Also healthy skin on the back was developing average PpIX intensities compared to the other sites of the body[8,9]. This made this site most suitable for the baseline. The results showed that the fluorescence distribution was mostly uniform in all subjects. The fluorescence varied between the subjects and continued to grow over three hours of the measurement time. There was no statistical significance between the Ameluz and the Metvix® groups (p-value>0.005 in a two sample t-test with unequal variances). This suggested that healthy skin metabolises PpIX equally efficiently from both creams during three hours of the measured time and there were no specific fluorescence patterns in the uniform healthy skin on the back.

The results of PpIX fluorescence time course in 13 lesions of 13 patients (AK administered Ameluz PDT: n=5, AK administered Metvix® PDT: n=2, biopsy confirmed BCC administered Metvix® PDT: n=5) concurred with the findings in the healthy volunteers' cohort that the fluorescence varied and continued to grow during three hours of the measurement in all subjects. There was no statistical significance between the creams or between the lesions (p-values>0.05 for all groups: AK Ameluz vs AK Metvix vs BCC Metvix; AK (both creams) vs BCC). There was no significant correlation of the fluorescence to pain. The results of a 3 months (n=6) and a 1 year (n=6) follow up showed that PpIX fluorescence does not correlate to the lesions clearance. Although, it was demonstrated that PpIX fluorescence diagnostics can distinguish with a high degree of accuracy pre-clinical malignant changes in skin not visible to the naked eye, absence of correlation of PpIX fluorescence to the lesion clearance supports the opinions

that PpIX fluorescence alone is not the most reliable optical diagnostics technique for NMSC or for predicting PDT outcomes.

However, there are still no better ways of studying PpIX metabolism *in-vivo* than by measuring its fluorescence. The device and the method developed allowed for selecting and integrating fluorescence over an area in the time course images compared to one point measurement in the conventional fibre optics spectroscopes. Fluorescence time course analysis showed that in small regions on the same lesion with only 2-3 mm distance between the regions there was a 2-3 times difference in the fluorescence intensity. So integrating the fluorescence over an identical region of interest increases accuracy in the time course measurements compared to a one point measurement with an optical fibre. Another advantage is low excitation irradiance which was equal to 0.1 mW/cm^2.This, combined with synchronisation of the illumination during image acquisition reduces sensitivity to ambient light and the delivered light dose during the measurements. A small light dose eliminates the possibility of induced photobleaching of PpIX during the experiments.

The body sites were not specified in the patients' inclusion criteria as this would reduce the recruitment rates. In the end it was found to be the only significant factor influencing the fluorescence time course. The groups of "the head & neck" vs "trunk & hands" vs "lower leg & feet" were statistically significant ($p\text{-value}<0.05$). PpIX metabolism was higher in the head and the neck compared to the lower leg. It was found that fluorescence had a positive correlation to skin temperature across the body. This is of great relevance to PDT treatment, as the waiting times before commencing the treatment could be shortened by increasing the skin temperature, or ambient temperature for daylight PDT should be considered. Also it could explain the fact that cooling air for pain management reduces PDT outcomes.

This developed camera proved itself as a useful and accurate tool and enabled the discovery of interesting processes such as body site dependence of PpIX metabolism. Considering the capabilities of current camera technology, miniature LED, fast prototyping equipment, instrument development becomes easy, fast and relatively cheap. Therefore an upgrade of the current instrument to a multi-band imaging system could be easily implemented by adding extra red and white LED in the current illuminator PCB. Extra filters could be slided in and out with slight modification of the plastic casing of the camera yet keeping it compact and handheld. The current USB control module has the capability to drive another 6 channels of different colour wavelength illumination. Alternatively monochromatic CCD could be replaced by a colour camera, green and red pixels could be separately analysed in Matlab to separate auto-fluorescence and PpIX fluorescence as was implemented by Kurachi and Bagnato group[10]. In

order to keep high selectivity to PpIX narrow band pass filters such as was used in the fluorescence camera could be used in addition with a colour CCD sensor and the images could be converted in black and white to be able to analyse the fluorescence intensity.

In addition to multi-band fluorescence imaging, the future studies should include temperature measurement in order to provide more evidence to support the findings discovered in this study. Temperature distribution at large area of the body sites where the lesions are located could be imaged once before the treatment with an infrared camera, before PDT, then in the middle and after the treatment. Before the application of the cream the skin will have a base line temperature. Considering the fact that the cream is covered with an occlusive dressing the temperature may rise during the three hours of PpIX metabolism under the cover so it would be necessary to monitor the change of the temperature due to the dressing. Also it would be interesting to monitor the temperature change and the erythema development before during and after the PDT. This information will be useful to investigate the correlation of PpIX metabolism, the development of erythema, pain and PDT responses and to support the hypothesis that natural temperature distribution across the body pays a role in PpIX metabolism and PDT outcomes. PpIX photobleaching during PDT remains useful parameter for improving PDT dosimetry and predicting the outcomes, so similar to measuring the temperature it would be useful to measure PpIX fluorescence in the middle and after the treatment. Also, it becomes evident that PDT response can be predicted by the development of erythema on the next day after the PDT[7] so this would also be relevant to investigate in the future studies.

Alongside expanding the knowledge on the photosensitizer side, the work also focused on improving the other PDT treatment factor – light penetration into skin. ***Chapter 4*** focused on the development of an optical apparatus to study light transport in tissue. The high priority in this chapter was to apply commercial optical design software for the modelling. This would open up opportunities to design and optimise the devices.

The modelling was applied to simulate optical wireless power transmission through a brain phantom for potential applications in implantable robots. The power transmission was measured by a solar panel made of a few commercial photodiodes in a gel brain phantom. It was possible to collect 0.1 % of the source power at 5 cm in depth in the phantom, and 10 % at 1 cm depth. According to reports in the literature on power consumption of miniature robots, the current set up could allow powering a small robot deeper than 3 cm in the brain phantom. However, the current size of the solar panel and the size of the existing robots have to be miniaturised at least ten times before it would be possible to implant them in a real brain. There are many possible applications for such developments; one of the examples, collecting signals in

the brain during normal daily activity could help to learn about the hard problem of consciousness[11].

This project validated the software on a direct power comparison and gave confidence to use it for modelling of PDT light sources and light transport in skin. Even illumination is important in PDT devices. The modelling investigated how natural diffusion processes in skin can help to reduce non-uniformities in the model of the Ambulight PDT device. If incident illumination was 25 % non-uniform, at 1 mm in depth of skin it is compensated by 10 % leaving 15 % of ultimate non-uniformities. This is still not enough to compensate large especially very localized variations in incident irradiance and even illumination is essential in treatment PDT light sources. By using many LEDs and adding two diffusers to it, even illumination is achieved in the Ambulight PDT device, but at the cost of considerable complexity and thickness. OLEDs are desirable for application in ambulatory PDT devices because they are thin single-component surface-emitting light sources, they provide uniform emission and they do not require the use of the diffusers. A test OLED device from a potential supplier was characterised for future ambulatory PDT light sources. The OLED was modelled based on the measured characteristics. The result showed that the size of the device should be substantially larger to compensate for the drop of the intensity at the edges because of Lambertian emission. For instance for a 2 cm diameter treated area the OLED diameter should be approximately 3.5 cm.

The observations from ***Chapter 4*** led to the hypothesis that PDT light sources could benefit from forward scattering in skin. This was investigated in ***Chapter 5***. Directional emission could improve light transport. Directionality from OLEDs can be less than 15° [12]. Modelling suggested it would be possible to achieve 10 % improved light transmission in skin from such OLEDs. However, the measurement of light transmission from organic light emitting films with structured and Lambertian emission through fresh porcine skin did not show the expected improvement. During this study it was discovered that pig skin may not be the best choice for optical measurements as a surrogate of human skin and also as a robust phantom due to non-uniform structure, variation of optical properties between the animals and as a result of skin treatment by the butchers and during the measurements, etc. Therefore, the most robust optical measurement would be to use well-established phantoms. Intralipid with blood becomes a golden standard for representing absorption and scattering properties of skin[13]. Measurements on liquid phantoms in cuvettes or custom containers would enable simple protocols and avoid many assumptions and complications with measurement on fresh tissue. However, considering that there are so many differences for *in-vivo* and *ex-vivo* light transport in skin, probably the ultimate solution to investigate whether directionality can bring significant improvements in PDT

treatment would be a randomised double-blind clinical trial comparing directional and Lambertian OLEDs. There is no reason to believe that PDT outcomes should be worsened by using directional OLEDs compared to identical Lambertian OLEDs. Taking into account the experience in the group and the collaborating hospital where the first time OLED devices were successfully used in a clinical trial for ambulatory PDT[14,15] already established protocols and routines for implementing a trial could be adjusted for a new trial comparing directional and Lambertian OLEDs.

In ***Chapter 6*** optical modelling was used to understand the design of a different wearable device – a muscle contraction sensor. In this case also different light-tissue interaction processes were employed – anisotropic scattering by muscle. Due to the fibrous structure of muscle there is more light scattering along than across the fibres. When muscle contracts the aspect ratio of the fibres changes which results in the relative change in scattering in the parallel and the perpendicular direction to the muscle fibres. Detecting this change enables measurement of the degree and the type of muscle contraction[16]. The reported inorganic sensor was implemented on a flexible substrate with all organic flexible components and made on a wearable bandage. The signals measured by the sensor were used to actuate a robotic arm to mimic the motion of the arm of the person wearing the sensor[17,18]. This demonstrated the potential to use this sensor in prosthetic devices. The fact that the sensor successfully distinguished two types of contractions which has not been achieved by the electromyography (EMG) sensors so far, demonstrates the superiority of optical sensors to EMG sensors. For the actuation of prosthetic devices it means that optical sensors can offer improved functionality by mimicking the motions requiring resisting or withstanding pressure which relates to isometric contractions. In addition organic optoelectronics avoids the problems of electromagnetic interference. Optical sensing is non-invasive; it does not cause an immune response and eliminates the need to replace degradable EMG and the performance of a simple but still a surgical procedure. In addition the sensor can be thin and flexible conforming body shape and easily integrating in the design of prosthetic devices.

Optical modelling helped to understand the performance of the sensor and find an optimal distance between the light source and the detectors. The results showed that the light from an OLED made of a Super Yellow polymer allowed penetration and probing of muscle activity to approximately 20-25 mm in depth. The largest and optimal distance between the source and the detector in a model with a 2 mm thick layer of skin on top of the muscle can be 20 mm. At this distance the discrimination between the two signals relating to backscattering in parallel and perpendicular direction with respect to muscle fibres is the largest while the intensity

of the signal is still sufficient for optical detection. Adipose fatty tissue has adverse effects on the detected signals. Because of high scattering and low absorption, fatty tissue diffuses the light, reduces penetration depth and the discrimination between the transverse and longitudinal backscattering. After a layer of fatty tissue 5 mm thick the light interacted with only a shallow layer of the muscle; it would not be possible to detect muscle activity in individuals with a much thicker layer of fatty tissue. The measurements in skin type II and V (by Fitzpatrick scale) showed that the levels of the signal varied by two orders of magnitude (because of the difference in absorption). For the application of the sensor in prosthetic devices it means that the sensor calibrated for one type of the skin would over respond or would be insensitive to the signals measured on individuals with different skin type. So another useful application of the modelling could be to help with the calibration of the sensor on the levels of the signals and the degree of the motion of the prosthetic devices by taking into account the differences in absorption of different skin types.

Overall, the work in this thesis demonstrates the great potential of light to revolutionise current health care by employing various processes of how light interacts with tissue. Only a few processes were covered in this thesis, but there are many more which can be pursued with the same or similar approaches. Light can be used in treatment of many diseases. The thesis has shown that new light emitting devices such OLEDs can be tuned, shaped, structured and implemented on wearable bandages for ambulatory treatment and point of care diagnostics. Optical modelling helps with the design of the devices. The simulations improve our understanding of how light interacts with different types and layers of tissue. Diffuse reflectance measurement and regression modelling allows for extraction of optical properties. Fluorescence and thermal imaging can help to monitor PDT, diagnose malignant changes in skin and provide information about relevant biological factors such as temperature and PpIX concentration in skin to improve the treatment. All of these methods (optical sensing, imaging, and modelling) could be combined. Monitoring of PpIX fluorescence, measuring optical properties of skin and blood volume in the skin could allow for controlling light delivery during PDT in real time.

7.1 Reference

1. Schardt D, Elsässer T, Schulz-Ertner D. Heavy-ion tumor therapy: Physical and radiobiological benefits. *Rev Mod Phys*. 2010;82(1):383-425. doi:10.1103/RevModPhys.82.383.

2. Ansari MA, Mohajerani E. Mechanisms of laser-tissue interaction: I. Optical properties of tissue. *J*

Lasers Med Sci. 2011;2(3):119-125.

3. Ibbotson SH, Dawe RS, Morton C a. A survey of photodynamic therapy services in dermatology departments across Scotland. *Clin Exp Dermatol*. 2013;38:511-516. doi:10.1111/ced.12051.

4. Braathen LR, Szeimies R-M, Basset-Seguin N, et al. Guidelines on the use of photodynamic therapy for nonmelanoma skin cancer: an international consensus. International Society for Photodynamic Therapy in Dermatology, 2005. *J Am Acad Dermatol*. 2007;56:125-143. doi:10.1016/j.jaad.2006.06.006.

5. Fritsch C, Lehmann P, Stahl W, et al. Optimum porphyrin accumulation in epithelial skin tumours and psoriatic lesions after topical application of delta-aminolaevulinic acid. *Br J Cancer*. 1999;79(9-10):1603-1608. doi:10.1038/sj.bjc.6690255.

6. Angell-Petersen E, Sørensen R, Warloe T, et al. Porphyrin formation in actinic keratosis and basal cell carcinoma after topical application of methyl 5-aminolevulinate. *J Invest Dermatol*. 2006;126(2):265-271. doi:10.1038/sj.jid.5700048.

7. Lerche CM, Fabricius S, Philipsen PA, Wulf HC. Correlation between treatment time, photobleaching, inflammation and pain after photodynamic therapy with methyl aminolevulinate on tape-stripped skin in healthy volunteers. *Photochem Photobiol Sci*. 2015;14(5):875-882. doi:10.1039/C5PP00069F.

8. Lesar A, Ferguson J, Moseley H. An investigation of the fluorescence induced by topical application of 5-aminolaevulinic acid and methyl aminolaevulinate at different body sites on normal human skin. *Photodiagnosis Photodyn Ther*. 2011;8(2):97-103. doi:10.1016/j.pdpdt.2010.12.004.

9. Ibbotson SH, Jong C, Barnetson R, Padgett M, O'Dwyer M, Ferguson J. Characteristics of 5-aminolaevulinic acid-induced protoporphyrin IXfluorescence in human skin in vivo. *Photodermatol Photoimmunol Photomed*. 2006;22(2):105-110. doi:10.1111/j.1600-0781.2006.00202.x.

10. Blanco KC, Moriyama LT, Inada NM, et al. Fluorescence guided PDT for optimization of the outcome of skin cancer treatment. *Front Phys*. 2015;3(April):1-7. doi:10.3389/fphy.2015.00030.

11. The ultimate puzzle: What is consciousness? *Econ*. 2015. http://www.economist.com/news/science-and-technology/21664284-without-consciousness-we-have-no-way-proving-we-or-anything-else-exists-what-it-and?fsrc=scn/fb/wl/vi/st/whatisconsciousness.

12. Zhang S, Turnbull GA, Samuel IDW. Highly Directional Emission and Beam Steering from Organic Light-Emitting Diodes with a Substrate Diffractive Optical Element. *Adv Opt Mater*. 2014;2(4):343-347. doi:10.1002/adom.201300441.

13. Kanick SC, Davis SC, Zhao Y, et al. Dual-channel red/blue fluorescence dosimetry with broadband reflectance spectroscopic correction measures protoporphyrin IX production during photodynamic therapy of actinic keratosis. *J Biomed Opt*. 2014;19:075002. doi:10.1117/1.JBO.19.7.075002.

14. I.D.W. Samuel JF and AM. OLEDS: Next generation photodynamic therapy of skin cancer. In: *PDT Book Chapter*.; :1-6.

15. Attili SK, Lesar A, McNeill A, et al. An open pilot study of ambulatory photodynamic therapy using a wearable low-irradiance organic light-emitting diode light source in the treatment of nonmelanoma skin cancer. *Br J Dermatol*. 2009;161(1):170-173. doi:10.1111/j.1365-2133.2009.09096.x.

16. Chianura A, Giardini ME. An electrooptical muscle contraction sensor. *Med Biol Eng Comput*. 2010;48(7):731-734. doi:10.1007/s11517-010-0626-x.

17. Bansal AK, Hou S, Kulyk O, Bowman EM, Samuel IDW. Wearable Organic Optoelectronic Sensors for Medicine. *Adv Mater*. 2014. doi:10.1002/adma.201403560.

18. Engineering: Muscle sensor controls robot arm. *Nature*. 2015;517(7533):124-124. doi:10.1038/517124b.

By believing passionately in something that still does not exist, we create it. The non-existent is whatever we have not sufficiently desired.

— Franz Kafka (1883-1924),
German-speaking Jewish writer

Appendix I: Author's contributions

Publications

1. O Kulyk, et all, Development of a handheld fluorescence imaging device to investigate the characteristics of protoporphyrin IX fluorescence in healthy and diseased skin, Photodiagnosis and Photodynamic Therapy Journal (accepted subject to minor corrections)
2. Ifor Samuel, Ashu Kumar Bansal, Shuoben Hou, and Olena Kulyk. An organic optoelectronic muscle contraction sensor for prosthetics / SPIE Newsroom, Apr 2015. DOI 10.1117/2.1201503.005812
3. Ashu K. Bansal, Shuoben Hou, Olena Kulyk, Eric M. Bowman and Ifor D. W. Samuel, Wearable Organic Optoelectronic Sensors for Medicine. Advanced Materials, 14 Dec 2014 (Invited contribution), DOI: 10.1002/adma.201403560

Oral presentations at conferences

4. O Kulyk, et all, SPIE Photonics West 2015, San Francisco CA, Optical Methods for Tumour Treatment and Detection: Mechanisms and Techniques in Photodynamic Therapy XXIV, "Fluorescence time course imaging of healthy and diseased skin for PpIX metabolic maps used in topical PDT and its correlation to the skin and lesions structures," SPIE Paper Number 9308-25, 2/8/2015.
5. O Kulyk, et all, SPIE Photonics West 2015, San Francisco CA, Bioinspired, Biointegrated, Bioengineered Photonic Devices III, "Optical design and modelling of tissue for application as wearable optoelectronic sensors," PIE Paper Number 9341-8, 2/7/2015
6. O Kulyk, et all, Laser Europe 2014, Amsterdam, PDT & Biophotonics, Session 2, Fluorescence Imaging for Healthy and Diseased Skin to Develop Better Understanding of Metabolism and Uniformity of 5-Aminolaevulinic Acid (ALA) and Methyl Aminolevulinate (MAL) used in topical PDT, May 23, 2014

Appendix II: Capturing fluorescence – Protocol v.1 21.10.2013

Protocol title: Capturing fluorescence imaging of the skin: patients with skin tumours and healthy volunteers

University of St Andrews Teaching and Research Ethics Committee UTREC Approval Reference No: PA10783,

East of Scotland Research Ethics Service EoSRES Tayside medical science Centre TACS REC Ref # 13/ES/0151,

Tayside medical science Centre TACS R&D Ref # 2013DS03,

Integrated Research Approval System IRAS Project ID: 136393

Capturing fluorescence imaging of the skin: patients with skin tumours and healthy volunteers

Study Protocol

Chief Investigator: Dr Sally Ibbotson
Photobiology Unit
Ninewells Hospital & Medical School
Dundee DD1 9SY

Investigators: Professor James Ferguson
Photobiology Unit
Ninewells Hospital & Medical School
Dundee DD1 9SY

Professor Harry Moseley
Photobiology Unit
Ninewells Hospital & Medical School
Dundee DD1 9SY

Dr Julie Woods
Photobiology Unit

Ninewells Hospital & Medical School
Dundee DD1 9SY

Professor Ifor Samuel
SUPA, School of Physics & Astronomy,
University of St. Andrews, North Haugh
St. Andrews
Fife KY16 9SS

Miss Olena Kulyk
SUPA, School of Physics & Astronomy,
University of St. Andrews, North Haugh
St. Andrews
Fife KY16 9SS

Dr Ronan Valentine
Photobiology Unit
Ninewells Hospital & Medical School
Dundee DD1 9SY

Introduction

Photodynamic therapy (PDT) is an effective treatment for superficial non-melanoma skin cancers (NMSC) and dysplasia with excellent cosmetic outcome, [1]. Topical PDT describes light activation of a photosensitiser (PpIX) derived from a pro-drug in a cream (methyl aminolevulinate acid [Metvix®], aminolaevulinic acid [Ameluz®]), in the presence of molecular oxygen, which together activate PplX. Concentration and distribution of the drug in the skin is one of the most important parameters influencing efficacy of treatment. Information about the amount of photosensitiser present can be acquired by measuring its fluorescence. For PpIX, the fluorescence is red light (635 nm wavelength) emitted by healthy and diseased skin following application of the drug. Fluorescence occurs when violet or blue light (405 nm wavelength) illuminates the skin containing the photosensitiser. Routinely Wood's light (405nm is used to qualitatively estimate the fluorescence from the lesion before PDT treatment. The optical biopsy system, (OBS) is used as a quantitative tool to measure average fluorescence intensity over wavelength ranges at specific sites. The fluorescence intensity is measured at several points on the lesion and the result

is averaged. During PDT the concentration of PpIX decays which is called photobleaching. The OBS is used in photobleaching experiments to gain information about the average concentration of the photosensitizer present and photobleached during treatment. Photobleaching experiments help expand the knowledge regarding how PDT works and optimal treatment parameters.

This study aims to quantitatively measure fluorescence intensity at each point on the skin. Fluorescence will be imaged with a camera we have developed, and quantified with a computer program. Fluorescence imaging is a powerful tool for PDT diagnostics and has been used in a number of qualitative and quantitative clinical studies at the Photobiology Unit (PBU), Ninewells Hospital, Dundee and other institutions, [2-6]. Unlike the OBS, fluorescence imaging gives information about spatial distribution of fluorescence. These images show how well the cream is absorbed by skin and converted into the photosensitiser and how uniformly this is distributed over the treated area.

The two key differences between an earlier photobleaching study we have undertaken in the department, which employed the OBS, A Quantitative Study of In Vivo Protoporphyrin IX Fluorescence Photobleaching during Photodynamic Therapy*, and the current study are that during the previous photobleaching experiments* data were taken infrequently during treatment and were point source measurements, whereas the current study aims to image spatial distribution and amount of fluorescence using a camera system each 10-15 minutes over 3 hours after cream application. The data gathered during the current fluorescence imaging experiments will help to determine the optimal time when the treatment should start. The study will also compare the effectiveness of two PDT creams, Metvix® and Ameluz®. Imaging two types of lesions, basal cell carcinoma (BCC) and actinic keratosis (AK), will improve understanding of the response to PDT of different people and with different diagnoses.

For the healthy volunteer cohort, study participation will last one day and is not expected to cause any discomfort or side effects. Five volunteers will have Metvix

applied to a selected skin site and five volunteers will have Ameluz applied to a selected skin site.

For the patient cohort, the study will be carried out on the day of the planned PDT treatment. Five patients diagnosed with AK will have Ameluz® applied, five will have Metvix® applied, and five patients with BCC will have Metvix® applied. The fluorescence imaging procedure is not expected to cause any discomfort or side effects to the patient and should have no influence on treatment outcome.

Aims

This research aims to improve our understanding of how we can optimise PDT treatment by identifying the peak time(s) of fluorescence under the experimental conditions studied.

We are also aiming to compare the efficiency of the creams, Metvix® and Ameluz®, at producing PplX and the response of two lesions, BCC and AK, to PDT.

Research questions

1. How much, how uniformly and how fast is the photosensitiser being formed from
   the pro-drug cream in healthy and diseased skin?
2. What is the optimal time to start treatment?
3. Is fluorescence intensity, distribution or photobleaching associated with persistence or recurrence of BCC and AK

Study Design

On the day of the study, the cream will be applied to a small area of up to 2 cm by 2 cm to the skin of healthy volunteers or to the lesion of patients. A disposable alignment pattern will be used to accurately position the camera for taking fluorescent images. The contour along the alignment pattern will be drawn. The camera will be aligned with the contour. The parameters of the camera will be set based on preliminary experimental data. The images of the spot will be taken every 10-15 minutes for three hours. For healthy volunteers; after three hours the remaining

cream will be wiped off and the area will be covered with a small occlusive dressing to prevent reaction of the skin to the sunlight. Their participation will be completed and the volunteers will be free to go. For the patients; after the last measurement the cream will be wiped off and they will have their planned PDT treatment. Both patients and volunteers will be advised to contact the research group if they have any questions or concerns.

Study Population

The study will include:

- 5 healthy volunteers administered Metvix®
- 5 healthy volunteers administered Ameluz®
- 5 patients diagnosed with AK and administered Ameluz® PDT
- 5 patients diagnosed with AK and administered Metvix® PDT
- 5 patients diagnosed with BCC and administered Metvix® PDT

Potential participants with superficial non-melanoma skin cancer and dysplasia who are suitable for the study will be identified by a consultant dermatologist (Chief Investigator) during screening of referral letters of patients referred for PDT and an invitation to consider this study and Participant Information Sheet will be sent out with the PDT appointment letter. The study will then be discussed with the patient when they attend clinic, by which time they will have received and read the Participant Information Sheet. Written informed consent will be obtained at that stage if the patient is happy to go ahead and participate in the study.

Healthy volunteers will be identified from the healthy volunteer database and will be contacted by the Clinical Trials Coordinator as previously arranged (email or text). If they reply with interest, they will be sent the study Participant Information Sheet (PIS). All subjects will be given at least 24 hours to read the PIS and have the opportunity to have any questions answered. If willing to proceed, informed consent will be obtained by the consultant dermatologist or a delegated suitably qualified member of the research team.

Inclusion Criteria (patient cohort)

1. Patients presenting with superficial non-melanoma skin cancer and dysplasia.

2. Age 18 years and over

3. Males and females

4. Capable of giving informed consent

5. Able to understand and adhere to protocol requirements

Inclusion Criteria (healthy volunteer cohort)

1. Age 18 years and over (age matched to patient cohort as is practicably possible)

2. Males and females

3. Capable of giving informed consent

4. Able to understand and adhere to protocol requirements

Exclusion Criteria

1. Patient's skin lesion has had previous treatment within the last four months.

2. Unable to give informed consent

3. Known allergy to Metvix or Ameluz

4. Known to have a light sensitivity disorder

Study Procedure

On the day of the study, after informed consent has been taken, a baseline reading of the skin site will be taken. Then the cream will be applied by technical staff to healthy or diseased skin of the subject and left for absorption. Every 10-15 minutes, images of fluorescence will be taken. Before taking an image the cream will be wiped off. After taking the image a small amount of the cream will be re-applied and covered again. Ambient light will be kept low to prevent exposure of the skin site during the procedure of taking images. The images will be recorded for further processing and stored on a secure NHS Tayside computer. After three hours, when the measurement will have finished, the remaining cream will be wiped off the skin and the skin will be covered with a small occlusive dressing to the site for 24 hours to prevent exposure from daylight causing photobleaching of reaccumulated PplX.

After that the subject will have completed the study.

Patients will have their planned PDT treatment straight after the last measurement.

Equipment Description

The camera being used to take fluorescence images of healthy and diseased skin has a UV flash with the power of 0.1 mW/cm^2 with the duration of the pulse of less than one second, depending on the exposure time of the camera. Total dose delivered to the skin is much below MPE and exposure time. The camera has a filter to pass only red fluorescence. The field of view of the camera is 23 x 31 mm. The size of the image is 480 x 640 pixels. The camera has fixed focal distance of 8.5 cm. The camera is USB powered. The camera connects to a laptop with user interface. Although not CE marked, the use of the camera in clinical research has been approved by the Instrumentation Department of NHS Tayside Medical Physics.

Checking System Performance

The camera will be checked periodically, twice a month, against a fluorescence standard solution coproporphyrin III regularly used in the PBU to check the performance of the optical biopsy system (OBS) which is used for photobleaching experiments during PDT treatment. Also, the camera will be checked against fluorescent phantoms, fabricated at School of Physics, University of St Andrews, which have the same fluorescence intensity as is expected from the skin with accumulated drug after three hours of cream application. Fluorescent patterns will be used to check the focus of the camera. This process will assess the ability of the system to produce fluorescence images with consistent intensity at 635 nm ensuring repeatability and reproducibility.

Incidental Findings

Although we do not foresee any adverse events, any abnormal reactions detected will be managed in the conventional manner, i.e., the participant will be reviewed by a consultant dermatologist in the Photobiology/Dermatology department.

Reimbursement

Healthy volunteers will receive £50 as reimbursement for inconvenience and travel expenses. Patients will not receive reimbursement as will be attending for treatment anyway.

Statistical Analysis

The images will be analysed using digital image processing algorithms. Comparisons of fluorescence time course between and within individuals will be performed using Student's t-test or equivalent non-parametric methods where applicable. As this is a pilot study a power calculation is not applicable but the numbers stated are considered realistically achievable for these investigations.

Feasibility

The study is a straightforward and non-invasive procedure.

Conclusion

We are planning the study to gather fluorescence images from healthy and diseased skin. This information will enable us to develop better understanding of how the cream used for PDT works, how well it is absorbed by the skin and converted into the drug PpIX and how uniform it distributes over an area of healthy skin and diseased skin. We will also collect data on different lesions, AK and BCC, which will help us to understand how different lesions respond to PDT treatment. Finally, the information on fluorescence intensity during three hours of cream application will help to identify the optimal time when the treatment should start. All of the aspects of the study will help to optimise PDT treatment protocols.

Dissemination of Knowledge Gained

Finalised anonymous data will be presented at scientific meetings and conferences, published thesis and scientific journals.

References

1. National Health Service (NHS), UK (Last reviewed: 03/10/2012). http://www.nhs.uk/Conditions/Cancer-of-the-skin/Pages/Introduction.aspx
2. Hewett, J., McKechnie, Sibbett, W., Ferguson, J, Clark, C., Pdgett, M. *"Fluorescence detection of superficial skin cancers",* Journal of Modern Optics, 2000. **40** (11)**:** p. 37-41.
3. Sandberg, C., Paoli, J., Halldin, C. B., Gillstedt, M., Larkö, O., Wennberg, A.M., *"Photodynamic therapy for "difficult-to-treat" basal cell carcinomas. Do poorly responding BCCs lack accumulation of protoporphyrin IX after ALA/MAL application?"*, Proc. of SPIE, 2009. **7380** (73805K)
4. Sandberg, C., Paoli, J., Gillstedt, M., Halldin, C.B., Larkö, O., Wennberg, A.M., *"Fluorescence diagnostics of basal cell carcinomas comparing methyl-aminolaevulinate and aminolaevulinic acid and correlation with visual clinical tumour size"*, Acta dermato-venereologica, 2011. **91** (4): p. 398-403
5. Togsverd-Bo, K., Idorn, L. W., Philipsen, P., Wulf, H. C., Hædersdal, M., *"Protoporphyrin IX formation and photobleaching in different layers of normal human skin: methyl- and hexylaminolevulinate and different light sources"*, Experimental dermatology, 2012. **21** (10): p. 745-750
6. Tyrrell, J., Campbell, S., Curnow, A., *"Validation of a non-invasive fluorescence imaging system to monitor dermatological PDT"*, Photodiagnosis and photodynamic therapy, 2010. **7** (2): p. 86-97

Appendix III: Capturing fluorescence –Device assessment for clinical trials

Appendix IV: Capturing fluorescence – Standard Operating Procedure (SOP)

Standard Operating Procedure SOP 001 cleaning of fluorescence device

Document Number: SOP 001

Title: Cleaning of fluorescence imaging device

Version: 1.0

Authors: Olena Kulyk

Effective from:	01 November 2013
Valid to:	31 October 2014
Superceded Version Number & Date (if applicable)	

Revision History: This is the original version of this document

Comments:

Reviewed by:

Signature:

1. Purpose/Background

To ensure safe and effective standard of hygiene of the imaging device being used in a patient/volunteer clinical study.

2. Scope

Applies to all research team members who handle the imaging device

3. Responsibilities

All research team members are responsible for reading this SOP and signing to state that they understand this SOP.

4. Procedure

- Device 'patient contact' area to be covered with Tegaderm™ dressing when in use.
- Tegaderm™ dressing to be replaced after each subject.
- Device to be cleansed between subjects using 'azowipes' as supplied in the clinical area of the Photobiology Unit
- Once cleaned, the device should be allowed to air dry.
- Device to be stored in a clean, dry secure area

5. Related documents

NHS Tayside Infection Control Policy (13/09/2013)

6. Approval and sign off

Author:

Name: Olena Kulyk

Designation: Researcher

Signature: Date: 10 October 2013

Approved by:

Name:

Designation: Clinical Trials & Project Coordinator

Signature: Date:

Member of staff PRINT NAME	Version number of SOP	SOP read and understood (sign)	Date

Appendix V: Capturing fluorescence – Healthy Volunteer Participant Information Sheet PIS v.2 17.12.2013PIS

PARTICIPANT INFORMATION SHEET
HEALTHY VOLUNTEER COHORT

Capturing fluorescence imaging of the skin: patients with skin tumours and healthy volunteers

My name is Olena Kulyk and I am a 2nd year PhD Physics Student at the University of St. Andrews. **I am required to undertake a project as part of my course and invite you to take part in the following study.** However, before you decide to do so, I need to be sure that you understand firstly why I am doing it, and secondly what it would involve if you agreed. I am therefore providing you with the following information. Please read it carefully and be sure to ask any questions you might have and, if you want, discuss it with others including your friends and family. I will do my best to explain the project to you and provide you with any further information you may ask for now or later.

Why are we doing this study?

Photodynamic therapy is a treatment used to treat areas of sun damage and skin cancer. It works by applying a cream which contains a chemical in it which is taken up into the skin and converted to another chemical which is light sensitive. This light sensitive chemical fluoresces (produces a crimson red light) when blue light is shone on it. This crimson red fluorescence can be detected by an imaging camera. This allows us to work out how much accumulates in normal skin and whether there are increased amounts present in abnormal diseased skin. We

hope that monitoring fluorescence of this chemical (protoporphyrin IX, PpIX) will increase our understanding of how PDT works and allow us to improve treatment regimes.

Why have I been chosen?
One part of our study is to try and increase our understanding of what happens when the cream applied in PDT is applied to normal skin, and when the peak fluorescence occurs and it is because you are a healthy normal volunteer that you have been selected to participate.

Do I have to take part?
Participation in this study is entirely voluntary and you are free to refuse to take part or to withdraw from the study at any time without having to give a reason and without this affecting any future healthcare.

What will happen to me if I take part?
We will invite you to come to the Photobiology Unit, Level 8, Ninewells Hospital & Medical School, Dundee to speak with one of our Research Team when you will be given the opportunity to ask any questions you may have regarding the research study. If you agree to take part in the study, a member of the research team will then ask you to sign a consent form and the study procedure will be performed. You will receive a copy of this Participant Information Sheet and signed Consent Form to keep.

Once the PDT cream has been applied we will take measurements of the study skin site every 10 -15 minutes throughout the three hour period. The cream will be removed and we will apply a small adhesive dressing to the site. You will then be free to leave. This will complete your participation in the study.

What are the possible discomforts, risks and side effects?
We do not anticipate any study-specific side-effects, however, there may be some redness and slight itch or discomfort at the site of cream application, especially if exposed to bright light for up to 48 hours after application. This will be minimized by keeping the area covered for this period.
Your health and safety are the most important considerations to the doctors performing this study. The research team will take responsibility for your clinical care during the study. They will halt your participation at any time if it is felt that continued participation would be detrimental to you in any way. There are certain things you should consider about the procedure in the study which may affect your willingness to participate.

What are the possible benefits of taking part?
There are no personal benefits to you as a volunteer. However, this study may influence patient care and treatment in the future

How long will my participation last?
Your participation in this study will consist of one study visit which will last approximately four hours. We understand that this may impact on you financially and so we will reimburse you with £50 to cover expenses and inconvenience.

Is there a person I can speak to about the research study who is independent from the research team?
Yes, you can contact:

What if something goes wrong?
If you have a complaint about your participation in the study you should first talk to a researcher involved in your care. You can ask to speak to a senior member of the research team or the Complaints Officer for NHS Tayside. In the event that something goes wrong and you are harmed during the study there are no special compensation arrangements.
If you are harmed and this is due to someone's negligence then you may have grounds for a legal action for compensation against the University of Dundee or NHS Tayside but you may have to pay your legal costs. The normal National Health Service complaints mechanisms will still be available to you (if appropriate).

Complaints and Claims Manager

Some insurance companies consider that participation in medical research such as this is a 'material fact' which should be mentioned in any proposal for health-related insurance, or which could influence their judgement in consideration of claims made under existing insurance policies. You should check that participation in this research does not affect any policy you might be thinking about taking out or any existing policy.

Will my taking part in the study be kept confidential?
All the information collected will be kept strictly confidential. The information will be kept in a locked room and held on a secure password protected computer with your name and other identifying details removed. Only the researchers involved in the study and the regulatory authorities will have access to the information. We will keep the non-identifiable information for five years after completion of the study. With your permission, we will notify your GP of your participation in this study.

What will happen to the results?
The results will be examined by the researchers who have organised the study, and a short report will be produced. You will not be identified in this report. The results may then be published in the PhD thesis and scientific journals and presented at academic meetings. Again, you will not be identified in the thesis, any journal articles or presentations.

Who is funding and organising this research?
The study has been sponsored by the University of Dundee and NHS Tayside, organised by . The Photobiology Trust is funding this study.

Who has reviewed this study?
The East of Scotland Medical Research Ethics Service REC 1 which has responsibility for scrutinising proposals for Medical Research on Humans in Tayside, has examined the proposal and has raised no objections from the point of view of Medical Ethics. It is a requirement that your records in this research together with any relevant medical records be made available for scrutiny by monitors from NHS Tayside, University of Dundee and University of St. Andrews.

For further information contact:

Thank you for reading this information sheet and considering taking part in this study

Appendix VI: Capturing fluorescence – Patients

Participant Information Sheet PIS v.2 17.12.2013

PARTICIPANT INFORMATION SHEET

PATIENT COHORT

Capturing fluorescence imaging of the skin: patients with skin tumours and healthy volunteers

My name is Olena Kulyk and I am a 2nd year PhD Physics Student at the University of St. Andrews. **I am required to undertake a project as part of my course and invite you to take part in the following study.** However, before you decide to do so, I need to be sure that you understand firstly why I am doing it, and secondly what it would involve if you agreed. I am therefore providing you with the following information. Please read it carefully and be sure to ask any questions you might have and, if you want, discuss it with others including your friends and family. I will do my best to explain the project to you and provide you with any further information you may ask for now or later.

Why are we doing this study?

Photodynamic therapy is a treatment used to treat areas of sun damage and skin cancer. It works by applying a cream which contains a chemical in it which is taken up into the skin and converted to another chemical which is light sensitive. This light sensitive chemical fluoresces (produces a crimson red light) when blue light is shone on it. This crimson red fluorescence can be detected by an imaging camera. This allows us to work out how much accumulates in normal skin and whether there are increased amounts present in abnormal diseased skin. We hope that monitoring fluorescence of this chemical (protoporphyrin IX, PpIX) will increase our understanding of how PDT works and allow us to improve treatment regimes.

Why have I been chosen?

You have been diagnosed as having sun damaged skin/ a non-melanoma skin cancer (basal cell carcinoma)/ pre-cancer (Bowen's

Disease) or actinic keratosis and have been referred to the Photobiology Unit to have photodynamic therapy (PDT).

Do I have to take part?

Participation in this study is entirely voluntary and you are free to refuse to take part or to withdraw from the study at any time without having to give a reason and without this affecting any future healthcare. If you would like to discuss taking part in the study, please fill in the attached slip and send it back in the stamped addressed enveloped which has been supplied or phone any of the people listed at the end of this information leaflet.

What will happen to me if I take part?

We will invite you to come to the Photobiology Unit, Level 8, Ninewells Hospital & Medical School, Dundee to speak with one of our Research Team when you will be given the opportunity to ask any questions you may have regarding your treatment and the research study. If you agree to take part in the study, a member of the research team will then ask you to sign a consent form. You will receive a copy of this Participant Information Sheet and signed Consent Form to keep.

Once the PDT cream has been applied we will take photographic measurements of the study skin site every 10 -15 minutes throughout the three hour period. You will then have your PDT treatment and be allowed to go home. This one visit completes your participation in this research study.

What are the possible discomforts, risks and side effects?

We do not anticipate any study-specific side effects, however, there may be some redness at the treatment site which is expected as a normal response to PDT. Your consultant will have explained how PDT works and the measures that we take to minimise any pain or discomfort you may experience.

Your health and safety are the most important considerations to the doctors performing this study. The research team will take responsibility for your clinical care during the study. They will halt your participation at any time if it is felt that continued participation would be detrimental to you in any way. There are certain things you should consider about the procedure in the study which may affect your willingness to participate.

What are the possible benefits of taking part?

There is no personal benefit to you as a patient. However, this study may influence patient care and treatment in the future.

Will I have extra visits to the hospital?

No, we will be taking measurements every 10-15 minutes during the routine three hours cream application and after the last measurements you will have your planned PDT treatment.

Is there a person I can speak to about the research study who is independent from the research team?

Yes, you can contact:

What if something goes wrong?

If you have a complaint about your participation in the study you should first talk to a researcher involved in your care. You can ask to speak to a senior member of the research team or the Complaints Officer for NHS Tayside. In the event that something goes wrong and you are harmed during the study there are no special compensation arrangements.

If you are harmed and this is due to someone's negligence then you may have grounds for a legal action for compensation against the University of Dundee or NHS Tayside but you may have to pay your legal costs. The normal National Health Service complaints mechanisms will still be available to you (if appropriate):

Complaints and Claims Manager

Some insurance companies consider that participation in medical research such as this is a ‘material fact’ which should be mentioned in any proposal for health-related insurance, or which could influence their judgement in consideration of claims made under existing insurance policies. You should check that participation in this research does not affect any policy you might be thinking about taking out or any existing policy.

Will my taking part in the study be kept confidential?

All the information collected will be kept strictly confidential.

The information will be kept in a locked room and held on a secure password protected computer with your name and other identifying details removed. Only the researchers involved in the study and the regulatory authorities will have access to the information. We will keep the non-identifiable information for five years after completion of the study.

What will happen to the results?

The results will be examined by the researchers who have organised the study, and a short report will be produced. You will not be identified in this report. The results may then be published in scientific journals and presented at academic meetings. Again, you will not be identified in any journal articles or presentations.

Who is funding and organising this research?

The study has been sponsored by the University of Dundee and NHS Tayside and organised by

The Photobiology Trust is funding this study.

Who has reviewed this study?

The East of Scotland Medical Research Ethics Service which has responsibility for scrutinising proposals for Medical Research on Humans in Tayside, has examined the proposal and has raised no objections from the point of view of Medical Ethics. It is a requirement that your records in this research together with any relevant medical records be made available for scrutiny by monitors from NHS Tayside and the regulatory authorities.

For further information contact:

Thank you for reading this information sheet and considering taking part in this study

✂----------

I agree to discuss participating in the study.

I understand that this study will take place when I am attending the Photobiology Unit

for photodynamic therapy.

Name …… **Date of birth** …….

Telephone No. ……

Appendix VII: Capturing fluorescence – Healthy Volunteer Consent Form 21.10.2013 V.1

CONSENT FORM

(healthy volunteer cohort)

Subject Identification Number for this study: ☐

Title of Project: Capturing fluorescence imaging of the skin: patients with skin tumours and healthy volunteers

Chief Investigator:

Please initial box

1. I confirm that I have read and understand the information sheet dated / /2013 (version) for the above study. I have had the opportunity to consider the information, ask questions and have had these answered satisfactorily. ☐

2. I understand that my participation is voluntary and that I am free to withdraw at any time without giving any reason, without my medical care or legal rights being affected. ☐

3. I understand that data collected during the study, may be looked at by individuals from NHS Tayside, where it is relevant to my taking part in this research. I give permission for these individuals to have access to my records. ☐

4. I agree to digital images being taken of the study skin sites to be used for presentation, publication and research purposes. ☐

5. I agree to take part in the above study. ☐

_____	_____	_____
Name of Participant	Date	Signature
_____	_____	_____
Name of Person taking consent	Date	Signature

When completed, 1 for participant; 1 for researcher file

Appendix VIII: Capturing fluorescence – Patient Consent Form 21.10.2013 V.1

CONSENT FORM

(patient cohort)

Subject Identification Number for this study: ☐

Title of Project: Capturing fluorescence imaging of the skin: patients with skin tumours and healthy volunteers

Chief Investigator:

Please initial box

1. I confirm that I have read and understand the information sheet dated / /2013 (version) for the above study. I have had the opportunity to consider the information, ask questions and have had these answered satisfactorily. ☐

2. I understand that my participation is voluntary and that I am free to withdraw at any time without giving any reason, without my medical care or legal rights being affected. ☐

3. I understand that relevant sections of my medical notes and data collected during the study, may be looked at by individuals from NHS Tayside, where it is relevant to my taking part in this research. I give permission for these individuals to have access to my records. ☐

4. I agree to digital images being taken of the study skin sites to be used for presentation, publication and research purposes. ☐

5. I agree to take part in the above study. ☐

_____	_____	_____
Name of Participant	Date	Signature
_____	_____	_____
Name of Person taking consent	Date	Signature

When completed, 1 for participant; 1 for researcher file; 1 to be kept in medical notes

Appendix IX: Capturing fluorescence – Letter of Invitation v.1 21.10.2013

Dear

Research Study: **Capturing fluorescence imaging of the skin: patients with skin tumours and healthy volunteers**

I am writing to invite you to participate in the above research project. You have been identified as a possible participant in this study because you have been referred to the Photobiology Unit for photodynamic therapy.
For your information, I have enclosed a copy of the Participant Information Leaflet. Please let me know if you have any questions about this when you attend for your treatment.

Yours Sincerely

Consultant Dermatologist

Appendix X: Capturing fluorescence – Participant Travel Expenses Form 2013 V.1

Appendix XI: Capturing fluorescence – Sponsor Letter Insurance Note 2013DS03

Appendix XII: Capturing fluorescence – East of Scotland Research Ethics Service EoSRES Favourable Opinion Letter

Appendix XIII: Capturing fluorescence – University of St Andrews Teaching and Research Ethics Committee UTREC Approval Letter 10.02.2014

Appendix XIV: Capturing fluorescence – Fluorescence Imaging System Specifications v.1 09.10.2013

Fluorescence imaging system

The fluorescence imaging system records images of PpIX fluorescence and processes the images. The system consists of a CCD camera and collection optics, laptop, custom illuminator assembled with low power LED, a USB control. All components are comprised in a custom PMMA plastic casing. The camera has a fixed focal distance of 8.5 cm. The illumination, 405 nm LED, is controlled via a user interface and turns on for less than 1 s when an image of fluorescence is acquired. The user interface has such functions as recording fluorescence images, subtracting background, reducing noise, analysing fluorescence intensity in various regions of an image, plotting the 2D and 3D fluorescence intensity, and analysis of multiple images.

Components

1. A Lumenera LM075M USB 2.0 powered CCD camera
2. The Collection optics: a Thorlab interference band pass filter, FL635 – Ø1″ CWL 635±2 nm, FWHM 10±2 nm threaded to screw into an optical lens M118FM16, focused at 8.5 cm
3. A laptop
4. A custom illuminator – a ring of 14 low power 405 nm LEDs built on a custom made round shaped PCB with a hole in the middle, LED VAOL-5GUV0T4 Ø5 mm through hole, (160 mcd, 3 V, 20 mA), connected to a INFINEON BCR402W/SOT343 LED drive, and a MMBF170L/SOT23 N-MOSFET switch; with an optical output equal to 0.1 mW/cm^2 at the end of the rectangular tube, 8.5 cm, around 1 s pulse;
5. A custom made bio-thermoplastic casing containing the battery, the illumination PCB and the camera
6. 9V battery
7. A flash control: a USB 2.0 Parallel FIFO interface (TTL) development module UM245R connected via a 2.0 Type-A Male to Type-B Male USB cable to a laptop
8. Matlab Graphical User Interface

The intensity of the illuminator and the LED emission spectrum

The emission of one of the LEDs was measured using an Ocean Optics spectrometer (Fig 1). Spectral power for UV-A and Vis was calculated in %.

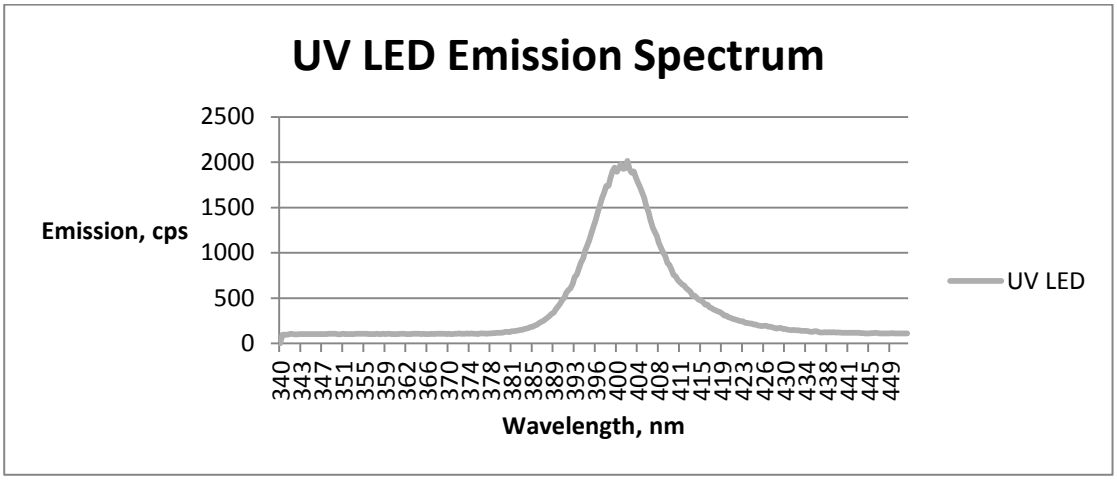

Fig 1 – Emission spectrum of UV LED used for illumination

Power = (Counts / sec) x Energy of Photon @ wavelength

Spectral power in UV-A, % = Power in 340-399 nm range / Power for full spectrum x 100%

Spectral power in Vis, % = Power in 400-700 nm range / Power for full spectrum x 100%

32 % spectral power in 340 – 399 nm

68 % spectral power in 400 – 700 nm

The output intensity of the illuminator for the fluorescence imaging system

The output power at a distance of 8.5 cm which corresponds to the end of the cylinder of the illuminator was measured using a Thorlabs PM100D power meter (Appendix 1).

Measured power = 0.074 mW

Are of the sensor = π x r^2 = 3.14 x 0.475^2 cm^2 = 0.7085 cm^2

Intensity = Measured power / Area of the sensor = 0.074 mW / 0.7085 cm^2 = 0.1 mW/cm^2

Appendix 1: The optical power output measurements for the fluorescence imaging system

Parameters of the Thorlabs PM100D power meter with S120C - Standard Photodiode Power Sensor, Si, 400 - 1100 nm, 50 mW

Aperture Size: Ø9.5 mm sensor

Wavelength Range: 400 nm – 1100 nm

Power Range: 50 nW – 50 mW

Detector Type: Si Photodiode

Linearity: ±0.5%

Resolution: 1 nW

Measurement Uncertainty: ±3% (451 nm – 1000 nm), ±5% (over Rest of Range)

Appendix 2: The eye and the skin risk assessment of the optical power output for the fluorescence imaging system

14th December 2012

Illuminator for St Andrews' Fluorescence Imaging System

Risk Assessment: Non-coherent Optical Radiation

Irradiance at end of the cylinder

0.32 mW cm^{-2} (340-399 nm)

0.68 mW cm^{-2} (400-700 nm)

- **UV exposure limit, H_{eff} = 30 J m^{-2}**

Effective irradiance E_{eff} = measured irradiance weighted by Sλ.

Simplifying assumption based on LED emission spectrum:

Assume UV emission is at 380 nm.

Sλ = 0.000064

E_{eff} = 0.32 x 0.000064 = 2.05 x 10^{-5} mW cm^{-2}

MPE time = 30 x 10^{-1} / 2.05 x 10^{-5} sec > 8 hours

- **UVA exposure limit, $H_{UVA} = 10^4$ J m^{-2}**

UVA irradiance, E_{UVA} = 0.32 mw cm^{-2}

MPE time = 10^4 x 10^{-1} / 0.32 sec = 52 min

- **Blue light exposure limit is 100 W m^{-2} sr^{-1}**

Blue light irradiance L_B = measured irradiance weighted by Bλ.

Simplifying assumption based on LED emission spectrum:

Assume 300-700 nm emission is at 400 nm.

$B\lambda = 0.1$

Effective irradiance = 1.0 x 0.1 = 0.1 mW cm^{-2}

Solid angular subtense = 0.7085 / 8.5 x 8.5 = 0.01 sr

L_B = 0.1 / 0.01 = 10 mW cm^{-2} sr^{-1} = 100 W cm^{-2} sr^{-1}

The exposure limit is 100 W m^{-2} sr^{-1}

The blue light exposure limit value is not exceeded.

- **CONCLUSIONS**

H_{eff} exposure limits are not exceeded. No special precautions are required to protect from short wavelength UV radiation.

H_{UVA} limit is exceeded if exposure exceeds 52 minutes. Eye exposure should not exceed 53 minutes.

Blue light weighted radiance at the end of the cylinder is equal to the exposure limit. The device should not be placed on the unprotected eye.

Appendix XV: Capturing fluorescence – Printed Circuit Board PCB

The drawings for the custom printed circuit board for the illuminator for the fluorescence system have been developed using DipTrace electronics design software and can be used for PCB cutting (outline drawing), printing coper traces (top and bottom traces drawing), drilling holes (holes drawing) and as a guidance for the assembly (assembly drawing).

	ISO A4 Portrait 4x6 zones: X 47.5 mm Y 46.17 mm	Drawing No	2	

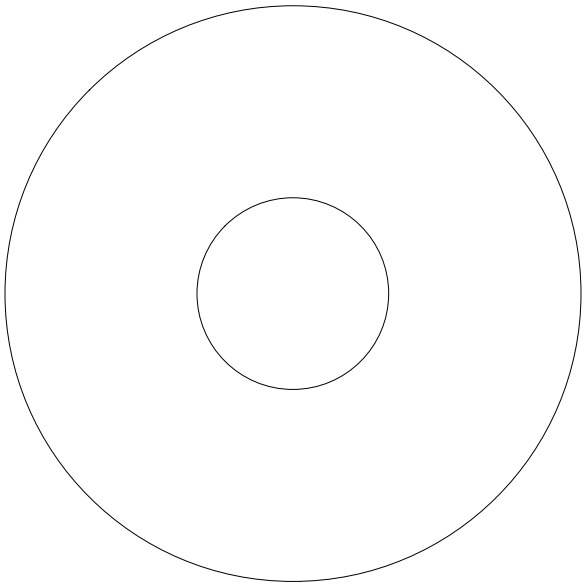

Software	DipTrace	Fabrication format: Gerber .gbr Drawing format: .XPS			Original format: .dip	
Designed by Olena Kulyk		File name: PCB Round V.1	Extension: Board Outline Cut	Date 05/08/13	Review Date 22/01/2015	Scale 1:1
PCB Board for Illuminator used in Fluorescence Imaging Camera Project R&D Ref # 2013DS03 Title: Capturing fluorescence...			Layers on: Board. For: PCB Cut			
			Use drawing for: PCB cutting		Page	

	ISO A4 Portrait 4x6 zones: X 47.5 mm Y 46.17 mm	Drawing No	4

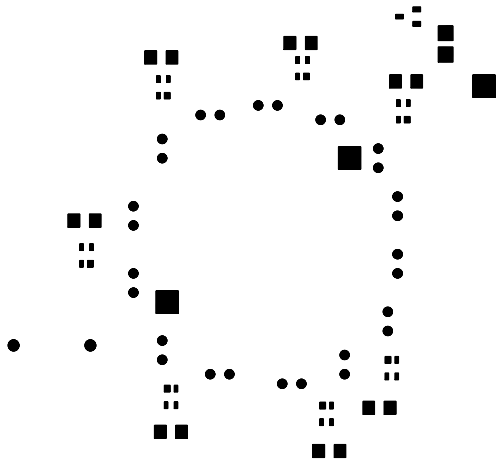

Software: DipTrace	Fabrication format: Gerber .gbr Drawing format: .XPS				Original format: .dip	
Designed by Olena Kulyk	File name: PCB Round V.1	Extension: Copper Traces Bottom	Date 05/08/13		Review Date 22/01/2015	Scale 1:1
PCB Board for Illuminator used in Fluorescence Imaging Camera Project R&D Ref # 2013DS03 Title: Capturing fluorescence...	Layers on: Pads. For: PCB Copper Traces - Bottom					
	Use drawing for: Printing copper traces			Page		

	ISO A4 Portrait 4x6 zones: X 47.5 mm Y 46.17 mm	Drawing No	3

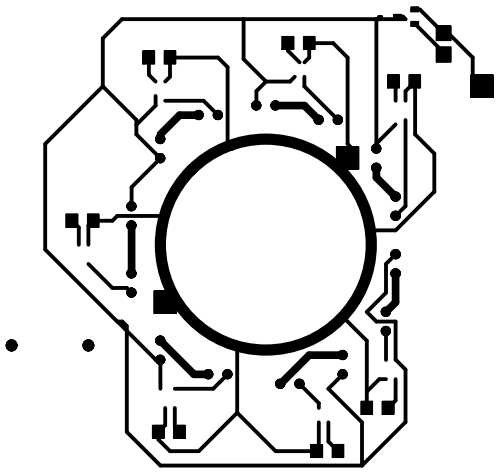

Software: DipTrace	Fabrication format: Gerber .gbr Drawing format: .XPS				Original format: .dip	
Designed by Olena Kulyk	File name: PCB Round V.1	Extension: Copper Traces Top	Date 05/08/13		Review Date 22/01/2015	Scale 1:1
PCB Board for Illuminator used in Fluorescence Imaging Camera Project R&D Ref # 2013DS03 Title: Capturing fluorescence...		Layers on: Pads, Traces. For: PCB Copper Traces - Top				
		Use drawing for: Printing copper traces		Page		

	ISO A4 Portrait 4x6 zones: X 47.5 mm Y 46.17 mm	Drawing No	5	

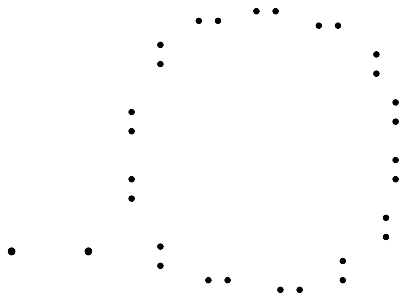

Software	DipTrace	Fabrication format: Drill .drl Drawing format: .XPS			Original format: .dip	
Designed by Olena Kulyk		File name: PCB Round V.1	Extension: Holes Drill Top Bottom	Date 05/08/13	Review Date 22/01/2015	Scale 1:1
PCB Board for Illuminator used in Fluorescence Imaging Camera Project R&D Ref # 2013DS03 Title: Capturing fluorescence...			Layers on: Holes, Pads - Negative. For: Holes drill			
			Use drawing for: PCB holes drilling		Page	

Appendix XVI: Capturing fluorescence – 3D Plastic Casing Design

The design of the casing has been developed in Rhino 4.0 3D CAD software.

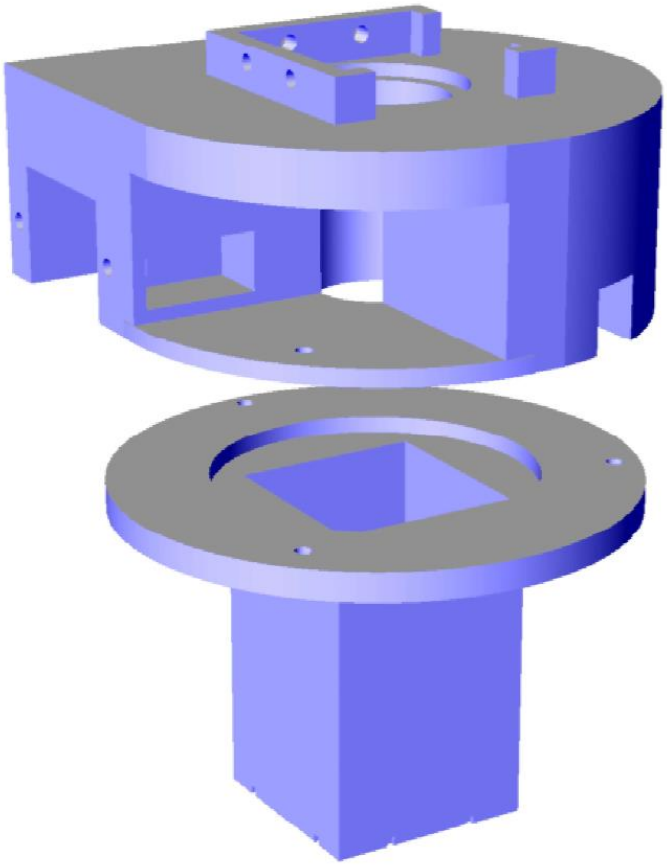

ISO A4 Portrait 4x6 zones: X 47.5 mm Y 46.17 mm	Drawing No	2

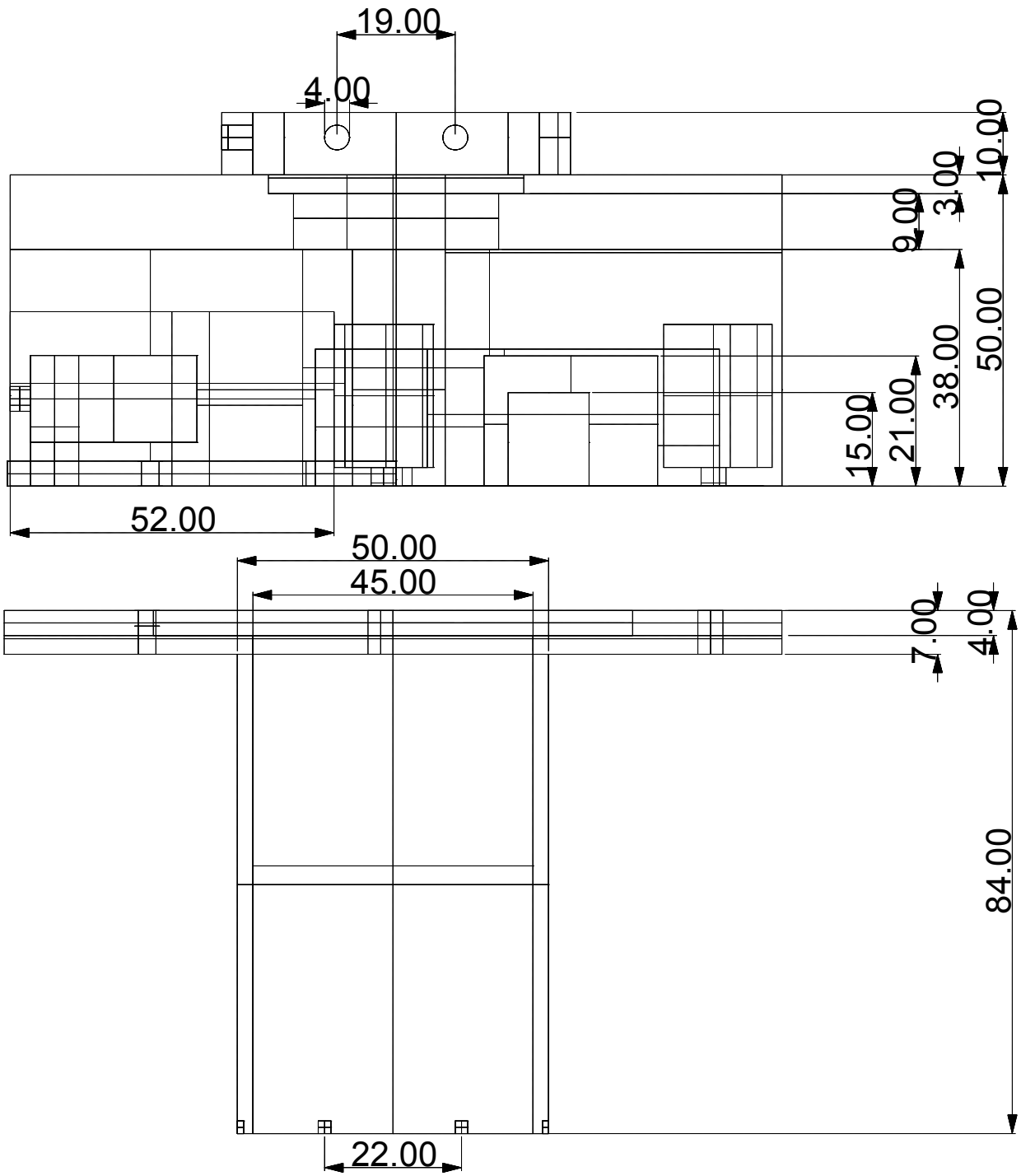

Software: Rhino	Exported format: AutoCAD drawing exchange file .dxf			
Designed by Olena Kulyk	Date 14/05/13	Review Date 22/01/15	View: Front	Original format: .3dm Fabrication format: .stl
Plastic Casing for Fluor. Camera Project R&D Ref # 2013DS03 Title: Capturing fluorescence...	File name: Two Parts Casing V1			
	Use drawing for: PLA Plastic Printer	Scale 1:1	Page	

ISO A4 Portrait 4x6 zones: X 47.5 mm Y 46.17 mm	Drawing No	3

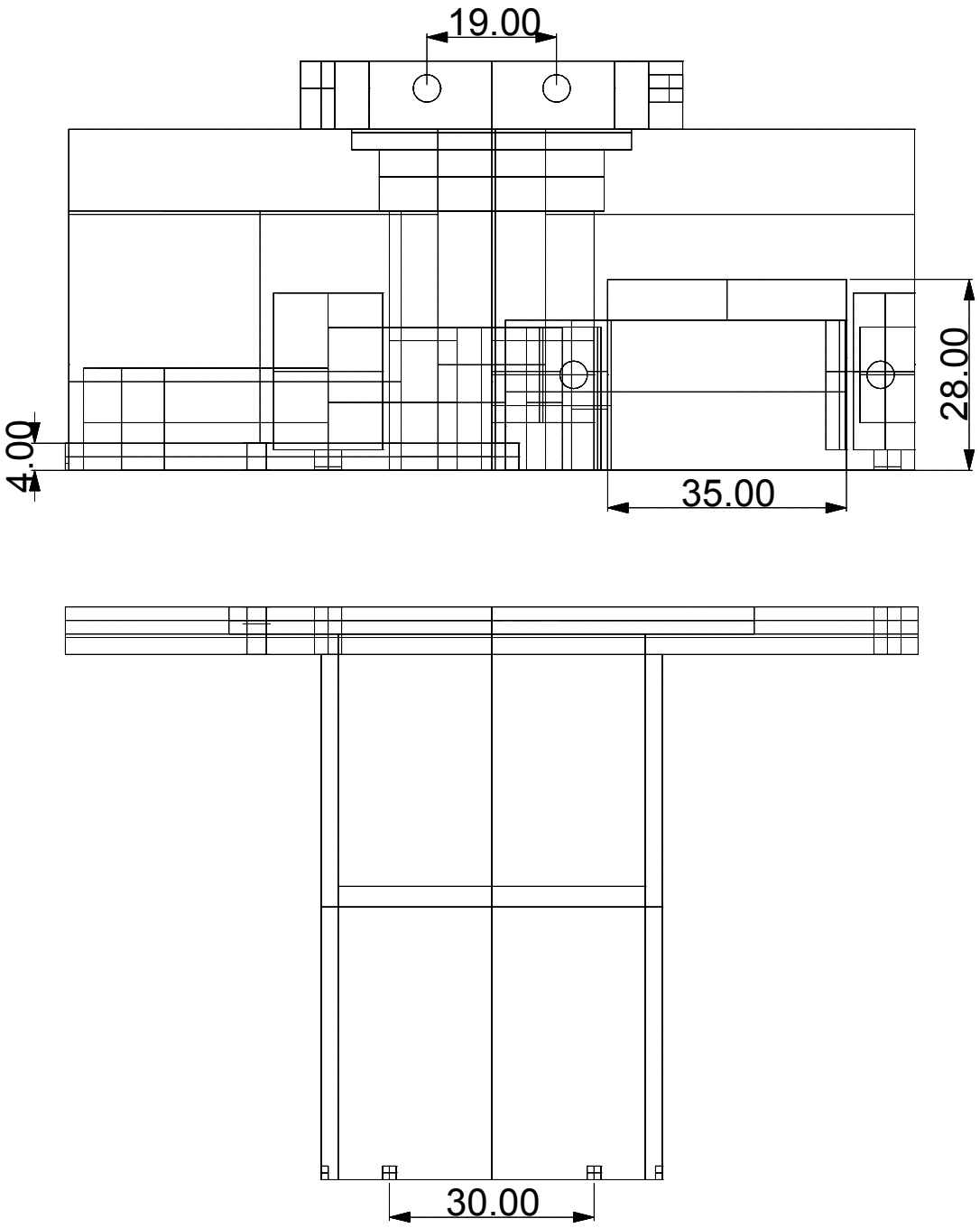

Software: Rhino	Exported format: AutoCAD drawing exchange file .dxf			
Designed by Olena Kulyk	Date 14/05/13	Review Date 22/01/15	View: Right	Original format: .3dm Fabrication format: .stl
Plastic Casing for Fluor. Camera Project R&D Ref # 2013DS03 Title: Capturing fluorescence...	File name: Two Parts Casing V1			
	Use drawing for: PLA Plastic Printer	Scale 1:1	Page	

ISO A4 Portrait 4x6 zones: X 47.5 mm Y 46.17 mm	Drawing No	1

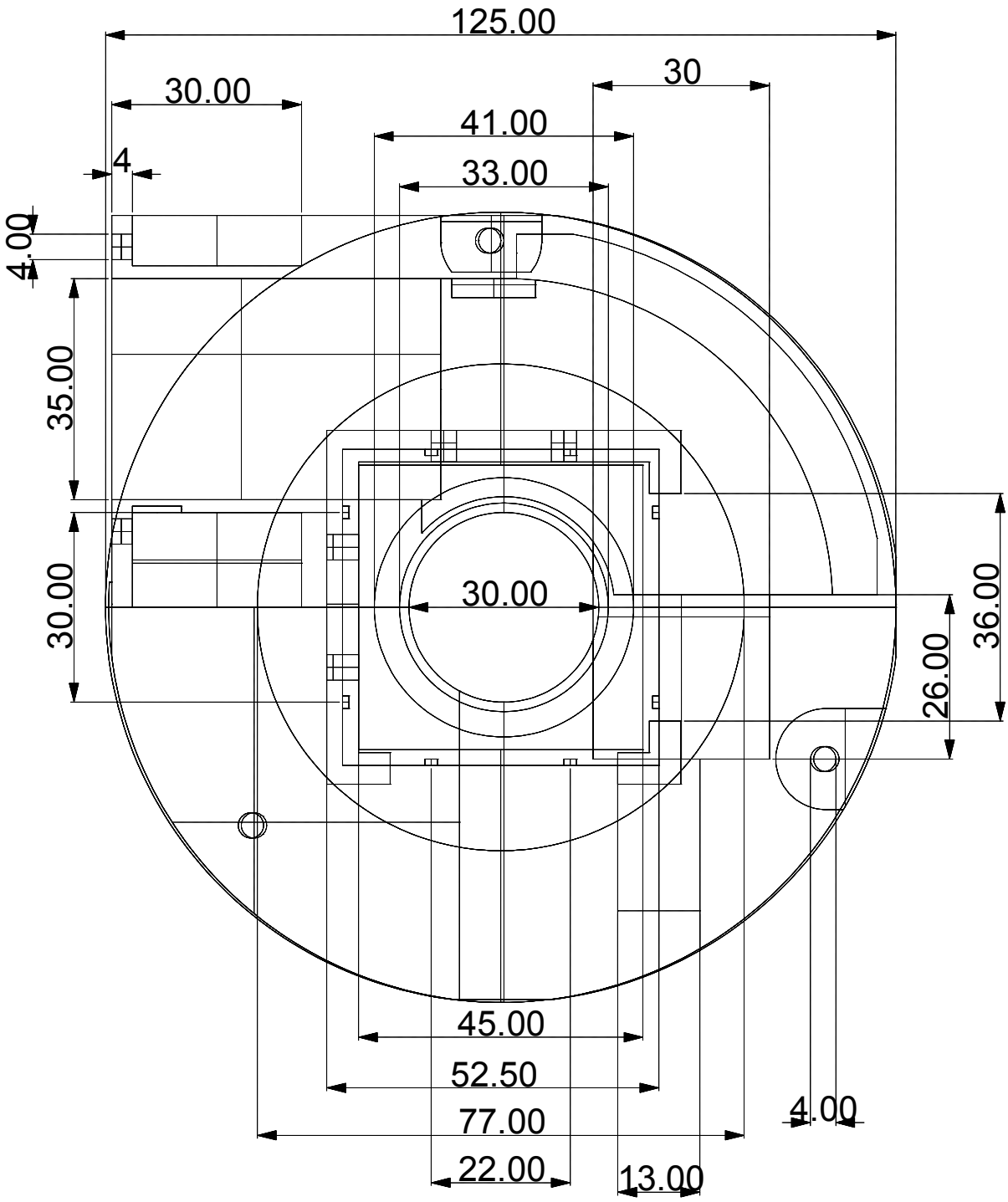

Software: Rhino	Exported format: AutoCAD drawing exchange file .dxf			
Designed by Olena Kulyk	Date 14/05/13	Review Date 22/01/15	View: Top	Original format: .3dm Fabrication format: .stl
Plastic Casing for Fluor. Camera Project R&D Ref # 2013DS03 Title: Capturing fluorescence...	File name: Two Parts Casing V1			
	Use drawing for: PLA Plastic Printer	Scale 1:1	Page	

	ISO A4 Portrait 4x6 zones: X 47.5 mm Y 46.17 mm	Drawing No	1	

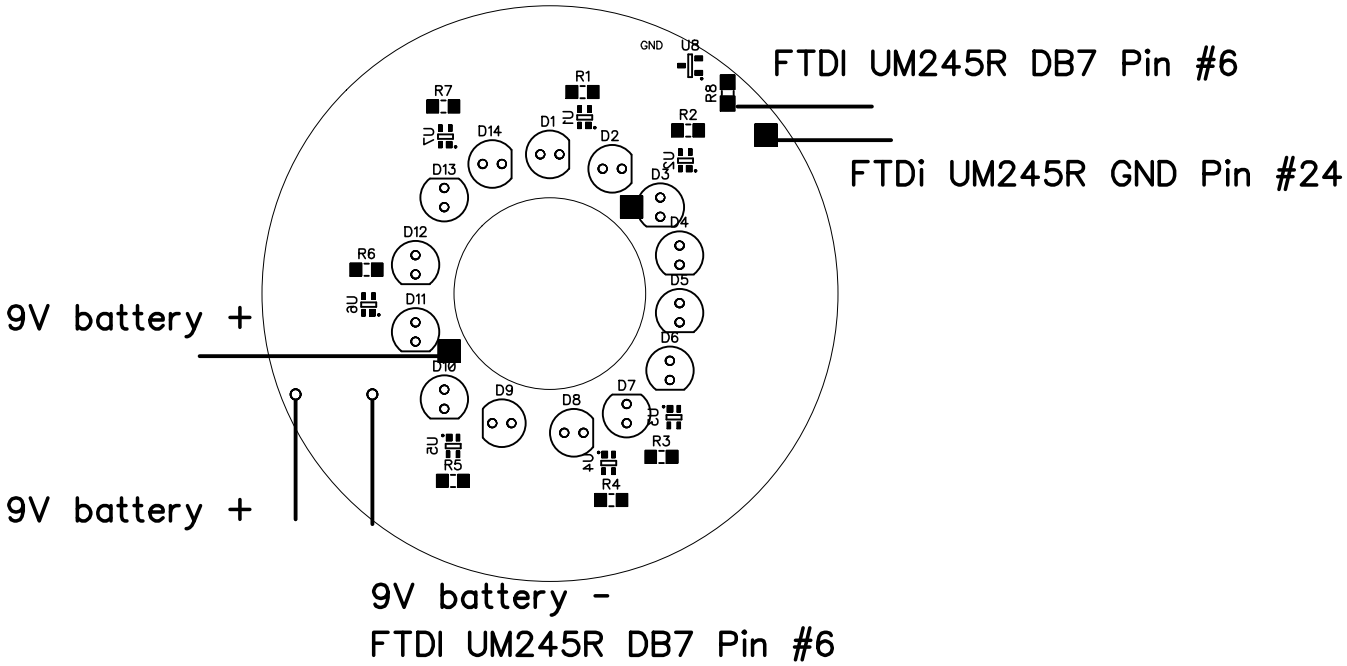

Component	Type	Name/Packaging
D1-D14	LED 405 nm	VAOL-5GUV0T4/ 5 mm
U1-U7	LED driver	INFINEON BCR402W/ SOT343
U8	N-MOSFET switch, +3V	MMBF170L/ SOT23
R1-R7	Resistor 1k	/RES_1206
R8	Resistor 10k	/RES_1206

Software	DipTrace	Exported into formats: .dxf, .XPS, P-CAD ASCII			Original format: .dip	
Designed by Olena Kulyk		File name: PCB Round V.1	Extension: Assembly	Date 05/08/13	Review Date 22/01/2015	Scale 1:1
PCB Board for Illuminator used in Fluorescence Imaging Camera Project R&D Ref # 2013DS03 Title: Capturing fluorescence...			Layers on: Pads, Holes, Tables, Board, Assy, Silk. For: PCB outline, components, wiring connection			
			Use drawing for: Assembly, component list		Page	

Appendix XVII: Capturing fluorescence – The Software Installation and Operation Instructions

The software for the fluorescence system has been developed in Matlab. The archive with all the necessary installation files: the Lumenera software from the manufacturer of the camera, the manufacturer's Matlab adapter for the camera, the manufacturer's USB FTDI UM245R driver and Matlab adapters, and the written Matlab software with all the functions' files are provided on a CD in a folder titled FluoImLu3.rar.

The system requirements are Windows 7 64-bit operating system or higher and Matlab 2012b or higher with the installed Image Acquisition Toolbox, and the Image Processing Toolbox. Matlab Computer Vision Toolbox is necessary at later stages for image processing.

Installation procedure

1. Run installation for the software for the Lumenera camera. The installation file is called LuCamSoftware-v6.0.3.exe.
2. Extract and install Matlab driver from the archive called Lumenera Matlab Driver V2.0.1.rar. Read ReadMe.txt file for the installation instructions and setting up the path in Matlab, the installation file is called install.bat
3. Run install.bat file for LumCamPlug-in.
4. Install FTDI driver for UM245R USB module. Run CDM20824_Setup which is located in FTDI USB245 folder.
5. Add USB245.mex32 or USB245.mex32 in the Matlab directory and add them to the path. The explanation of the commands in Matlab to control the USB unit can be found at this link. http://apps.usd.edu/coglab/psyc770/USB245.html. Make sure that the folder contains all mex-files and a Matlab functions for both the camera and the USB control before the operation.

Operation procedure

1. Start Matlab. Set the correct working directory. Open FluoImLu3.fig graphical user interface.
2. Open Lumenera software. Set the exposure time, the gain, and start live preview for camera's focus, if necessary use the button LEDsOn in the FluoImLu3.fig window to turn the illumination.

Figure 1 shows the graphical user interface FluoImLu3 written in GUI Toolbox, Matlab. Each button has Matlab function in the root folder of the archive.

Record test and Record control buttons on the GUI initiate the camera, the illuminator USB control unit, send high and low signals to the DB7 pin which controls a MOSFET switch which turns on the power for illumination. Once the illumination is on an image is acquired. The Lumenera software is in sync with the Matlab GUI, the Matlab GUI reads the exposure and the gain set in the Lumenera software. After the image is acquired, the illumination is turned off and the image is saved automatically with a given name which is the current date and time. A folder with a given name of the current date is created in the working directory of Matlab when the first image is taken. Once the folder is created all the following images will

be saved in this folder on that day. The format for the folder is dd-mmm-yyyy. The format for the images is Test_dd-mmm-yyyy_hhmmss.jpeg or Control_dd-mmm-yyyy_hhmmss.jpeg when the Record Test or Record Control buttons are pressed correspondingly. The only difference between the test button and the Control button is that the Test button records a series of 3 images, and the Control button records one image at a time. The Control button gives faster readings as less time is needed for the exposure and saving of images.

LEDsOn and LEDsOff buttons turn the illumination on and off and also initiate the driver. An error message can occur in the Matlab window (error: No FTDI USB devices attached. FTDI installation failed!) when the FTDI module is not plugged into the computer or the driver needs an update. Sometimes it takes some time before automatic installation of the driver is complete. Typical debugging procedure is to press the Reset LED button which will re-install the USB driver. If the message still appears, restart the computer making sure that the operating system and the dirvers are up to date.

The rest of the buttons open and display images, cross sections and export the data into excel files for convenience.

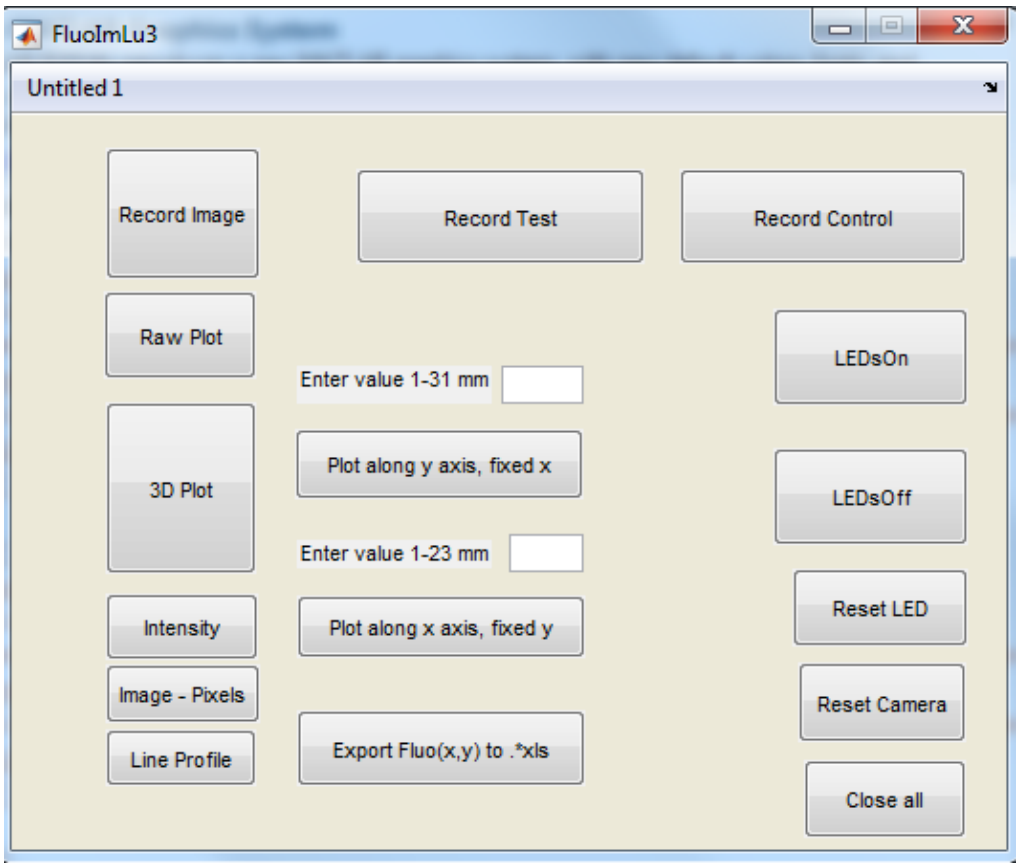

Figure 1 FluoImLu3 Graphical User Interface

FluoImLu3 Matlab software script

FluoImLu3.m

function varargout = FluoImLu3(varargin)

%{

FLUOIMLU3 MATLAB code for FluoImLu3.fig

Written by O. Kulyk,

St Andrews, 13.05.2013 */

/* FLUOIMLU3, by itself, creates a new FLUOIMLU3 or raises the existing singleton

H = FLUOIMLU3 returns the handle to a new FLUOIMLU3 or the handle to the existing singleton*.

FLUOIMLU3('CALLBACK',hObject,eventData,handles,...) calls the local function named CALLBACK in FLUOIMLU3.M with the given input arguments.

FLUOIMLU3('Property','Value',...) creates a new FLUOIMLU3 or raises the existing singleton*. Starting from the left, property value pairs are applied to the GUI before FluoImLu3_OpeningFcn gets called. An unrecognized property name or invalid value makes property application stop. All inputs are passed to FluoImLu3_OpeningFcn via varargin.

*See GUI Options on GUIDE's Tools menu. Choose "GUI allows only one instance to run (singleton)".

See also: GUIDE, GUIDATA, GUIHANDLES

Edit the above text to modify the response to help FluoImLu3

Last Modified by GUIDE v2.5 13-May-2013 21:07:59 **%}**

```
% Begin initialization code - DO NOT EDIT
gui_Singleton = 1;
gui_State = struct('gui_Name',       mfilename, ...
                   'gui_Singleton',  gui_Singleton, ...
                   'gui_OpeningFcn', @FluoImLu3_OpeningFcn, ...
                   'gui_OutputFcn',  @FluoImLu3_OutputFcn, ...
                   'gui_LayoutFcn',  [] , ...
                   'gui_Callback',   []);
if nargin && ischar(varargin{1})
    gui_State.gui_Callback = str2func(varargin{1});
end

if nargout
    [varargout{1:nargout}] = gui_mainfcn(gui_State, varargin{:});
else
    gui_mainfcn(gui_State, varargin{:});
end
```

```
% End initialization code - DO NOT EDIT

% --- Executes just before FluoImLu3 is made visible.
function FluoImLu3_OpeningFcn(hObject, eventdata, handles, varargin)
% This function has no output args, see OutputFcn.
% hObject    handle to figure
% eventdata  reserved - to be defined in a future version of MATLAB
% handles    structure with handles and user data (see GUIDATA)
% varargin   command line arguments to FluoImLu3 (see VARARGIN)

% Choose DefaultShutter command line output for FluoImLu3
handles.output = hObject;

% Update handles structure
guidata(hObject, handles);

% UIWAIT makes FluoImLu3 wait for user response (see UIRESUME)
% uiwait(handles.figure1);

% --- Outputs from this function are returned to the command line.
function varargout = FluoImLu3_OutputFcn(hObject, eventdata, handles)

% Get DefaultShutter command line output from handles structure
varargout{1} = handles.output;

% --- Executes on button press in pushbutton1.
function pushbutton1_Callback(hObject, eventdata, handles)
RecordImageLu;
%Fun1RecordImage;

% --- Executes on button press in pushbutton2.
function pushbutton2_Callback(hObject, eventdata, handles)
Fun5ThreeDPlotCompensIm;

% --- Executes on button press in pushbutton3.
function pushbutton3_Callback(hObject, eventdata, handles)
Fun2OpenImagePixels;

% --- Executes on button press in pushbutton8.
function pushbutton4_Callback(hObject, eventdata, handles)
```

```
Fun3OpenImageLine;

% --- Executes on button press in pushbutton2.
function pushbutton5_Callback(hObject, eventdata, handles)
Fun4PlotPhotobleachOver21Min;

% --- Executes on button press in pushbutton2.
function pushbutton6_Callback(hObject, eventdata, handles)
LEDsOn;

% --- Executes on button press in pushbutton2.
function pushbutton7_Callback(hObject, eventdata, handles)
LEDsOff;

% --- Executes on button press in pushbutton2.
function pushbutton8_Callback(hObject, eventdata, handles)
ResetUSB245;

% --- Executes on button press in pushbutton8.
function pushbutton9_Callback(hObject, eventdata, handles)
CloseAllClearAll;

% --- Executes on button press in pushbutton10.
function pushbutton10_Callback(hObject, eventdata, handles)
RawImage;

% --- Executes on button press in pushbutton11.
function pushbutton11_Callback(hObject, eventdata, handles)
ExportToExcel;

function [Exposure_Value, varargout] = edit_Callback(hObject, eventdata, handles)
% Hints: get(hObject,'String') returns contents of edit as text
%str2double(get(hObject,'String')) returns contents of edit as a double
%set(hObject,'String',num2str(1200)); %set value in the edit box
%get(hObject); %get properties of hObject
%Shutter_Value = str2double(get(hObject, 'String')); %gets Shutter_Value from edit box
handles = get(hObject, 'String');
Exposure_Val = str2double(handles);
Exposure = 'ExposureFileLu.mat';
/*changes the excel file ExposureFileLu.mat*/
```

```
save(Exposure, 'Exposure_Val');

% --- Executes during object creation, after setting all properties.
function edit_CreateFcn(hObject, eventdata, handles)
% hObject    handle to edit (see GCBO)
% eventdata  reserved - to be defined in a future version of MATLAB
% handles    empty - handles not created until after all CreateFcns called
% Hint: edit controls usually have a white background on Windows.
%       See ISPC and COMPUTER.
if ispc && isequal(get(hObject,'BackgroundColor'), get(0,'defaultUicontrolBackgroundColor'))
set(hObject,'BackgroundColor','white');
end

% --- Executes on button press in pushbutton10.
function pushbutton10_Callback(hObject, eventdata, handles)

% --- Executes on button press in pushbutton11.
function pushbutton11_Callback(hObject, eventdata, handles)

function edit2_Callback(hObject, eventdata, handles)

% Hints: get(hObject,'String') returns contents of edit2 as text
%        str2double(get(hObject,'String')) returns contents of edit2 as a double
handles=get(hObject, 'String');
x_val = str2double(handles);
x = 'xFileForPlot.mat';
save(x, 'x_val');

% --- Executes during object creation, after setting all properties.
function edit2_CreateFcn(hObject, eventdata, handles)

% Hint: edit controls usually have a white background on Windows.
%       See ISPC and COMPUTER.
if ispc && isequal(get(hObject,'BackgroundColor'), get(0,'defaultUicontrolBackgroundColor'))
   set(hObject,'BackgroundColor','white');
end

function edit3_Callback(hObject, eventdata, handles)

handles=get(hObject, 'String');
```

```
y_val = str2double(handles);
y = 'yFileForPlot.mat';
save(y, 'y_val');

% --- Executes during object creation, after setting all properties.
function edit3_CreateFcn(hObject, eventdata, handles)

if ispc && isequal(get(hObject,'BackgroundColor'), get(0,'defaultUicontrolBackgroundColor'))
    set(hObject,'BackgroundColor','white');
end



% --- Executes on button press in pushbutton12.
function pushbutton12_Callback(hObject, eventdata, handles)
TwoDPlotY;



% --- Executes on button press in pushbutton13.
function pushbutton13_Callback(hObject, eventdata, handles)
TwoDPlotX;

function edit8_Callback(hObject, eventdata, handles)

handles = get(hObject, 'String');
Gain_Val = str2double(handles);
Gain = 'GainFileLu.mat';
save(Gain, 'Gain_Val');

% --- Executes during object creation, after setting all properties.
function edit8_CreateFcn(hObject, eventdata, handles)

if ispc && isequal(get(hObject,'BackgroundColor'), get(0,'defaultUicontrolBackgroundColor'))
    set(hObject,'BackgroundColor','white');
end

% --- Executes on button press in pushbutton20.
function pushbutton20_Callback(hObject, eventdata, handles)
RecordTestLu;

% --- Executes on button press in pushbutton21.
```

```
function pushbutton21_Callback(hObject, eventdata, handles)
RecordControlLu;

% --- Executes on button press in pushbutton22.
function pushbutton22_Callback(hObject, eventdata, handles)
ResetImaqDevice;
```

Fun5ThreeDPlotCompensIm.m

```
function Fun5ThreeDPlotCompensIm ()
%{ This function opens a fluorescence image, compensate it on optical distortions using scale factor which is estimated by imaging an even surface and adjusting each pixel on the non-uniformity, and performs 3D display in calibrated x, y coordinates in real size, 23 mm x 31 mm, at 8.5 cm distance. The function will be executed when pushbutton2 - 3D Plot button is pressed.
Written by O. Kulyk, St Andrews, 14.05.2014 %}

Scale=load('ScaleFactor.mat');
Scale = getfield(Scale,'ScaleFactor');

RawImage = imread(uigetfile({'*.jpeg'}));
RawImage_Norm = double(RawImage)./250;

[n, m] = size(RawImage);
[x, y] = meshgrid(1:m, 1:n);
c1 = double(RawImage_Norm);

figure,
colormap('jet');
cbar1 = colorbar;
set(get(cbar1, 'ylabel'),'String','Fluorescence, au', 'Rotation', 90);
hold on,
surf1 = surf(x./640.*31, y./480.*23, c1,'FaceColor', 'texturemap', 'EdgeColor', 'none');
hold on,
axis([0 31 0 23]);
get(gcf);
get(gco);
get(gca); set(gca,'YDir','reverse');
xlabel('x, mm'); ylabel('y, mm'); zlabel('Fluorescence, a.u.');
```

```
hold off;
```

Fun2OpenImagePixels.m

```
function Fun2OpenImagePixels ()
%{This function opens an image and displays it in impixelregion Image Processing Tool . The function will be executed when pushbutton3 button is pressed.
Written by O. Kulyk, St Andrews, 16.11.2012%}

Im = imread(uigetfile({'*.jpeg'}));

figure;
impixelregion(imshow(Im));
colorbar; colormap('jet'); %shows pixelregion of an image
```

Fun3OpenImageLine.m

```
function Fun3OpenImageLine ()
%{This function displays a cross section profile of an image along a selected interactive line in the Matlab image viewer. The function will be executed when the Line Profile button is pressed.
Written by O. Kulyk, St Andrews, 16.11.2012%}

Im = imread(uigetfile({'*.jpeg'}));
ImNormalised = double(Im)./250;

figure;
[CX,CY,C]=improfile(imshow(ImNormalised));colormap('jet'); colorbar;
hold on;
improfile(ImNormalised,CX./640.*41,CY./480.*31);
grid on;
hold off;
figure;plot(C);xlabel('distance, pixel');ylabel('Fluorescence, au');
```

LEDsOn.m

```
function LEDsOn ()
%{ This function turns the LED on by clearing the cache data in Matlab, re-configuring FTDI circuit and sending high signal to the DB7 pin. The function will be executed when LEDsOn button is pressed.
Written by O. Kulyk, St Andrews, 16.11.2012%}
clear all;
config_ftdi;
writeUSB245(128);
```

LEDsOff.m

function LEDsOff ()

%{ This function turns the LED off by clearing the cache data in Matlab, re-configuring FTDI circuit and sending low signal to the DB7 pin. The function will be executed when LEDsOff button is pressed.

Written by O. Kulyk, St Andrews, 16.11.2012%}

clear all;

config_ftdi;

writeUSB245(0);

ResetUSB245.m

function ResetUSB245()

%{ This function resets the LED off by clearing the cache data in Matlab, re-configuring FTDI circuit and sending low signal to the DB7 pin. The function will be executed when Reset LED button is pressed.

Written by O. Kulyk, St Andrews, 15.11.2012%}

clear all;

config_ftdi;

writeUSB245(0); clear all;

CloseAllClearAll.m

function CloseAllClearAll ()

%{ This function ends the session by closing all Matlab windows, clearing Matlab editor window and cache memory. The function will be executed when CloseAllClearAll button is pressed.

Written by O. Kulyk, St Andrews, 15.11.2012%}

close all; clear all; clc; end

RawImage.m

function RawImage ()

%{ This function displays an image in Matlab viewer on a 'jet' false colour map without any modification to the image. The function will be executed when Raw Plot button is pressed.

Written by O. Kulyk, St Andrews, 29.11.2012%}

RawImage = imread(uigetfile({'*.jpeg'}));

figure;imshow(RawImage);colormap('jet');colorbar;

ExportToExcel.m

function ExportToExcel()

%{ This function converts 480 x 640 pixel image into 23 mm x 31 mm x- and y-axis calibrated at 8.5 cm distance from the lens plane of the fluorescence imaging system. The function extracts the values with 1 mm step (23 x 31 array of values), substracts background fluorescence values, applies

digital filters to smoothen out random noise and exports the values into *.xls spreadsheet for convenience.

Written by O. Kulyk, St Andrews, 02.06.2013%}

```
Scale=load('ScaleFactor.mat');
Scale = getfield(Scale,'ScaleFactor');

RawImage = imread(uigetfile({'*.jpeg'}));
Bckgr= imread(uigetfile({'*.jpeg'}));

RawImageScaled = double(RawImage).*(1-Scale)./250;
BckgrScaled = double(Bckgr).*(1-Scale)./250;
CompensImage = RawImageScaled-BckgrScaled;

FilteredImage_Median = medfilt2(CompensImage, [3 3]);
Filter_Gaussian = fspecial('gaussian',[15 15], 0.9);
FilteredImage_Median_Gaussian = imfilter(FilteredImage_Median, Filter_Gaussian, 'replicate');

[n, m] = size(RawImage);
[x_axis, y_axis] = meshgrid(1:m, 1:n);
c = double(FilteredImage_Median_Gaussian);

i=1:31;
indexi=round(i.*20.6452);
j=1:23;
j_=j';
indexj=round(j.*20.6452);
Fluorescence = c(indexj,indexi);
file = 'Results.txt';
save(file,  '-ascii', '-tabs','Fluorescence');
```

TwoDPlotY.m

```
function TwoDPlotY ()
```

%{ This function a plots fluorescence cross section along y-line from 1-31 mm. The function will be executed when “Plot along y-axis, fixed x” button is pressed.

Written by O. Kulyk, St Andrews, 02.06.2013%}

```
Scale=load('ScaleFactor.mat');
```

```
Scale = getfield(Scale,'ScaleFactor');

x=load('xFileForPlot.mat');
x_val = getfield(x,'x_val');

% y=load('yFileForPlot.mat','y'); %for plot along x-axis
% y_val = getfield(y, 'y');

RawImage = imread(uigetfile({'*.jpeg'}));
RawImageScaled = double(RawImage).*(1-Scale)./250;
AverageImage = max(max(RawImageScaled));
CompensImage = RawImageScaled-round(min(max(RawImageScaled)));
%IntensityCompensImage = mean(mean(CompensImage));

FilteredImage_Median = medfilt2(CompensImage, [3 3]);
Filter_Gaussian = fspecial('gaussian',[15 15], 0.9);
FilteredImage_Median_Gaussian = imfilter(FilteredImage_Median, Filter_Gaussian,
'replicate');

[n, m] = size(RawImage);
[x_axis, y_axis] = meshgrid(1:m, 1:n);
c = double(FilteredImage_Median_Gaussian);

j = round(x_val*640/31);
figure;
plot(y_axis./480.*23.25, c(:,j));
xlabel('y, mm'); ylabel('Fluorescence, a.u.');grid on;

figure;
surf(x_axis./640.*31, y_axis./480.*23.25, c,...
   'FaceColor', 'texturemap', 'EdgeColor', 'none');
axis([0 31 0 23.25]);
get(gcf);
get(gco);
get(gca); set(gca,'YDir','reverse');
xlabel('x, mm'); ylabel('y, mm'); zlabel('Fluorescence, a.u.');
```

RecordTestLu.m

```
function RecordTestLu()
```

```
%{ This function records 3 images, one after another, with the current fluorescence set up which has a Lumenera LM057m camera in it. The function creates a folder and automatically generates a name with the current date. It records 3 images with automatic names of date and time. The function will be executed when Record Test button is pressed.
Written by O. Kulyk, St Andrews, 11.07.2013%}
%write images with automatic names in specified folder

folderName = sprintf(datestr(now,'dd-mmm-yyyy'));
mkdir(folderName);
p=pwd;
addpath(p,folderName);

config_ftdi;

vid = videoinput('lumeneraimaqw64', 1, '640x480');
src = getselectedsource(vid);

%this is optional, the gain and the exposure parameters are updated and taken from the Lumenera manufacturer's software.
Gain=load('GainFileLu.mat');
Gain_Val = getfield(Gain,'Gain_Val');
src.Gain = Gain_Val; %max 16
Exposure=load('ExposureFileLu.mat');
Exposure_Val = getfield(Exposure,'Exposure_Val');
src.Exposure = Exposure_Val; %max 16
vid.ReturnedColorspace = 'grayscale';

writeUSB245(128);
start(vid);

for i=1:1:3
TempSnap=getsnapshot(vid);
pause(1);
filename = sprintf('%s','Test_',datestr(now,'dd-mmm-yyyy_HHMMSS'),'.jpeg')
imwrite(TempSnap,fullfile(p,folderName,filename));
end
writeUSB245(0);
stop(vid);
delete(vid);
clear vid;
```

```
clear USB245;
```

RecordControlLu.m

```
function RecordControlLu()
```

%{ This function records an image with the current fluorescence set up which has a Lumenera LM057m camera in it. The function creates a folder and automatically generates a name with the current date. It gives the image a name with the current date and time. The function will be executed when Record Control button is pressed

```
Written by O. Kulyk, St Andrews, 11.07.2013%}
%write images with automatic names in specified folder

folderName = sprintf(datestr(now,'dd-mmm-yyyy'));
mkdir(folderName);
p=pwd;
addpath(p,folderName);

clear USB245;
config_ftdi;
```

%this is optional, the gain and the exposure parameters are updated and taken from the Lumenera manufacturer's software.

```
Gain=load('GainFileLu.mat');
Gain_Val = getfield(Gain,'Gain_Val');
src.Gain = Gain_Val; %max 16
%for PpIX
Exposure=load('ExposureFileLu.mat');
Exposure_Val = getfield(Exposure,'Exposure_Val');
src.Exposure = Exposure_Val; %max 16
vid.ReturnedColorspace = 'grayscale';
writeUSB245(128);
start(vid);
TempSnap=getsnapshot(vid);
writeUSB245(0);

filename = sprintf('%s','Control_',datestr(now,'dd-mmm-yyyy_HHMMSS'),'.jpeg')
imwrite(TempSnap,fullfile(p,folderName,filename));

stop(vid);
delete(vid);
clear vid;
```

clear USB245;

ResetImaqDevice.m

function ResetImaqDevice

%{ This function resets an image acquisition device (whichever was initialised, Lumenera or Unibrain CCD cameras). The function will be executed when Reset Camera button is pressed.

Written by O. Kulyk, St Andrews, 13.05.2013%}

clear all;

imaqreset;

clear all;

Appendix XVIII: Capturing fluorescence – Image Processing

Matching features algorithms – RANSAC Image transformation

In order to compensate for camera displacement during the repetitive time course measurements an automated m-file has been written which asks to open a reference image, which would normally be a background image or the best aligned image. The algorithm will ask to open a second image which will be transformed using matching features (inliers and outliers points) on the reference fluorescent contour. Then RANSAC geometrical transformation is applied to the second image, the image is rotated and positioned to correspond to the position of the fluorescence reference contour of the first image, Figure 2. The algorithm then requests a name for the transformed image.

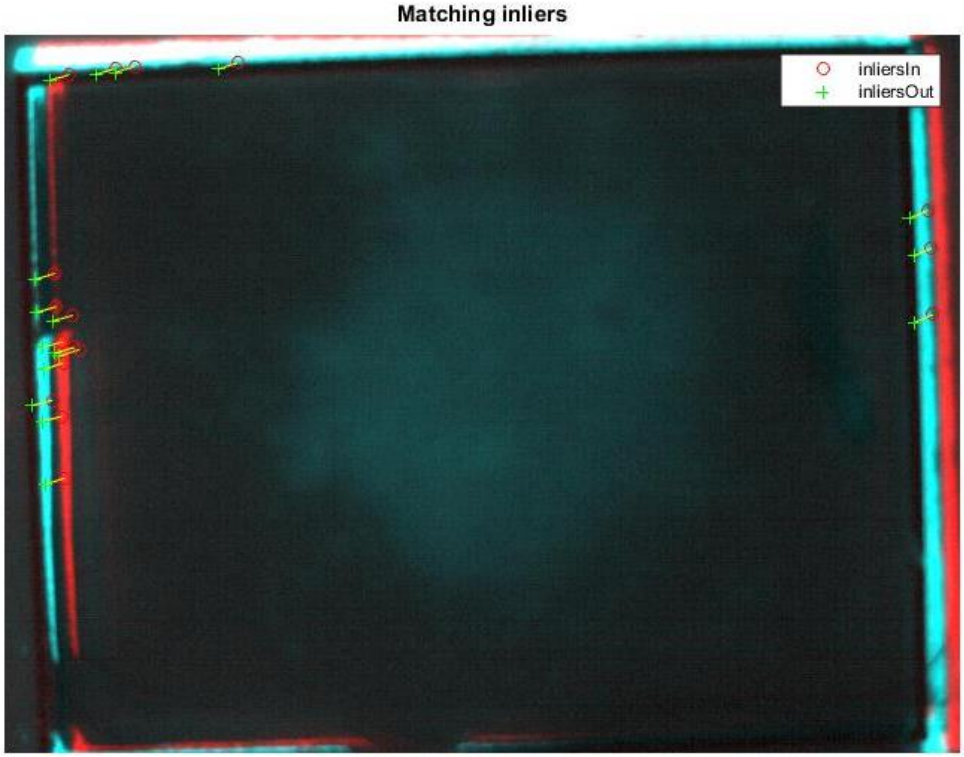

Figure 2 RANSAC geometrical transformation – the blue and the red contours are the fluorescent reference contours of the first and the second images correspondingly. The inliers and the outliers are the corresponding points which allow the rotation and the positioning of the second image with the regard to the first image.

```
% Written by Olena Kulyk, St Andrews, 2014
% Matching features algorithms, P010 recovery reference image is 0 min
% http://www.mathworks.co.uk/help/vision/ref/matchfeatures.html
% align images by matching features
% % image recovery by matching features
%
http://www.mathworks.co.uk/help/vision/ref/vision.geometrictransformestimat
or-class.html#btdyt0u
%
```

```
%Detect, extract, and match SURF features from two images.

%Read for the transform
close all; clear all;
Iin = imread(uigetfile({'*.*'})); imshow(Iin); title('Base image');
Iout = imread(uigetfile({'*.*'}));
figure; imshow(Iout); title('For the transform');

%Detect and extract features from both images.

ptsIn  = detectSURFFeatures(Iin);
ptsOut = detectSURFFeatures(Iout);
[featuresIn   validPtsIn]  = extractFeatures(Iin,  ptsIn);
[featuresOut validPtsOut]  = extractFeatures(Iout, ptsOut);

%Match feature vectors.

index_pairs = matchFeatures(featuresIn, featuresOut);

%Get matching points.

matchedPtsIn  = validPtsIn(index_pairs(:,1));
matchedPtsOut = validPtsOut(index_pairs(:,2));
figure; showMatchedFeatures(Iin,Iout,matchedPtsIn,matchedPtsOut);
title('Matched SURF points, including outliers');

%Compute the transformation matrix using RANSAC.
http://www.mathworks.co.uk/discovery/ransac.html?refresh=true

gte = vision.GeometricTransformEstimator;
gte.Transform = 'Nonreflective similarity';
[tform inlierIdx] = step(gte, matchedPtsOut.Location,
matchedPtsIn.Location);
figure;
showMatchedFeatures(Iin,Iout,matchedPtsIn(inlierIdx),matchedPtsOut(inlierId
x));
title('Matching inliers'); legend('inliersIn', 'inliersOut');

%Recover the original image.

agt = vision.GeometricTransformer;
Ir = step(agt, im2single(Iout), tform);
figure; imshow(Ir); title('Recovered image');
imwrite(Ir,uiputfile('*.jpeg'));
```

Cropping images algorithm for reference contour removal

The fluorescent reference contour is cropped from the images. The cropped area is 540 x 380 pixels area (for some cases is smaller, up to 380 x 380 pixels due to reduced study area) out of 640 x 480 pixels of not cropped image. A Matlab file is created which contains the information on cropping coordinate for each patient. An example of such Matlab script is provided below.

```
% Written by Olena Kulyk, St Andrews, 2014
```

```
% Cropping Images algorithm

close all; clear all;

Iin = imread(uigetfile({'*.*'})); imshow(Iin); title('Base image');

%identify one reference corner and a crop area for all the fluorescence
images
Iout = imcrop(Iin,[63,39 540, 380]); imshow(Iout); title(Cropped image');

imwrite(Iout,uiputfile('*.jpeg'));
```

Integrated intensity algorithm, image sectioning and correlation analysis

The fluorescence pattern is visually assessed and the fluorescence images are sectioned into the areas of interest which are “Area 1” - a peak fluorescence area, “Area 2” – an area with middle fluorescence and “Area 3” – the area with the lowest fluorescence.

A Matlab file is created for each area which contains the coordinates of the area and calculates integrated fluorescence over this area, correlates it to the monochromatic image of the skin and writes the results into an excel file.

An example of a Matlab file for such image processing is provided below.

```
% Written by Olena Kulyk, St Andrews, 2014
%for image batch processing look at
http://uk.mathworks.com/help/vision/ug/batch-process-image-
files.html?refresh=true
%Integrated intensity for a data region algorithm, 540x380 size, minus 100
pixels each side

close all; clear all;

fileFolder =
fullfile('C:\Users\ok4\Dropbox\WorkFiles\MATLAB\FluoresecnceImagingSoftware
2\data_region\Proccessing Matlab\Recovered images\Cropped rect 540 x 380
ref X47 Y35');
dirOutput = dir(fullfile(fileFolder,'*c.jpeg'));

Image0 = imread('0c.jpeg');
Image1 =   imread('10c.jpeg');
Image2 =   imread('20c.jpeg');
Image3 =   imread('30c.jpeg');
Image4 =   imread('40c.jpeg');
Image5 =   imread('50c.jpeg');
Image6 =   imread('60c.jpeg');
Image7 =   imread('70c.jpeg');
Image8 =   imread('80c.jpeg');
Image9 =   imread('90c.jpeg');
Image10 =  imread('100c.jpeg');
Image11 =  imread('110c.jpeg');
Image12 =  imread('120c.jpeg');
Image13 =  imread('130c.jpeg');
Image14 =  imread('140c.jpeg');
```

```
Image15 =  imread('150c.jpeg');
Image16 =  imread('160c.jpeg');
Image17 =  imread('170c.jpeg');
Image18 =  imread('180c.jpeg'); figure; imshow(Image18);
tumour = imread('tumourc.jpeg');

Image0 = Image0(218:263, 199:283); %the area of interest - dimensions
Image1 =   Image1(218:263, 199:283);
Image2 =   Image2(218:263, 199:283);
Image3 =   Image3(218:263, 199:283);
Image4 =   Image4(218:263, 199:283);
Image5 =   Image5(218:263, 199:283);
Image6 =   Image6(218:263, 199:283);
Image7 =   Image7(218:263, 199:283);
Image8 =   Image8(218:263, 199:283);
Image9 =   Image9(218:263, 199:283);
Image10 =  Image10(218:263, 199:283);
Image11 =  Image11(218:263, 199:283);
Image12 =  Image12(218:263, 199:283);
Image13 =  Image13(218:263, 199:283);
Image14 =  Image14(218:263, 199:283);
Image15 =  Image15(218:263, 199:283);
Image16 =  Image16(218:263, 199:283);
Image17 =  Image17(218:263, 199:283);
Image18 =  Image18(218:263, 199:283); figure; imshow(Image18);
tumour = tumour(218:263, 199:283);figure; imshow(tumour);

mean_data_region = [mean2(Image0), mean2(Image1), mean2(Image2),
mean2(Image3), mean2(Image4), mean2(Image5), mean2(Image6),...
    mean2(Image7), mean2(Image8), mean2(Image9), mean2(Image10),
mean2(Image11), mean2(Image12), mean2(Image13),...
    mean2(Image14), mean2(Image15), mean2(Image16), mean2(Image17),
mean2(Image18)];
mean_data_region_comp = mean_data_region - mean2(Image0);
mean_data_region_norm = mean_data_region_comp./255;
time = 0:10:180;
t = {'time'};
%'Mean Fluorescence over an Image', 'B2'
xlswrite('data_region.xls', mean_data_region', 'B2:B20');
xlswrite('data_region.xls', mean_data_region_comp', 'C2:C20');
xlswrite('data_region.xls', mean_data_region_norm', 'D2:D20');
xlswrite('data_region.xls', time', 'A2:A20');
xlswrite('data_region.xls', t, 'A1:A1');
xlswrite('data_region.xls', {'Mean Fluorescence'}, 'B1:B1');
xlswrite('data_region.xls', {'Minus Bckgr'}, 'C1:C1');
xlswrite('data_region.xls', {'Normilised'}, 'D1:D1');

% Fluorescence image correlation to the background
cor_to_0 = [corr2(Image0, Image0),... % Image correlation to itself
    corr2(Image0, Image1),...
    corr2(Image0, Image2),...
    corr2(Image0, Image3),...
    corr2(Image0, Image4),...
    corr2(Image0, Image5),...
    corr2(Image0, Image6),...
    corr2(Image0, Image7),...
    corr2(Image0, Image8),...
    corr2(Image0, Image9),...
    corr2(Image0, Image10),...
    corr2(Image0, Image11),...
```

```
    corr2(Image0, Image12),...
    corr2(Image0, Image13),...
    corr2(Image0, Image14),...
    corr2(Image0, Image15),...
    corr2(Image0, Image16),...
    corr2(Image0, Image17),...
    corr2(Image0, Image18)];
xlswrite('data_region.xls', {'cor_to_0'}, 'E1:E1');
xlswrite('data_region.xls', cor_to_0', 'E2:E20');

% Fluorescence images correlation to the last reading at 180 min
cor_to_18 = [corr2(Image18, Image0),...
    corr2(Image18, Image4),...
    corr2(Image18, Image2),...
    corr2(Image18, Image3),...
    corr2(Image18, Image4),...
    corr2(Image18, Image5),...
    corr2(Image18, Image6),...
    corr2(Image18, Image7),...
    corr2(Image18, Image8),...
    corr2(Image18, Image9),...
    corr2(Image18, Image10),...
    corr2(Image18, Image11),...
    corr2(Image18, Image12),...
    corr2(Image18, Image13),...
    corr2(Image18, Image14),...
    corr2(Image18, Image15),...
    corr2(Image18, Image16),...
    corr2(Image18, Image17),...
    corr2(Image18, Image18)];
xlswrite('data_region.xls', {'cor_to_18'}, 'q1:q1');
xlswrite('data_region.xls', cor_to_18', 'q2:q20');

% Fluorescence image correlation to the tumour
cor_to_tumour = [corr2(tumour, Image0),...
    corr2(tumour, Image4),...
    corr2(tumour, Image2),...
    corr2(tumour, Image3),...
    corr2(tumour, Image4),...
    corr2(tumour, Image5),...
    corr2(tumour, Image6),...
    corr2(tumour, Image7),...
    corr2(tumour, Image8),...
    corr2(tumour, Image9),...
    corr2(tumour, Image10),...
    corr2(tumour, Image11),...
    corr2(tumour, Image12),...
    corr2(tumour, Image13),...
    corr2(tumour, Image14),...
    corr2(tumour, Image15),...
    corr2(tumour, Image16),...
    corr2(tumour, Image17),...
    corr2(tumour, Image18)];
xlswrite('data_region.xls', {'cor_to_tumour'}, 'r1:r1');
xlswrite('data_region.xls', cor_to_tumour', 'r2:r20');
xlswrite('data_region.xls', {'data_region'}, 'A22:A22');
```

Appendix XIX: Diffuse reflectance measurements in phantoms

Measured voltage @2,38 MV/A gain at 50 Ohm load, V	Current @2,38 MV/A gain, A	Absolute current, A	Absolute power, W	Power, au	Simulated power, W	Power, au
1,14E-04	2,29E-06	9,6E-13	1,48E-12	1	5,29E-09	1
2,42E-05	4,85E-07	2,04E-13	3,13E-13	0,212106	1,34E-09	0,2532235
7,07E-06	1,41E-07	5,94E-14	9,15E-14	0,061894	5,07E-10	0,0958453
3,84E-06	7,69E-08	3,23E-14	4,97E-14	0,033638	2,18E-10	0,0412034
1,32E-06	2,64E-08	1,11E-14	1,71E-14	0,011567	8,49E-11	0,0160458
6,72E-07	1,34E-08	5,65E-15	8,69E-15	0,00588	4,38E-11	0,0082808
3,16E-07	6,32E-09	2,66E-15	4,09E-15	0,002765	2,69E-11	0,0050788

Appendix XX: Light transmission in brain phatnoms

BPW34 X 6 (in tissue phantom); LED = 1 A; Photodiodes response 0,48 A/W

Distance (mm)	Short circuit current (A)	Measured peak power from voltage-load, W	Measured power from current, W	Measured power from current, au	Simulated power, W	Simulated power, au
5	0,01505	0,017533164	0,031354167	1	8,568557	1
10	0,007375	0,012586761	0,015364583	0,490033223	10,52536	1,22837
15	0,004655	0,008924327	0,009697917	0,309302326	13,08922	1,527587
20	0,002668	0,005391684	0,005558333	0,177275748	15,33258	1,7894
30	0,000521	0,001069741	0,001085417	0,03461794	20,19089	2,356394
50	0,0000338	5,21678E-05	7,04167E-05	0,002245847	30,03729	3,505525

SLSD-71N300 (in tissue phantom) LED = 1 A; Photodiode response 0,55 A/W

Distance (mm)	Short circuit current (A)	Measured peak power from voltage-load, W	Measured power from current, W	Measured power from current, au	Simulated power, W	Simulated power, au
5	0,07594	0,079897441	0,138072727	1	1,21797	1
10	0,0597	0,064144081	0,108545455	0,786146958	0,910321	0,747408
15	0,02204	0,031057824	0,040072727	0,290229128	0,958836	0,787241
20	0,010695	0,016134987	0,019445455	0,14083487	0,554922	0,455612
30	0,001782	0,002709916	0,00324	0,023465894	0,36136	0,29669
50	0,000117	0,000141919	0,000212727	0,00154069	0,176415	0,144844

Appendix XXI: Ambulight PDT model

Table – Position of LED in Ambulight PDT devices

Number of LED	X position, mm	Y position, mm
1	-4	10
2	0	10
3	4	10
4	8	6
5	3	6
6	-3	6
7	-8	6
8	-8	2
9	-2	2
10	2	2
11	8	2
12	8	-2
13	2	-2
14	-2	-2
15	-8	-2
16	-8	-6
17	-3	-6
18	3	-6
19	8	-6
20	4	-10
21	0	-10
22	-4	-10
23	-10	-13
24	10	-13
25	-4	13
26	0	13
27	4	13
28	10	10
29	12	6
30	13	2
31	13	-2
32	12	-6
33	10	-10
34	4	-13
35	0	-13
36	-4	-13
37	-10	-10
38	-12	-6
39	-13	-2
40	-13	6
41	-12	10
42	-10	13

Table – Power and irradiance simulations of Ambulight device with removing LEDs from the array

Amount of LEDs removed	Number of LED taken out	Power, mW	Irradiance, mW/cm2
0	All in	50.816	7.19264
1	1	49.47	7.002123
1	2	49.44	6.997877
1	25	49.467	7.001699
1	23	50.42	7.136589
1	21	49.375	6.988677
2	21, 2	47.991	6.792781
2	23, 24	50.031	7.081529
4	23, 24, 21, 2	47.255	6.688606
8	23, 24, 21, 2, 25, 27, 34, 36	43.122	6.103609
10	23, 24, 21, 2, 25, 27, 34, 36, 9, 13	40.175	5.686483
12	23, 24, 21, 2, 25, 27, 34, 36, 9, 13, 4, 16	37.404	5.294268
14	23, 24, 21, 2, 25, 27, 34, 36, 9, 13, 4, 16, 7, 19	34.623	4.900637

Appendix XXII: Test OLEDs characterisation

Luminance and irradiance of OLED have been measured using Minolta luminance meter LS-100. For Minolta luminance meter the following settings were used:

- C.C.F. (colour correction factor) ON. CCF is used to adjust the response of the meter to measure colours greatly different from the calibration standard. CCF of 1.05 of three band fluorescence lamp is used.
- Peak mode ON. When peak mode is on only peak measurement is displayed taken during trigger time.

In order to convert luminance, cd/m2 into irradiance, mW/cm2 the following formulas are used (*):

$$\mathrm{k} = \frac{\sum E\,V}{\sum E}, effective\ spectrum$$

E – spectrum

V – eye response

$$\mathrm{Km} = 683.002\,\frac{lm}{W}, multiplicative\ constant$$

$$\mathrm{Irradiance}, \frac{\mathrm{mW}}{\mathrm{cm2}} = Luminance, \frac{cd}{m2} * solid\ angle(\pi\ for\ Lambertian\ emitter)/(\mathrm{k}\cdot\mathrm{Km})$$

Table – Test OLED devices optical power output

Test OLED 33788-02			
		Minolta Luminance measurements	
Current, mA	Voltage, V	Luminance, cd/m2	Irradinace, mW/cm2
10	3.18	101.7	0.18516
50	4.39	850	1.54756
100	5.19	1778	3.23713
150	5.79	2665	4.85206
200	6.24	3527	6.42147
250	6.6	4402	8.01455
300	6.9	5238	9.53662
350	7.18	6092	11.09147
370	7.16	6463	11.76693

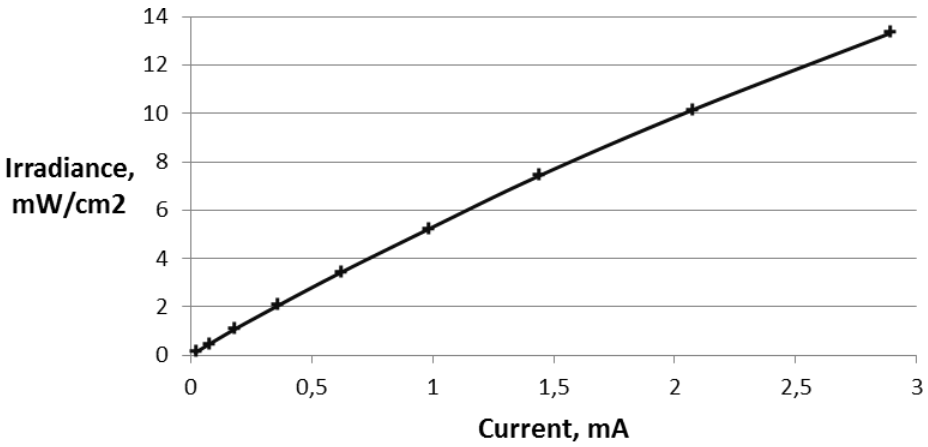

Figure - Angular emission from test OLEDs device for potential application in ambulatory devices for non-melanoma cancer treatment measured by a former group member Dr Shuyu Zhang.

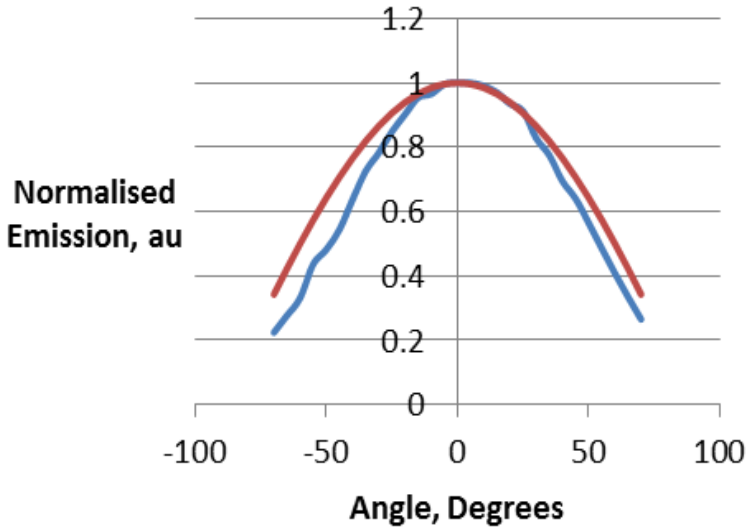

Figure - The angular dependent emission was measured when the sample was at fixed position and the detector fibre was rotated to detect the emission from the OLED. The blue line on the graph is the emission from the OLED and the dark red line is a typical Lambertian angular distribution.

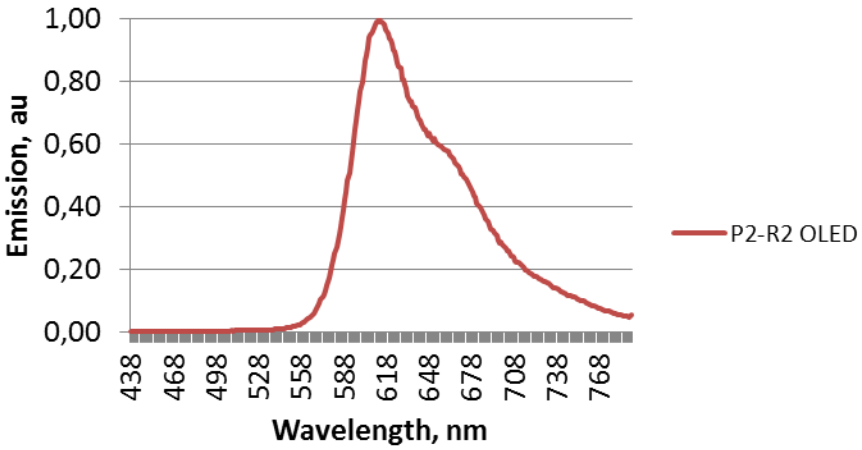

Figure - The test OLED emission spectrum measured with an Ocean Optics fibre based spectrometer.